FISH SCALE-CELLULAR COMPOSITE SYSTEM AGAINST IMPACT

CHUA YIE SUE

NATIONAL UNIVERSITY OF SINGAPORE

2016

FISH SCALE-CELLULAR COMPOSITE SYSTEM AGAINST IMPACT

CHUA YIE SUE

(B. Eng. (Civil) (Hons.), USM)

A THESIS SUBMITTED

FOR THE DEGREE OF DOCTOR OF PHILOSOPHY

DEPARTMENT OF CIVIL AND ENVIRONMENTAL ENGINEERING

NATIONAL UNIVERSITY OF SINGAPORE

2016

DECLARATION

I hereby declare that the thesis is my original work and it has been written by me in its entirety. I have duly acknowledged all the sources of information which have been used in the thesis. This thesis has also not been submitted for any degree in any university previously.

Chua Yie Sue

5 August 2016

Acknowledgements

First of all, I am very thankful to God for his great blessing and amazing grace in loving and strengthening me along this journey. I would also like to thank my family and loved ones for their continuous support, tolerance, and always encouraging me to persevere and remain focused.

I would like to express my gratitude to my supervisors, Prof. Pang Sze Dai, Prof. Quek Ser Tong, and Dr. Elliot Law. Their knowledge, insightful advice, and encouragement have helped me to complete this thesis and in the process have made me a better person in many aspects.

I would like to extend my sincere thanks to all the final year projects students, particularly Mr. Teo Fwu Chyi, Ms. Kang Mi, Mr. Foo Chee Chong, Mr. Koh Zhen Xiang, and Mr. Raja Aravindh Raj, who have helped me tremendously in my experimental and simulation work. The commitment they have shown is very much appreciated.

I would like to thank all staff members at the Structural Engineering Laboratory and the Impact Mechanics Laboratory. Special thanks go to Mr. Ang Beng Oon, Mr. Wong Kah Wai, Mr. Koh Yian Kheng, and Mr. Low Chee Wah for their generous, patient, and continuous help during my experimental work. Last but not least, I would like to extend my gratitude to all my friends that I have met in NUS for being there through all my ups and downs.

Table of Contents

Summary

Fish scale structure has been known for its good penetration resistance under localized loading while cellular material is lightweight and has excellent energy absorption capacity under compression. Hence, combining fish scale structure with cellular material can lead to a novel composite structure with improved performance against low-velocity impact. Nevertheless, past studies on fish scale structures and cellular materials have been focused on their mechanical behaviours in isolation despite the potential of improved impact performance by combining them to create a hybrid structure. Therefore, in this study, the mechanical behaviour and feasibility of a fish scale-cellular composite system for protection against low-velocity impact were investigated. Two-dimensional plane strain finite element simulations were primarily used in this study, supported by experimental validations for a number of critical aspects. The composite system comprises an assembly of overlapping plates (which represent scales) that is underlain by a cellular material layer and used to protect a surface or object from impact. Optimization of this composite system was explored and a design procedure was proposed.

The simulations and experiments showed that the composite system resists impact through two primary deformation modes: (a) bending of the scales, and (b) compression of the underlying cellular layer. The scales dissipate part of the impact energy while the underlying cellular layer acts as a cushion to absorb the remaining impact energy in order to minimize the peak stress transferred. It was shown that the composite system with curved scales can perform better than a conventional sandwich design with the same amount of materials. This is due to the additional hoop resistance from the curved shape of the scales which allows them to dissipate more impact energy as they deform. For optimum impact performance, the scales should dissipate more impact energy than

that absorbed by the underlying cellular layer so as to minimize compression on the latter in order to keep the peak stress transferred below the densification limit of the underlying cellular layer.

The deformation behaviour and impact performance of the composite system are governed by the geometrical and material properties of the scales and underlying cellular layer. The impact performance of the composite system generally improves with decreasing aspect ratio, increasing curvature, increasing degree of overlapping, and decreasing size of the scales. A geometric stiffness factor $K_{geometry}$ was proposed in this study to account for their combined effects, and it was shown that there are optimum bounds for this parameter, the four aforementioned quantities, as well as stiffness, strength, and volume of the scales relative to those of the underlying layer that can lead to optimum impact performance. When this occurs, the scales can deform and dissipate a significant amount of impact energy instead of collapsing easily or becoming over-stiff and puncturing into the underlying layer. Furthermore, it was found that the optimum range for $K_{geometry}$ reduces with increasing ratio of the yield strength of the scales to the average plateau stress of the underlying cellular layer.

Finally, with the size and energy of the impactor and limiting stress of the protected object or surface as input parameters, a design procedure for the composite system was proposed in this study. It involves three key steps: (a) selection of materials for the scales and the underlying layer, which control the deformation behaviour and the range of stress transferred when the composite system is subject to impact; (b) determining the amount of materials for the scales and the underlying layer, which governs the energy absorption capacity of the composite system; and (c) selecting a right design configuration of the scales to ensure that they deform in the intended manner. Simple methods to estimate the impact energy that can be dissipated by the scales and absorbed

by the underlying cellular layer without causing it to densify have also been proposed as part of the design procedure. The design procedure was validated numerically using an example and shown that it is able to result in optimum designs of the fish scale-cellular composite system.

List of Tables

List of Figures

List of Symbols

D	Width of impactor
H	Height of scale
$K_{geometry}$	Geometric stiffness factor of scales
L	Span of underlying cellular layer
L_h	Span of scale
L_s	Length of scale
M	Mass of impactor
R	Radius of scale
S	Horizontal spacing between scales
t_s	Thickness of scale
T	Thickness of underlying cellular layer
v	Velocity of impactor
V_s	Volume of scales
V_u	Volume of underlying cellular layer
W_i	Energy exerted by impactor
W_s	Impact energy dissipated through plastic deformation of scales
W_u	Impact energy absorbed by underlying cellular layer

1.0 Introduction

This chapter provides a background on impact problems and a review of existing man-made approaches and natural systems that provide protection against such external threats. In particular, the mechanical behaviour of fish scale structures and cellular materials are discussed. Thereafter, a novel bio-inspired composite system that combines fish scale structures with cellular materials is proposed for protection against impact. The chapter ends with the formulation of the objective and scope of this research.

1.1 Impact problems

In recent years, the development of protective systems against impact has been gaining worldwide attention due to increasing threats and awareness of security and safety issues. Generally, impact can be categorized under either low or high velocity. Low-velocity impact typically involves slow moving objects such as drop weights, while high-velocity impact normally includes high-speed projectiles such as bullets and blast debris. However, definitions for these categories may vary widely as the transition between them is not well-defined in the literature. For example, several authors (Shivakumar *et al.*, 1985; Sjoblom *et al.*, 1988; Cantwell and Morton, 1991) defined low-velocity impact as events which can be treated as quasi-static, the upper limit of which can vary from 1 m/s to 10 m/s depending on the target stiffness, material properties, and mass and stiffness of the impactor. Conversely, Abrate (1991) stated that impact speeds of less than 100 m/s may be considered as low. Naik and Shirirao (2004) defined low-velocity impact based on the duration of contact with an impactor, while other authors (Liu and Malvern, 1987; Joshi and Sun, 1987) suggested that the type of impact be categorized by damage patterns. Low-velocity impact may also be defined as that which produces strain rates between 10^{-1} s^{-1} to 10^{1} s^{-1}, as shown in Table 1.1. For high-velocity impact, the typical speed encountered ranges from 300 m/s for handguns to 800 m/s for assault rifles to several thousand m/s for explosions, which may correspond to strain rates of 10^4 s^{-1} to 10^6 s^{-1} (Zhu, 2012).

While high-velocity impact has been getting a lot of attention from military and defense-related industries due to the high visibility and more spectacular damage caused by such events, low-velocity impact occurs more frequently and in some situations can be significant and have severe consequences. Low-velocity impact is potentially dangerous mainly because the damage is usually undetected or underestimated. The damage may worsen under service load and cause significant reduction in strength, which may lead to deterioration in performance or even structural failure and loss of human lives (Abrate, 1998). Low-velocity impact commonly occurs in many engineering applications such as in the aerospace, marine, wind turbines and sporting goods industries. For aircraft structures, such impact may be caused by a tool dropped during maintenance, hail strike in service, or impact with other structures at the runway during taxiing (Tsartsaris *et al*., 2011; Mohotti *et al*., 2013; Wang *et al*., 2013). In marine and offshore structures, a wide range of low-velocity impact may occur due to the operating environment, such as those caused by sea ice, moorings, and other floating objects (Liu *et al*., 1987; Dvorak and Suvorov, 2006; Liew *et al*., 2009). Railway and highway structures require protection from vehicle crash, while piers and bridges such as the Stonecutters Bridge in Hong

Table 1.1: Loading classifications due to strain rate (adapted from Zhu, 2012).

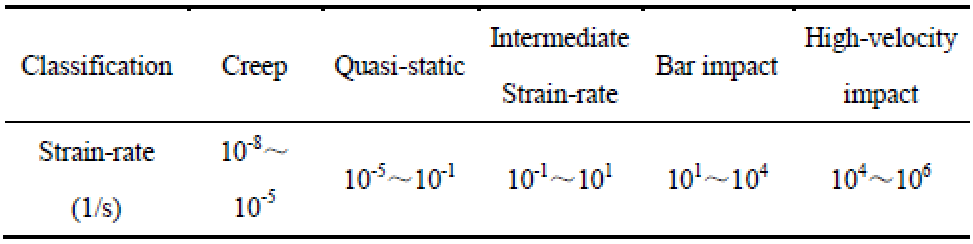

Classification	Creep	Quasi-static	Intermediate Strain-rate	Bar impact	High-velocity impact
Strain-rate (1/s)	10^{-8}～10^{-5}	10^{-5}～10^{-1}	10^{-1}～10^{1}	10^{1}～10^{4}	10^{4}～10^{6}

Kong must be designed against impact from ships (Svensson, 2009; Sharma *et al*., 2012; Jiang and Chorzepa, 2014).

According to Song *et al.* (2011), impact may lead to severe injury or damage to a protected object through two ways. Firstly, an impactor could penetrate or puncture the protected object, causing damage deep within the object. Secondly, the impactor might transfer a large amount of impact energy and high stresses to the protected object, leading to severe deformation and disintegration of the protected object. Hence, in principle, a good protective system should have an outer layer that has high stiffness and strength to prevent penetration, coupled with an inner layer that has high energy dissipation capacity and able to limit stresses transferred to the protected object.

1.2 Man-made protective systems

In recent years, many high-performance engineering components and systems that have high strength and toughness have been developed and used for protection against impact loads. They include heavily reinforced concrete, high strength metal alloys, and sandwich structures.

1.2.1 Reinforced concrete

The application of concrete against impact is not limited only to primary structural members. It is also used as barriers and sacrificial layers to protect against impact loads. For instance, in addition to preventing or mitigating the uncontrolled release of radioactive materials to the environment during operation or when an accident occurs, the containment structures of nuclear power plants are designed to withstand the impact of an aircraft (Riera, 1980). Another example where reinforced concrete is used for protective purpose is buffer stops to prevent railway vehicles from going past the end of a physical section of a track. The popularity of reinforced concrete as a protective system arises from its high compressive strength, durability, relatively low cost, and ease of being shaped into various forms. However, since concrete is inherently brittle and has low tensile resistance, it has to be sufficiently thick and heavily reinforced to provide effective protection against impact loads. This may lead to difficulties during casting if the reinforcement is too dense which can result in loss in strength.

Many approaches have been examined in past studies to improve the impact performance of reinforced concrete. These include the use of high strength concrete which is produced by reducing the water-to-cement ratio and the addition of silica fume to improve its strength and workability (Marar *et al*., 2001). However, scabbing at the rear face is expected to be more severe in elements that are made of high-strength concrete because of its relatively high brittleness (Dancygier and Yankelevsky, 1996). Another form of concrete that has been investigated is reactive powder concrete which has compressive strengths ranging from 200 MPa to 800 MPa (Richard and Cheyrezy, 1995). This material is produced by elimination of coarse aggregates, reduction of water-to-cement ratio, and introduction of mineral admixtures. However, even though this material has very high compressive strength, its ductility is no better than that of conventional mortar (Richard and Cheyrezy, 1995).

To improve the ductility and tensile strength of concrete, the inclusion of fibers has been considered in many studies. Fiber-reinforced concrete has been reported to have superior performance under impact loads compared to normal concrete, for example increased resistance to cracking and spalling (Song and Hwang, 2004), as well as reduced crater diameter, crack propagation, and disintegration when subject to impact loads (O'Neil *et al*., 1999; Luo *et al*., 2000). Steel fibers are normally used for this purpose. The combined use of steel and polypropylene fibres have also been proposed to increase ductility (Qian and Stroeven, 2000; Afroughsabet and Ozbakkaloglu, 2015).

Despite having high compressive strength, protective systems made of reinforced concrete are typically bulky and have relatively low strength-to-weight ratio. It is susceptible to cracking under impact which may lead to structural instability and failure. Even though the use of fibre reinforcements does improve its tensile properties and ductility, good quality mix is not easy to achieve and hence pose problems when a huge quantity of concrete is needed.

1.2.2 High strength metal plates

Other than concrete, steel and aluminium are also common materials used for protection against impact loads due to their high strength and ductility. Design optimization of metal plates for protection against impact has long been of interest in shipbuilding industries, offshore structures, and nuclear power plants.

At present, protective plates are commonly made of steel due to its high strength and lower cost (Kasten, 2010). Several authors have studied and produced charts and empirical equations for perforation resistance of steel plates under low-velocity impact (Lepareaux *et al.*, 1989; Jones, *et al.*, 2008; Jones and Paik, 2012). However, Kasten (2010) compared the properties of aluminium and steel plates as shown in Table 1.2 and recommended that steel should be replaced with aluminium for lightweight structures. This is because aluminium alloys are 45 percent lighter than steel and has higher energy absorption capacity per unit density (Herrington and Latorre, 1998; Kasten, 2010; Lamb and Beavers, 2010; Mohotti *et al.*, 2013).

Nevertheless, while high strength metal plates provide good resistance against impact loading, they are not efficient in distributing the impact forces transferred to an underlying protected object or surface as shown in Figure 1.1. Hence, this results in high stress concentrations exerted on a protected object or surface.

1.2.3 Sandwich structures

Sandwich structures possess many advantages: improved stability; weight savings; and in some cases, ease of manufacture and repair. In a sandwich structure, composite laminates and metals are commonly used as facesheets, while the core is made of metallic and nonmetallic honeycombs, cellular foams, balsa wood, or lattice structures (Daniel, 2010; Kim, 2011). The overall performance of sandwich structures depends on the material properties of their constituents (i.e. facesheet, adhesive, and core), geometric dimensions, and type of loading. Under impact loads, the facesheets are subjected primarily to tension or compression to resist bending while the core helps to stabilize the facesheets and resist the shear stresses. However, according to Abrate (1998), deformation of a sandwich structure is dominated by the behaviour of the core material when it is subject to localized loading. Due to low fracture toughness of the core material, the rigidity of a sandwich structure in the transverse direction, i.e. across its thickness, is usually low. Abrate (1998) also reported that sandwich structures subject to concentrated loads may fail due to tensile fracture of the facesheets, debonding at the interfaces between the core and the facesheets, indentation failure of the facesheets, core crushing, wrinkling of the facesheets under compression, and global buckling. As shown in Figure 1.2, damage of a sandwich structure is rather localized when subject to impact.

To sum up, man-made protective systems such as reinforced concrete and high strength metal plates are typically bulky, have relatively low performance-to-weight ratio, and are inefficient in distributing impact forces. On the other hand, sandwich structures are lightweight but susceptible to localized damage and exhibit relatively low damage tolerance when subject to localized impact.

Table 1.2: Comparison of aluminium and steel plates (Kasten, 2010).

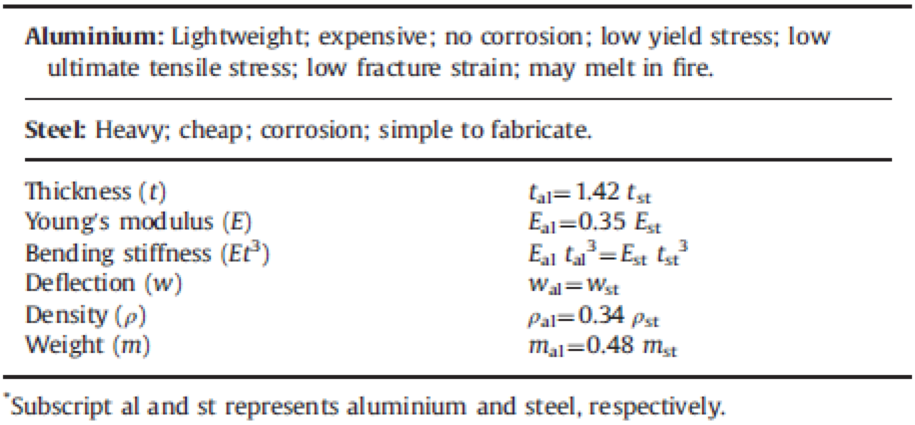

Aluminium: Lightweight; expensive; no corrosion; low yield stress; low ultimate tensile stress; low fracture strain; may melt in fire.	
Steel: Heavy; cheap; corrosion; simple to fabricate.	
Thickness (t)	$t_{al} = 1.42\ t_{st}$
Young's modulus (E)	$E_{al} = 0.35\ E_{st}$
Bending stiffness (Et^3)	$E_{al}\ t_{al}^3 = E_{st}\ t_{st}^3$
Deflection (w)	$w_{al} = w_{st}$
Density (ρ)	$\rho_{al} = 0.34\ \rho_{st}$
Weight (m)	$m_{al} = 0.48\ m_{st}$

*Subscript al and st represents aluminium and steel, respectively.

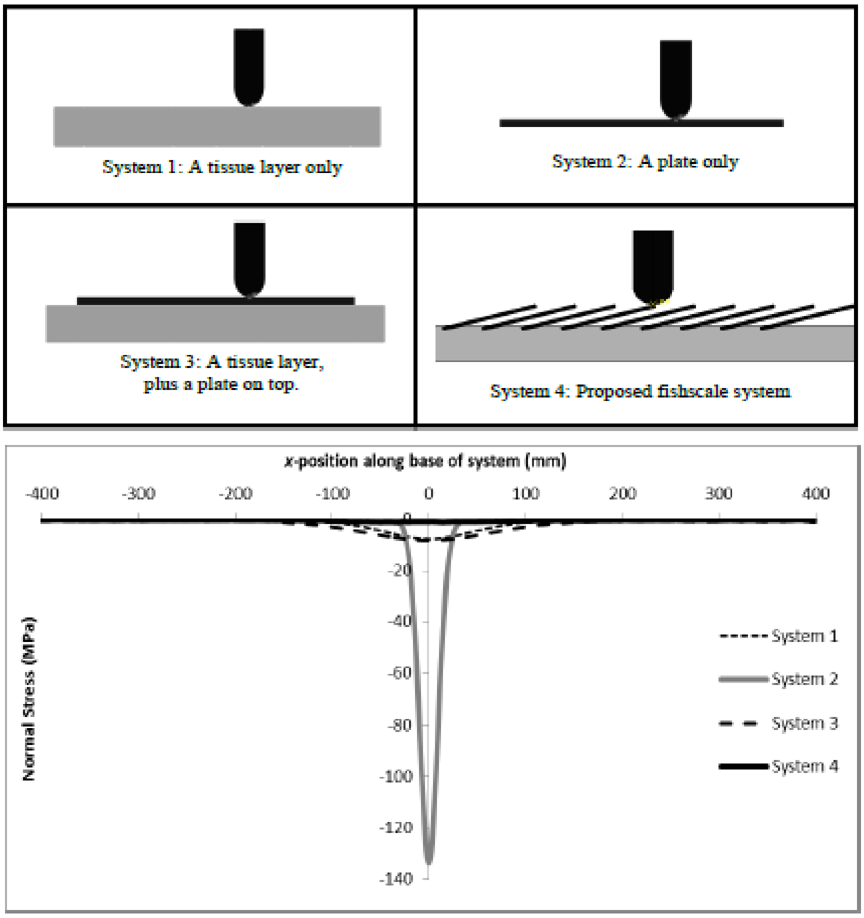

Figure 1.1: Normal compressive stress envelopes along underside of protective systems with various configurations (Oh, 2013).

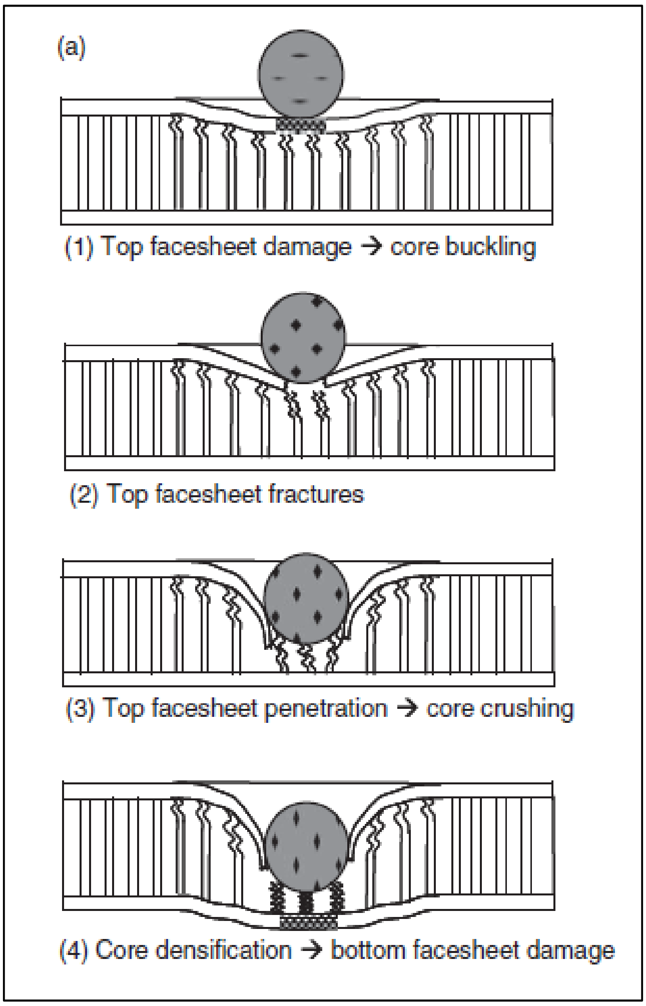

Figure 1.2: Damage evolution in sandwich plates (Abrate, 1998).

1.3 Natural armours and fish scale structures

Protective systems found in nature are often lightweight but have relatively high load bearing capacities and toughness. In some cases, they are made of seemingly inferior building blocks. Such natural design and materials may serve as inspiration for novel solutions to many engineering problems (Barthelat, 2007). Using this concept of biomimicry, many man-made materials and structures with remarkable properties have recently been created (Sanchez *et al*., 2005). For example, the earthquake-resistant structure of the Beijing National Aquatics Center (nicknamed the "Water Cube") is inspired by the natural formation of soap bubbles, while formaldehyde-free wood glue that is used to produce PureBond hardwood plywood is inspired by the adhesive proteins produced by blue mussels to attach themselves to rocks (Miles, 2011).

Many animals have armours that protect them from external threats. These include mammals (e.g., armadillo and pangolin), reptiles (e.g. alligator, crocodile, lizard, and turtle), and numerous species of fish as shown in Figure 1.3. Despite the wide variation in their structure and composition, these natural armours have a distinctly similar design concept: they are composed of hard plates attached to a soft body by collagen fibers or muscles. The strength of these armours results from their hierarchical structure (Ajdari *et al*., 2009; Yang *et al.*, 2013) as shown in Figure 1.4. For example, the armour of a nine-banded armadillo (*Dasypus novemcinctus*) has a sandwich structure with a dense outer layer that encloses a porous core (Figure 1.4(a)). Such a configuration is found in many animal structures requiring low density with good energy absorption capability (Chen *et al*., 2012; Yang *et al*., 2012).

Another example is Arapaima (*Arapaima gigas*) which has three layers of protection: dense lamellae of oriented collagen fibers, dense mineral, and overlapping scales as displayed in Figure 1.4(b). These scales have considerable flexibility as a result of the softer internal collagen layer (Yang *et al*., 2012, Yang *et al*., 2014). On the other hand, the alligator gar (*Actractosteus spatula*) has scales with jagged edges that are attached to the musculature of the fish as presented in Figure 1.4(c). When it is threatened, the cutting edges of the scales are exposed as a defense mechanism when the fish flexes its body. In addition, the scales of the alligator gar are more rigid than those of the Arapaima due to the complex arrangement of mineralized collagen fibers in the scales since they are designed for slashing and puncturing (Yang *et al*., 2012).

Figure 1.3: Some animals having flexible dermal armour: (a) arapaimas, (b) alligator gar, (c) armadillo, (d) alligator (e) leatherback turtle, and (f) Gila monster (adapted from Yang *et al.*, 2012).

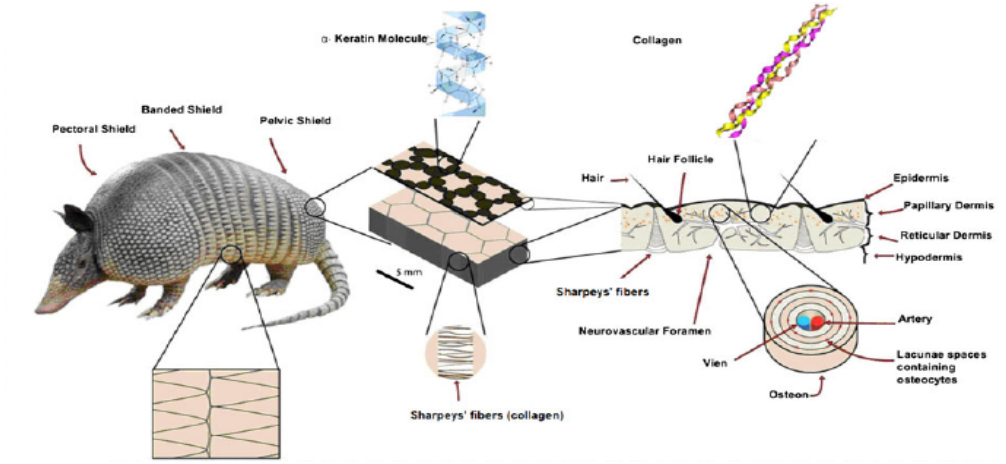

(a) Armadillo

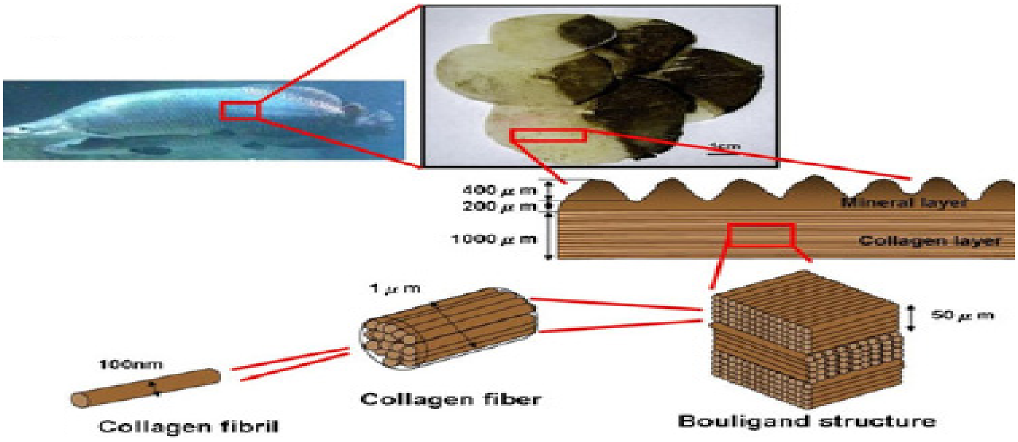

(b) Arapaima

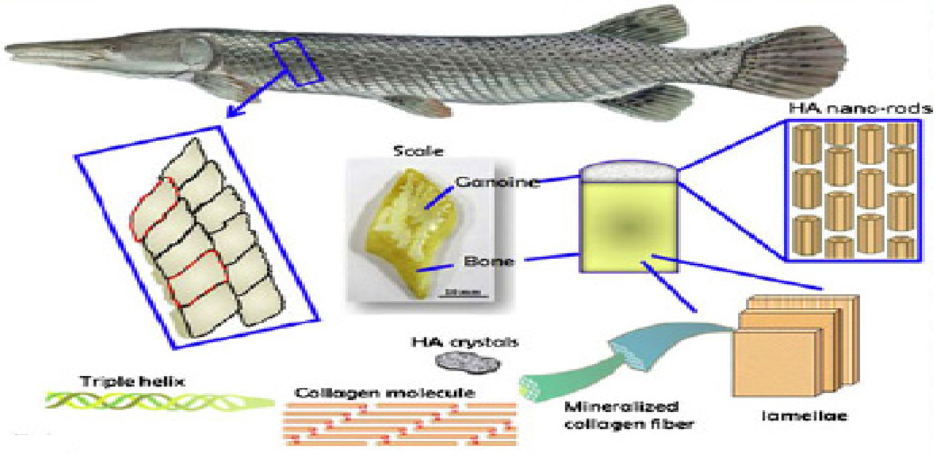

(c) Alligator gar

Figure 1.4: Hierarchical structure of flexible dermal armours (adapted from Yang *et al*., 2012).

Many of the above-mentioned examples of protective systems found in nature consist of small plates (i.e. the scales) growing out of a tissue layer, that are characterized by a large variety of shapes, sizes, and properties as depicted in Figure 1.5. Such structures are termed as fish scale structures. They provide a flexible and lightweight protective outer layer on the dermis of a wide variety of fish and reptiles to protect against penetration. Vernerey and Barthelat (2010) studied the response of a fish scale structure with different arrangements and properties of the scales using a two-dimensional mathematical model assuming a constant curvature of bending. They found that fish scale structures possess strain stiffening response as displayed in Figure 1.6, which can play a large role in preventing local unstable deformation that can threaten a fish during swimming and predator attack by distributing the stress over a larger area. Also, scale density (i.e. average number of overlapping scales per unit span of the fish scale structure) and attachment-scale stiffness ratio (i.e. stiffness of joints between the scales and the underlying skin relative to bending resistance of the scales) affect the deformation response of the system as shown in Figure 1.7. They found that higher scale density and lower scale-attachment stiffness ratio result in improved penetration resistance.

Browning (2012) examined the performance of macroscale fish scale structure prototypes made of acrylonitrile butadiene styrene (ABS) scales that are embedded within a silicon rubber layer (Figure 1.8). Through simulations and experimental tests on the prototypes, they examined the effects of various structural parameters including angle, degree of overlapping, volume fraction, and aspect ratio of the scales on the deformation mechanisms of the fish scale structure such as scale bending, scale rotation, and tissue shear as shown in Figure 1.9. These deformation mechanisms were found to govern the ability of the composite structure to protect an underlying substrate.

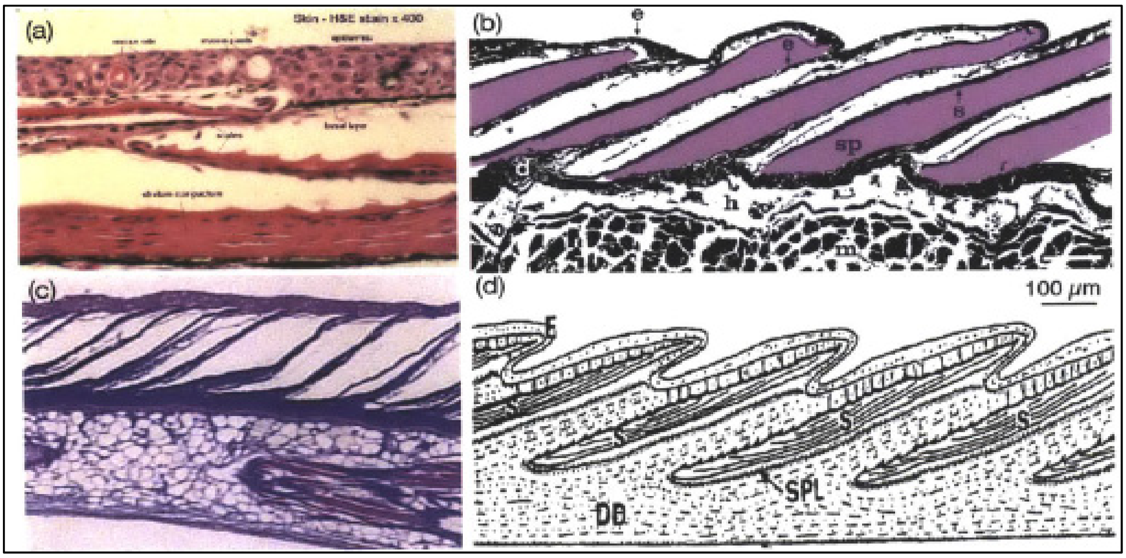

Figure 1.5: Histology of integument in different species of teleost fish: (a) trout, (b) mangrove killifish, (c) unknown, and (d) cichlid (adapted from Browning, 2012).

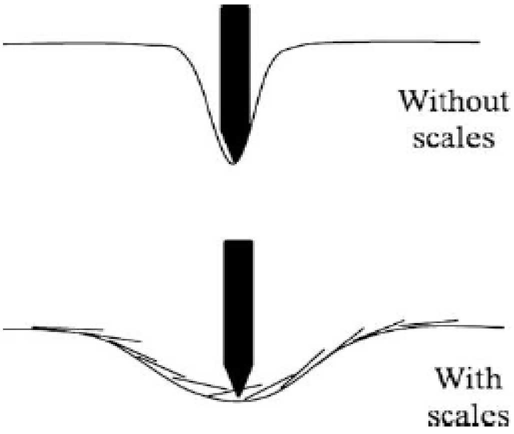

Figure 1.6: Illustration of the role of fish scales in preventing unstable localized deformation (Vernerey and Barthelat, 2010).

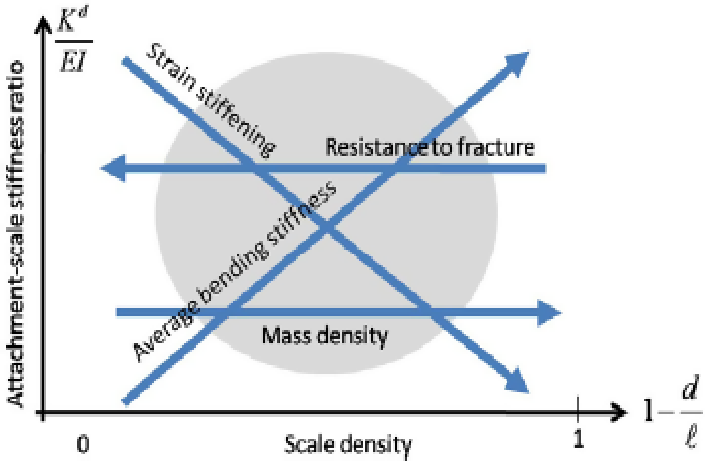

Figure 1.7: Properties of a fish scale structure as functions of its underlying microstructure (Vernerey and Barthelat, 2010).

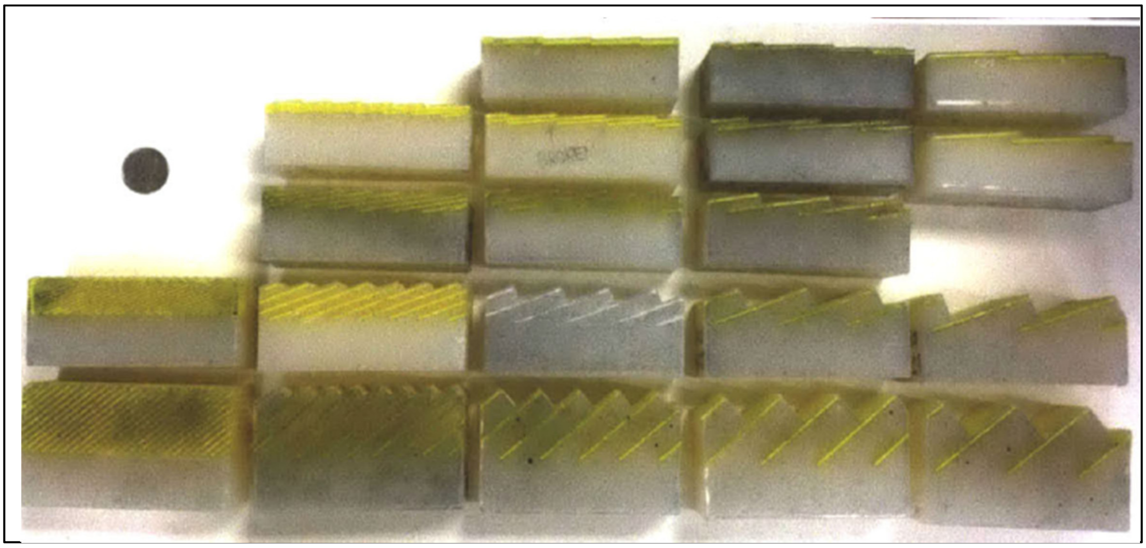

Figure 1.8: Macroscale fish scale structure prototypes made of ABS scales embedded within silicon rubber layer (Browning, 2012).

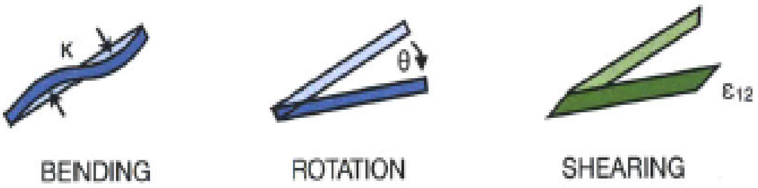

Figure 1.9: Deformation mechanisms of a scale under uniform compression (Browning, 2012).

Recently, Rudykh *et al.* (2015) investigated the trade-off between flexibility and penetration resistance of a bio-inspired 3D-printed scale-soft matrix composite by conducting indentation tests to obtain its protective properties and three-point bending tests for its flexibility as displayed in Figure 1.10. The results show that the trade-off between these conflicting properties (flexibility and penetration resistance) is governed by the scale inclination angle and volume fraction. A good balance between these properties is required for optimum performance of the flexible armour system.

1.4 Cellular materials

Besides providing penetration resistance, a good protective system requires the ability to dissipate impact energy (Song *et al.*, 2011). A class of materials that has such a protective quality is those with cellular structures, which are known to have excellent energy absorption capacity under compressive loading.

A cellular structure consists of a large number of enclosed spaces (or cells), formed by an interconnected network of struts or plates that form the faces of the cells. There are

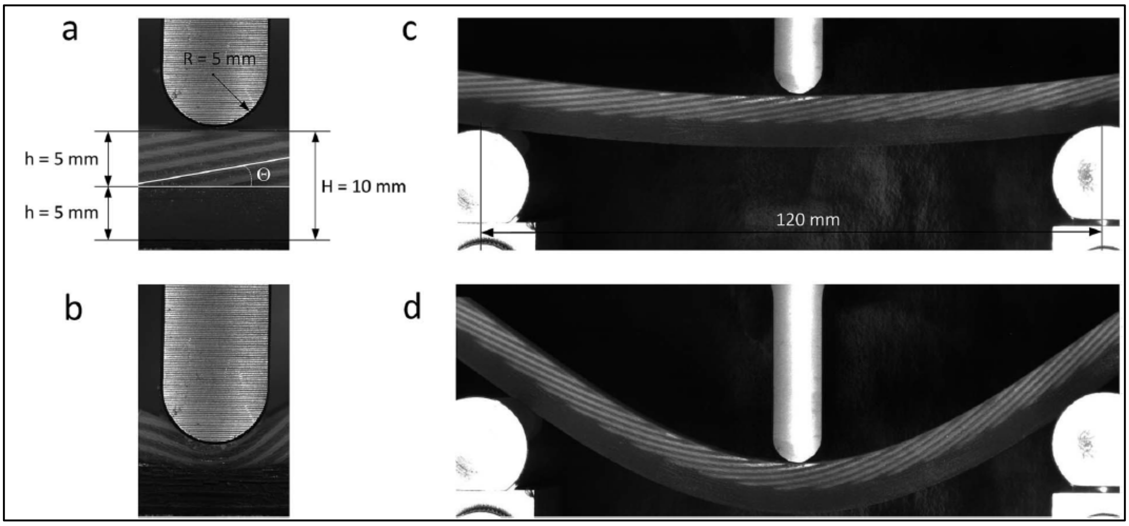

Figure 1.10: Fish scale structure specimens subject to indentation and three-point bending tests: (a) specimen before indentation, (b) finite indentation, (c) specimen at initial bending, and (d) finite bending of specimen (Rudykh *et al.*, 2015).

many cellular materials found in nature such as wood and cork (that have prismatic, honeycomb-like cells), and the inner core of plant stems and trabecular bone (which have polyhedral cells) as shown in Figure 1.11. Natural cellular materials such as wood and bamboo have been widely used as structural materials due to their relatively low cost but good strength and versatility.

In recent years, the structure of natural cellular materials has been mimicked in engineering honeycombs and foams, with applications ranging from lightweight structural panels to energy absorbing padding and thermal insulation (Gibson and Ashby, 1997). Polymer foam is one of the man-made foams widely used in the automotive, transport, and building industries due to its superior capabilities as mentioned above (Flores-Johnson and Li, 2010). Compared to elastomers, natural and man-made cellular materials have relatively high stiffness but low density as shown in Figure 1.12. Hence, natural cellular materials such as bamboo, cork, and soft wood, as well as man-made cellular materials such as polymer and metallic foams have good performance-to-weight ratios and are suitable for applications where lightweight is an important factor.

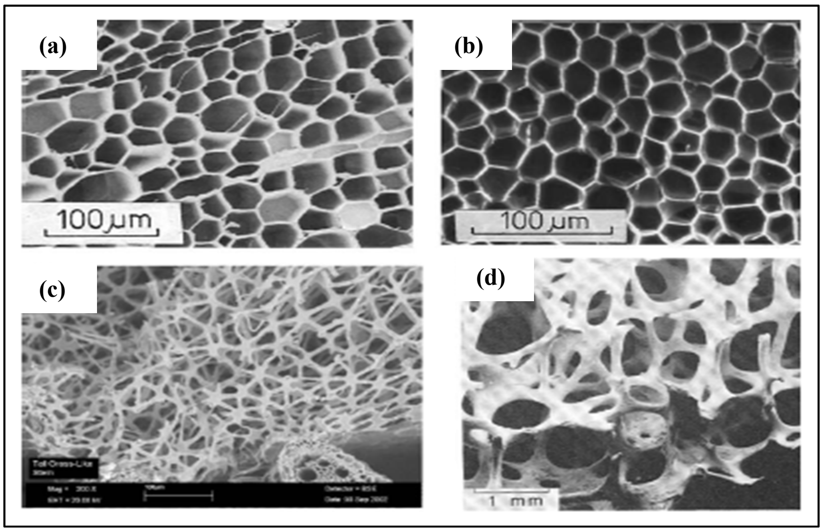

Figure 1.11: Examples of cellular solids in nature: (a) balsa wood, (b) cork, (c) inner core of plant stem, and (d) trabecular bone (adapted from Gibson *et al.*, 2010).

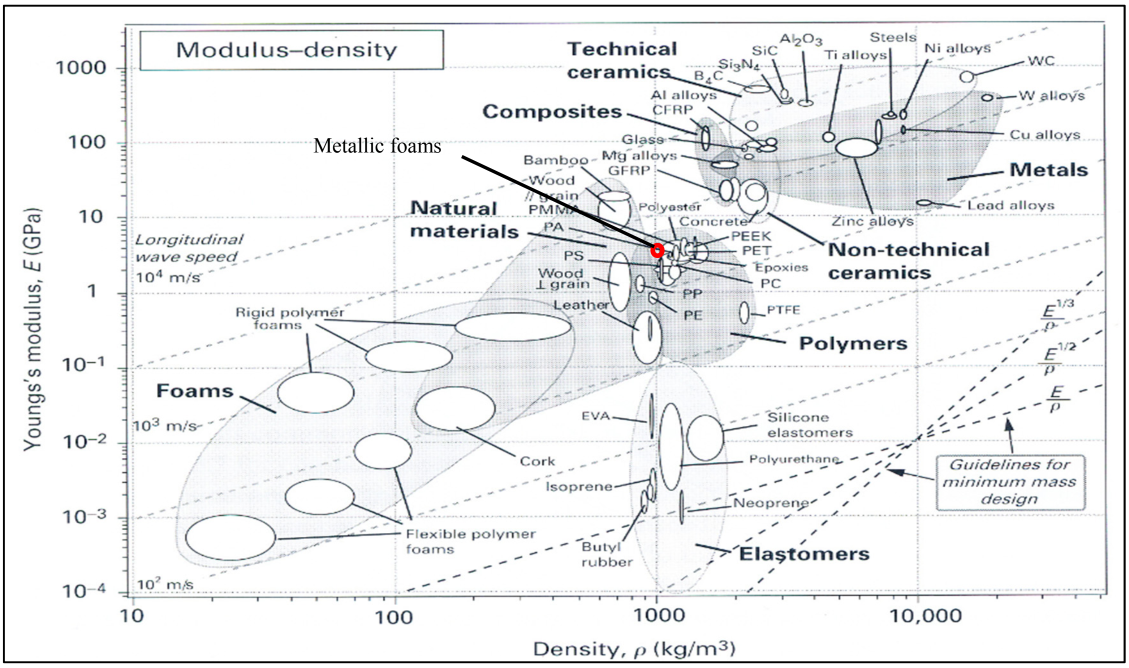

Figure 1.12: Plot of the Young's modulus as a function of density for different materials (adapted from Gibson and Ashby, 1997; Gibson *et al.*, 2010).

1.4.1 Mechanical response under compression and tension

As shown in Figure 1.13, the uniaxial compressive stress-strain curves for cellular structures with different cell wall materials are characterized by three stages: (a) a linear elastic regime, corresponding to cell edge bending or face stretching; (b) a stress plateau, corresponding to progressive cell collapse by elastic buckling, plastic yielding, or brittle crushing; and (c) a final regime of densification, corresponding to the complete collapse of the cells throughout the material and subsequent loading of the cell edges and faces against one another. Cellular solids are able to undergo large strains of up to 80 percent before densification occurs due to their high porosities of up to 90 percent. Consequently, cellular structures have good potential for impact protection as they can absorb considerable amount of energy while maintaining low stresses (Han *et al.*, 1998; Gibson and Ashby, 1997).

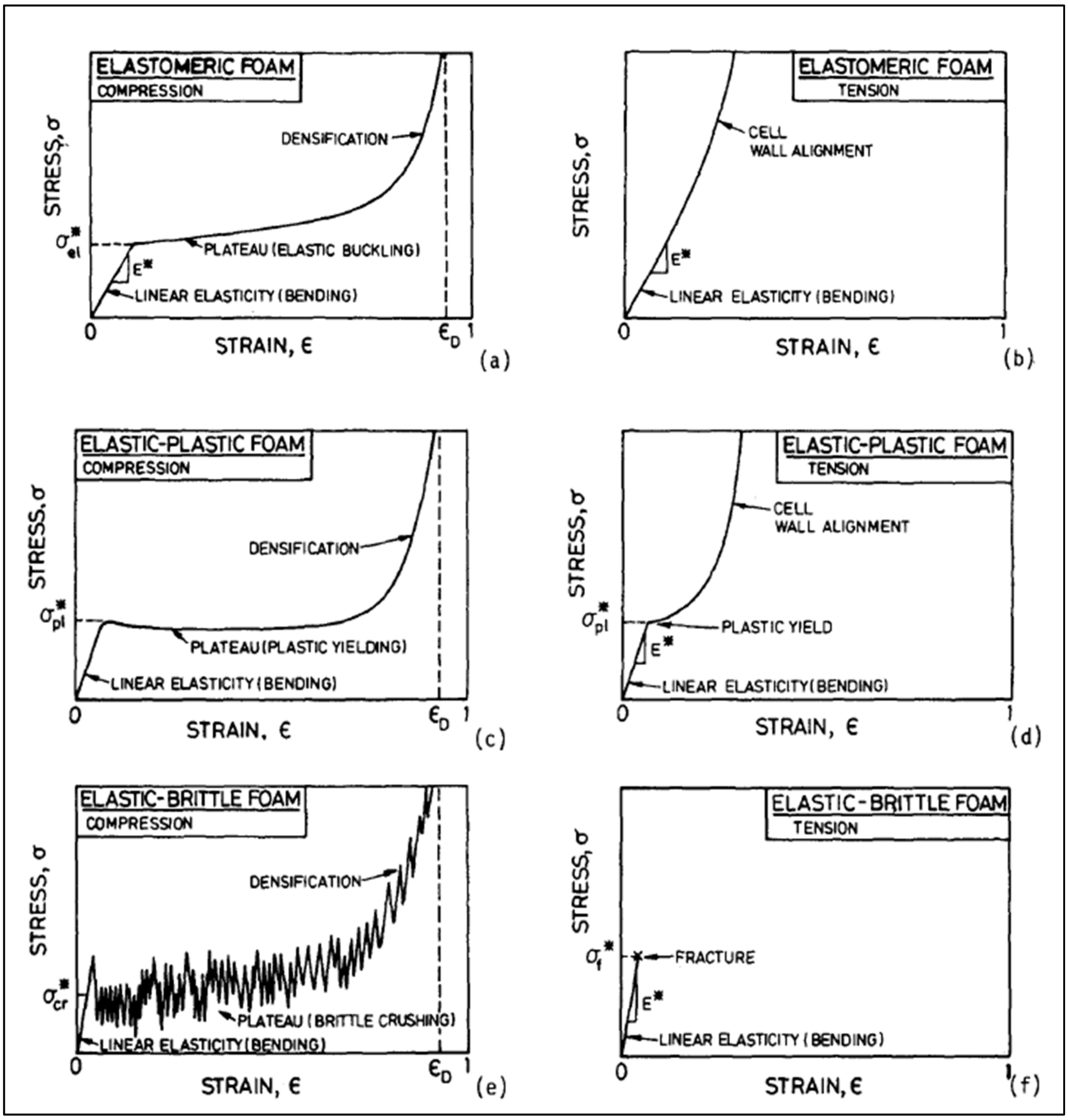

Figure 1.13: Schematic uniaxial compressive and tensile stress-strain curves for cellular materials: (a) and (b) elastomeric foam; (c) and (d) elastic-plastic foam; (e) and (f) elastic-brittle foam (Gibson, 1989).

The tensile behaviour of cellular solids varies with cell wall material as depicted in Figure 1.13. The linear elastic response of cellular materials under tension at small strains is caused by cell wall bending. However, as the tensile strain increases the stress plateau disappears for elastomeric and brittle foams. This is because the cell walls of elastomeric foams become more oriented with the loading direction resulting in increased tensile stiffness, while the cell walls of brittle foams rupture when their tensile strength is reached. On the other hand, elastic-plastic foams undergo plastic yielding when their tensile yield stress is reached, following by an increase in tensile stiffness due to cell wall alignment and ultimately fracture of the cell walls.

1.4.2 Example of natural cellular material: cork

Cork is a honeycomb-like cellular material which possesses high stiffness-to-weight ratio; high strength-to-weight ratio; excellent fatigue properties, thermal and acoustic insulation; corrosion resistance; and high compressibility and energy absorption capability (Pereira *et al.*, 1987; Pina and Fortes, 1996; Silva *et al.*, 2005; Pereira, 2007; Sousa-Martins *et al.*, 2012). The cells in cork are roughly hexagonal across their tangential section, whereas in the transverse and radial sections they are shaped like little bricks as shown in Figure 1.14 (Gibson *et al.*, 2010). The corrugations of the cell walls in cork play an important role in the different deformation behaviours of cork under compression and tension.

Cork has been used to make gaskets and for sealing wine reservoirs as it can accommodate large elastic distortion and volume change but its closed cells are impervious to liquid. The recovery capability of cork after compression is also important for gaskets, allowing a continuous pressure against both sealed surfaces. Due to its excellent energy absorption capability and high friction, it is commonly used for flooring purposes and footwear soles. It also functions as a good packaging material because it is able to absorb energy and reduce stress exerted to a protected object. In buildings and other civil construction works, cork products may be used for thermal insulation, vibration insulation, acoustic correction, floor covering, wall covering, false ceilings, and expansion joints.

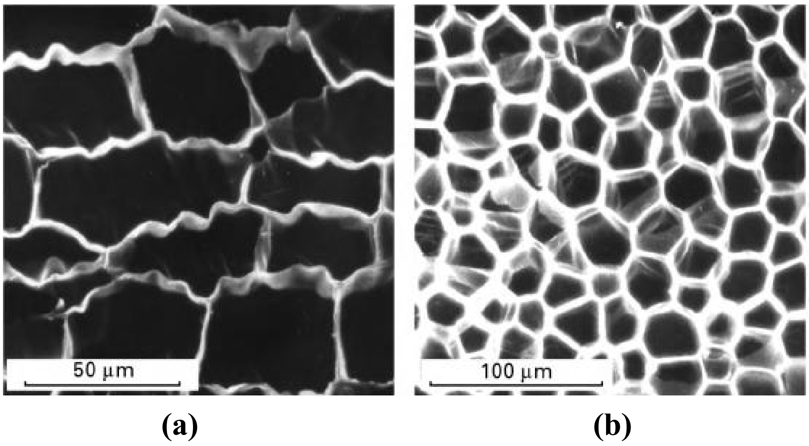

Figure 1.14: Scanning electron micrographs of cork cells, showing corrugations: (a) transverse/radial section, and (b) tangential section (Gibson *et al.*, 2010).

The mechanical behaviour of natural cork and cork agglomerates (which are produced by mixing cork granules with epoxy resin as binding agent) under uniaxial compressive loading has been studied by several authors including Fortes and Rosa (1992), Gibson *et al.* (1997), Fortes *et al.* (2004), Gameiro *et al.* (2007), Anjos *et al.* (2008), and Soares *et al.* (2011). Its compressive stress-strain response as shown in Figure 1.15 demonstrates three distinct stages of deformation as displayed earlier in Figure 1.13. Generally, maximum strains up to 80 percent or 85 percent can be reached by cork under compression.

On the other hand, tensile behaviour of cork has been less widely studied compared to its compressive behaviour. As shown in Figure 1.16, the tensile stress-strain response of cork is very different from its compressive response. There is no significant plateau stage in the tensile stress-strain response of cork and the material fractures at relatively small strains after the cell walls are straightened and once their tensile strength is reached (Rosa and Fortes, 1991; Gibson *et al.*, 2010). Pereira (2007) and Moreira *et al.* (2010) reported that the tensile modulus of cork is higher than its compression modulus due to the difference in cell wall deformation under tensile and compressive loads (Rosa and Fortes, 1991; Anjos *et al,*. 2008).

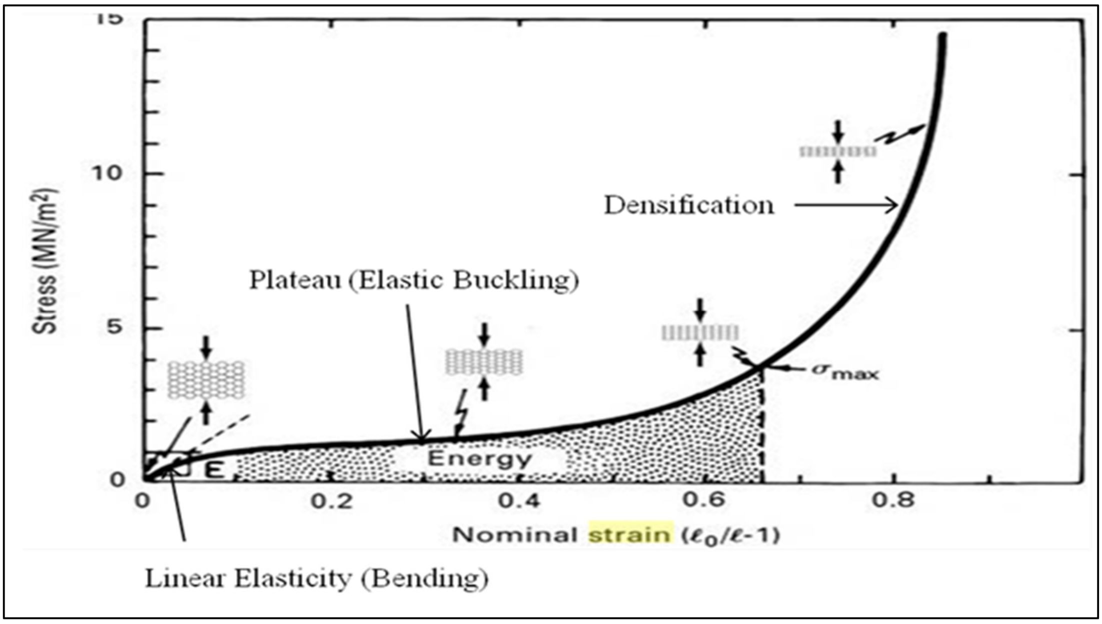

Figure 1.15: Uniaxial compressive stress-strain curve of cork (adapted from Pereira, 2007).

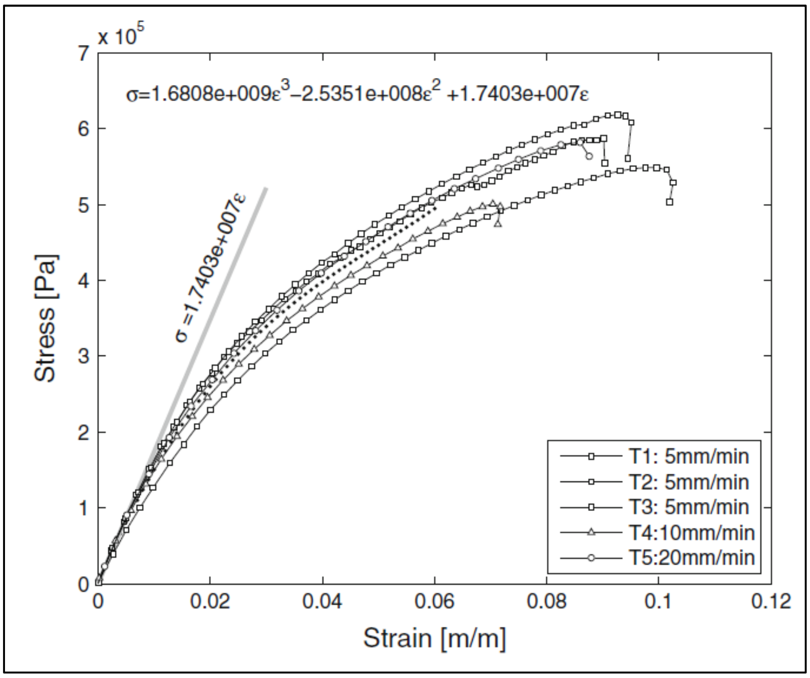

Figure 1.16: Uniaxial tensile stress–strain curve of cork (Moreira *et al*., 2010).

Gameiro *et al*. (2007) found that the Young's modulus and plateau stress of cork increase with higher strain rate up to a value of 200 s^{-1}, but stabilize thereafter when the strain rate is further increased. In addition, they reported that natural cork has poorer mechanical performance than cork agglomerates.

Castro *et al*. (2010) carried out bending and drop-weight tests on a sandwich structure with agglomerated cork as the core material and found that its performance depends on the cork granule size and density. Moreover, when compared with other synthetic core materials such as Nomex and Rohacell, agglomerated cork showed minimal damage as displayed in Figure 1.17. Gameiro *et al.* (2010) also found that cork has good recovery capacity which is attributed to its corrugated cell walls.

1.4.3 Example of man-made cellular material: polymer foam

An example of man-made cellular materials is polymer foam, which has three-dimensional cells. Two examples of polymer foam are shown in Figure 1.18. They may have an open-cell structure which allows fluids to flow between the cells, or a closed-cell structure where the cells are fully enclosed by cell walls. As shown in Figure 1.19,

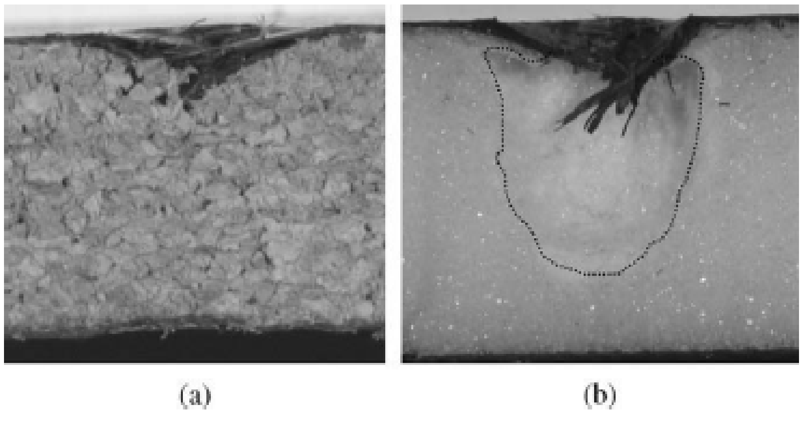
(a) (b)

Figure 1.17: Transversal section view of the damaged zone in sandwich panels subject to local impact: (a) cork agglomerate specimen, and (b) Rohacell specimen (Castro *et al.*, 2010).

the compressive behaviour of polymer foams such as polyurethane foam shows the three typical and distinct regions: initial elastic, plateau, and densification (Shim and Yap, 1997; Lu and Yan, 2003). As with other cellular materials, the mechanical behaviour of polymer foams depends highly on the structure of the cell walls, and the density and material properties of which they are made (Lu and Yan, 2003; Rizov, 2007).

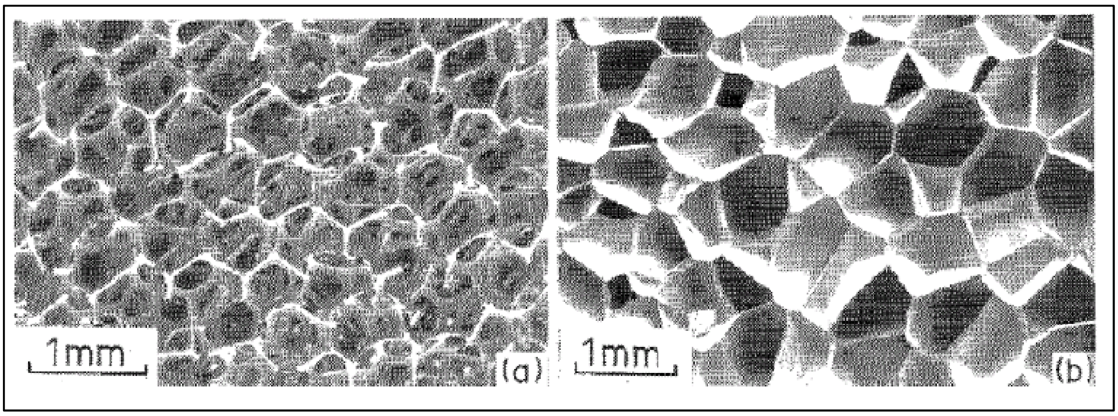

Figure 1.18: Example of (a) open cell, and (b) closed cell polyethylene foam (Lu and Yu, 2003).

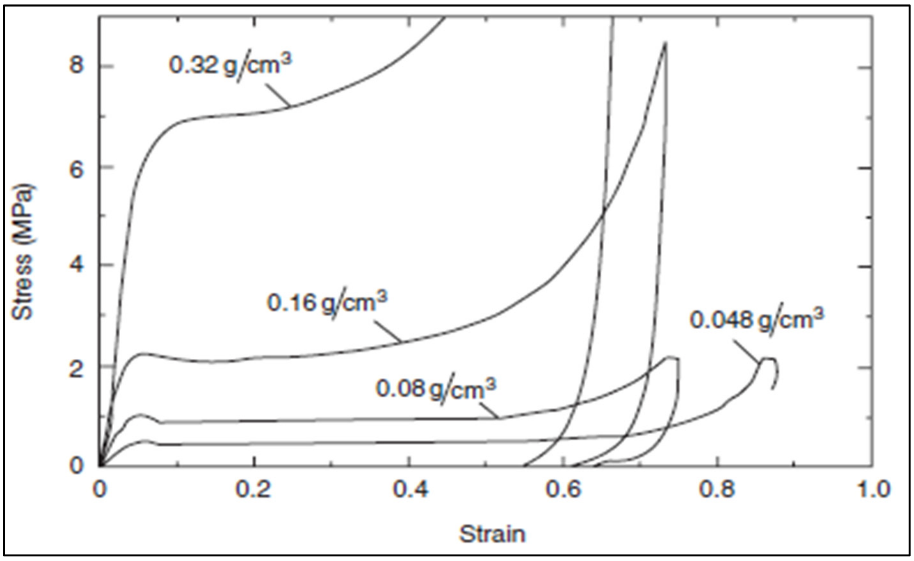

Figure 1.19: Compressive stress-strain curves of closed cell rigid polyurethane foam with different densities (Lu and Yu, 2003).

Due to their excellent thermal, acoustic, buoyancy, and structural properties, the use of polymer foams has increased immensely in aerospace, automotive, and marine applications. For instance, polymer foams such as closed-cell polyurethane are frequently used in shock absorption applications, as filler material inside a structure, or as packaging material around a fragile component because the foam can serve as a cushion to limit the transmitted force (Green *et al.*, 1969; Meinecke and Schwaber, 1971; Maji *et al.*, 1995). Furthermore, they are used as core material in sandwich panels in order to increase bending resistance and flexural rigidity while minimizing total weight (Gibson and Ashby, 1997; Vinson, 1999; Rizov, 2007).

1.5 Proposed fish scale-cellular composite system

As discussed in Section 1.3, fish scale structure possesses good penetration resistance. On the other hand, cellular materials have excellent energy absorption capacity under compressive loading and are lightweight, but they have lower damage tolerance and exhibit highly localized deformation under concentrated loads as depicted in Figure 1.17 due to their relatively weak tensile resistance. Therefore, combining fish scale structure as an outer layer with cellular structures as an underlying material (as shown in Figure 1.20) may enable these two systems to compensate each other's weaknesses and lead to a novel composite structure that potentially has improved performance against impact loading. Conceptually, when subject to impact, the assembly of scales can stop the penetration of an impactor while the underlying cellular layer provides a cushioning effect to minimize the stresses transferred and absorb the impact energy. This composite structure would most probably be more effective for protection against low-velocity impact by relatively slow-moving objects than by high-velocity impact such as bullets that are small and can easily puncture the scales and cellular layer.

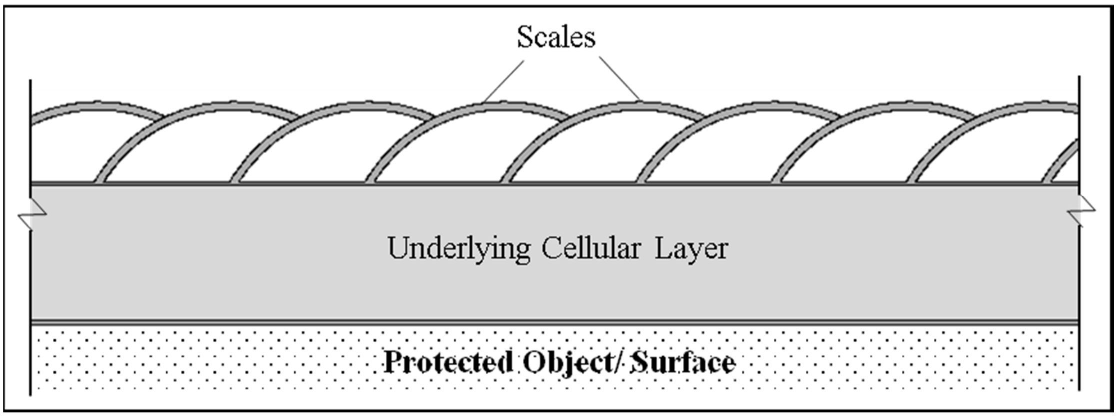

Figure 1.20: Proposed fish scale-cellular composite system.

However, no significant work on combining fish scale structure with cellular materials to create a hybrid structure aimed at improving impact performance has been carried out so far despite its apparent potential. Past studies on fish scale structures and cellular materials have focused on their mechanical behaviour in isolation. Vernerey and Barthelat (2010) looked into the behaviour of an assembly of scales without considering the influence of an underlying layer, while Browning (2012) examined the performance of fish scale structures underlain by silicone rubber which is an incompressible elastic material. Since the underlying layer is expected to have significant effects on the deformation mode of the scales and the energy absorption capacity of the composite system, the composite action between the scales and its underlying layer should be accounted for when assessing the performance of the composite system under impact.

1.6 Objective and scope

Therefore, the objectives of this study were to:

i. Examine the mechanical behaviour and feasibility of a fish scale-cellular composite system for protection against low-velocity impact.
ii. Propose a procedure for the optimal design based on an understanding of the interaction between the key parameters of the proposed composite system.

As shown in Figure 1.20, this composite system consists of an assembly of overlapping plates (which represent scales) that is underlain by a cellular material layer and is used to protect a surface or object against impact. The impact performance of the composite system was assessed mainly based on the peak stresses transferred to the protected object or surface. Finite element simulations were primarily used for this study, supported by experimental work. The versatility of finite element simulations facilitates their efficient use to perform parametric studies in order to provide an understanding of the mechanical behaviour of the composite system and to deduce the optimal configuration of the composite system for specific applications. Limited experimental work was also necessary to validate the numerical model. However, constraints imposed by the availability of suitable equipment and fabrication resources restricted the extent to which experimental validation could be satisfactorily done.

In view of the above, this study was divided into five stages:

i. A finite element model was created for the analysis of the impact performance of the fish scale-cellular composite system. This included the selection of suitable material models, in particular, the calibration of these models for the cellular layer.

ii. Experimental tests were carried out to validate the finite element model before it was used for the simulations.

iii. Proof-of-concept simulations were performed for specimens with different design configurations, followed by physical drop-weight impact tests on selected configurations to assess the feasibility of the composite system for impact protection.

iv. Parametric studies were conducted to examine the effects of various geometrical and material properties of the scales and underlying layer to deduce the optimum configurations for protection against impact loads.

v. Finally, a design process for the composite system was established.

1.7 Organization of this thesis

The ***methodology*** adopted in this study is discussed in Chapter 2. The problem description and an overview of the model used in this study are presented, followed by discussion on the finite element implementation and experimental setup.

The ***typical response*** of the fish scale-cellular composite system is presented in Chapter 3 together with experimental validation of the finite element model. Subsequently, the impact performance of several specimens with different design configurations are examined numerically and experimentally to assess the feasibility of this composite system as a protective structure.

The ***effects of geometrical properties of the scales*** on the impact performance of the composite system are discussed in Chapter 4. They include aspect ratio, curvature, degree of overlapping, and relative size of the scales. The combined effects of these geometrical parameters on the deformation mode and impact performance of the composite systems are considered, and the optimum bounds for these parameters are proposed.

In Chapter 5, the ***effects of material properties of the scales and underlying cellular layer***, specifically their stiffness and strength, are investigated and the optimum ranges of these quantities are proposed. Thereafter, the combined effects of material and geometrical properties of the scales and underlying cellular layer on the impact performance of the composite system are explored.

A ***design procedure*** for the composite system is proposed in Chapter 6. Three key steps of the design process are examined: (a) selection of materials for the scales and underlying cellular layer; (b) determining the amount of materials for the scales and underlying layer, as well as the energy absorption capacity of the composite system; and (c) selecting an optimal design configuration of the scales. The design process is validated numerically using an example problem.

Finally, Chapter 7 concludes the main findings from this study and discusses several recommendations for future work.

2.0 Finite element model and experimental set-up

The mechanical behaviour of the fish scale-cellular composite system was examined primarily using finite element simulations, supported by experimental work for a number of critical aspects. The problem description and an overview of the model adopted in this study will be presented in this chapter. Details of the finite element implementation and setup for the experimental work are thereafter discussed.

2.1 Problem description

Figure 2.1 shows the schematic view of one of the fish scale-cellular composite system with a finite span used in this study. An assembly of overlapping plates (which represents scales) was formed by attaching the lower end of each scale to a continuous top plate that connected all the individual scales. The scale assembly was combined with a cellular material layer which functions as the underlying layer to protect an object or surface (henceforth called the protected object or surface) from transverse impact by an impactor.

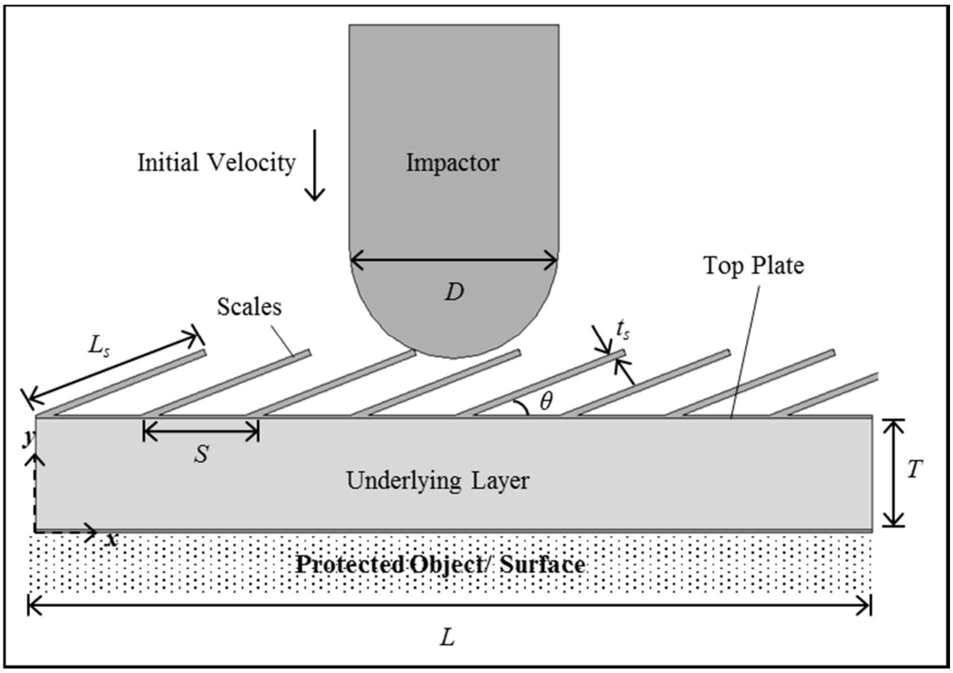

Figure 2.1: Schematic view of fish scale-cellular composite system with flat scales.

The geometrical properties and topological arrangement of the scales are defined by the following parameters: length L_s, thickness t_s, inclination angle θ, and spacing S between adjacent scales, as shown in Figure 2.1. In this study the response of the system, including the influence of the shape of the scales, is explored. Figure 2.2 shows another configuration involving an assembly of curved scales. The shape of these scales is characterized by their curvature, defined as the ratio of the curved length L_s to radius of curvature R. The aspect ratio of each scale is defined as the ratio of its curved length L_s to thickness t_s. The degree of overlapping is defined as the ratio of the span L_h of a scale to spacing S between adjacent scales, while the relative size of a scale is the ratio of its span L_h to the impactor width D. Unless otherwise stated, all cases were modelled with a span L of 400 mm and underlying layer thickness T of 50 mm. As shown in Figure 2.3 there was no perceivable change in the stress distribution along the base of the composite system and the peak stress transferred when the span-to-thickness ratio L/T was greater than 8, hence it was the minimum L/T ratio required to minimize edge effects. The impactor had a semi-circular tip with width D of 100 mm and total length of 150 mm.

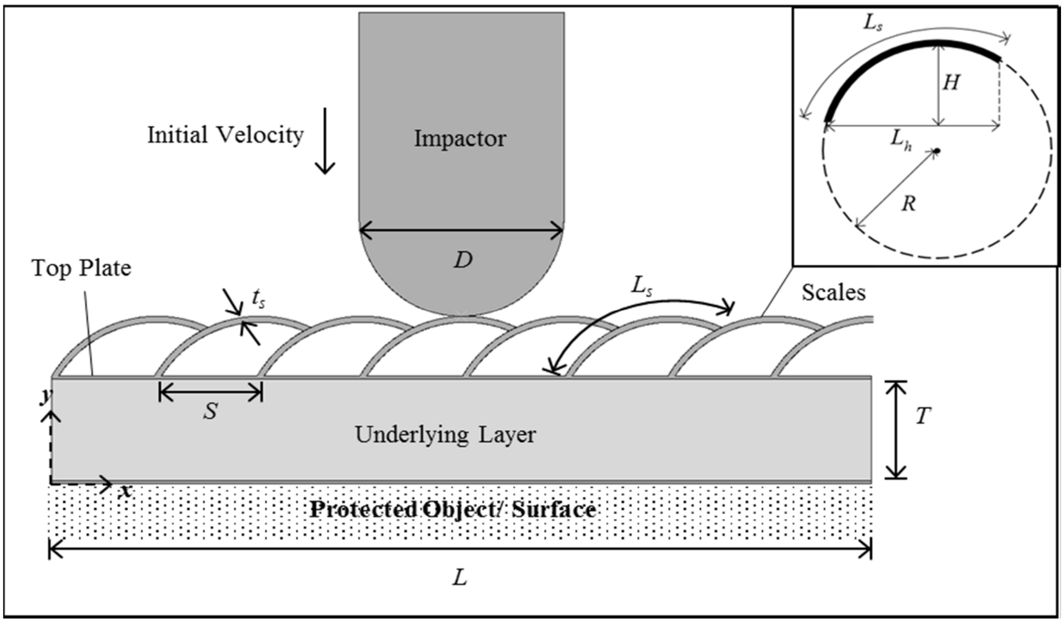

Figure 2.2: Schematic view of fish scale-cellular composite system with curved scales.

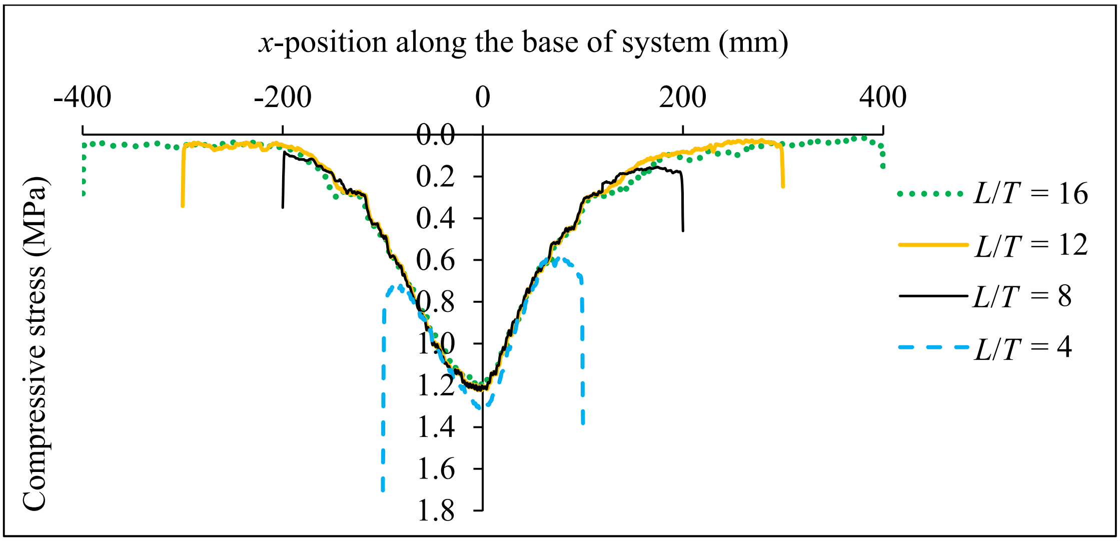

Figure 2.3: Normal compressive stress envelope along the base of fish scale-composite system with different span-to-thickness ratios *L*/*T*.

2.2 Finite element implementation

Finite element simulations using Abaqus/Explicit were adopted to investigate the mechanical response of the fish scale-cellular composite system under impact loads. Details of the finite element model are discussed in this section.

2.2.1 Loading and boundary conditions

Unless otherwise stated, the specimens of the composite system were subject to a normal impact force exerted by an impactor with mass of 64.15 kg/mm and a fixed initial velocity of 10 m/s for all cases. The initial velocity was defined using the "Predefined Fields" function in Abaqus. The impactor was aligned along the centerline of the specimen as shown in Figure 2.1 and was constrained from rotation and displacement in the *x*-direction. On the other hand, the base of the specimen was constrained from displacements in both *x* and *y*-directions while the lateral edges of the specimen were free.

2.2.2 Constraints and contact interactions

For convenience in assigning the contact interactions, the scales and top plate were modeled as a single instance in Abaqus instead of separate instances. Contact interaction between the impactor and the external surfaces of the scale assembly was defined using the surface-to-surface penalty contact algorithm whereas the contact interaction within the external surfaces of the scale assembly itself was assigned using self-contact kinematic contact algorithm in Abaqus. To prevent penetration between contacting surfaces, the default "hard" contact option was used in the normal direction. Unless otherwise stated, the tangential direction was assumed to be frictionless.

The assembly of scales was assumed to be perfectly bonded to the underlying cellular layer. To model this, a tie function was used to attach the bottom surface of the assembly of scales to the top surface of the underlying cellular layer. On the other hand, the impactor was constrained as a rigid body since it was assumed to be relatively undeformable compared to the composite system.

2.2.3 Material properties of scales

Aluminium was chosen as the first candidate material for the scales as well as the top plate. It was modeled as an elastic-perfectly plastic material with Young's modulus of 70 GPa, Poisson's ratio of 0.32, yield strength of 250 MPa, and mass density of 2700 kg/m^3.

2.2.4 Material properties of cellular layer

Cork was selected for the underlying cellular material due to its high compressibility and energy absorption capacity as discussion is Section 1.4.2. Agglomerated cork with mass density of 180 kg/m^3 and average cork granule size of 4 mm to 6 mm was chosen for this study. Figure 2.4 displays its compressive stress-strain response that was

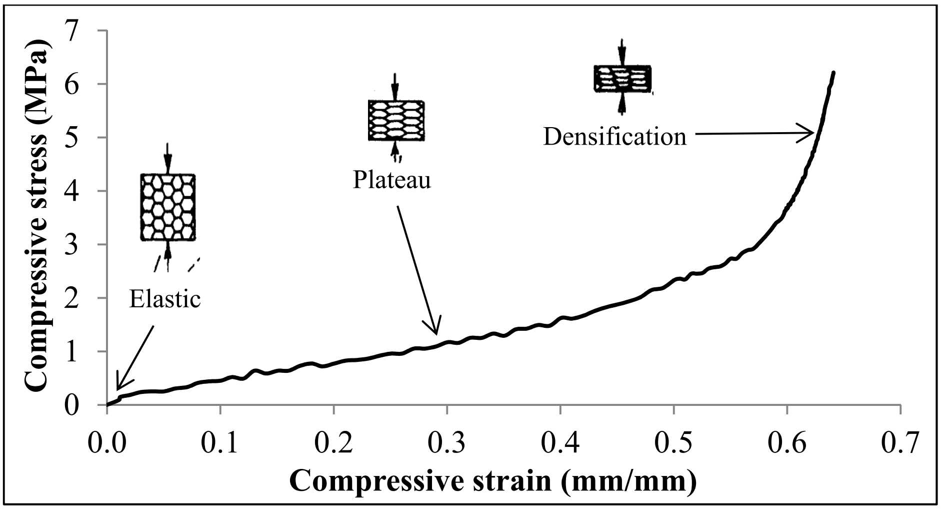

Figure 2.4: Compressive stress-strain curve of cork from experiment.

obtained from uniaxial dynamic compression tests. It is observed that the stress-strain response of the cork material shows the three distinct deformation stages typical of cellular materials: (a) linear elastic, (b) plateau, and (c) densification. The Young's modulus of the cork during its elastic phase is 88 MPa while its Poisson's ratio was assumed to be zero.

To capture the mechanical behaviour of cork in the numerical simulations, the low-density foam material model was chosen. A detailed discussion of the selection of material models for the underlying cellular layer can be found in Appendix A.

2.2.5 Mesh convergence and computational time-step

The finite element model was discretized using bilinear quadrilateral (Q4) plane strain elements. Mesh convergence tests were carried out to make sure the selected element sizes were appropriate. These tests were conducted on a composite specimen with curved scales of $L_s/t_s = 28.6$, $L_s/R = 1.5$, $L_h/D = 0.8$, and $L_h/S = 1.5$. Figure 2.5 shows the overall force-displacement response of the specimen with different average element sizes as displayed in Figure 2.6. It is clear that the maximum element size should not be greater than 0.3 mm, i.e. there must be at least five elements across the thickness of each scale, in order for the results to converge. However, the underlying layer is quite large relative to the scales. Hence, to cut down the computational time a larger average element size of 1.0 mm was used for the underlying layer as shown in Figure 2.6(d) instead of using a constant average element size of 0.3 mm throughout the model. As shown in Figure 2.5, the result obtained using this larger element size for the underlying layer agrees well with the case with small elements throughout. Therefore, these element sizes were adopted for the simulations in this study. Consequently, the total number of elements in each simulation ranged from 80,000 to 100,000 depending on the geometry of the scales.

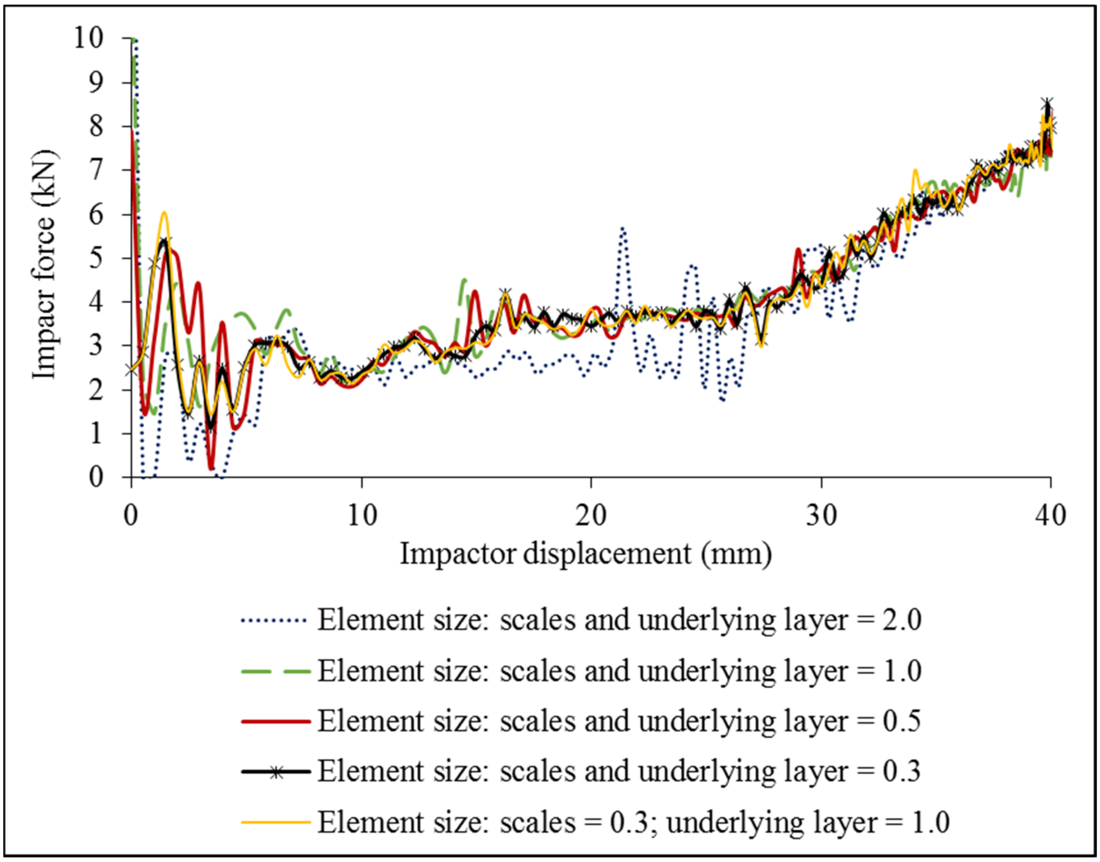

Figure 2.5: Overall force-displacement response for specimen with various element sizes (units are in mm).

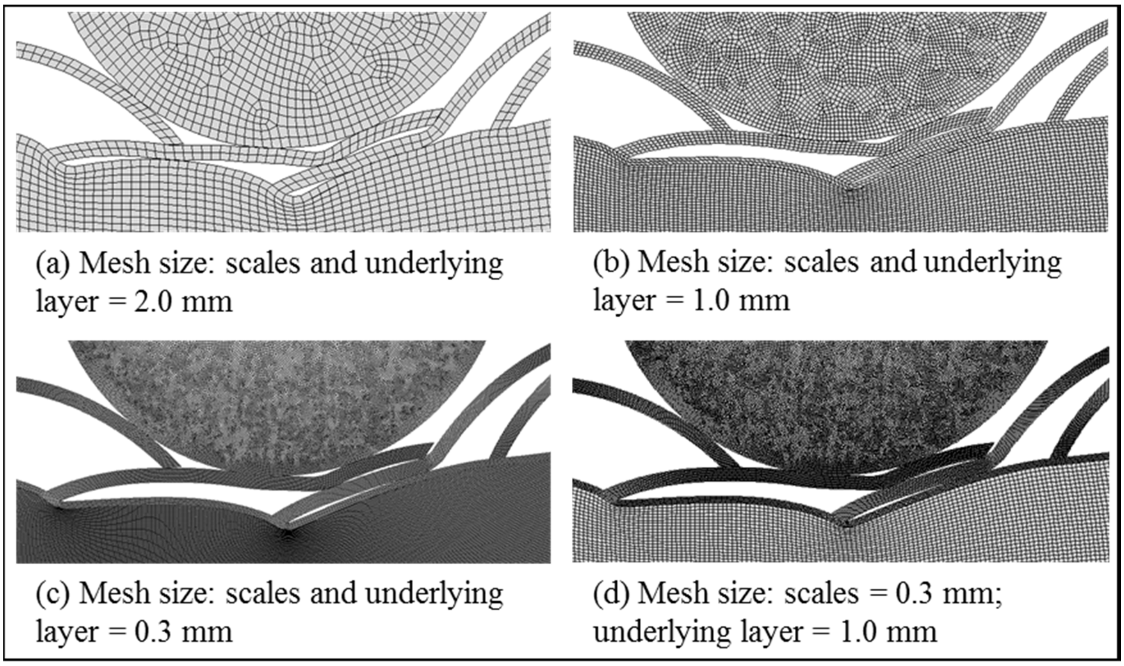
(a) Mesh size: scales and underlying layer = 2.0 mm

(b) Mesh size: scales and underlying layer = 1.0 mm

(c) Mesh size: scales and underlying layer = 0.3 mm

(d) Mesh size: scales = 0.3 mm; underlying layer = 1.0 mm

Figure 2.6: Deformation of specimens with curved scales of L_s/t_s = 28.6, L_s/R = 1.5, L_h/D = 0.8, and L_h/S = 1.5 at maximum impactor penetration for different mesh sizes.

Moreover, an average computation time-step of 8.2 x 10^{-9} s was used in the simulations. This was determined automatically by Abaqus based on the size of the smallest element in the mesh and the material wave speed (which is a function of Young's modulus and mass density of the material) so as to ensure stability of the explicit dynamic analysis. Based on the material properties adopted in the finite element model, this average time-step is about one order of magnitude lower than the time taken for a stress wave to propagate through the smallest element in the mesh. The duration of the impact event simulated in this study generally varied from 6 ms to 14 ms. Using parallel processing with 12 CPUs, the computational time of each simulation ranged from 1 hour to 2 hours.

2.2.6 Data output

As mentioned earlier in Section 1.6, the impact performance of the fish scale-cellular composite system was assessed based on the peak stresses transferred to a protected object or surface. These stresses were measured along the base of each specimen of the composite system. To determine the maximum stresses at every point along the base of the specimen throughout the impact duration, the stress distributions at various instants were extracted using the “Path” function in Abaqus and then post-processed using a self-written program in Matlab to produce stress envelopes along the base of the specimen such as the one depicted in Figure 2.7.

Apart from stresses along the base of the composite system, field output such as displacement, stress, and strain components were captured in order to examine the deformation response of the composite system. Time history output for different types of energy such as kinetic energy, plastic dissipation, and strain energy were also recorded to find out their evolution and distribution in the composite system during the impact process. For each quantity of interest, the average number of data points captured for the entire duration of impact was about 150.

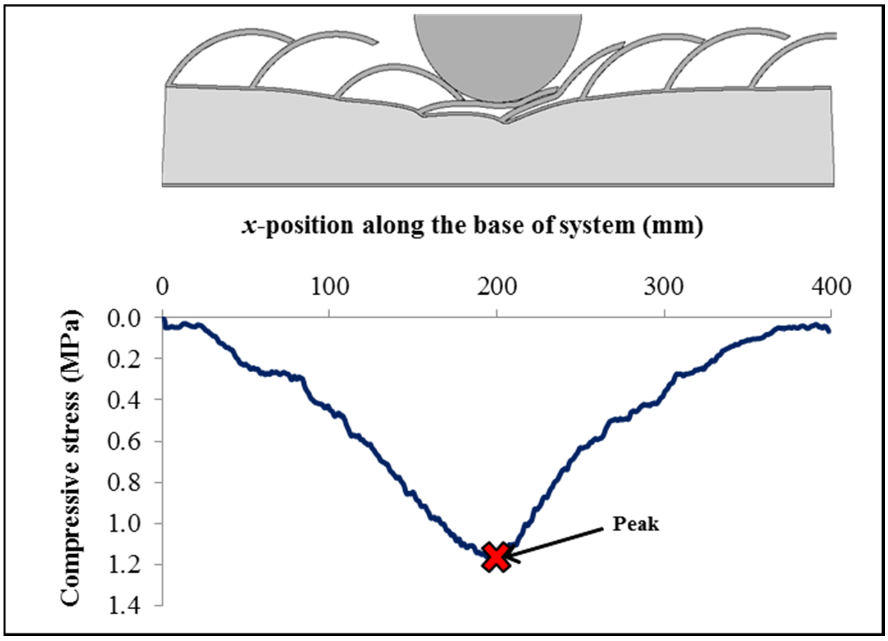

Figure 2.7: Normal compressive stress envelope along base of fish scale-cellular composite specimen.

2.3 Experimental setup

While this study was primarily conducted using the finite element model presented in Section 2.2, experimental work was also carried out to validate the finite element model and the impact performance predicted by the numerical simulations. The experimental tests were conducted using a drop-weight impact machine as shown in Figure 2.8. The drop weight was a rectangular steel block with a mass of 12.5 kg. It was constrained horizontally by four posts along which it slid downwards when released from a pre-determined height. A wedge impactor with a semi-circular tip was attached to the underside of the drop weight to create a concentrated impact force as shown in Figure 2.8. The impactor had a tip diameter of 50 mm, total length of 100 mm, and out-of-plane width of 60 mm. It was made of aluminium and had a mass of 0.767 kg. The clear drop height was adjusted based on the required impact energy for the drop-weight impact test, which was a function of the type and amount of materials used to fabricate the specimens.

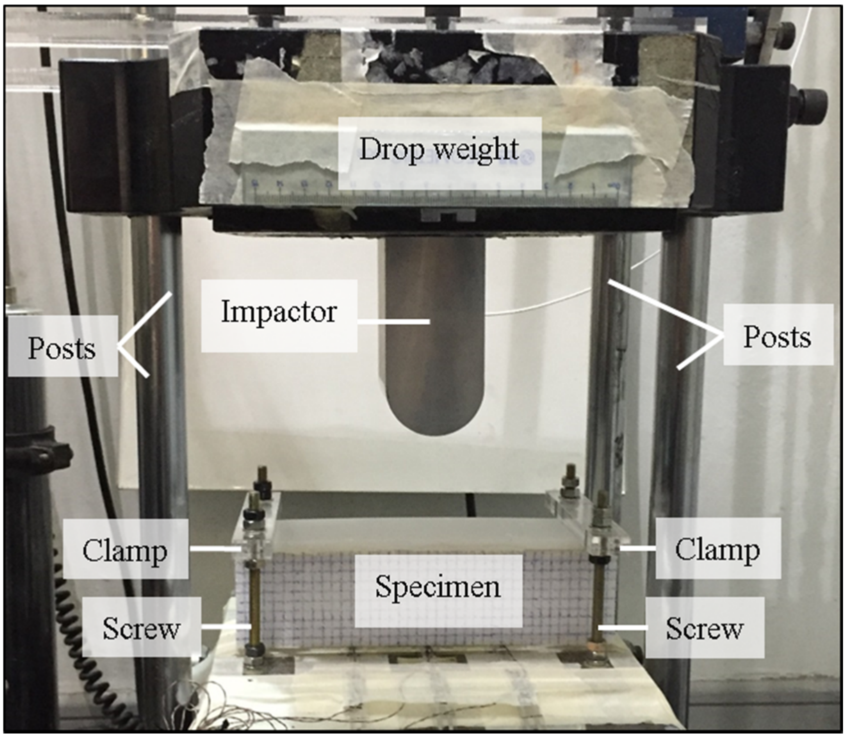

Figure 2.8: Experimental setup for drop-weight impact test.

An acrylic rig was fabricated to secure the specimen and align the specimen with the centerline of the impactor. It consisted of a base plate used to constrain the specimen vertically with clamps on the two sides to prevent uplift of the specimen at its two ends as shown in Figure 2.8. A set of screws was used to secure the clamps to the base plate, and a double-nut method was adopted to secure the screws and the clamps so that they were restrained from movement during the impact event.

An accelerometer was mounted on the drop weight to measure its acceleration. Based on the combined mass of the drop weight and impactor, the impact force F applied on the specimen was estimated from the acceleration data. The accelerometer was connected to a Yokogawa digital oscilloscope that recorded the data from the tests. A record duration of 1 s with sampling frequency of 100 kHz was used based on the estimated impact duration in order to obtain sufficient data throughout the impact event.

Deformation of the specimens was captured using a high-speed camera with lighting setup. A frame rate of 5000 frames per second and resolution of 512 x 512 pixels were found to be sufficient to capture the impact event in adequate detail.

3.0 Mechanical behaviour of fish scale-cellular composite system against impact

In this chapter, the response of a typical fish scale-cellular composite specimen under impact is first examined to understand its general mechanical behaviour. At the same time, experimental validation of the finite element model that was performed before it was used for subsequent simulations is presented. Thereafter, feasibility of the fish scale-cellular composite system as a protective structure is discussed using results obtained from the validated numerical model for specimens with different shapes and material properties (namely stiffness and strength) of the scales. Lastly, results from the proof-of-concept experimental tests that were performed for specimens with different shapes of overlapping scales are presented.

3.1 Mechanical response of fish scale-cellular composite system and experimental validation

Multiaxial and non-uniform stress distributions result in the fish scale-cellular composite system when it is subject to impact. Before parametric studies were conducted to investigate the effects of various factors on the impact performance of the composite system, the mechanical behaviour of a typical specimen was first examined to identify the key deformation characteristics of the composite system. Experimental validation of the finite element model was also performed before it was subsequently used to investigate the mechanical behaviour of the composite system.

For experimental validation, two different configurations of the composite system were used. Figure 3.1 shows the first specimen (labelled as Specimen 1) which comprised flat scales with L_s = 30 mm, t_s = 1.5 mm, θ = 20°, and S = 20 mm. The second specimen (Specimen 2) also had flat scales but longer scale length L_s compared to Specimen 1,

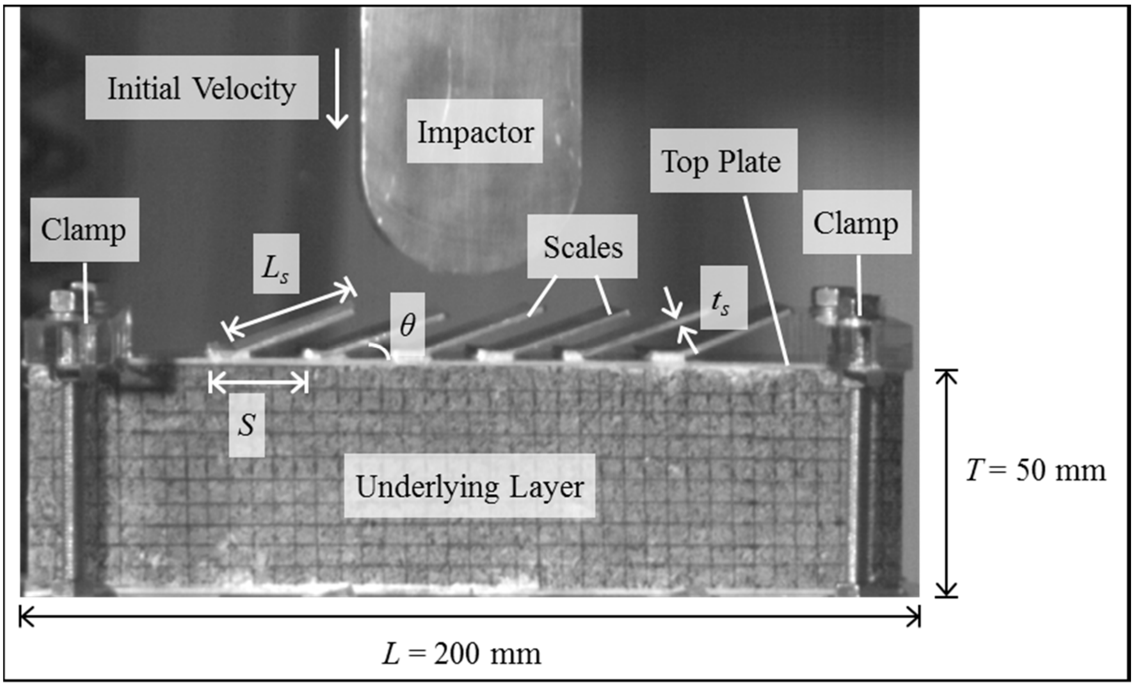

Figure 3.1: Specimen 1 for experimental validation of finite element model.

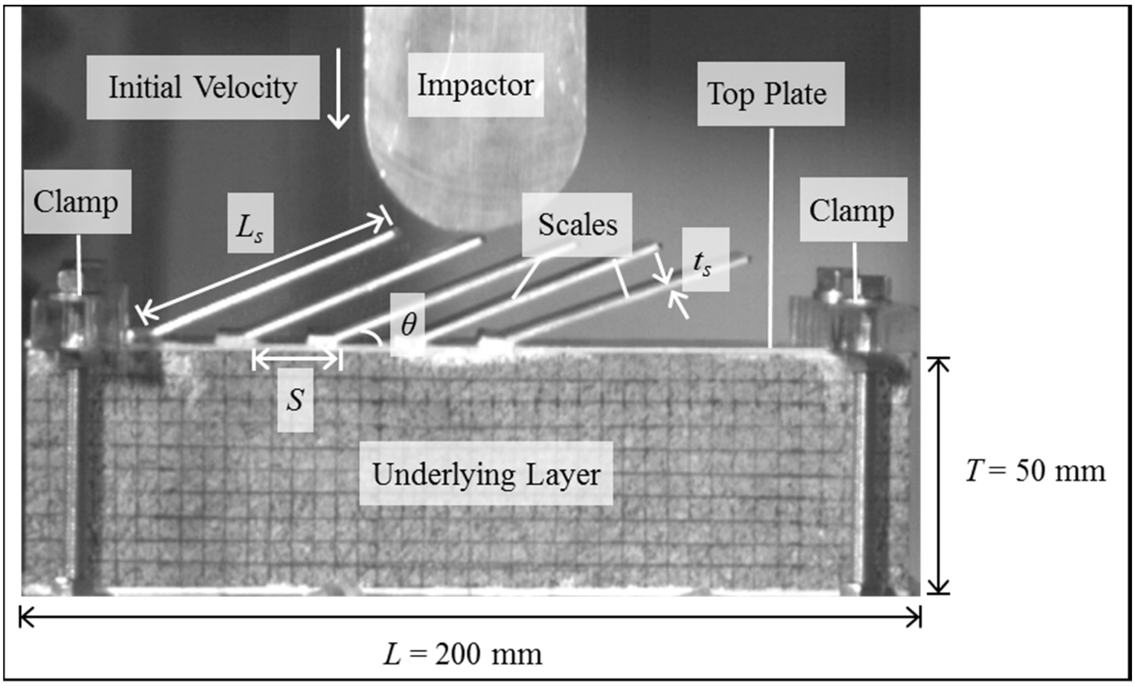

Figure 3.2: Specimen 2 for experimental validation of finite element model.

with L_s = 60 mm, t_s = 1.5 mm, θ = 20°, and S = 20 mm as displayed in Figure 3.2. In both specimens, the base of each scale was attached to the top plate by bending a small segment (5 mm) to provide anchorage and 2-ton epoxy containing bisphenol A diglycidyl ether resin was used as the gluing agent. The span L of both specimens was 200 mm while the thickness T of the cork layer was 50 mm due to the spatial constraint of the drop-weight impact machine. The width of the specimens (i.e. in the out-of-plane direction) was 50 mm. The specimens were subject to impact using the experimental setup shown in Section 2.3, with a clear drop height of approximately 156 cm.

The same setup (Figure 2.8) was modeled numerically in the finite element simulations as shown in Figure 3.3. The mesh is not shown in Figure 3.3 because it is too fine. Contact interactions between the specimen, acrylic clamps and base plate were defined using surface-to-surface interactions in Abaqus. Friction coefficients specified for the various contacting surfaces are listed in Table 3.1. These values were obtained experimentally by measuring the friction angle between each pair of materials.

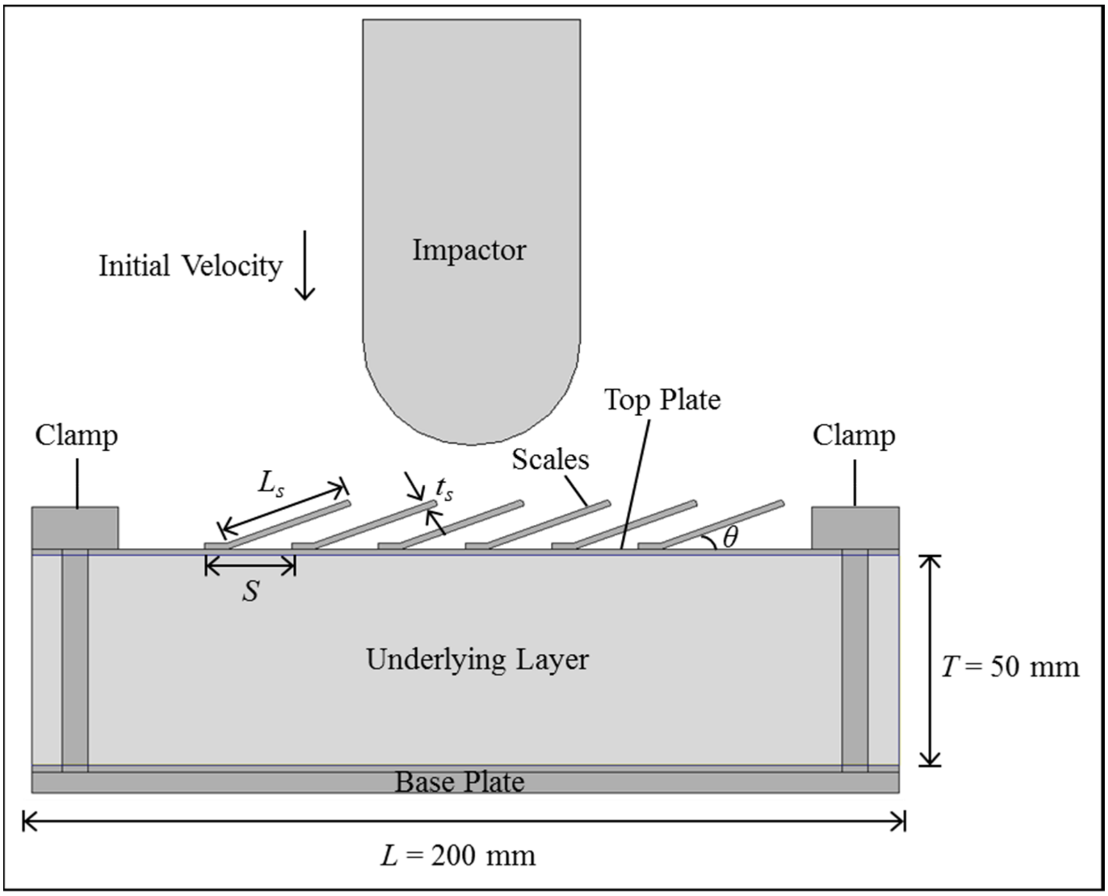

Figure 3.3: Schematic view of numerical model of the experimental validation.

Table 3.1: Friction coefficients used between surface pairs of various materials.

Material 1	**Material 2**	**Friction Coefficient**
Aluminium	Aluminium	0.268
Aluminium	Cork	0.364
Aluminium	Acrylic	0.325
Acrylic	Cork	0.577

Figure 3.4 shows the overall impact force-time response of the two specimens, while Figure 3.5 displays the deformation-time history for Specimen 1 obtained from the experiments and finite element simulations. As depicted in Figure 3.5(a), when the impactor presses on the scales the impact force is transferred through the scales to their joints with the top plate and to the compressible underlying layer, causing axial compression, transverse shear, and flexure in the scales. The scales deform through bending and rotation about the scale-to-plate joints, and eventually they press onto adjacent scales as shown in Figure 3.5(b) which results in transfer of the impact force from one scale to another scale.

Subsequently, the scales immediately underneath the impactor are flattened and the assembly of scales bends further, with the underlying cellular layer undergoing significant compression as shown in Figure 3.5(c). When the yield strength of the scales underneath the impactor is reached, plastic hinges are formed in the scales which help to dissipate part of the impact energy. However, the formation of plastic hinges causes stress concentrations which lead to the yielding of the top plate underneath the deformed scales as well as localization of deformation around the location of impact. At the same time, the underlying cellular layer is compressed by the impactor but the stresses in this layer are expected to be relatively low at this stage as the material does not densify until

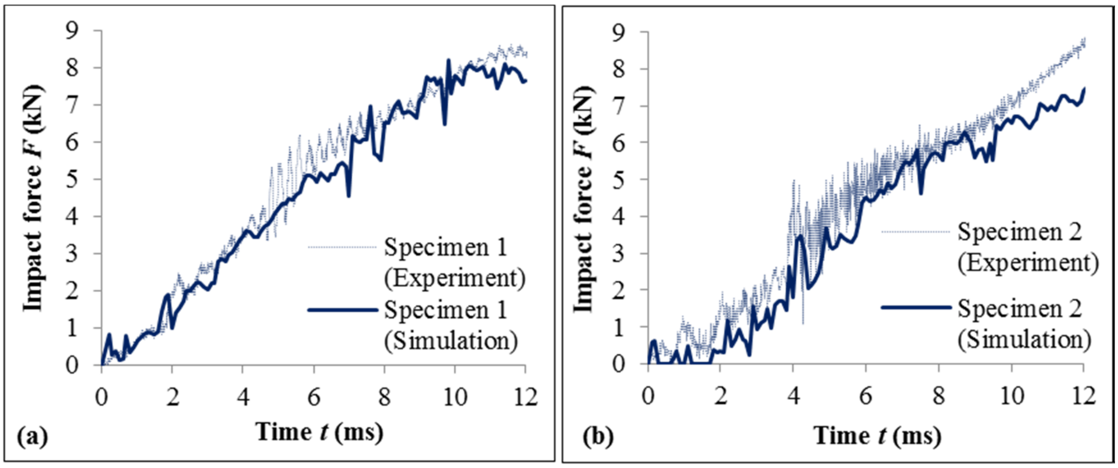

Figure 3.4: Impact force-time response of composite system (experimental and numerical).

a large strain is reached as shown by the plateau region in its stress-strain response in Figure 2.4.

Finally, the maximum penetration of the specimen occurs when all the kinetic energy of the impactor has been expended, after which it begins to rebound from the specimen. As shown in Figure 3.5(d), the underlying layer beneath the location of impact is subject to high strains at its densified state.

The results presented in Figures 3.4 and 3.5 show that the impact resistance of the composite system arises from two primary mechanisms of deformation: (a) bending of the scales, and (b) compression of the underlying cellular layer. Apart from acting as a stiffer and stronger outer layer to stop the penetration of the impactor, the scales also dissipate the part of the impact energy as they deform plastically after their yield strength is reached. On the other hand, the underlying cellular layer is expected to act as a cushion by maintaining low stresses even at relatively high strains when compressed by the impactor. Altering the configuration of the composite system may change its deformation behaviour and the relative contributions of these two mechanisms towards its impact resistance.

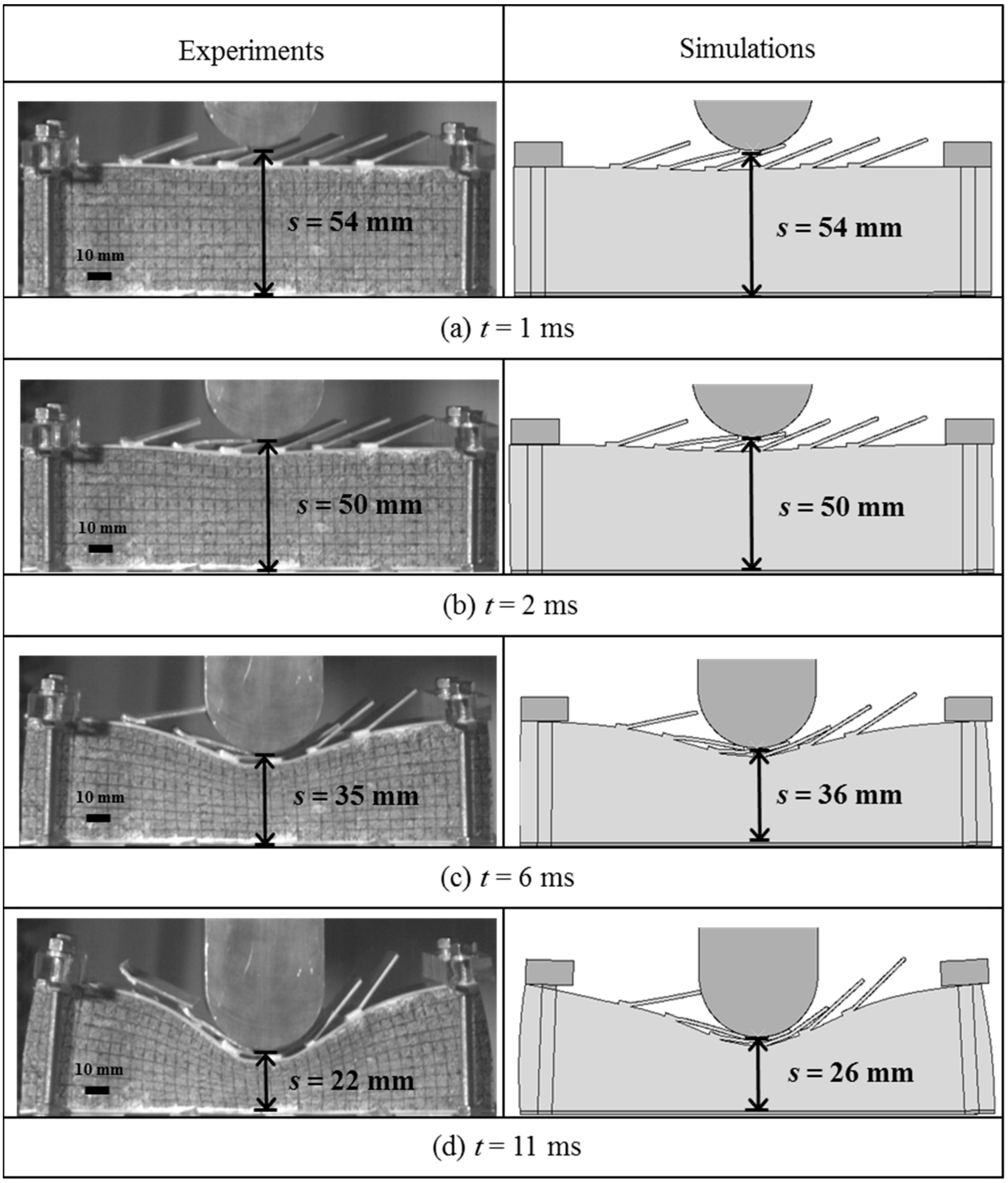

(a) $t = 1$ ms

(b) $t = 2$ ms

(c) $t = 6$ ms

(d) $t = 11$ ms

Figure 3.5: Deformation-time history of Specimen 1 obtained from experiment and finite element simulation.

Finally, Figures 3.4 and 3.5 show that there is generally good agreement between the experimental results and the finite element simulations, although some higher frequency fluctuations are observed in the experimental data in Figure 3.4 which were caused by the vibrations in the test setup during the impact event. No debonding is observed between the top plate and the underlying layer. However, there is a discrepancy between the specimen deformation obtained experimentally versus that from the finite element simulations which seems to be negligible initially but it increases with time as shown in Figure 3.5. The discrepancy is most probably due to the inaccuracy of the compressive stress-strain data for the cork that was used in the simulations. Since the compressive strain of the cork under dynamic uniaxial compression was estimated using images taken by the high-speed camera instead of being measured directly, its accuracy was affected by the visual estimation of the specimen deformation and also the angle of the camera relative to the specimen. Moreover, the inaccuracy of the stress-strain data appears to have more significant effect on the simulation results only after the cork layer has been compressed by more than half of its original thickness. This is understandable since the cork begins to be densified at this stage and hence its resistance is very sensitive to the magnitude of the applied strain.

In addition, the discrepancy between the experimental and simulation results might be caused by the difference between the actual impact velocity experienced in the experiments and the one applied in the simulations. A value of 4.5 m/s was used in the latter, while the former was estimated to be between 4.0 m/s and 5.0 m/s based on high-speed camera images taken over different time durations before the impactor struck the specimens. As highlighted in Table 3.2, the impact velocity prescribed in the simulation has a significant effect on the deformation of Specimen 1 especially at later stages of the impact event. Hence, it is very likely that the discrepancy between the simulation and experimental results may be attributed to the impact velocity assumed in the simulations. Nonetheless, despite the above-mentioned discrepancies the finite element model was still able to capture the actual behaviour of the fish scale-cellular composite system well enough, and was thereafter used to further examine the mechanical response of the composite system with different design configurations.

Table 3.2: Deformation-time histories of Specimen 1 (from simulation) under different impact velocities.

t (ms)	Distance from the base of the underlying layer to tip of impactor *s* (mm)			
	Impact velocity (m/s)			
	4.0	**4.5**	**5.0**	**Experiment**
1	55	54	54	54
2	51	50	50	50
6	40	36	34	36
11	31	26	24	26

3.2 Feasibility of fish scale-cellular composite system against impact

The feasibility of this composite system for protection against impact was evaluated numerically through an understanding of its mechanical behaviour and impact performance under different design configurations. The results shall be discussed in this section. Firstly, specimens with different shapes (flat, bent, and curved) of the overlapping scales were compared. Secondly, the material properties of the scales (namely stiffness and strength) relative to the underlying cellular layer were considered. The impact performance of the fish scale-cellular composite specimens was also evaluated against that of an equivalent (in terms of volume) sandwich specimen. Unless otherwise stated, the total volume of materials was kept constant for all cases for purpose of comparison. The impact performance of various specimens was evaluated based on the peak normal stress transferred to the protected object or surface, which was obtained from the stress envelopes along the base (i.e. underside) of the specimens as depicted in Figure 2.7. Under the same impact energy, the specimen that produces the lowest peak stress transferred is considered to have the best impact performance.

3.2.1 Shape of overlapping scales

The impact performances of the fish scale-cellular composite system with different scale shapes, namely, (a) flat scales, (b) bent scales, i.e. flat scales with bent tips, and (c) curved scales were examined. For the configuration with curved scales, two different specimens were compared. The first specimen with curved scales (labelled as "Curved scales 1") had relatively higher scale curvature L_s/R of 1.5 while the second one (labelled as "Curved scales 2") had relatively lower scale curvature L_s/R of 0.5. The geometric parameters L_s, t_s, and S were approximately the same for these specimens.

Figure 3.6 shows the stress envelopes along the base of the specimens with different scale configurations as well as for a sandwich specimen, while Figure 3.7 summarizes the peak stress transferred by these specimens. Figure 3.8 illustrates their deformed states at the instant of maximum impactor penetration. As can be seen in Figure 3.7, the peak stress transferred by the sandwich specimen is lower than specimens with flat and bent scales. The sandwich specimen has relatively higher impact resistance due to the high bending resistance of the thicker top plate (arising from keeping the total volume of materials constant) compared to the scales. As the underlying layer has high compressibility, deformation of the sandwich specimen under impact is governed by bending of the top plate as shown in Figure 3.8(e). The higher bending stiffness of this top plate activates a larger area for load transfer and minimizes the local deformation of the plate until a plastic hinge is formed beneath the point of impact where higher level of localized deformation occurs. Hence, the underlying layer is compressed more uniformly over a wider area which results in a more even stress distribution along the base of the specimen. Consequently, a lower peak stress is observed along the base of the specimen as the impact force is spread out more effectively.

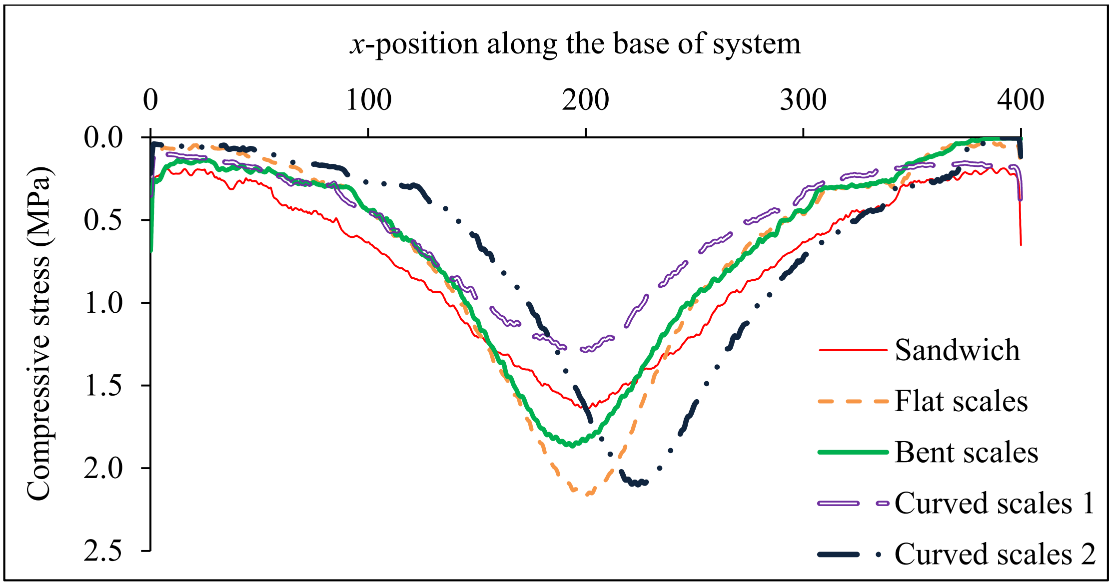

Figure 3.6: Normal compressive stress envelope along base of sandwich and composite specimens with various shapes of overlapping scales obtained from numerical simulations.

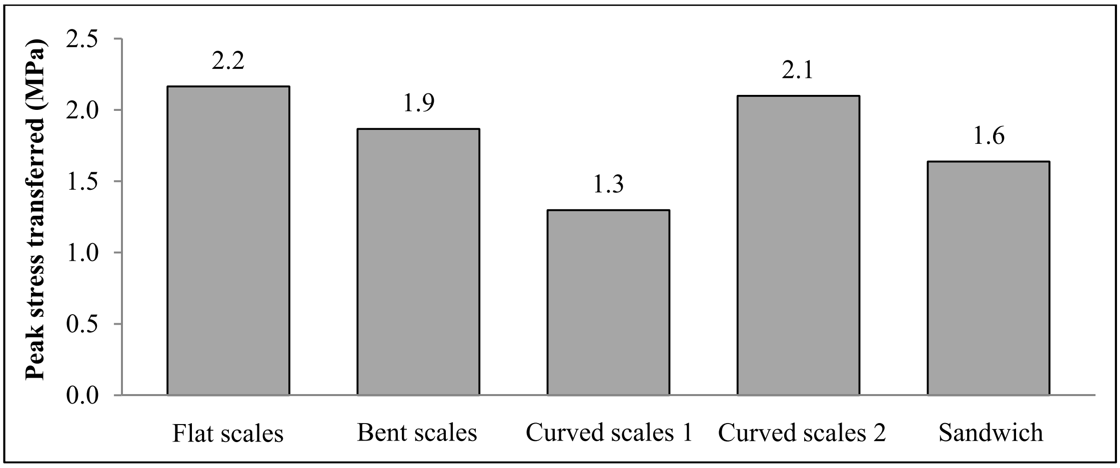

Figure 3.7: Peak stress transferred by sandwich and composite specimens with various shapes of overlapping scales obtained from numerical simulations.

On the other hand, the specimen with flat scales sustains the highest peak stress along the base of the specimen as displayed in Figure 3.7. The flat scales are not in contact with each other initially. At the beginning of the impact event, the scales underneath the impactor deform through bending and rotation about their joints until they touch the adjacent scales. Once the scales are flattened, they compress on the underlying cellular layer. Significant localization of deformation is observed underneath the point of impact

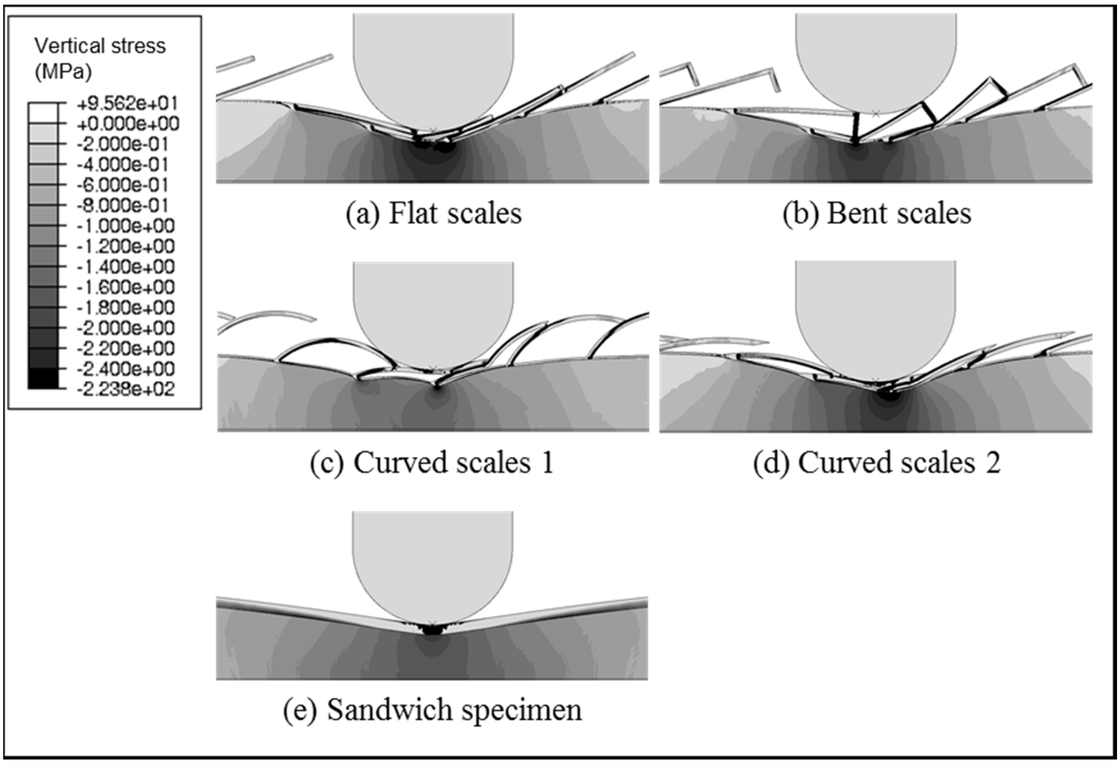

Figure 3.8: Deformation and vertical stress contour for sandwich and composite specimens with various shapes of overlapping scales at the instant of maximum impactor penetration obtained from numerical simulations.

as only a few scales are activated to resist the impact force because the scales are not connected to each other as shown in Figure 3.8(a). The formation of plastic hinges also leads to localization of deformation and stresses at the plastic hinges, and reduces the interaction between adjacent scales. This localization is further exacerbated by the compressibility of the underlying cellular layer. Thus, the scales could not dissipate much energy after being flattened as there is not much room for the scales to deform, resulting in most of the impact energy being taken by the underlying cellular layer and causing high peak stress transferred along the underside of the specimen. Therefore, the performance of the composite specimen with flat scales is worse than the sandwich specimen due to the lower bending stiffness of the scale assembly.

The same drawback is observed for the specimen with bent scales, i.e. flat scales that are bent at their tips so that they are in contact before loading. Since the scales are initially in contact, they are more effective in spreading the impact force to adjacent scales as shown in Figure 3.8(b) compared to the case with flat scales. Hence, the resistance of the assembly of scales is increased and the scales are able to dissipate more impact energy before they are flattened and start compressing on the underlying layer. Consequently, as can be seen in Figure 3.7, the peak stress transferred is slightly lower than the specimen with flat scales but is still higher than that of the sandwich specimen due to the distribution of part of the sandwich specimen's top plate material to form individual scales.

The specimen "Curved scales 1" has the lowest peak stress transferred compared to those with scales of other shapes as depicted in Figure 3.7, including the sandwich specimen. The curvature of these scales provides additional hoop resistance to distribute the impact force. Consequently, the curved scales are able to dissipate more impact energy before they are flattened and start compressing on the underlying cellular layer. This is evident based on the results shown in Figure 3.9 whereby the specimen "Curved scales 1" has the highest amount of impact energy dissipated through plastic deformation of the scale (henceforth called "plastic dissipation of scales", which is determined by Abaqus).

However, it is not a given that all specimens with curved scales can perform better than a sandwich specimen with the same volume of materials. Figure 3.7 shows that the specimen "Curved scales 2" suffers relatively higher peak stress transferred compared to the specimen "Curved scales 1" and also the sandwich specimen. This is because the scales of specimen "Curved scales 2" have lower curvature, hence their hoop resistance is lower and as a result they bend more easily when subject to the impact force. Moreover, the scales underneath the impactor have less room to deform before they are flattened

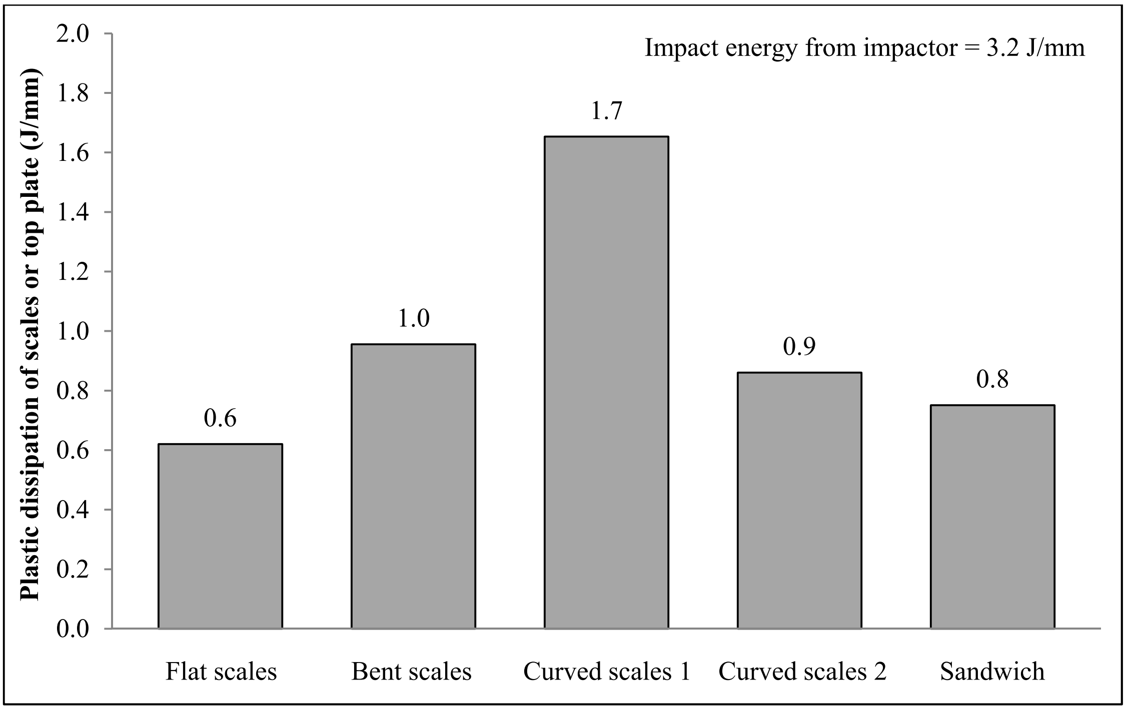

Figure 3.9: Plastic dissipation of scales or top plate for sandwich and composite specimens with different shapes of overlapping scales from numerical simulations.

and start compressing on the underlying cellular layer, as shown in Figure 3.8(d). This reduces the amount of impact energy that is dissipated by the scales as shown in Figure 3.9, which leads to more significant compression on the underlying cellular layer and higher peak stress transferred along the underside of the specimen.

Finally, Figures 3.10 and 3.11 depict the overall impact force-time response and stress-time response at the mid-point along the underside of the sandwich and composite specimens with different shapes of overlapping scales. It is obvious that the design of the scales affects the impulse duration and the stress-time response. Specimen "Curved scales 1" is more efficient in prolonging the impulse duration, hence the impact force exerted on the specimen is lower. As a result, the magnitude of the stress transferred to the base of the specimen is lower as depicted in Figure 3.11. On the other hand, the impulse duration of other specimens such as the sandwich specimen is shorter while the impact force is higher as shown in Figure 3.10, hence the stress transferred to the base of the specimens is higher. Therefore, specimen "Curved scales 1" has the best impact performance because the scales are more effective in extending the impact duration, thus minimizing the effect of the impact force and magnitude of stresses transferred to the protected surface.

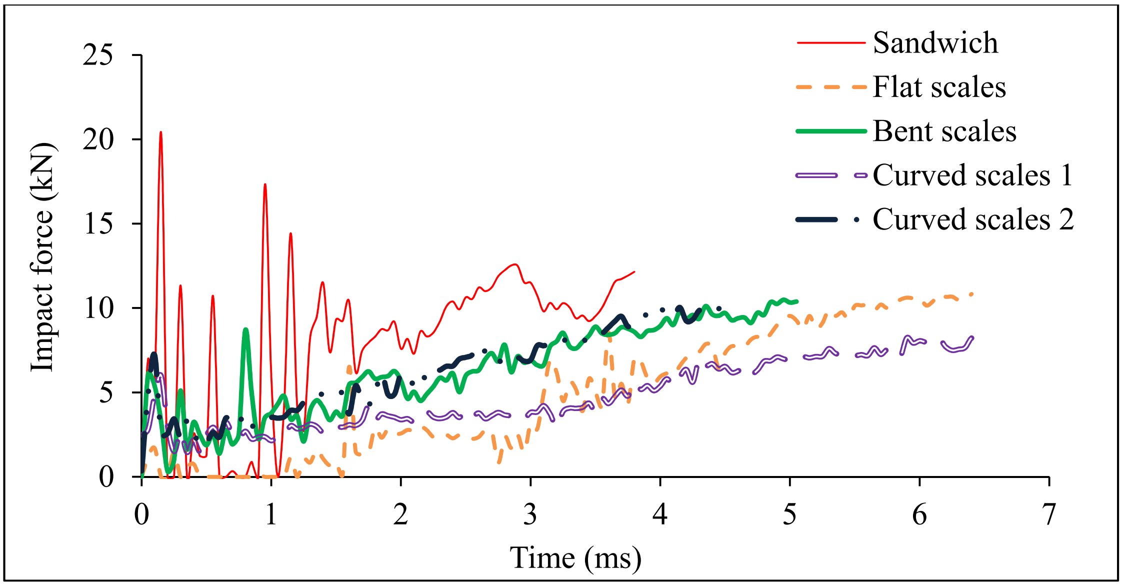

Figure 3.10: Impact force-time response of sandwich and composite specimens with different shapes of overlapping scales.

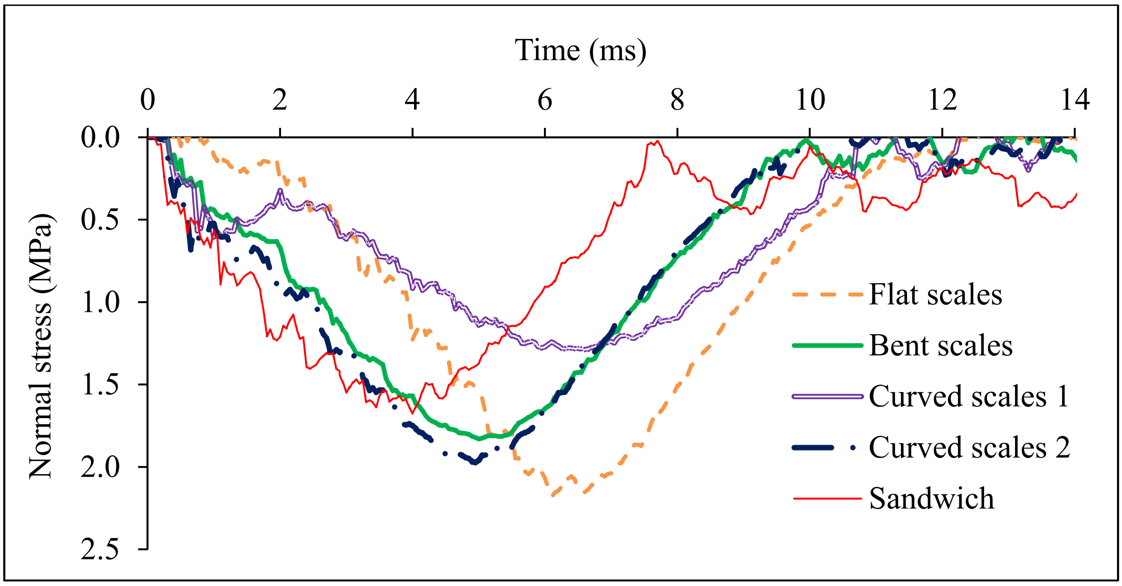

Figure 3.11: Stress-time response of sandwich and composite specimens with different shapes of overlapping scales (taken at mid-point of specimen).

In summary, specimens with curved scales indeed have the potential to provide better impact resistance compared to those with scales of other shapes and also a sandwich specimen with the same volume of materials, provided the right design configurations of the curved scales are used. Hence, the remainder of this thesis shall be focused on specimens with curved scales. The effects of various geometrical parameters of the curved scales on the impact performance of the composite system are discussed in further detail in Chapter 4.

Moreover, the impact location does not seem to have a significant influence on the results shown here. The peak stress transferred varies by a maximum of only 6 percent when the location of the impactor relative to the scales is shifted.

3.2.2 Material properties of scales

The material properties of the scales and underlying cellular layer govern the mode of deformation of the composite system and the manner in which the impact force is transferred through its different components. Thus, the feasibility of the composite system for impact protection for cases with different material stiffness and strength ratios are investigated in this section. The material stiffness ratio is defined here as the Young's modulus of the scales relative to that of the underlying cellular layer, while the material strength ratio is defined as the yield strength of the scales relative to the strength of the underlying cellular layer. The strength of the underlying cellular layer is taken as the average plateau stress, which is the average stress value in the region between its elastic and densification limits (as shown in Figure 2.4). Generally, the elastic limit for a cellular material is defined as engineering strain of between 5 percent to 7 percent. On the other hand, its densification limit corresponds to the point when there is a sharp increase in stress (i.e. sudden increase in slope of the compressive stress-strain curve), which may occur at engineering strain of around 50 percent (Pereira, 2007).

Figures 3.12 and 3.13 show the peak stress transferred and impact energy dissipated by plastic deformation of the scales for specimens with relatively low and high material stiffness ratios, respectively, while their deformed shapes are illustrated in Figure 3.14. Here, the Young's modulus of the scales is varied whereas the material properties of the underlying layer, including the material strength ratio, are kept constant. It is apparent that the peak stress transferred is high when the specimen has a relatively low material stiffness ratio of 40. This is because the scales are too soft to resist the impact force and are easily flattened resulting in significant compression on the underlying layer as shown in Figure 3.14(a). The scales are unable to dissipate the impact energy as shown in Figure 3.12, hence the underlying cellular layer has to absorb a significant amount of the impact energy which causes its densification and high peak stress transferred.

On the other hand, the peak stress transferred is reduced significantly when the material stiffness ratio is relatively high as shown in Figure 3.13. Due to their increased stiffness, the scales are able to resist the impactor more effectively by spreading the load over a

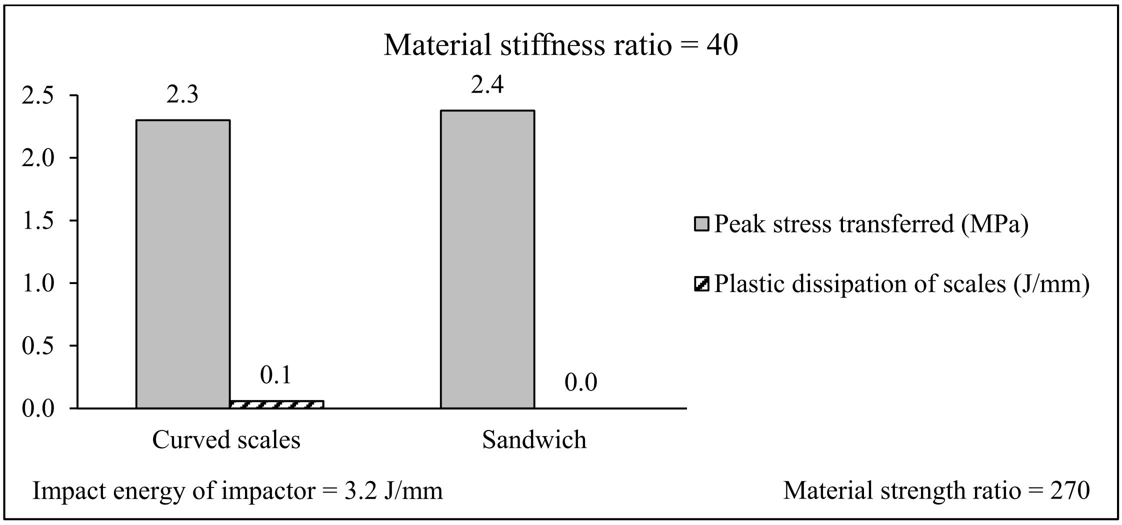

Figure 3.12: Peak stress transferred and plastic dissipation of scales for specimens (curved scales and sandwich) with low material stiffness ratio.

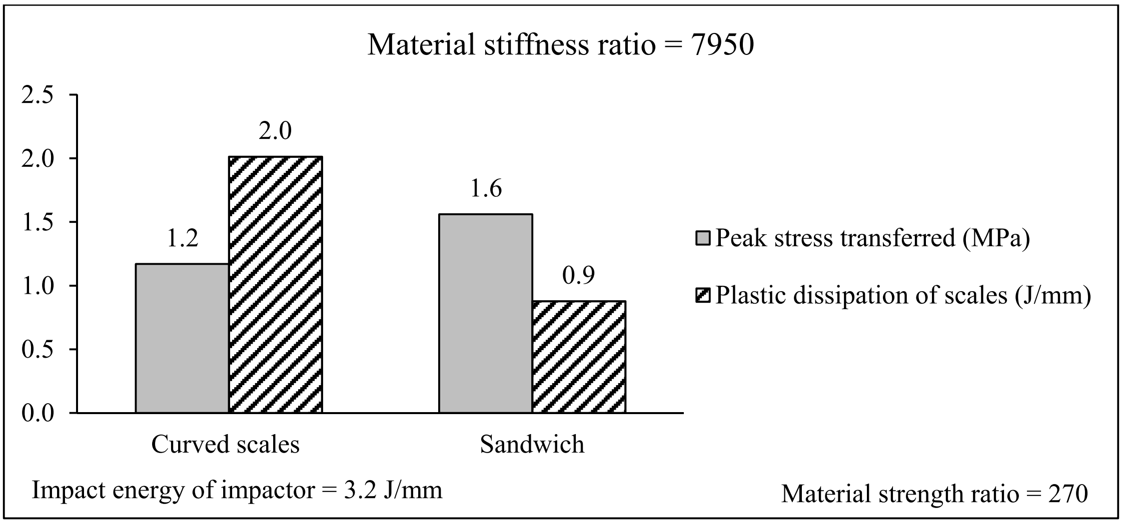

Figure 3.13: Peak stress transferred and plastic dissipation of scales for specimens (curved scales and sandwich) with high material stiffness ratio.

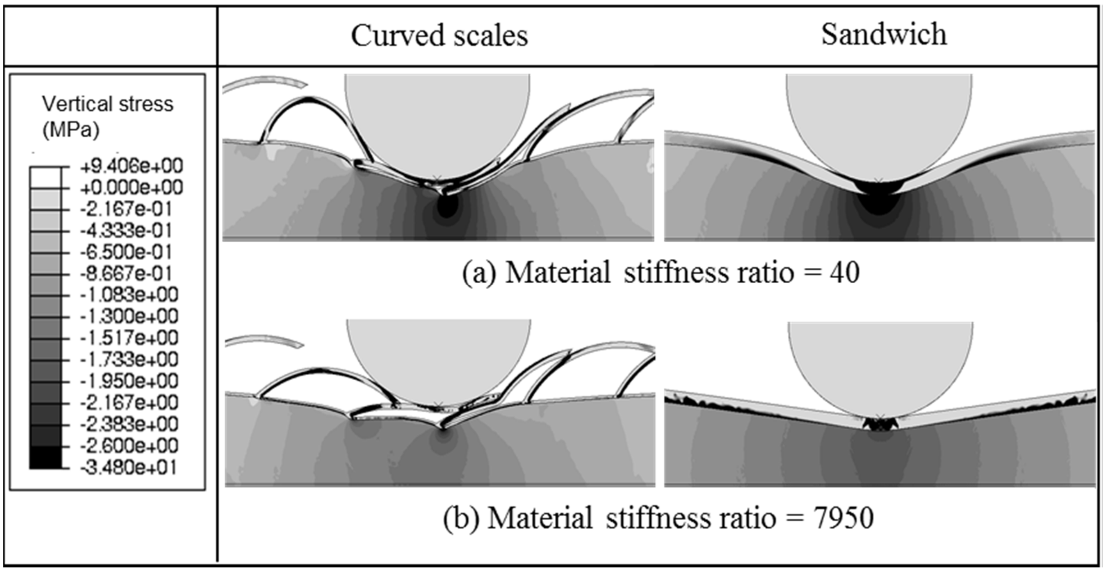

Figure 3.14: Deformation and vertical stress contour at maximum impactor penetration of specimens (curved scales and sandwich) with low and high material stiffness ratios.

wider area, dissipating a more significant amount of impact energy as shown in Figure 3.13, before they are flattened with the impactor starting to compress on the underlying cellular layer. The underlying layer is thus compressed less severely as depicted in Figure 3.14(b), resulting in lower peak stress transferred. Figures 3.12 and 3.13 also show that the impact performance of the specimen with curved scales becomes increasingly better than a sandwich specimen with the same volume of materials when the material stiffness ratio is increased. This is due to the increased plastic dissipation of the scales in the specimen with curved scales.

Figures 3.15 and 3.16 show the peak stress transferred and impact energy dissipated by plastic deformation of the scales for specimens with relatively low and high material strength ratios, respectively, while the deformed shapes of these specimens are illustrated in Figure 3.17. Here, the yield strength of the scales is varied whereas the material properties of the underlying layer and the materials stiffness ratio are kept constant. Similar to the effect of material stiffness ratio, the peak stress transferred is high when the specimen has relatively low strength ratio of 30. Scales with low yield strength are too weak to resist the impact force, as shown in Figure 3.17(a), thus they are unable to dissipate much impact energy. A significant proportion of the impact energy is taken by the underlying cellular layer causing it to densify, thereby resulting in significantly high stress on the underside of the composite specimen.

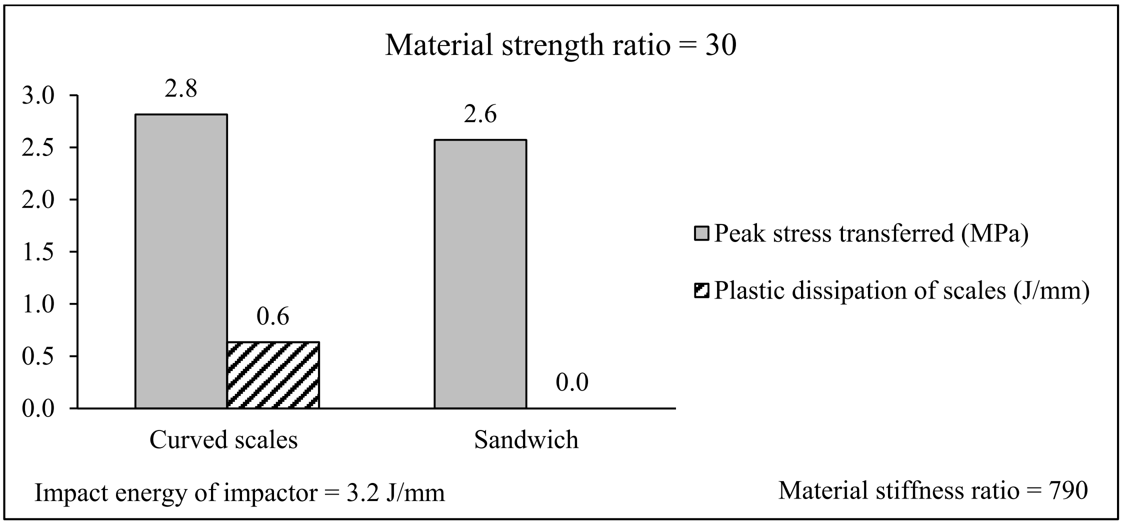

Figure 3.15: Peak stress transferred and plastic dissipation of scales for specimens (curved scales and sandwich) with low material strength ratio.

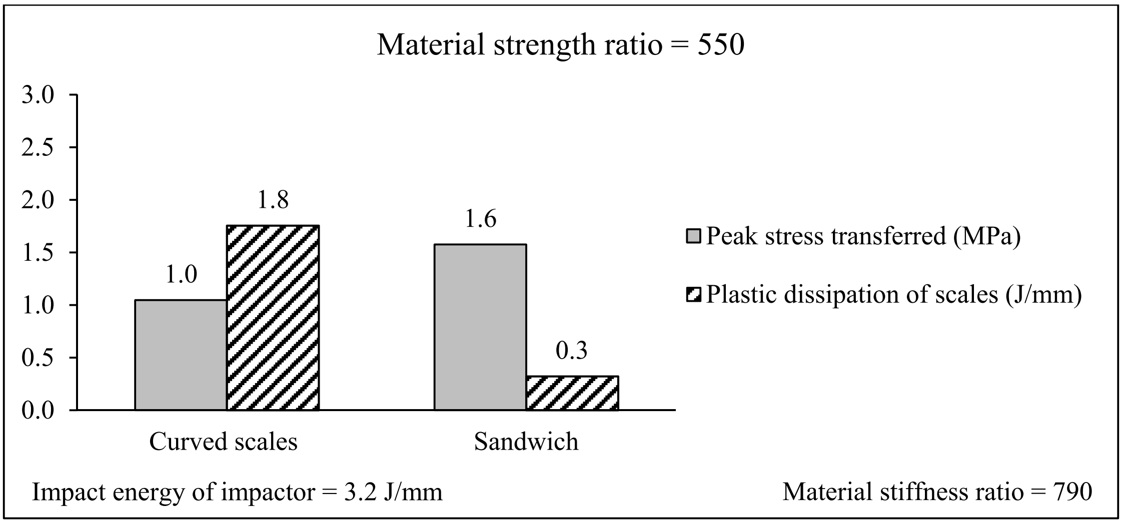

Figure 3.16: Peak stress transferred and plastic dissipation of scales for specimens (curved scales and sandwich) with high material strength ratio.

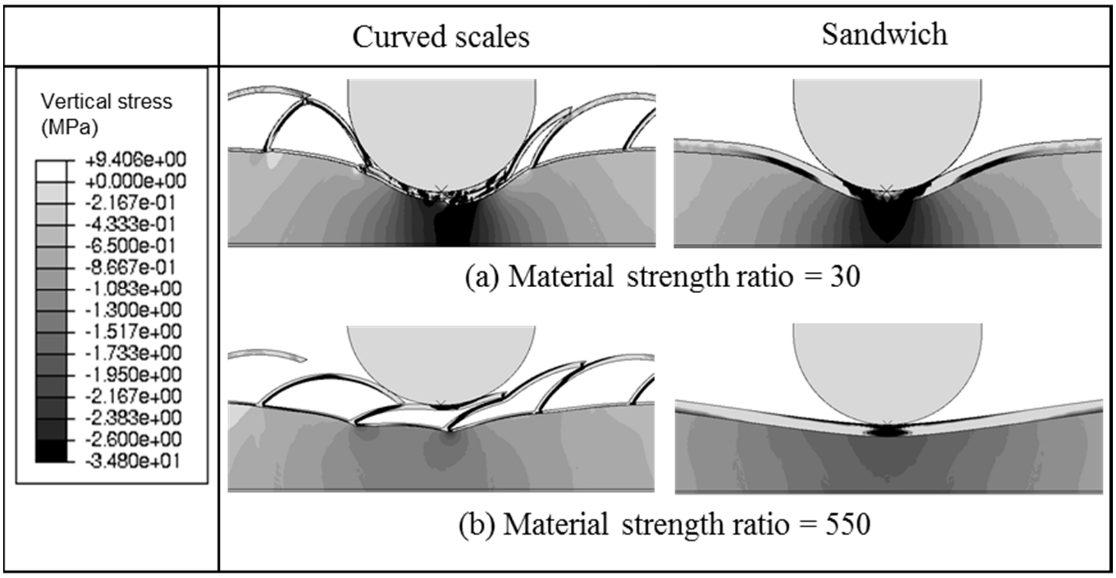

Figure 3.17: Deformation and vertical stress contour at the instant of maximum impactor penetration of specimens (curved scales and sandwich) with low and high material strength ratios.

On the other hand, the peak stress transferred is reduced when the material strength ratio is relatively high as shown in Figure 3.16. When the yield strength of the scales increases, the scales are able to dissipate more impact energy, minimizing compression on the underlying cellular layer and reducing the impact energy taken by the underlying layer. Figures 3.15 and 3.16 show that the impact performance of the specimen with curved scales becomes increasingly better than a sandwich specimen with the same volume of materials when the material strength ratio is increased.

Therefore, it can be concluded that the selection of materials for the scale assembly and underlying cellular layer is very important because their material properties control the deformation mode of the composite system. The material stiffness and strength ratios have to be high enough such that the scales are sufficiently stiff and strong yet still able to deform and dissipate a significant amount of impact energy through plastic deformation and the formation of plastic hinges. When this occurs, the impact energy taken by the underlying layer is lower and does not lead to its densification, resulting in lower peak stress transferred by the composite system. The effects of material properties of the scales and underlying layer on the impact performance of the composite system are further discussed in Chapter 5.

3.3 Experimental proof-of-concept of fish scale-cellular composite system against impact

In this section, experimental validation of the impact performance of the fish scale-cellular composite system with different scale shapes is presented. Firstly, the design and fabrication of the specimens which include selection of materials for the scales and underlying cellular layer, as well as the configurations of the scales, will be presented. Subsequently, the experimental results are discussed. Thereafter, the experimental results are used to validate the finite element model.

3.3.1 Selection of materials for scales and underlying layer

While the study described in Sections 3.1 and 3.2 was performed using aluminium for the scales and top plate and cork for the underlying layer, fabricating good and consistent specimens without introducing unnecessary variability in properties was not easy.

Although Section 3.1 presents a method to attach the flat scales which were fabricated from aluminium plates to the top plate to form the assembly of scales, the short anchorage length and the 2-ton epoxy may not be sufficient to prevent delamination of the scales from the top plate as shown in Figure 3.5(d). Welding the scales to the top plate may create stronger joints but the high temperature could cause warping of the plates (if they are very thin) as well as reduce the strength and ductility of the plates. It was also very challenging to fabricate an assembly of curved scales as the scales have to be cut from aluminium tubes with the right size and material properties and then welded to a flat aluminium plate with the required thickness. Therefore, for the purpose of this experimental validation, an alternative solution to realize quality specimens was needed.

For the purpose of experimental validation, whatever combination of materials is selected to ensure that the fabrication difficulties are overcome, it must be able to adequately reproduce the kind of deformation behaviour shown by the aluminium-cork system in the simulations. As shown in Section 3.2, the stiffness and strength of the scales relative to those of the underlying layer should be sufficiently high such that the scales are effective in dissipating the impact energy, minimizing compression on the underlying layer, and reduce the transfer of stresses. Thus, the key principle in the selection of materials is to preserve the material strength and stiffness ratios between the scales and the underlying layer as those used in the numerical simulations. The material selected for the scales should also have sufficient ductility so that the scales are able to dissipate impact energy through plastic deformation as seen in the numerical models.

To this end, acrylonitrile butadiene styrene (ABS) was chosen as the material for the scales since it is known to be tough, is readily available, and can be formed into complex shapes using relatively low cost 3D printing (it is also possible to fabricate aluminium scales by 3D printing, but the cost of metallic 3D printing is currently prohibitive). Printing the entire assembly of scales as a single piece eliminated the need to join individual scales, thus minimizing the introduction of weak zones in the assembly. For the underlying cellular layer, polyethylene (PE) foam with density of 64 kg/m^3 seemed to be the best option among a number of readily available candidate materials.

Experimental tests were carried out to characterize the material properties of ABS and PE foam; the results are summarized in Table 3.3, while a detailed discussion can be found in Appendix B. Based on the results shown in Table 3.3, it is evident that the material stiffness and strength ratios of the two material combinations, i.e. aluminium-cork and ABS-PE foam, are comparable and are of the same order of magnitude. Moreover, the mass density ratios (i.e. ratio of mass density of scale material to that of the underlying layer) of the two material combinations are also comparable. Hence, 3D-printed ABS scales with PE foam as underlying layer was deemed to be a suitable combination for the specimens in this experimental validation to produce a similar kind of mechanical response as the aluminium-cork system.

3.3.2 Configuration of specimens

To assess the impact performance of the fish scale-cellular composite system with different shapes of overlapping scales, three configurations were chosen, namely (a) flat scales, (b) curved scales, and (c) sandwich specimen as shown in Figure 3.18. The span L of the specimens was 200 mm while the thickness T of the foam layer was 50 mm. The width of the specimens (i.e. in the out-of-plane direction) was 50 mm.

The curved scales were fabricated with the following dimensions: L_s = 63.3 mm, t_s = 2.0 mm, R = 40.0 mm, and S = 40.0 mm. The thickness of the top plate to which the

Table 3.3: Material properties of aluminium, cork, ABS and PE foam.

Material	Aluminium	Cork	ABS	PE foam
Young's modulus (GPa)	70	0.088	1.83	0.001
Yield strength (MPa)	250	-	36.1	-
Average plateau stress (MPa)	-	0.91	-	0.14
Mass density (kg/m^3)	2700	180	1070	64
Material stiffness ratio	790		1800	
Material strength ratio	270		258	
Mass density ratio	15.0		16.8	

ends of the scales were joined was 2 mm. The volume of ABS per unit span of the specimen was 157 mm^3. For a fair comparison, the same volume of ABS per unit span was used for the other two design configurations. The flat scales were fabricated with the following configuration: L_s = 63.0 mm, t_s = 2.0 mm, S = 40.0 mm, and angle of inclination θ = 18°. The flat scales were designed such that their geometric parameters L_s, t_s, and S (as well as the top plate thickness) were approximately the same as the specimen with curved scales. For the sandwich specimen, the total thickness of the top plate was 5.055 mm.

The assembly of scales (i.e. scales with top plate) as well as the top plate of the sandwich specimen were fabricated using 3D printing. Each specimen with scales was printed layer-by-layer along the out-of-plane direction, while the top plate of the sandwich specimen was printed layer-by-layer along the direction of its thickness. Printing each

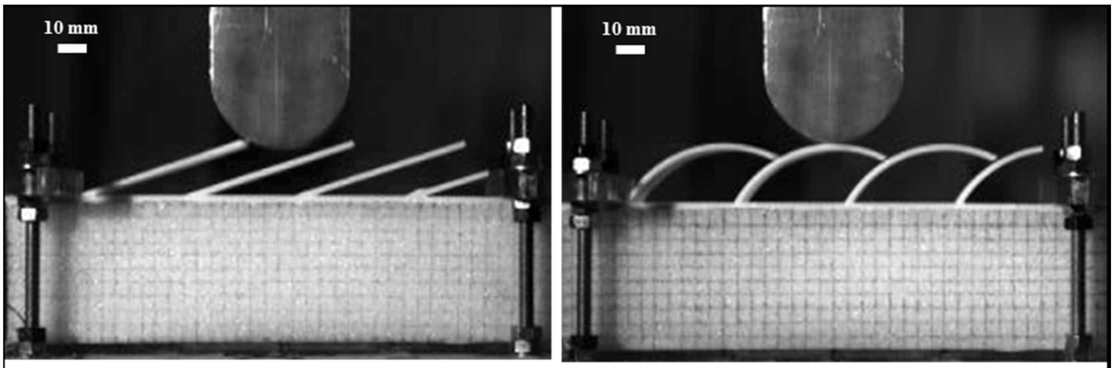

(a) Flat scales (b) Curved scales

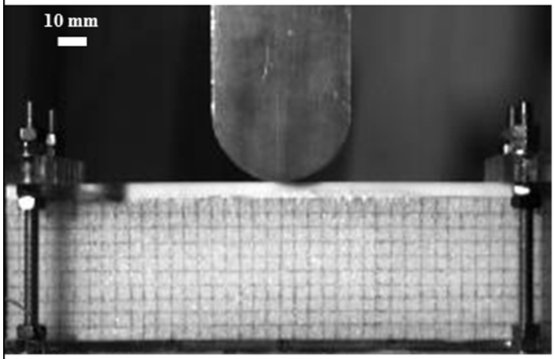

(c) Sandwich specimen

Figure 3.18: Specimen with (a) flat scales, (b) curved scales, and (c) sandwich specimen.

assembly of scales or top plate of the sandwich specimen took up to 5 hours to complete. The printed structures were attached to the underlying foam layer using 2-ton epoxy (similar to that in Section 3.1), and left to cure for at least 24 hours before testing. Due to budgetary limitations, only two samples of each design configuration were made for the experiments.

3.3.3 Impact performance of specimens

A similar experimental setup as shown in Section 2.3 was used to test the specimens. In addition, miniature pressure sensors were added to measure the stress transferred by the specimen to the protected surface. These sensors were obtained from Tokyo Sokki Kenkyujo; they had an overall thickness of 1.4 mm and circular sensing areas with diameter of 6.5 mm. They were mounted at pre-determined points between the underside of the specimens and the base plate of the rig as shown in Figure 2.8. One sensor was placed along the line of impact, while a sensor was placed on either side of this line at a distance of 40 mm from the line. The strain output from the sensor (in response of the pressure applied) was converted into the corresponding stress values using a calibration constant (unique to each sensor) that was provided by the manufacturer. The pressure sensors were connected to a Yokogawa digital oscilloscope that records the data from the tests using the same settings as those listed in Section 2.3.

The impact performance of the specimens was assessed by measuring the peak stress transferred and the maximum impactor penetration into the specimens. The peak stress transferred was obtained from the stress-time history of the pressure sensor that was placed underneath the specimens along the line of impact, i.e. the middle sensor, as depicted in Figure 3.19. The maximum impactor penetration into the specimens was measured using images captured by the high-speed camera and is defined as the distance travelled by the top surface of the specimen (excluding the scales) up to the point when the underlying foam layer is at its maximum compressed state as shown in Figure 3.20.

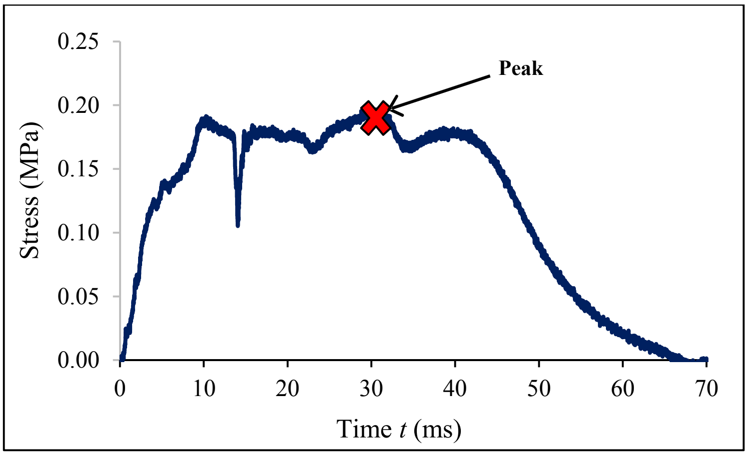

Figure 3.19: Stress-time history of middle sensor for specimen with curved scales.

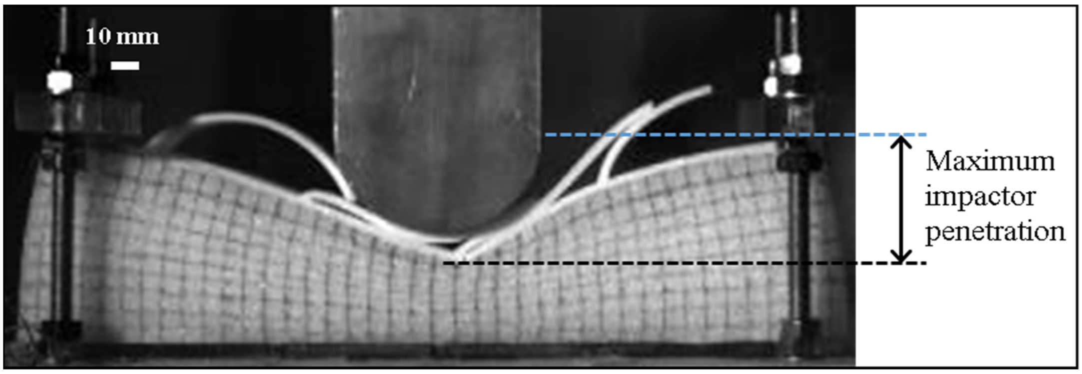

Figure 3.20: Maximum impactor penetration in specimen with curved scales.

Figure 3.21 shows the impact energies that were exerted on the specimens. They are calculated based on the impact velocities that are estimated from the high-speed camera images taken over different time durations *t* before the impactor struck the specimens. It is evident that the impact energy exerted on the sandwich specimen is slightly lower than those for the specimens with curved and flat scales. This difference could be due to the inaccurate adjustment made to the height from which the impactor was released. During the experiments, the sandwich specimens were tested first, after which the adjustment was made before the specimens with scales were tested in order to account for the difference in initial heights of the sandwich and scaled specimens.

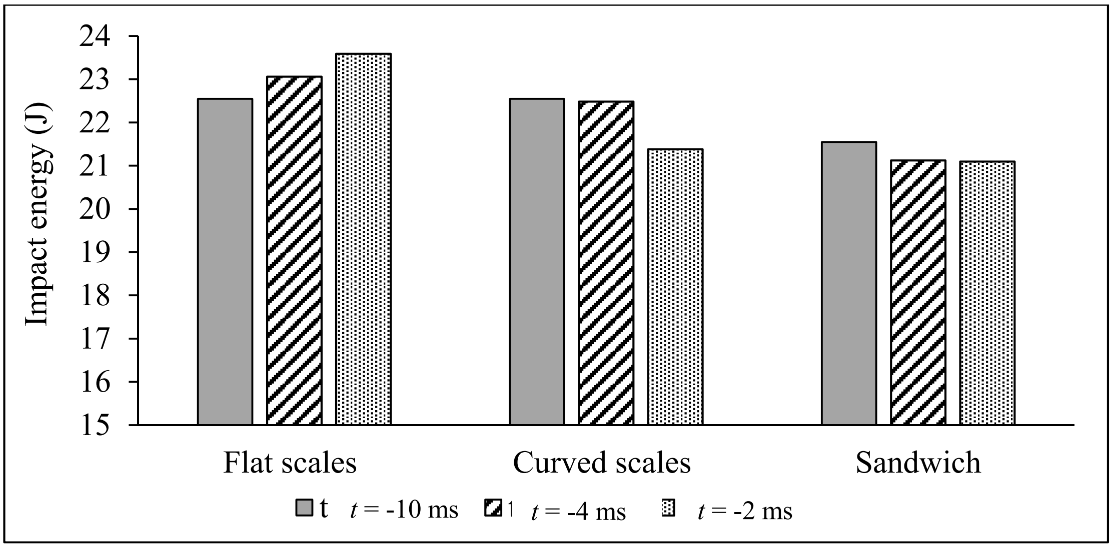

Figure 3.21: Impact energy exerted on sandwich and composite specimens with flat and curved scales.

Figure 3.22 shows the peak stress transferred by the specimens while Figure 3.23 shows the maximum impactor penetration. It is obvious that the specimens with flat scales have poorer impact performance than the other specimens. This is because the flat scales are not able to resist the impact load as effectively as curved scales. Unlike curved scales, flat scales do not have the additional resistance to bending provided by hoop resistance of a curved shell. When subject to impact, the flat scales rotate about their fixed ends and are easily flattened by the projectile. Moreover, flat scales bend rather easily and are ineffective in transferring the impact force to adjacent scales due to the absence of initial contact between scales (there is contact only after the scales have been deformed). Thus, the underlying foam layer is compressed more significantly by the impactor as shown in Figure 3.24(a). On the other hand, the sandwich specimens perform better than the specimens with flat scales as shown in Figure 3.22. This is because the thicker top plate has relatively higher bending resistance than the assembly of flat scales. Thus, it compresses on the underlying cellular layer more uniformly which results in more even stress distributions along the base of the specimen. However, the top plate starts cracking subsequently after it has been bent to a certain as shown in Figure 3.24(c). Once the top plate is cracked, the left and right halves of the plate undergo mostly rigid body motion with minimal bending. Therefore, its resistance to the impactor is reduced significantly resulting in a more considerable compression of the underlying foam layer.

Lastly, the specimens with curved scales perform just as well as the sandwich specimens, if not slightly better. The curved scales are more able to spread the impact force through the scale-to-scale interactions. Moreover, the curved scales are deformed more significantly before they are flattened and the underlying foam layer is compressed by the impactor. As explain in Section 3.2.1, this could lead to more dissipation of the impact energy via plastic deformation of the scales and thereby resulting in lower

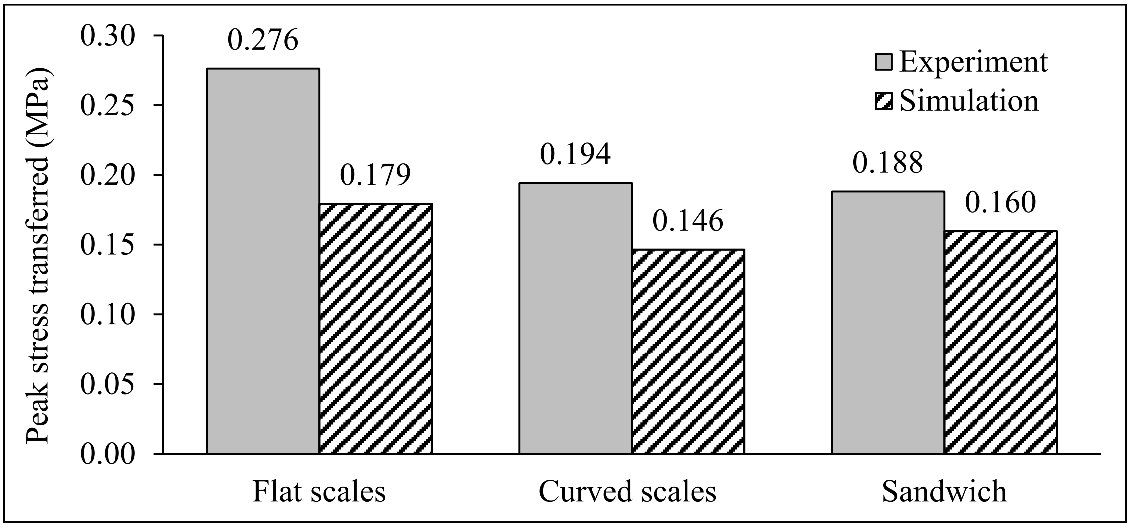

Figure 3.22: Peak stress transferred by sandwich and composite specimens with flat and curved scales obtained from experiments and numerical simulations.

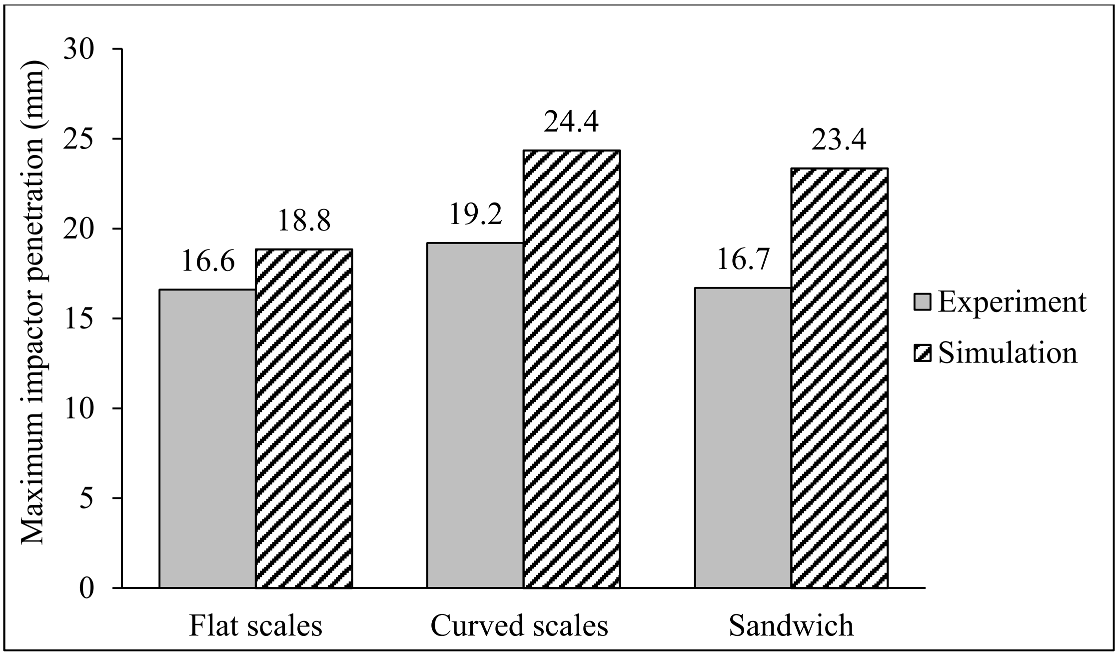

Figure 3.23: Maximum impactor penetration into foam of sandwich and composite specimens with flat and curved scales obtained from experiments and numerical simulations.

amount of impact energy being transferred to the underlying foam layer. Consequently, compression of the underlying layer is reduced as shown in Figure 3.24(b) and hence lower peak stress is transferred.

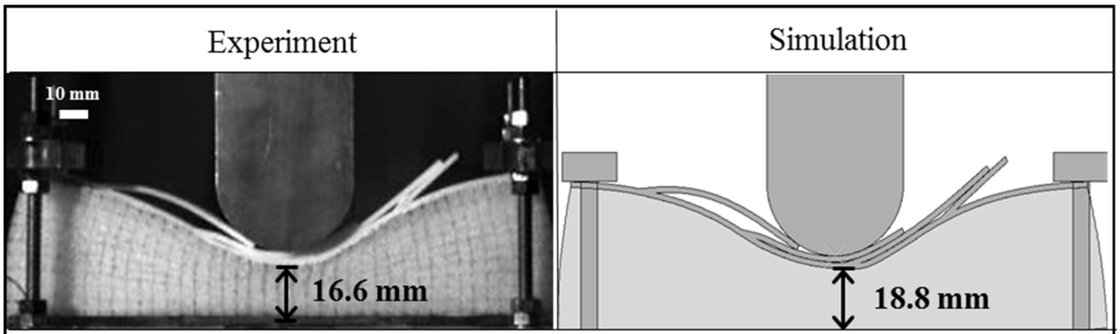

(a) Flat scales

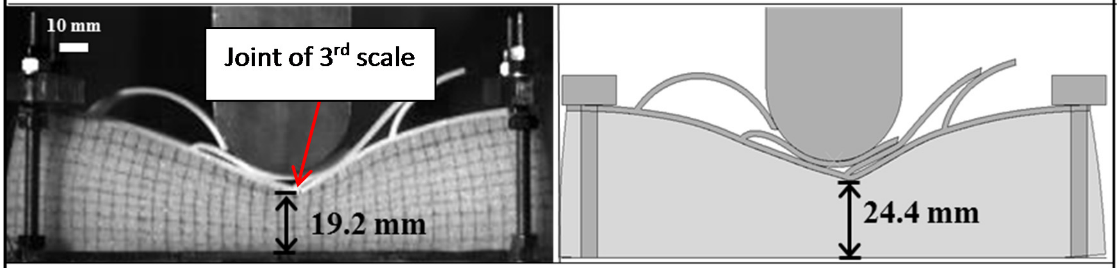

(b) Curved scales

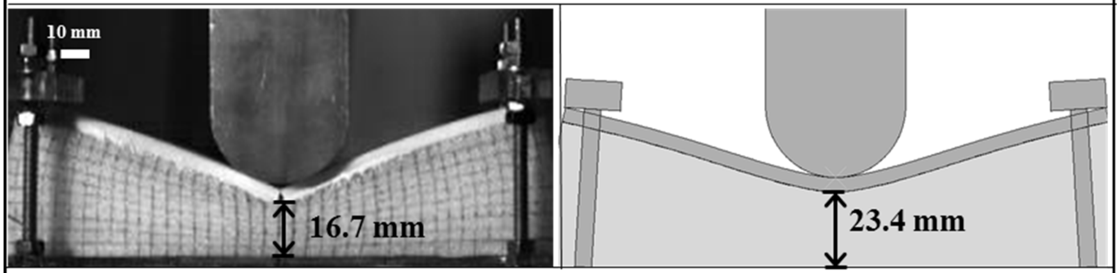

(c) Sandwich specimen

Figure 3.24: Deformation of sandwich and composite specimens with flat and curved scales at maximum impactor penetration obtained from experiments and numerical simulations.

However, compared to the results shown in Section 3.2, the impact performance of the specimen with curved scales in these experimental tests does not seem to be significantly better compared to the sandwich specimen. This is unexpected and somewhat goes against the hypothesis that the fish scale-cellular composite system can provide better impact performance (than a conventional sandwich specimen). Nevertheless, as highlighted earlier in Figure 3.21, this discrepancy is most probably due to the lower impact energy exerted on the sandwich specimen compared to the one with curved scales. Therefore, based on these results, it may be concluded that specimens with curved scales have better performance than the sandwich specimens. Even though the specimens with curved scales are subjected to higher impact energy, the peak stress transferred is not higher while the penetration depth is reduced compared to the sandwich specimens.

In addition, numerical simulations of these proof-of-concept experiments were also performed. Figure 3.25 displays the stress-time response at the mid-point along the underside of the specimens, where a pressure sensor was placed in the experiments. For the specimen with flat scales, the stress measured at the beginning of the impact event as shown in region 1 of Figure 3.25(a) matches that of the simulation rather well. However, the stress measured in the experiment shoots up more significantly than that of the simulation when the underlying is densified as shown in region 2 of Figure 3.25(a). The discrepancy is most probably due to the inaccuracy of the compressive stress-strain data for the foam that was used in the simulations and also the difference between the actual impact velocity experienced in the experiments and the one applied in the simulations as discussed in Section 3.1.

Similarly, the stress measured in the experiment for the sandwich specimen shows good agreement with the simulation results as shown in region 1 of Figure 3.25(c). Subsequently, the stress measured in the experiment reduces and a sharp drop was momentarily experienced when the top plate was cracked. This is because the top plate was made of 3D-printed ABS which is more brittle than aluminium. However, the stress extracted from the simulation does not follow this trend because the 3D-printed ABS was modeled as an elastic-perfectly plastic material, hence there was no tensile rupture in the simulation.

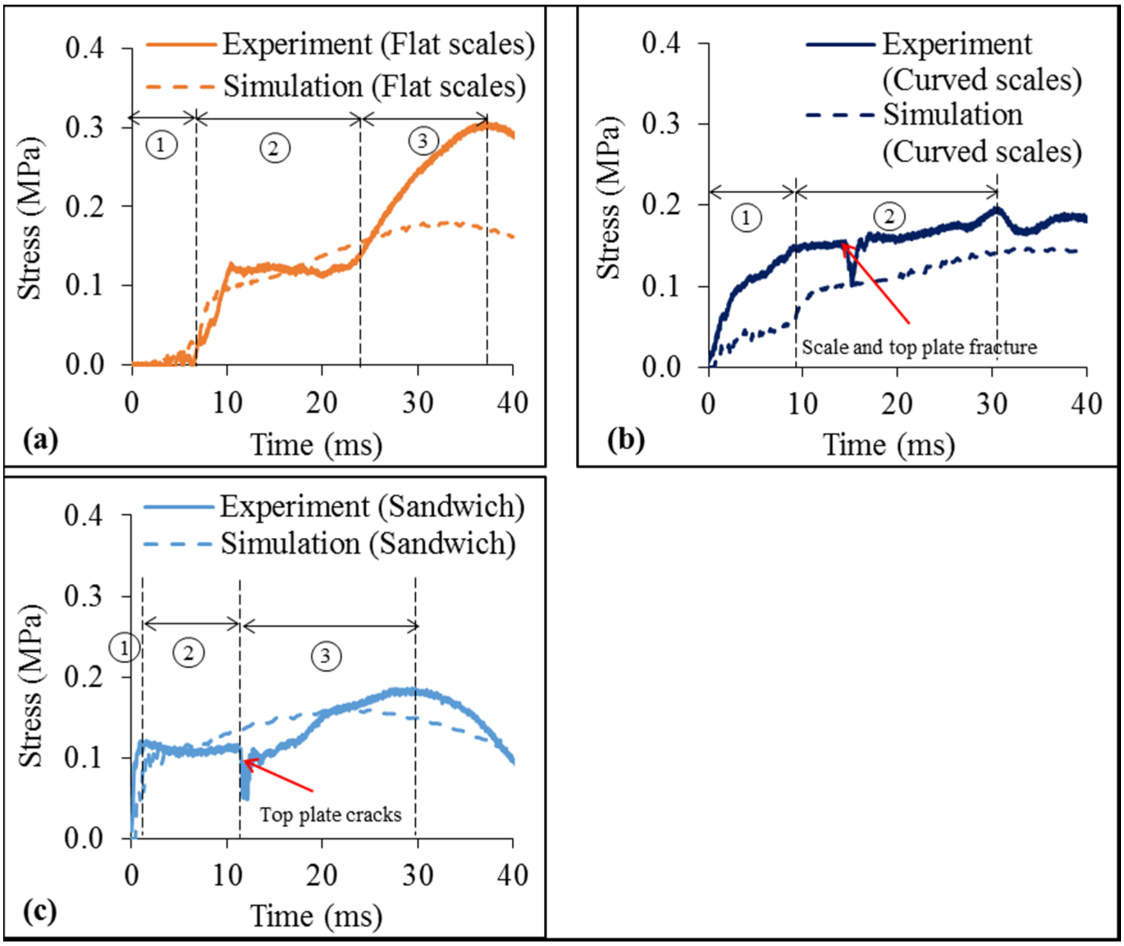

Figure 3.25: Stress-time response of the middle pressure sensor underneath sandwich and composite specimens with flat and curved scales obtained from experiment and finite element simulations.

For the specimen with curved scales, the stress-time response obtained experimentally is generally higher than that obtained numerically throughout the impact event as depicted in Figure 3.25(b). This may be caused by the difference in alignment of the impactor with respect to the specimen in the experiment and simulation. As can be seen in Figure 3.24(b), the impactor may have impacted almost directly on the joint of the third scale during the drop-weight impact test. On the other hand, the impactor was aligned slightly to the left of the same joint in the simulation, as shown in Figure 3.24(b). Therefore, the stress measured in the experiment may be higher than the one extracted from the numerical simulation for the specimen with curved scales because impact force could have been transferred more directly to the underlying layer through this joint instead of causing the scales to deform.

Lastly, Figures 3.22 to 3.25 show that the peak stresses transferred by these specimens are slightly higher while their deformations at maximum impactor penetration are lower in the simulations compared to the experimental results. These discrepancies might be caused by the factors discussed in Section 3.1.

3.4 Concluding remarks

The results presented in this chapter showed that the composite system resists the impact load via two deformation modes: (a) bending of scales, and (b) compression of the underlying layer. When subject to impact, the scales can deform to dissipate a part of impact energy while the remaining impact energy is absorbed by the underlying layer. As long as the underlying layer is not densified, it helps to minimize the peak stress transferred to the underside of the composite system.

The numerical simulations and experimental validation also showed that the composite system can perform better than a conventional sandwich specimen with the same volume of materials provided the scales are curved. Due to additional hoop resistance from their curved shape, the scales can dissipate a larger proportion of impact energy before they get flattened and the impactor starts compressing on the underlying layer. Nonetheless, a right geometrical configuration of the curved scales, as well as suitable material stiffness and strength ratios between the scales and the underlying layer, are required for the composite system to have improved impact performance. The effects of various geometrical and material properties of the scales and underlying layer on the impact performance of the composite system will be further examined in Chapters 4 and 5.

4.0 Effects of geometrical properties of scales

It was shown in Chapter 3 that the stiffness of the scale assembly affects the performance of the composite system against impact. The stiffness is controlled by both material and geometrical properties. In this chapter, the effects of the following geometrical properties of the scale assembly are examined: aspect ratio L_s/t_s, curvature L_s/R, degree of overlapping L_h/S, and relative size L_h/D of scales as defined earlier in Figure 2.2. Here, the scales are made of aluminium while the underlying cellular layer is made of cork as discussed in Sections 2.2.3 and 2.2.4. The combined effects of these parameters are studied and a geometric stiffness factor is introduced as a simple means to quantify the combined effects. Lastly, the effect of connectivity between adjacent scales is explored.

4.1 Aspect ratio of scales

The aspect ratio L_s/t_s is negatively correlated to the bending resistance of scales. Figure 4.1(a) shows the peak stress transferred by specimens with various L_s/t_s and a relatively low curvature $L_s/R = 0.5$, while their deformed shapes at maximum impactor penetration are illustrated in Figure 4.2. For these cases, L_s/t_s was varied by keeping L_s constant while changing t_s; the curvature, relative size as well as degree of overlapping were kept constant. It is evident from Figure 4.1(a) that the peak stress transferred reduces with decreasing L_s/t_s (in a sense, increasing stiffness). As can be seen in Figure 4.2(d), the underlying layer is highly densified. This is because scales with low curvature and high aspect ratio can be flattened more easily and hence inefficient in resisting the impactor. As a result, more impact energy is absorbed by the underlying cellular layer and high peak stress is transferred to the protected surface. As the aspect ratio decreases, the underlying layer is compressed relatively less severely because thicker scales provide higher resistance against the impactor. Furthermore, the plastic moment capacity of each scale increases with its thickness, and hence the thicker scales can dissipate more impact energy as shown in Figure 4.1(b). Thus, higher reduction in peak stress transferred is realized if sufficient plastic deformation of the scales occurs.

The stiffness of the scale system is also controlled by curvature of the scales. When the combination between aspect ratio and curvature of the scales leads to an “over-stiff” scale system relative to the underlying cellular layer, plastic dissipation in the scales

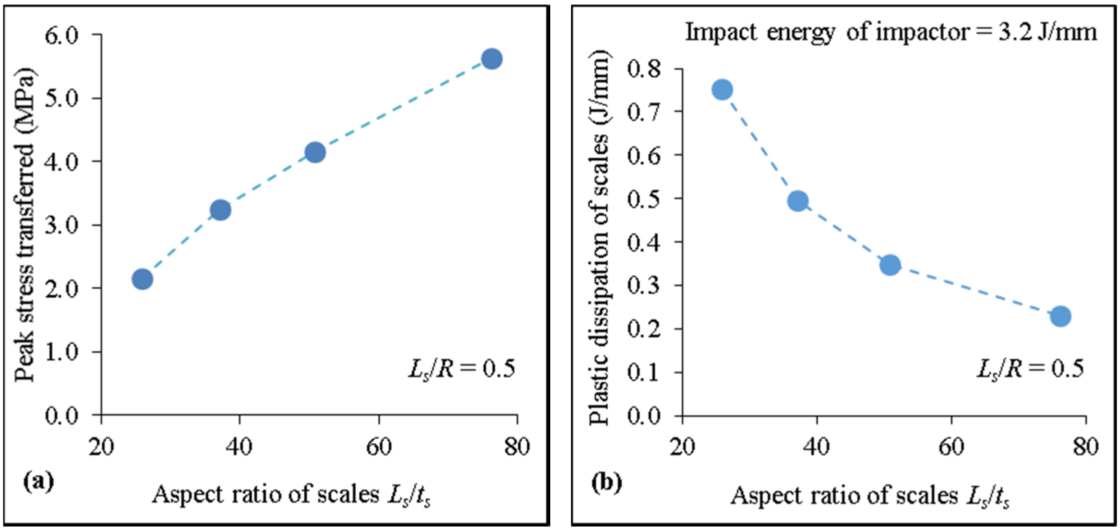

Figure 4.1: (a) Peak stress transferred, and (b) plastic dissipation of scales against L_s/t_s, with $L_s/R = 0.5$, $L_h/D = 0.8$, and $L_h/S = 1.5$.

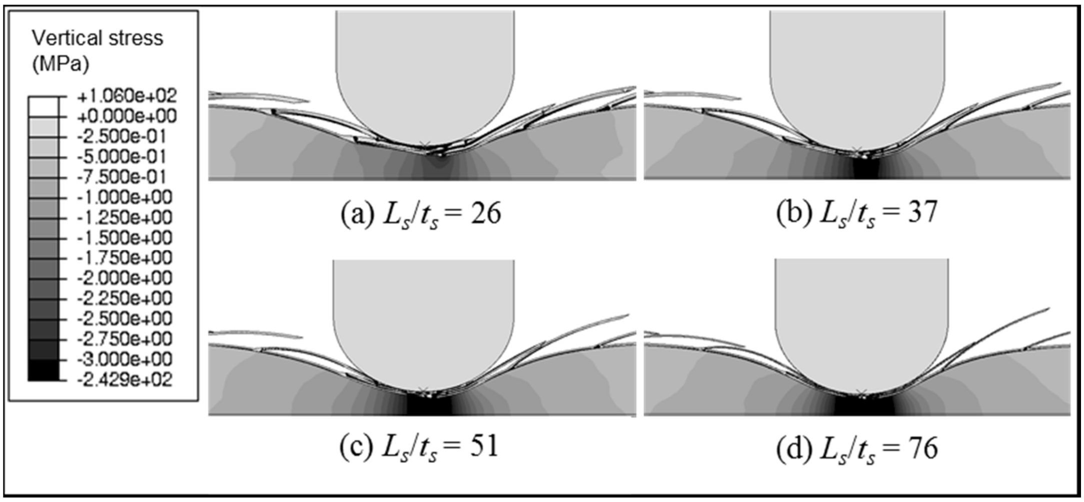

(a) $L_s/t_s = 26$

(b) $L_s/t_s = 37$

(c) $L_s/t_s = 51$

(d) $L_s/t_s = 76$

Figure 4.2: Deformation and vertical stress contour of specimens at maximum impactor penetration for specimens with different values of L_s/t_s, $L_s/R = 0.5$, $L_h/D = 0.8$, and $L_h/S = 1.5$.

may not be realized. This is demonstrated here for scales with a higher scale curvature L_s/R of 2.1 compared to 0.5 in the previous example. While the peak stress transferred decreases when L_s/t_s reduces from 67 to 37, a further reduction in L_s/t_s to 26 increases the peak stress transferred as shown in Figure 4.3(a). Similar to the cases shown earlier in Figure 4.2, scales with high aspect ratio of $L_s/t_s = 67$ are flimsy and collapse easily as shown in Figure 4.4(d), resulting in high peak stress transferred to the protected surface. As L_s/t_s decreases, the peak stress transferred also reduces as more impact energy is dissipated through plastic deformation of the thicker scales as shown in Figure 4.3, and the cellular layer is compressed less severely as can be observed from Figure 4.4(b). This is because most of the impact energy has been dissipated through plastic deformation of the scales. However, when L_s/t_s further decreases to 26, the peak stress increases. This trend is different compared to the set of specimens with lower curvature of 0.5 as shown earlier in Figure 4.1(a). This is because when aspect ratio is low and curvature is high, the scales are stiffer. Hence, their deformation is restricted, leading to significant stress concentrations at the joints of the scales underneath the impactor as shown in Figure 4.4(a). There is higher possibility of the scales puncturing into the underlying cellular layer instead of deforming through flexure.

Therefore, the optimum range for the aspect ratio in a particular application corresponds to the scales being able to sustain against collapse while undergoing sufficient plastic deformation to absorb the impact energy. This range is demonstrated to be dependent on scale curvature. It may also be influenced by the degree of overlapping and size of the scales.

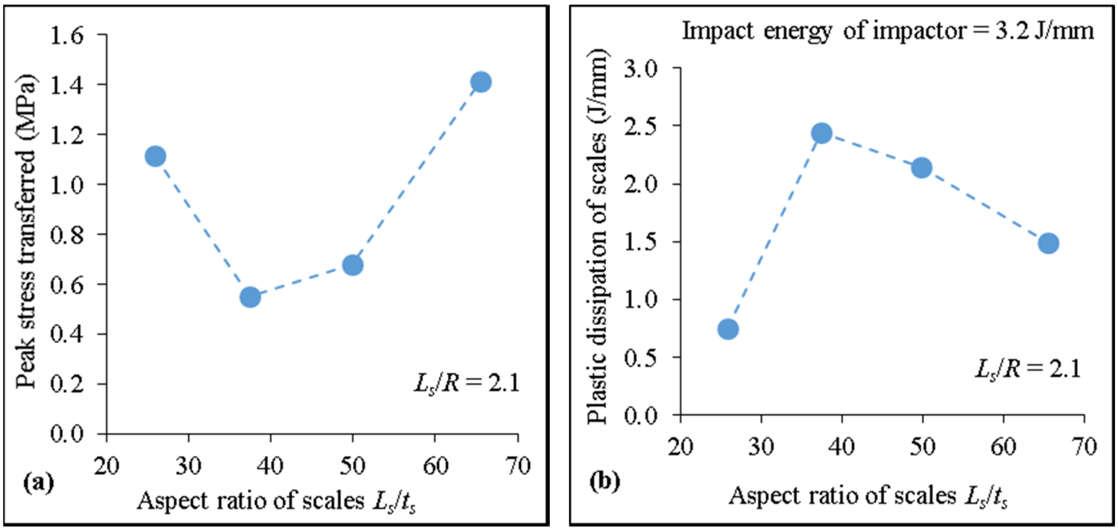

Figure 4.3: (a) Peak stress transferred, and (b) plastic dissipation against L_s/t_s, with $L_s/R = 2.1$, $L_h/D = 0.8$, and $L_h/S = 1.5$.

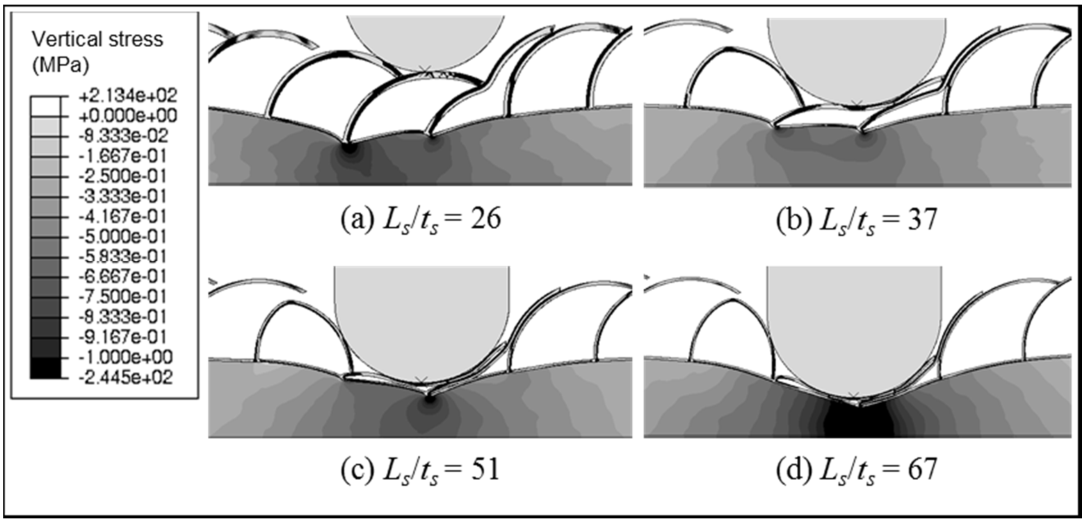

(a) $L_s/t_s = 26$ (b) $L_s/t_s = 37$

(c) $L_s/t_s = 51$ (d) $L_s/t_s = 67$

Figure 4.4: Deformation and vertical stress contour of specimens at maximum impactor penetration for specimens with different values of L_s/t_s, $L_s/R = 2.1$, $L_h/D = 0.8$, and $L_h/S = 1.5$.

4.2 Curvature of scales

As the scale curvature L_s/R is an important parameter that influences the stiffness of the scale system and hence the peak stress transferred, it is further explored in this section. Curvature affects the amount of free space available for the scales underneath the point of impact to deform before the impactor starts compressing on the underlying cellular layer. Figure 4.5(a) shows the peak stress transferred to the protected surface for specimens with different L_s/R, while Figure 4.6 depicts the deformation of the specimens. For these cases, L_s/R was varied without altering L_h and S, but t_s was also changed at the same time in order to maintain a constant L_s/t_s. As shown in Figure 4.5(a), the peak stress transferred reduces as L_s/R increases. This is because the scales in specimens with higher L_s/R have more room to deform (as shown in Figure 4.6) before they are flattened by the impactor. Hence, the plastic hinges formed in the scales undergo larger rotation. In addition, increased curvature may result in the formation of more plastic hinges in the scales. Consequently, specimens with higher scale curvature have higher impact energy dissipation as shown in Figure 4.5(b). This leads to lower peak stress transferred to the protected surface.

While increasing the scale curvature up to $L_s/R = 2.1$ results in improved performance, a further increase in L_s/R to 2.6 leads to higher peak stress transferred as shown in Figure 4.5(a). This could be caused by the increased hoop resistance of the scales with higher curvature. When subject to impact, the scales do not deform much through bending due to their increased stiffness, resulting in minimal increment in impact energy dissipated

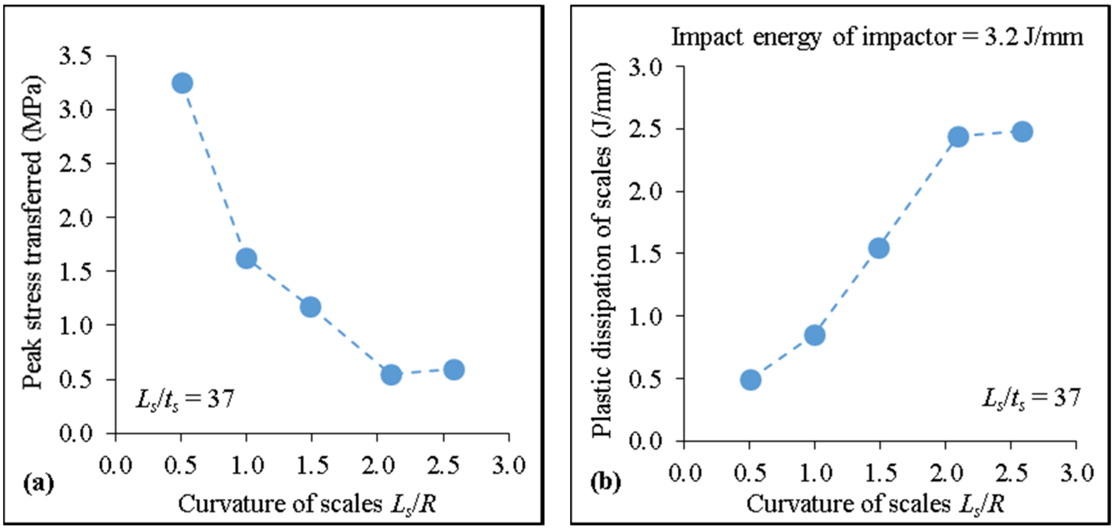

Figure 4.5: (a) Peak stress transferred, and (b) plastic dissipation against L_s/R, with $L_s/t_s = 37$, $L_h/D = 0.8$, and $L_h/S = 1.5$.

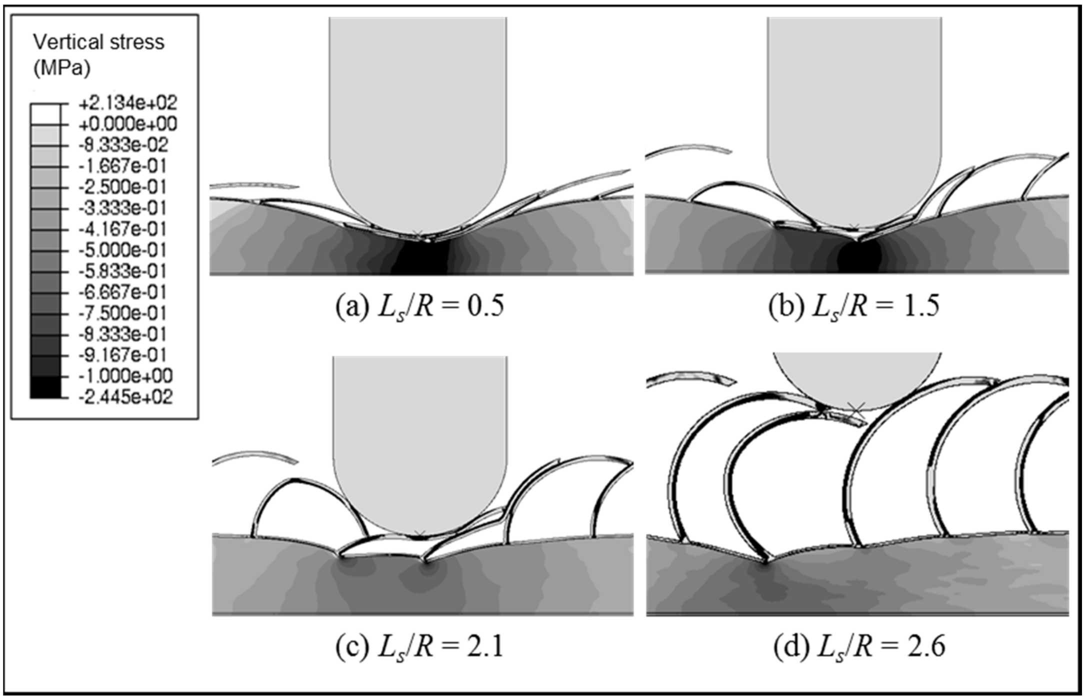

Figure 4.6: Deformation and vertical stress contour of specimens at maximum impactor penetration for specimens with different values of L_s/R, $L_s/t_s = 37$, $L_h/D = 0.8$, and $L_h/S = 1.5$.

by the scales as shown in Figure 4.5(b). Instead, it becomes easier for the impactor to push entire scales into the cellular layer at the joints between the scales and the cellular layer as displayed in Figure 4.6(d). Hence, the peak stress transferred to the protected surface is increased.

It is not possible to keep the total volume of the scales constant for the cases shown in Figure 4.5. The volume of the scales increases with curvature for these cases. If the volume of the scales is kept constant, the thickness t_s of the scales must be reduced while L_s/R is increased with R fixed. Consequently, L_s/t_s increases with L_s/R. Figure 4.7 shows the variation of peak stress transferred versus scale curvature L_s/R, for cases with different relative scale volumes V_s/V_u. Here, the volume V_u of the underlying layer is constant for all cases, while three cases with different volumes V_s of the scales are presented.

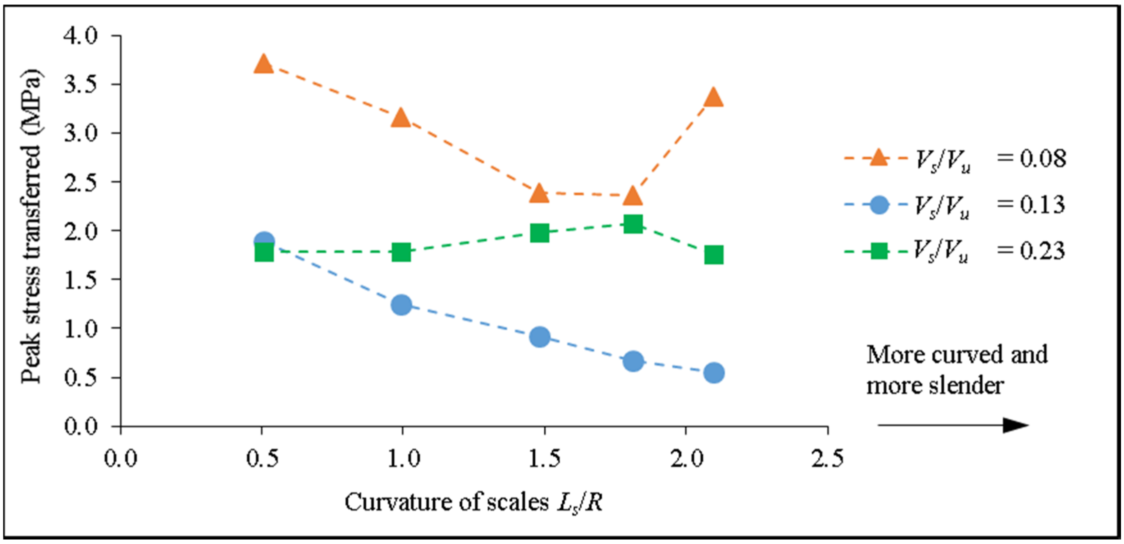

Figure 4.7: Peak stress transferred as a function of L_s/R for different values of V_s/V_u.

For cases with V_s/V_u = 0.13, the same trend of reducing peak stress transferred with increasing curvature (as shown earlier in Figure 4.5) can be observed. It is evident from Figure 4.8 that scales with higher curvature are more effective in resisting the impactor, even though they become more slender when the curvature is increased. This is because of the additional hoop resistance that arises from the curved shape of the scales, which becomes more significant with increasing curvature.

A different trend is observed for cases with lower V_s/V_u of 0.08. As shown in Figure 4.7, the peak stress transferred reduces when L_s/R increases from 0.5 to 1.5. However, when L_s/R further increases from 1.8 to 2.1, the peak stress transferred also increases. As shown in Figure 4.8, scales with high curvature become flimsy and collapse easily under impact. Thus, despite having more space to deform, the scales have weak resistance and low impact energy dissipation because of their high aspect ratio. This results in significant compression on the underlying cellular layer and hence higher peak stress is transferred. Moreover, comparing the values of peak stress transferred for V_s/V_u = 0.13

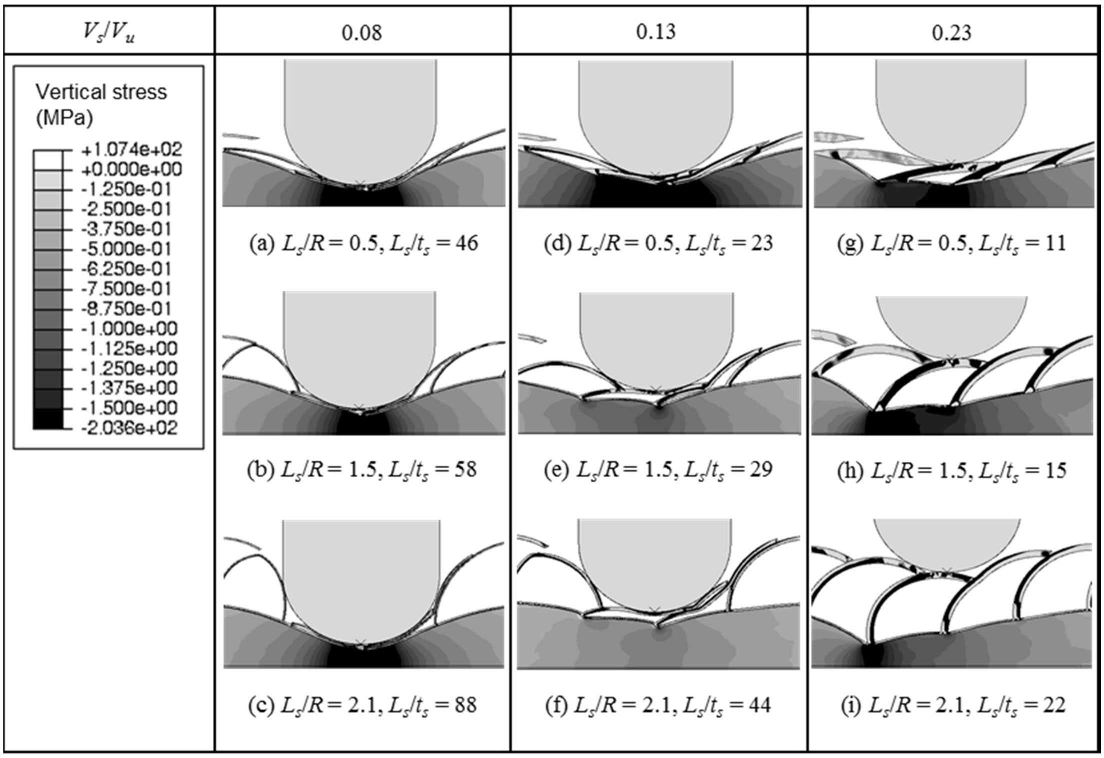

(a) $L_s/R = 0.5, L_s/t_s = 46$
(d) $L_s/R = 0.5, L_s/t_s = 23$
(g) $L_s/R = 0.5, L_s/t_s = 11$
(b) $L_s/R = 1.5, L_s/t_s = 58$
(e) $L_s/R = 1.5, L_s/t_s = 29$
(h) $L_s/R = 1.5, L_s/t_s = 15$
(c) $L_s/R = 2.1, L_s/t_s = 88$
(f) $L_s/R = 2.1, L_s/t_s = 44$
(i) $L_s/R = 2.1, L_s/t_s = 22$

Figure 4.8: Deformation and vertical stress contour of specimens at maximum impactor penetration for specimens with different values of V_s/V_u.

and 0.08, the thicker scales associated with higher scale volume allow higher energy dissipation through plastic deformation and hence lower peak stress transferred.

As the volume of the scales increases further, a different trend is observed. As shown in Figure 4.7, the peak stress transferred for $V_s/V_u = 0.23$ is higher than those for $V_s/V_u = 0.13$, and does not vary significantly when L_s/R increases from 0.5 to 2.1. This is because the thicker scales in these cases result in the scale assembly being very stiff relative to the underlying cellular layer. Hence when pressed by the impactor, virtually all the impact energy is transferred through the joints of the scales at the cellular layer as shown in Figure 4.8, instead of being dissipated through flexural deformation of the scales. The high stress concentrations at the joints induce high peak stress transferred along the underside of the composite system.

The results show that there is an optimum range of scale curvature L_s/R given fixed values of L_s/t_s, L_h/D, and L_h/S. From another angle, Figure 4.7 indicates that there is an optimum relative volume V_s/V_u of the scales. Specimens with overly low or high relative volume of scales are less effective in dissipating the impact energy through plastic deformation of the scales since the scales are too slender or too stiff. Hence, the stiffness of the scales is an important factor which influences the impact performance of the composite system as it determines whether the scales or underlying layer deform more significantly in resisting the impactor.

4.3 Degree of overlapping of scales

The degree of overlapping L_h/S of scales affects the interaction between adjacent scales and the number of scales mobilized to resist the impactor. To study the effect of this parameter, the degree of overlapping L_h/S was varied while keeping the total volume of scales constant by allowing the aspect ratio L_s/t_s to increase simultaneously with L_h/S.

Figure 4.9(a) shows the variation of peak stress transferred with L_h/S while Figure 4.10 shows the deformation of these specimens. There exists an optimum degree of overlapping when the total volume of the scales is kept constant. As can be seen in Figure 4.10(a), low degree of overlapping results in fewer scales being mobilized to resist the impactor. Thus, the scales are not able to dissipate much impact energy as shown in Figure 4.9(b). Moreover, the scales have less flexural resistance since they have longer spans. Consequently, the underlying cellular layer beneath the point of impact is deformed more severely, leading to higher peak stress transferred to the protected surface. On the other hand, as shown in Figure 4.10(d), the specimen with high degree of overlapping also does not perform well because the thinner and slender scales deform easily and dissipate less impact energy even though more scales are mobilized to resist the impact force. At an intermediate degree of overlapping, an optimal balance can be achieved between the number of scales mobilized to resist the impactor and the resistance provided by each scale. At the optimal point, the amount of energy dissipated by the scales is maximized as shown in Figure 4.9(b). When this occurs, the peak stress transferred is minimized since there is minimal compression on the underlying layer.

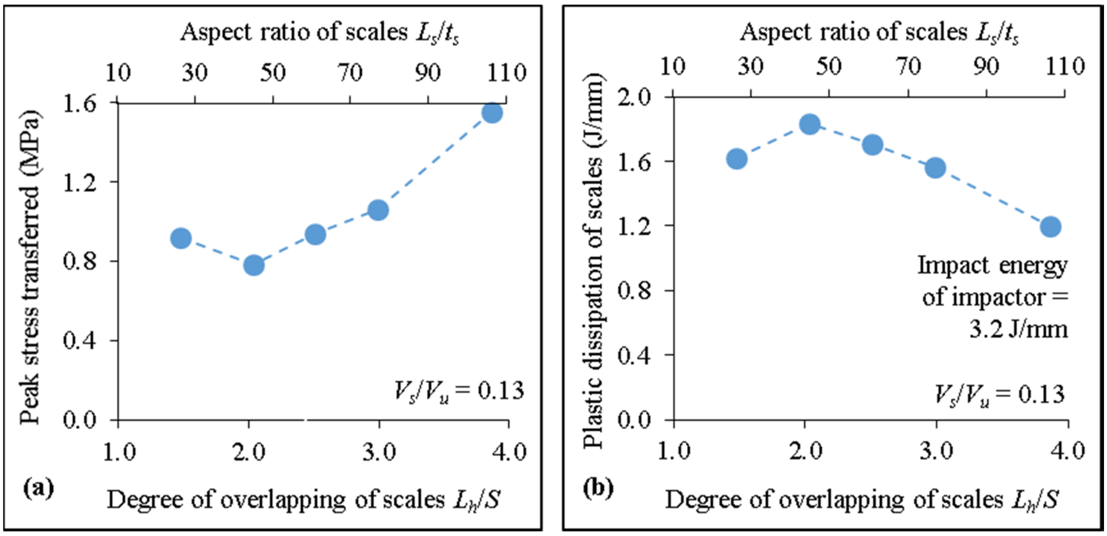

Figure 4.9: (a) Peak stress transferred, and (b) plastic dissipation of scales against L_h/S for specimens with various L_s/t_s, $L_s/R = 1.5$, $L_h/D = 0.8$, and $V_s/V_u = 0.13$.

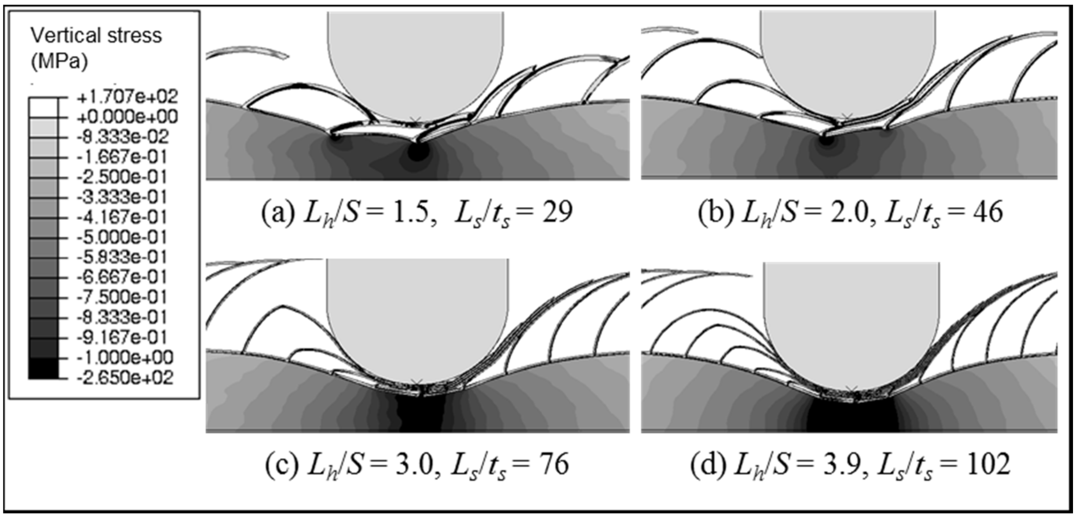

(a) $L_h/S = 1.5$, $L_s/t_s = 29$

(b) $L_h/S = 2.0$, $L_s/t_s = 46$

(c) $L_h/S = 3.0$, $L_s/t_s = 76$

(d) $L_h/S = 3.9$, $L_s/t_s = 102$

Figure 4.10: Deformation and vertical stress contour of specimens at maximum impactor penetration for specimens with different values of L_h/S and L_s/t_s, $L_s/R = 1.5$, $L_h/D = 0.8$, and $V_s/V_u = 0.13$.

4.4 Relative size of scales

The relative size L_h/D of scales determines the number of scales activated to resist the impactor, which in turn affects the resistance of the assembly of scales against impact. Figure 4.11(a) shows the peak stress transferred by the composite specimens as a function of L_h/D while the deformation of the specimens is displayed in Figure 4.12. Here, the total volume of the scales was kept constant by allowing aspect ratio L_s/t_s of the scales to increase simultaneously with L_h/D while other parameters including t_s were kept constant.

As can be seen in Figure 4.12(a), small scales (e.g. $L_h/D = 0.2$) are stiff and do not deform plastically when subject to impact. As a result, virtually no impact energy is dissipated through plastic deformation of the scales, leading to localized compression of the underlying cellular layer and hence higher peak stress is transferred to the protected surface. When L_h/D increases to 0.5 and 1.0, the peak stress transferred reduces significantly because the scales are able to deform as shown in Figures 4.12(b) and 4.12(c) and dissipate a significant proportion of the impact energy. This reduces

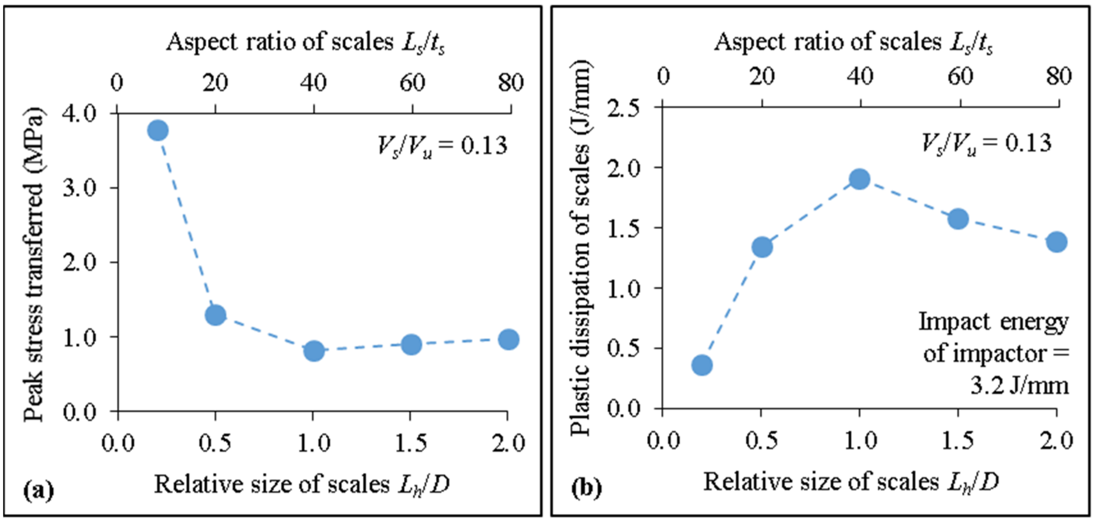

Figure 4.11: (a) Peak stress transferred, and (b) plastic dissipation of scales against L_h/D for specimens with $V_s/V_u = 0.13$, $L_s/R = 1.5$, and $L_h/S = 1.5$.

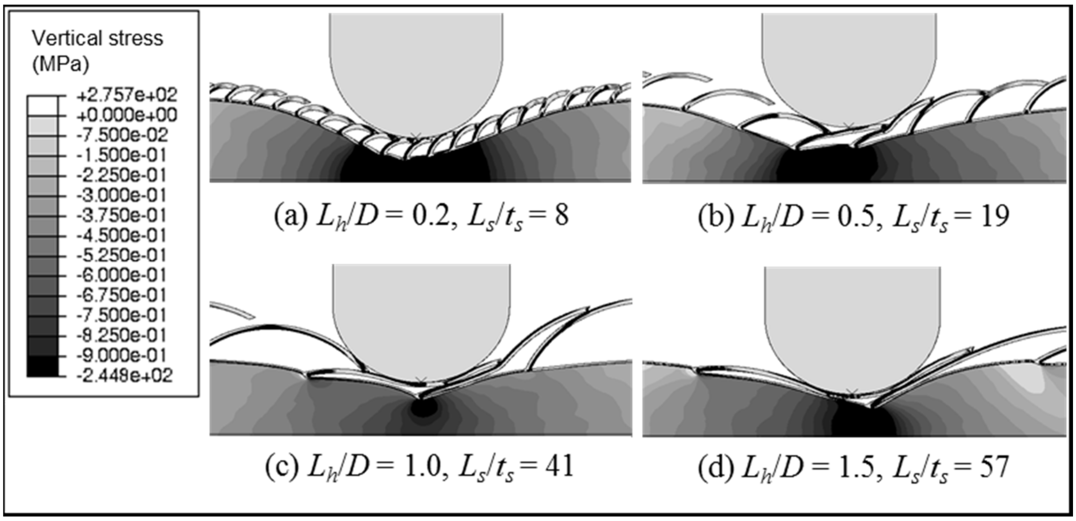

(a) $L_h/D = 0.2$, $L_s/t_s = 8$ (b) $L_h/D = 0.5$, $L_s/t_s = 19$

(c) $L_h/D = 1.0$, $L_s/t_s = 41$ (d) $L_h/D = 1.5$, $L_s/t_s = 57$

Figure 4.12: Deformation and vertical stress contour of specimens at maximum impactor penetration for specimens with different values of L_h/D and L_s/t_s, V_s/V_u = 0.13, L_s/R = 1.5, and L_h/S = 1.5.

the amount of compression on the underlying cellular layer. In addition, the size of the scales are such that the impact force is spread over a larger area of the specimen which also contributes to reducing the peak stress transferred to the protected surface. However, when the size of the scales increases further, there is an increase in the peak stress transferred because the scales become more slender. As a result, they are less effective in dissipating the impact energy and transferring the impact force to adjacent scales. Therefore, there is an optimum size of the scales such that the amount of impact energy dissipated by the scales is maximized.

4.5 Concept of geometric stiffness of scale assembly

The results in the preceding sections suggest that the stiffness of the assembly of scales must not be high nor too low compared to the underlying cellular layer to minimize the peak stress transferred to the protected surface. The composite system should be designed such that the plastic dissipation of scales is activated while minimizing the compression of the underlying cellular layer during impact.

Generally, the stiffness of the scale assembly is governed by its geometrical properties (which are examined in this chapter) and material properties (which have been kept constant for the cases shown in this chapter). The results presented in Sections 4.1 to 4.4 indicate that the stiffness of the scale assembly has an inverse relationship with the aspect ratio L_s/t_s. The flexural stiffness of each scale increases when L_s/t_s decreases. On the other hand, the stiffness of the scale assembly increases with scale curvature L_s/R due to the increase in hoop resistance of the scales. Furthermore, the results indicate that the stiffness of the scale assembly increases with the degree of overlapping L_h/S of scales as it affects the number of scales that are mobilized in order to resist the impact force. This agrees well with the findings of Vernerey and Barthelat (2010) and Browning (2012) as high degree of overlapping of scales indeed able to distribute the impact load over a larger region. Furthermore, the stiffness of the scale assembly is inversely proportional to the relative size L_h/D of scales because more scales are activated to resist the impactor when the size L_h of scales is smaller. As discussed by Browning (2012), larger indenters (i.e. bigger than the size of one scale) has larger contact area with the scales, reducing the deformation of the scales and stress concentration underneath the indenter.

Therefore, the combined effects of these geometrical parameters on the stiffness of the scale assembly may be captured by the following expression:

$$K_{geometry} = \frac{\left(\frac{L_s}{R}\right)^a \left(\frac{L_h}{S}\right)^b}{\left(\frac{L_s}{t_s}\right)^c \left(\frac{L_h}{D}\right)^d} \tag{4.1}$$

where $K_{geometry}$ is the stiffness factor that accounts for the combined effects of the above-mentioned geometrical parameters while a, b, c, and d are constants.

It is expected that there is a relationship between $K_{geometry}$ and the deformation mode as well as impact performance of the composite system. Specimens with approximately the same range of $K_{geometry}$ are expected to show the same deformation mode. Hence, the mechanical response of the composite system can be understood in a more general manner in terms of this overall stiffness factor $K_{geometry}$ instead of looking into the effects of aspect ratio, curvature, degree of overlapping, and relative size of the scales separately.

To determine the appropriate values for the exponents a and c, consider first the performance of an individual scale. A typical scale can be modelled as a curved cantilever since it is anchored to the underlying layer at one end but free at the other end. Following Castigliano's theorem, assuming the deformation mode of the scales is dominant by bending moment, the deflection δ of a semi-circular cantilever as shown in Figure 4.13 is given by the following equation:

$$\delta = \frac{\partial U}{\partial F} = \int_0^{\pi} \frac{MR}{EI}\left(\frac{\partial M}{\partial F}\right) d\theta \qquad (4.2)$$

where F is the applied load at the free end of the cantilever, R is the radius of curvature, E is the Young's modulus, and I is the second moment of area of the cantilever.

From Figure 4.13,

$$M = FRsin\theta \qquad (4.3)$$

$$\frac{\partial M}{\partial F} = Rsin\theta \qquad (4.4)$$

Substituting Equation 4.4 into Equation 4.2 gives the following:

$$\delta = \frac{\pi F R^3}{2EI} \qquad (4.5)$$

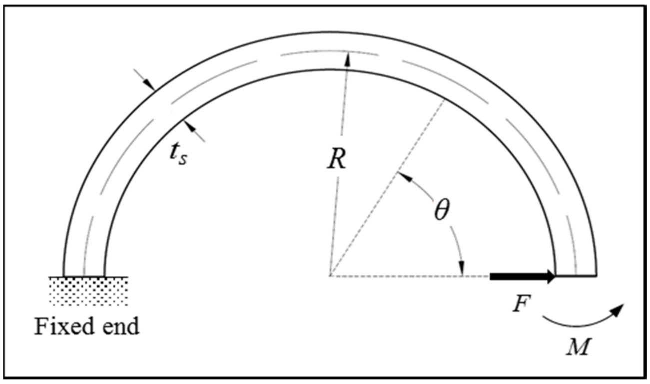

Figure 4.13: Semi-circular cantilever of thickness t_s and radius of curvature R under transverse load F at its free end.

Rearranging Equation 4.5, the stiffness of the semi-circular cantilever can be expressed in the following manner:

$$\frac{F}{\delta} = \frac{E}{6} \frac{\left(\frac{L_S}{R}\right)^2}{\left(\frac{L_S}{t_S}\right)^3} \tag{4.6}$$

where $I = \frac{{t_S}^3}{12}$ and $L_s = \pi R$.

Comparing Equations 4.1 and 4.6, the values of a and c may be taken as 2 and 3 respectively.

The stiffness of the assembly also includes the interaction between scales. The spacing and number of scales influence the degree of interaction besides the individual scale stiffness. This effect is captured by the parameters L_h/S and L_h/D, or in essence can be approximated by the number of scales activated to resist the impactor which is given by the ratio D/S. Consequently, the values of b and d may be taken as 1. Therefore, the stiffness factor $K_{geometry}$ may thus be assumed as

$$\boldsymbol{K}_{\boldsymbol{geometry}} = \frac{\left(\frac{L_S}{R}\right)^2 \left(\frac{L_h}{S}\right)}{\left(\frac{L_S}{t_S}\right)^3 \left(\frac{L_h}{D}\right)} \tag{4.7}$$

The usefulness of this stiffness factor is best assessed using the data generated in Sections 4.1 to 4.4. Figure 4.14 shows the peak stress transferred for each case normalized with the maximum allowable stress (i.e. stress at densification limit) of the underlying layer, plotted against the corresponding $K_{geometry}$ value determined using Equation 4.7. Interestingly, it can be observed that the cases can be grouped into three distinct regions based on the range of $K_{geometry}$ values. The specimens within each region seem to show the same deformation mode even though they have different combinations for L_s/t_s, L_s/R, L_h/S, and L_h/D.

For specimens with $K_{geometry}$ less than 0.04 x 10^{-3}, which are labelled as Group "*A*" in Figure 4.14, high peak stress is transferred to the protected surface. The stress transferred exceeds the maximum allowable stress of the underlying cellular layer. The specimens that fall within this region have scales that are slender and collapse easily under the

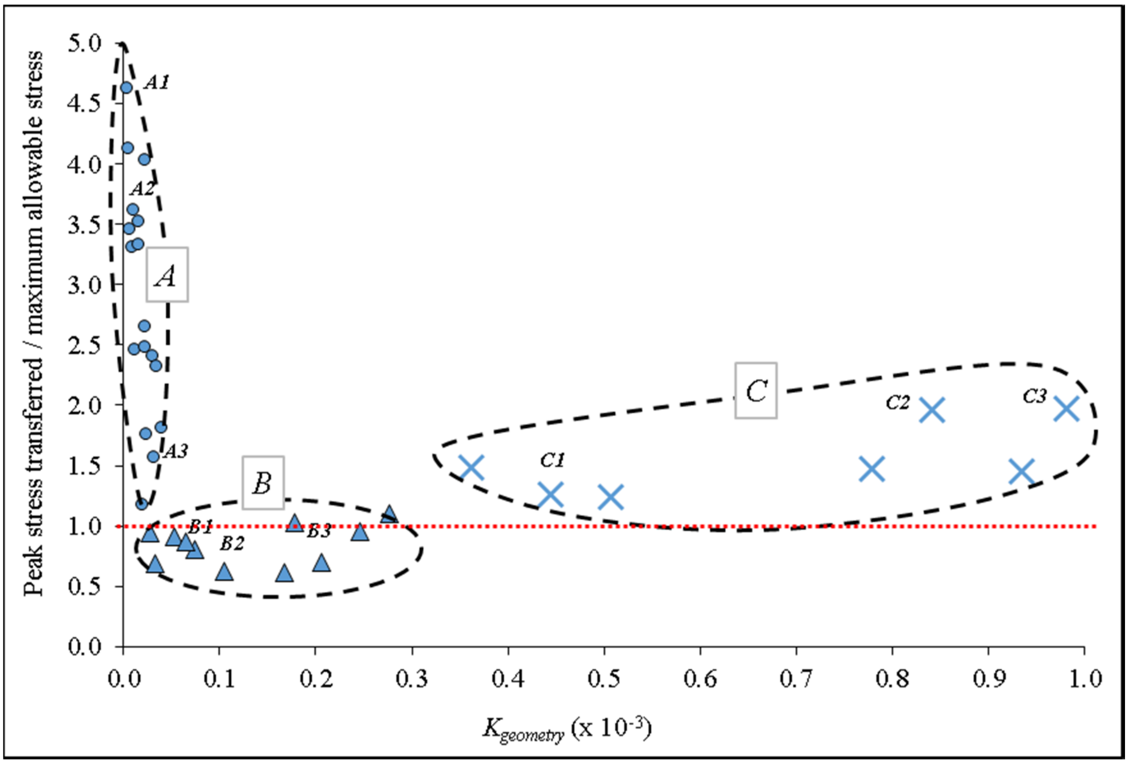

Figure 4.14: Peak stress transferred (normalized with maximum allowable stress of underlying layer) against geometric stiffness factor $K_{geometry}$ of scales.

impact, as shown in Figure 4.15. Since the scales have low resistance, little impact energy is dissipated through deformation of the scales and significant compression is observed in the cellular layer (and in extreme cases, densification occurs) beneath the region of impact. Thus, the peak stresses transferred by these specimens are more concentrated at the point of impact as can be seen in Figure 4.16(a).

Specimens with $K_{geometry}$ larger than 0.3 x 10^{-3}, which fall within Group "*C*" in Figure 4.14, also show relatively higher peak stress transferred. The stress transferred exceeds

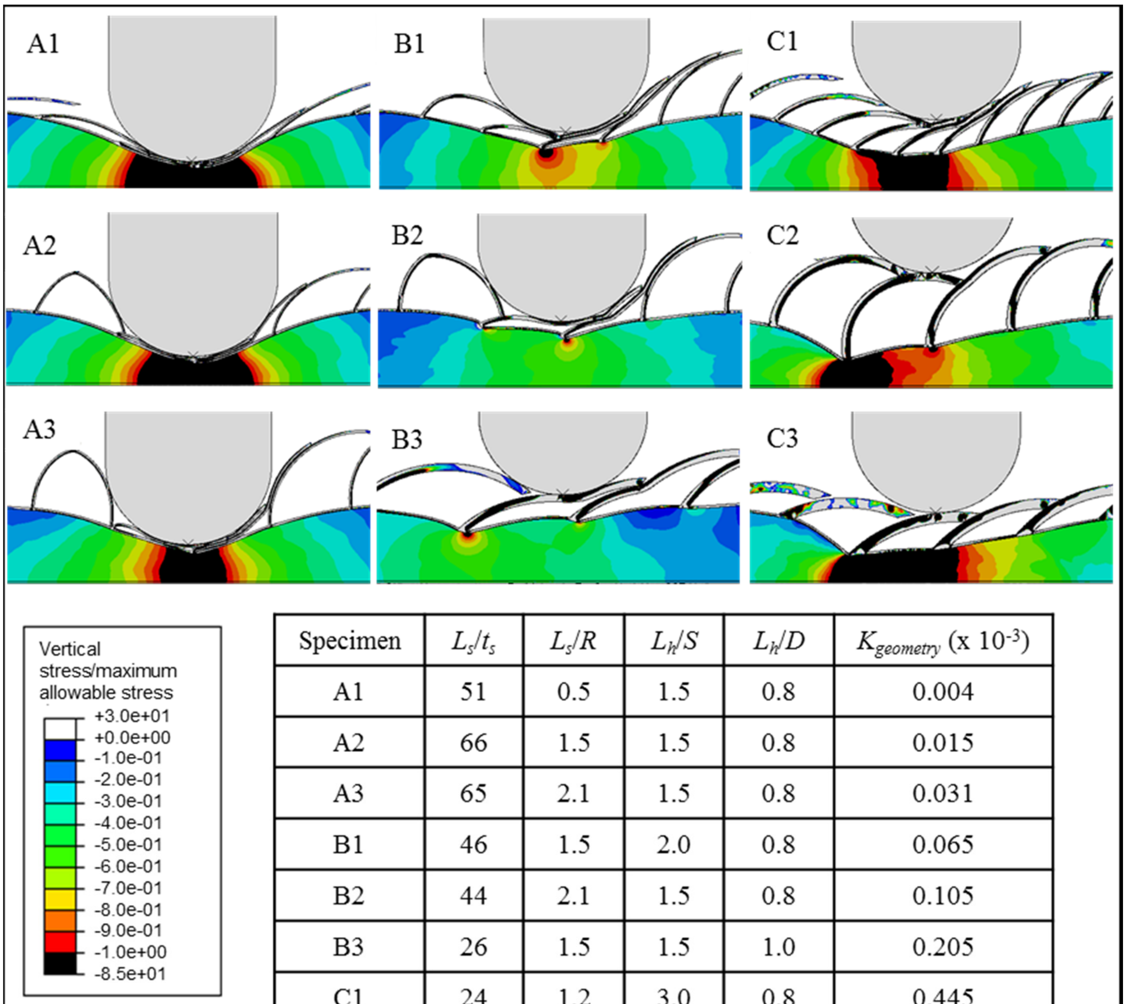

Specimen	L_s/t_s	L_s/R	L_h/S	L_h/D	$K_{geometry}$ (x 10^{-3})
A1	51	0.5	1.5	0.8	0.004
A2	66	1.5	1.5	0.8	0.015
A3	65	2.1	1.5	0.8	0.031
B1	46	1.5	2.0	0.8	0.065
B2	44	2.1	1.5	0.8	0.105
B3	26	1.5	1.5	1.0	0.205
C1	24	1.2	3.0	0.8	0.445
C2	22	2.1	1.5	0.8	0.842
C3	13	1.0	1.5	0.8	0.981

Figure 4.15: Deformation at maximum impactor penetration of selected specimens with various ranges of $K_{geometry}$ of scales.

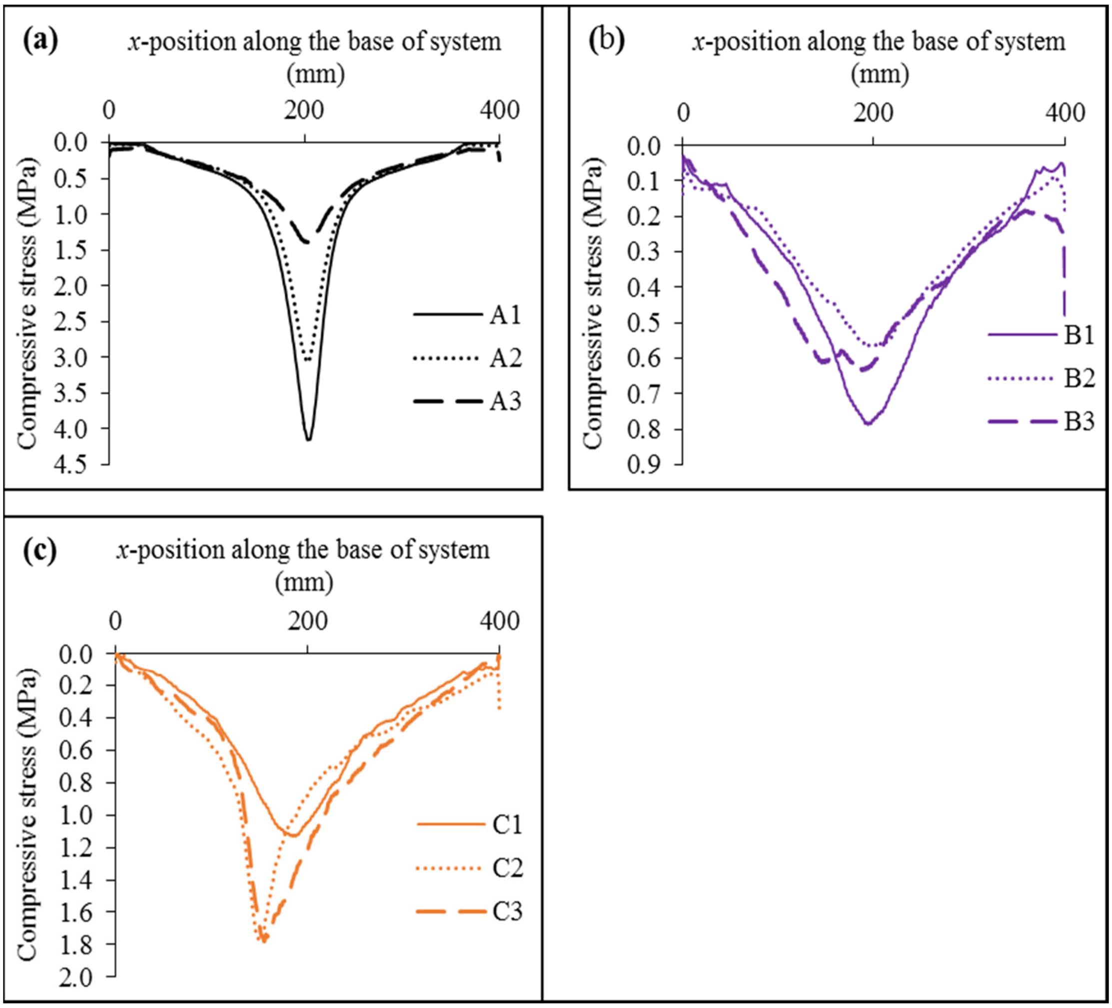

Figure 4.16: Normal compressive stress envelope along base of selected specimens with various ranges of $K_{geometry}$ of scales.

the maximum allowable stress of the underlying cellular layer, and the former increases with $K_{geometry}$ in this group. From Figure 4.15, it can be observed that the scales in these specimens are very stiff in bending and unable to dissipate impact energy through plastic deformation. Instead, they tend to push into the underlying layer when subject to the impact, causing significant stress concentrations in the cellular layer which will be transferred to the protected surface. As a result, the stress distributions along the base of the specimens are also rather concentrated underneath the impactor as displayed in Figure 4.16(c).

The peak stress transferred is minimal for specimens with $K_{geometry}$ between 0.04 x 10^{-3} and 0.3 x 10^{-3}, which fall under Group "*B*" in Figure 4.14. Within this range of $K_{geometry}$, the scales are sufficiently stiff such that they do not collapse easily, but at the same time they are not too rigid and hence can undergo plastic deformation as shown in Figure 4.15 and dissipate significant amount of impact energy. As a result, the stress distributions at the base of the specimens is wider as displayed in Figure 4.16(b). Moreover, due to reduced compression of the underlying cellular layer, the stresses transferred by the specimens in this range of $K_{geometry}$ does not exceed the maximum allowable stress of the underlying cellular layer. Therefore, for the cases shown, this range of $K_{geometry}$ seems to produce optimal impact performance of the composite system.

Figure 4.14 also shows that there is a rather considerable overlap in $K_{geometry}$ values when transiting from Groups "*A*" to "*B*". This is because the influence of volume V_s of the scales is not accounted for in the dimensionless geometric stiffness factor $K_{geometry}$ as shown earlier in Equation 4.7. A closer inspection of the results reveals that the cases from Group "*A*" have relative volume V_s/V_u less than 0.13, while the V_s/V_u values for those in Group "*B*" range from 0.11 to 0.19. The scale assembly of cases in Group "*B*" generally have higher volume compared to those in Group "*A*". As mentioned in Section 4.2, as long as the scales are able to deform by bending, cases with relatively higher volume of the scales are able to dissipate a larger amount of impact energy and hence minimize densification of the underlying cellular layer and the resulting peak stress transferred. Thus, for cases where the scales are deformable (i.e. $K_{geometry}$ less than 0.3 x 10^{-3} for the results shown here), the relative volume of the scales seems to control the proportions of impact energy that are dissipated by scales and absorbed by the underlying cellular layer. Figure 4.17 shows the ratio of energy absorbed by the underlying layer to the energy dissipated by the scales against various $K_{geometry}$ values. It is evident that the energy dissipated through plastic deformation of the scales is higher than the energy absorbed by the underlying cellular layer for cases in Group "*B*" whose $K_{geometry}$ values fall within the optimum range. Conversely, for cases in Groups "*A*" and "*C*" whose $K_{geometry}$ values fall outside the optimum range, the energy dissipated by the scales is smaller than that absorbed by the underlying layer.

Lastly, the fish scale-cellular composite specimens also perform better than their sandwich counterparts with the same volume of materials if their $K_{geometry}$ value falls within the optimum range, i.e. Group "*B*". As shown in Figure 4.18, the peak stresses transferred by the composite specimens in this group do not exceed those of their sandwich counterparts. On the other hand, the peak stresses transferred by specimens with relatively low and high $K_{geometry}$ values (Group "*A*" and "*C*", respectively) exceed those of the sandwich designs. Thus, compared to a conventional sandwich design, it is beneficial to adopt the fish scale-cellular composite design only if the right configurations are used.

Therefore, the results shown in this chapter suggest that both the stiffness as well as volume of the scale assembly relative to the underlying cellular layer control the impact performance of the fish scale-cellular composite system. The findings of this study facilitate the development of a procedure to determine the optimum combinations for aspect ratio, curvature, degree of overlapping, size, and volume of the scales to achieve a desired impact performance.

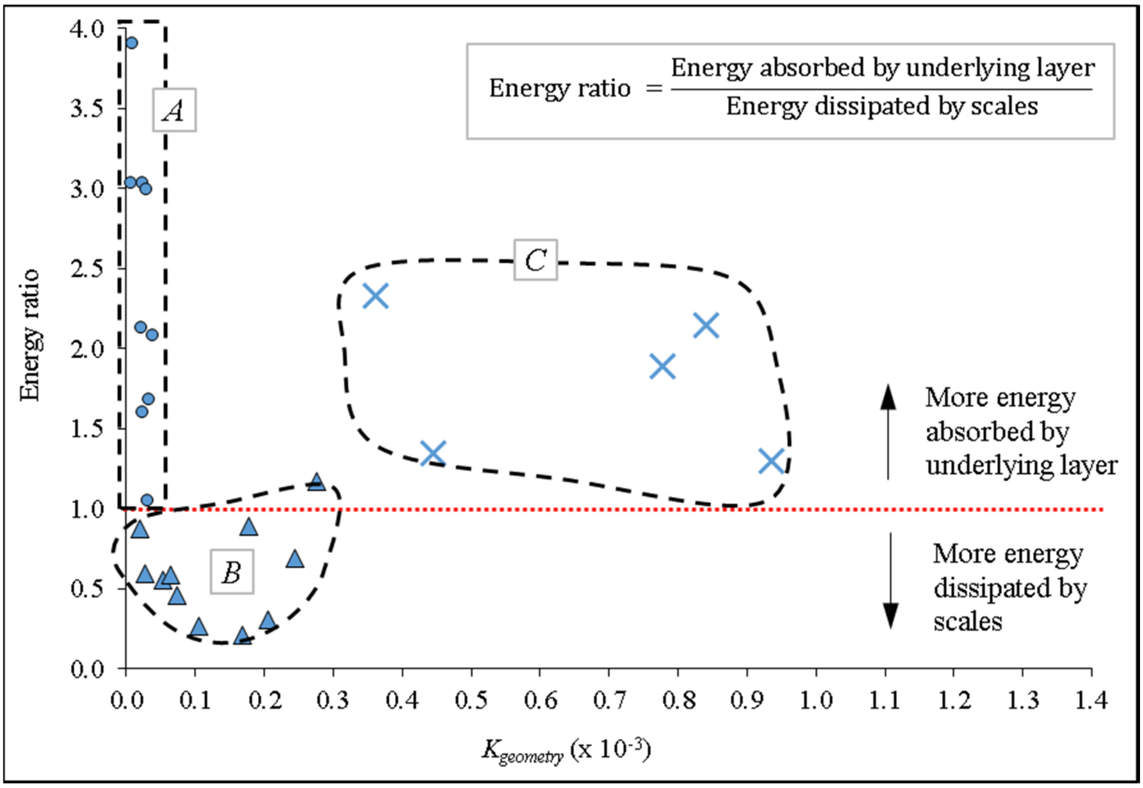

Figure 4.17: Ratio of energy absorbed by the underlying layer to energy dissipated by the scales against $K_{geometry}$ of scales.

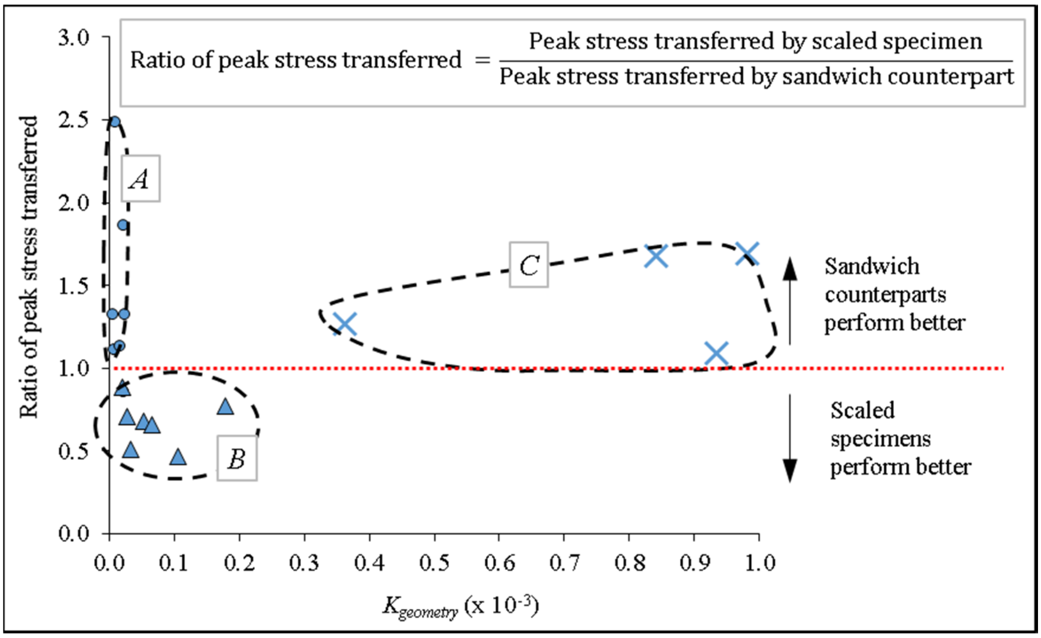

Figure 4.18: Ratio of peak stress transferred by the scaled specimen to peak stress transferred by sandwich counterpart against $K_{geometry}$ of scales.

4.6 Connectivity between adjacent scales

Based on the results presented in preceding sections, three scenarios can be encountered by the composite system when it is subject to impact. Firstly, when the scales are relatively softer than the underlying layer, they are ineffective for protection against impact hence the underlying layer absorbs most of the impact energy which causes it to be compressed severely. Secondly, when the scales are too stiff relative to the underlying layer, the impact performance is also poor because the scales tend to push into the underlying layer resulting in significant compression of the underlying layer. Thirdly, when the scales are neither too soft nor too stiff, optimum impact performance of the composite system may be achieved as the peak stress transferred is minimized. Nonetheless, the cases presented so far have scales that are connected at their bottom ends to the top plate while their top ends are free. For these cases, it can be observed that generally only the scales around the impactor are mobilized during impact while those to the left and right of the impactor do not seem to contribute to the impact resistance of the composite system. Moreover, due to the high compressibility of the underlying cellular layer, there is significant localized compression of this layer once the scales underneath the impactor collapse following the formation of plastic hinges in the scales. This leads to the densification of the underlying cellular layer beneath the point of impact.

Therefore, connecting the top ends of the scales may help to mobilize more scales to resist the impactor and increases the overall bending stiffness of the scale assembly, making it harder for individual scales to collapse under impact. In this section, the effect of scale connectivity on the three above-mentioned scenarios is examined for the specimens with different ranges of $K_{geometry}$. The joints between adjacent scales are modelled as continuous (i.e. rigid) connections, and such specimens are termed as "connected-scales specimens". On the other hand, those with disconnected scales (i.e.

connected to the top plate only while the other end is free) are termed as "disconnected-scales specimens". Figure 4.19 presents the peak stress transferred by selected specimens with connected and disconnected scales while Figure 4.20 shows the deformation of the specimens with connected scales (their counterparts with disconnected scales have been shown earlier in Figure 4.15).

From Figure 4.19, it can be observed that connected-scales specimens in Group "*A*" have lower peak stress transferred compared to their disconnected-scales counterparts. By connecting the scales at their top ends, the scales directly underneath the impactor are able to mobilize the adjacent scales more effectively to resist the impactor. Since the scales from cases in Group "*A*" are mostly slender and flimsy, connecting the scales of this specimen increases the overall bending stiffness of the scale assembly, resulting in reduced compression on the cellular layer as shown in Figure 4.20. Thus, as shown in Figure 4.21, the impact energy dissipated by the scales is higher for the connected-scales specimens.

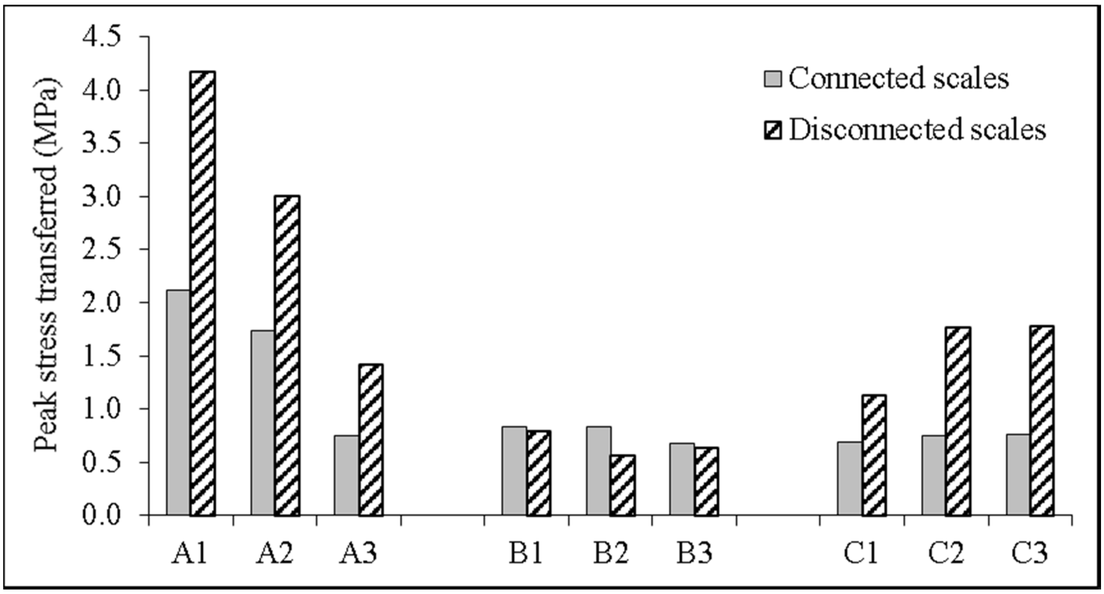

Figure 4.19: Peak stress transferred of selected specimens with connected scales and disconnected scales.

However, it is interesting to see that for specimens with $K_{geometry}$ values that are already within the optimum range, connecting the scales may not be beneficial. As shown in Figure 4.19, connecting the scales increases the peak stress transferred for cases in Group "*B*". The scales appear to be stiffer when they are connected as shown in Figure 4.20; it is harder to deform these scales when they are connected. As a result, there is less plastic deformation in the scales and hence the impact energy that is dissipated by the scales is reduced as shown in Figure 4.21. Also, due to the increased stiffness of the

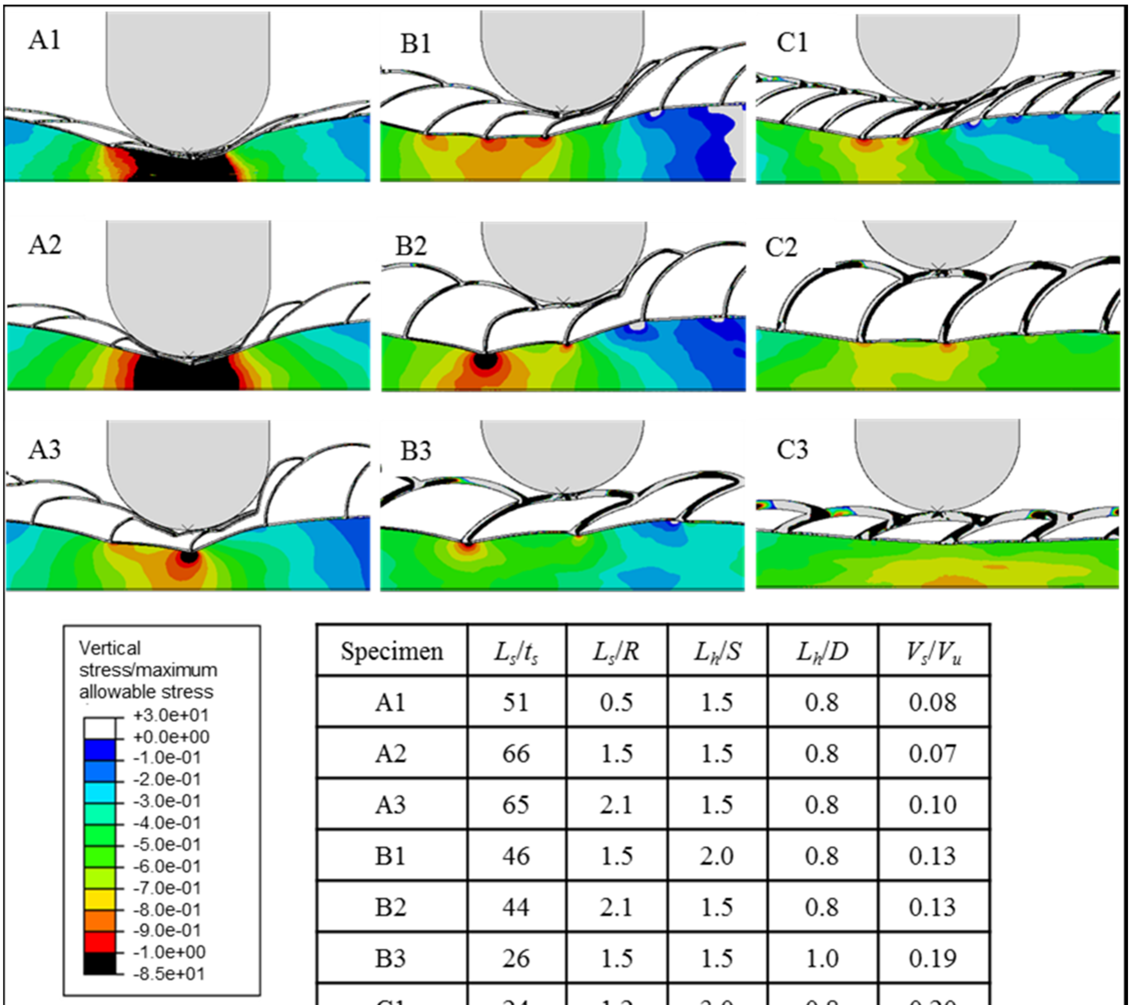

Specimen	L_s/t_s	L_s/R	L_h/S	L_h/D	V_s/V_u
A1	51	0.5	1.5	0.8	0.08
A2	66	1.5	1.5	0.8	0.07
A3	65	2.1	1.5	0.8	0.10
B1	46	1.5	2.0	0.8	0.13
B2	44	2.1	1.5	0.8	0.13
B3	26	1.5	1.5	1.0	0.19
C1	24	1.2	3.0	0.8	0.20
C2	22	2.1	1.5	0.8	0.23
C3	13	1.0	1.5	0.8	0.23

Figure 4.20: Deformation at maximum impactor penetration of selected specimens with connected scales.

assembly of scales when they are connected, the scales tend to puncture into the cellular layer causing stress concentrations at the joints. Therefore, higher peak stress is transferred when the scales are connected for these cases.

Lastly, for specimens whose $K_{geometry}$ values exceed the optimum range (i.e. Group "*C*" as shown in Figure 4.19), connecting the scales results in better impact performance. When the scales are connected, the assembly of scales behaves like a stiff truss and compresses more uniformly on the underlying cellular layer. This spreads the impact load over a larger area of the underlying layer as shown in in Figure 4.20, resulting in lower peak stress transferred to the protected surface. Moreover, the impact energy dissipated through plastic deformation of the scales for these cases seems to be significantly higher when they are connected as displayed in Figure 4.21. This is partly due to more scales being activated to resist the impactor. Therefore, connecting scales that are already stiff converts the assembly of scales into a stiff top layer that results in uniform compression of the cellular layer when the composite system is subject to impact. It seems that this deformation mode can only be achieved in specimens with connected scales.

Consequently, these results prove that connectivity is helpful in reducing peak stress transferred when $K_{geometry}$ values are less than the optimum range, but may be detrimental when they are already within the optimum range. However, when the $K_{geometry}$ values are already higher than the optimum range, connectivity may result in improved performance since the assembly of scales acts like a stiff top layer. Nevertheless, it should be noted that fabricating scales that are connected at both ends may be costly and this should be taken into account when designing the composite system.

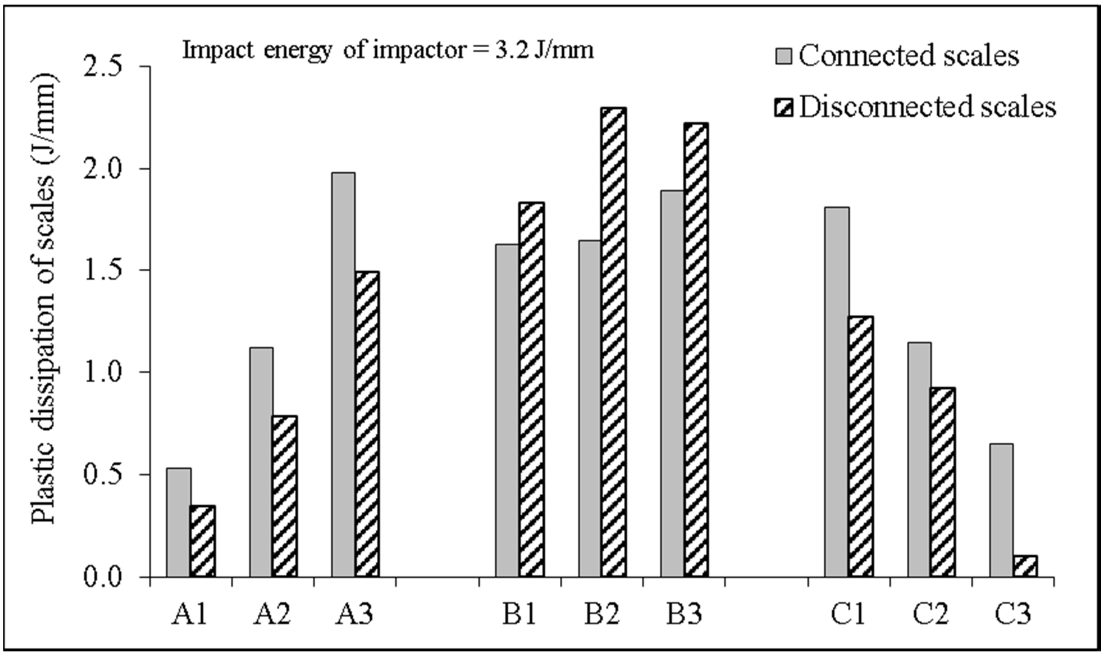

Figure 4.21: Plastic dissipation of scales of selected specimens with connected scales and disconnected scales.

4.7 Conclusion: optimum geometrical configuration of scales

In this chapter, the effects of geometrical properties of the scales was examined. The results showed that the impact performance of the composite system is governed by the stiffness of the scale assembly which is controlled by its geometrical properties. It was observed that the impact performance of the composite system generally increases with decreasing aspect ratio, increasing curvature, increasing degree of overlapping, and decreasing size of the scales. A geometric stiffness factor $K_{geometry}$ which accounts for the combined effects of the four aforementioned parameters was defined, and a range for this factor which leads to optimum impact performance was found. Within this optimum range, the scales are sufficiently stiff such that they do not collapse easily, but undergo plastic deformation and dissipate significant amount of impact energy. This results in peak stress transferred by the composite system that is lower than the maximum allowable stress of the underlying cellular layer. In addition, the energy dissipated by the scales is higher than that absorbed by the underlying cellular layer, and the peak stress transferred by the composite system is lower than that of a sandwich design with the same volume of materials.

Therefore, the results obtained in this study demonstrate that optimum combinations for aspect ratio, curvature, degree of overlapping, size, and relative volume of the scales can be determined in order to achieve optimum impact performance. Figures 4.22 to 4.26 show the peak stress transferred (normalized by the maximum allowable stress of the underlying layer) as the function of these parameters for specimens with various $K_{geometry}$ values labelled as Groups "*A*", "*B*", and "*C*" as defined earlier in Section 4.5. Since specimens in Group "*B*" have optimum impact performance, the extent of scale aspect ratio, curvature, degree of overlapping, size, and volume within which these cases lie as shown in Figures 4.22 to 4.26 would correspond to the optimum bounds for these parameters. They are summarized in Table 4.1 and may be used as the basis of designing the scales of the composite system.

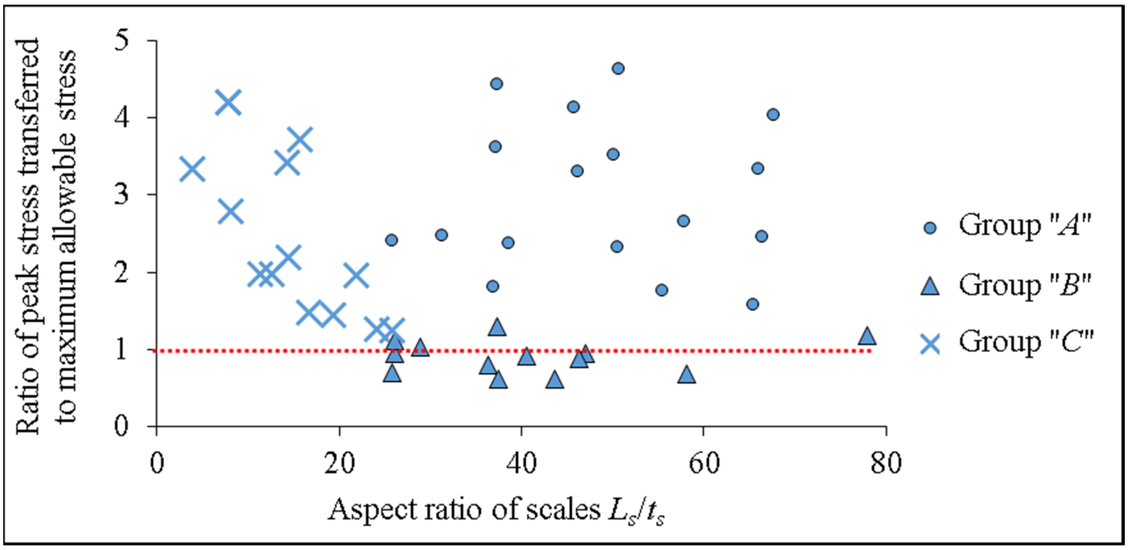

Figure 4.22: Peak stress transferred (normalized with maximum allowable stress of underlying layer) against L_s/t_s for cases with different groups of $K_{geometry}$ values.

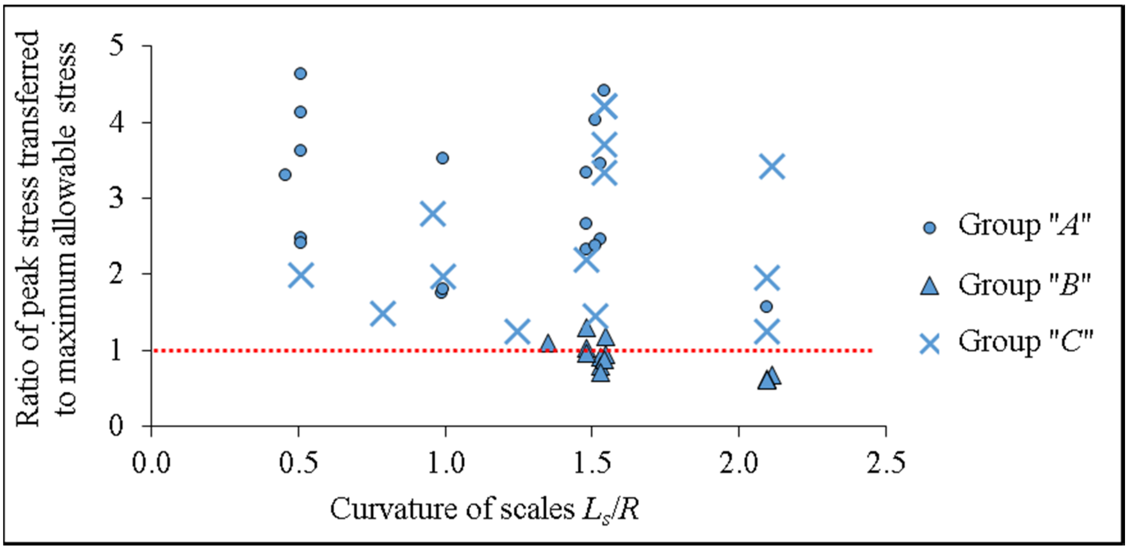

Figure 4.23: Peak stress transferred (normalized with maximum allowable stress of underlying layer) against L_s/R for cases with different groups of $K_{geometry}$ values.

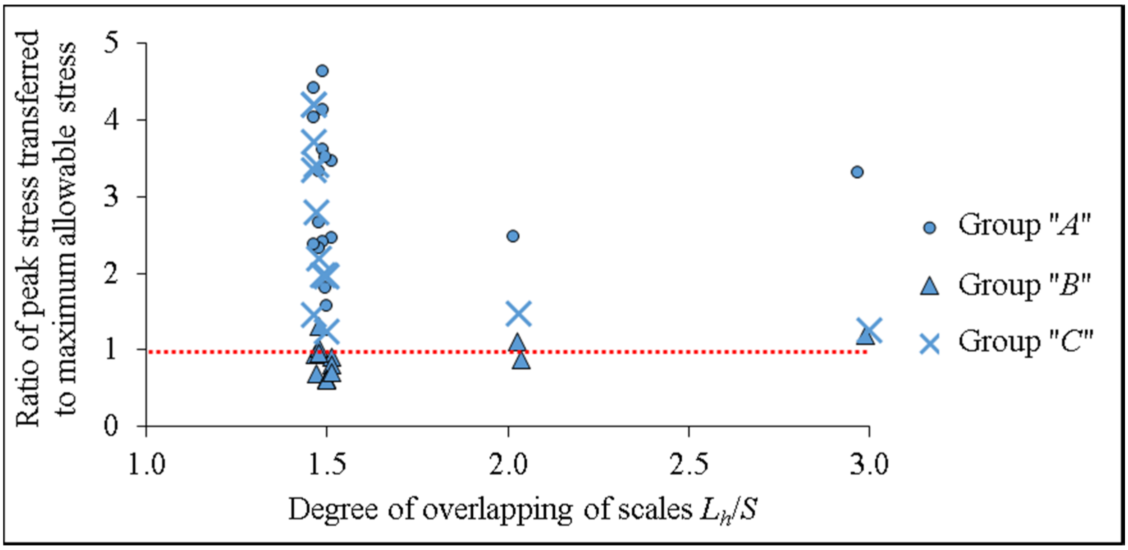

Figure 4.24: Peak stress transferred (normalized with maximum allowable stress of underlying layer) against L_h/S for cases with different groups of $K_{geometry}$ values.

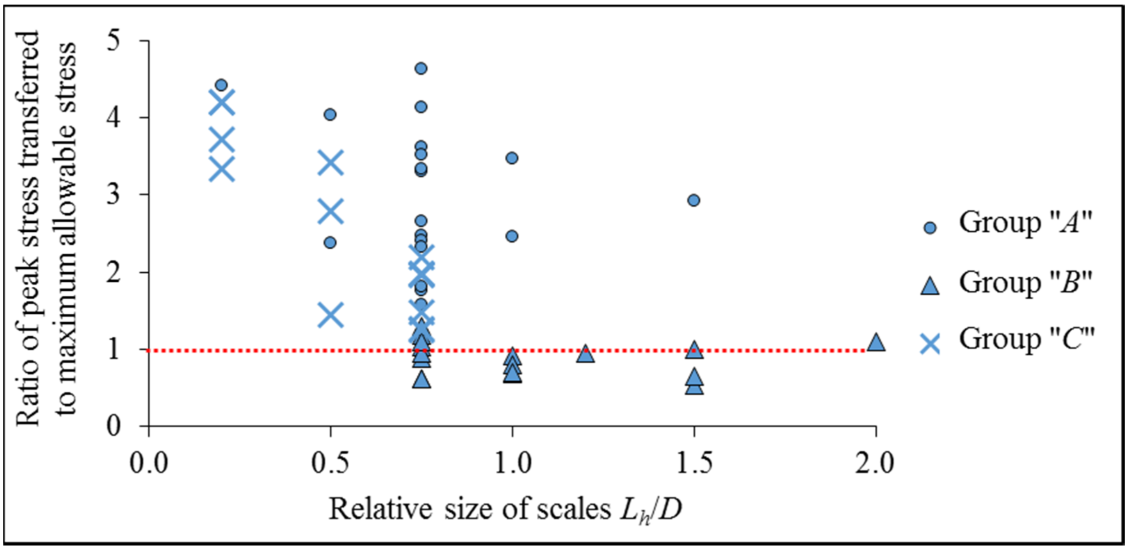

Figure 4.25: Peak stress transferred (normalized with maximum allowable stress of underlying layer) against L_h/D for cases with different groups of $K_{geometry}$ values.

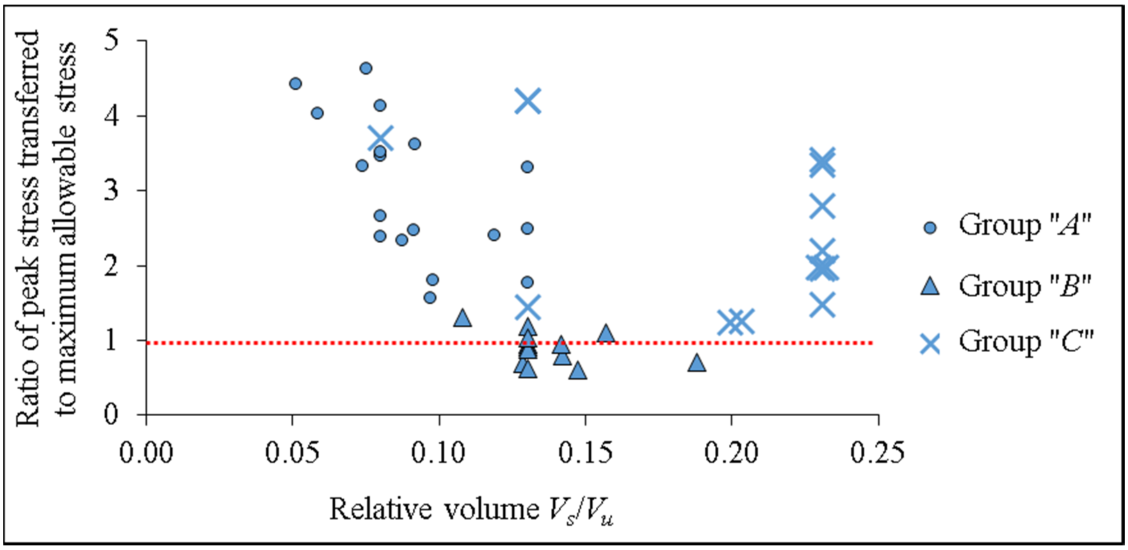

Figure 4.26: Peak stress transferred (normalized with maximum allowable stress of underlying layer) against V_s/V_u for cases with different groups of $K_{geometry}$ values.

Table 4.1: Optimum ranges for different geometrical properties of scales.

Geometrical properties	**Optimum range**
Scale aspect ratio L_s/t_s	25 – 50
Scale curvature L_s/R	1.0 – 2.1
Degree of overlapping of scales L_h/S	1.5 – 3.0
Relative size of scales L_h/D	0.75 – 2.0
Relative volume V_s/V_u	0.1 – 0.2

5.0 Effects of material properties of the composite system and thickness of cellular layer

The material properties of the scales and underlying cellular layer govern the mode of deformation of the composite system and the manner in which the impact force is transferred through its different components. As discussed in Chapter 3, the scales must have sufficient strength and stiffness such that they are able to dissipate a significant amount of impact energy in order to minimize compression on the underlying layer and hence lower the peak stress transferred. However, past studies on fish scale structures, such as those by Vernerey and Barthlelat (2010) and Browning (2012), have only focused on the geometrical configuration of the scale assembly. They have not considered the effects of material properties of the scales and underlying layer on the impact performance of the composite system. In this chapter, the effects of material properties, specifically stiffness and strength, are presented and their optimum ranges are proposed. Thereafter, the combined effects of material and geometrical properties of the scales and underlying cellular layer on the impact performance of the composite system are discussed. This chapter ends with an investigation on the effects of the thickness of the underlying cellular layer.

5.1 Young's modulus of scales

The effect of Young's modulus of the scales can be represented by the material stiffness ratio which is defined as the ratio of the Young's modulus of the scales to that of the underlying cellular layer. For the results presented in this section, the material stiffness ratio was varied by changing the Young's modulus of the scales while keeping the material properties of the underlying cellular layer constant. For all cases the same assembly of scales was used: $L_s/t_s = 28.6$, $L_s/R = 1.5$, $L_h/D = 0.8$, and $L_h/S = 1.5$. Figure

5.1 shows the peak stress transferred by specimens with different material stiffness ratios while their deformed shapes are illustrated in Figure 5.2. It is apparent that the peak stress transferred is high when the material stiffness ratio is very low (i.e. Young's modulus of the scales is relatively low compared to the underlying layer), as the scales are too soft to resist the impact force and are easily flattened. This results in significant compression on the underlying layer as shown in Figure 5.2(a). The scales are unable to dissipate much impact energy and hence the underlying cellular layer has to absorb most of it. When the impact energy exceeds its energy absorption capacity (i.e. the maximum energy that can be absorbed before densification occurs), the underlying cellular layer densifies and high peak stress is transferred to the protected surface.

As the material stiffness ratio increases, the peak stress transferred reduces. This is because the scales become stiffer and hence have improved bending resistance. Instead of being flattened easily, they are better able to transfer the impact force to adjacent scales. In addition, formation of plastic hinges in the scales becomes more prominent, and the amount of impact energy that is dissipated through plastic deformation of the scales increases as illustrated in Figure 5.3. At the same time, the impact energy that is absorbed by the underlying cellular layer reduces. This leads to reduced compression of the underlying layer as depicted in Figures 5.2(b) and 5.2(c), resulting in lower peak stress transferred.

However, as the material stiffness ratio increases further, there appears to be a threshold value above which there is minimal change in the peak stress transferred. As displayed in Figures 5.2(d) and 5.2(e), both cases with high material stiffness ratio respond in an almost identical manner: the scales underneath the impactor are deformed but there is minimal compression on the underlying layer. This is because the stiffer scales are able

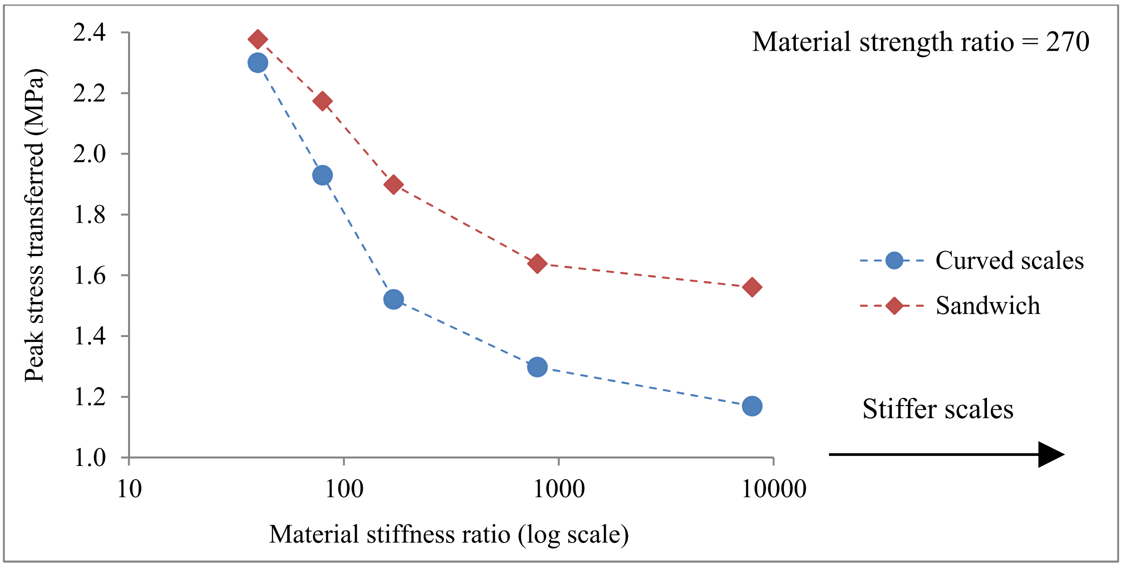

Figure 5.1: Peak stress transferred versus material stiffness ratio for curved scales and sandwich specimens.

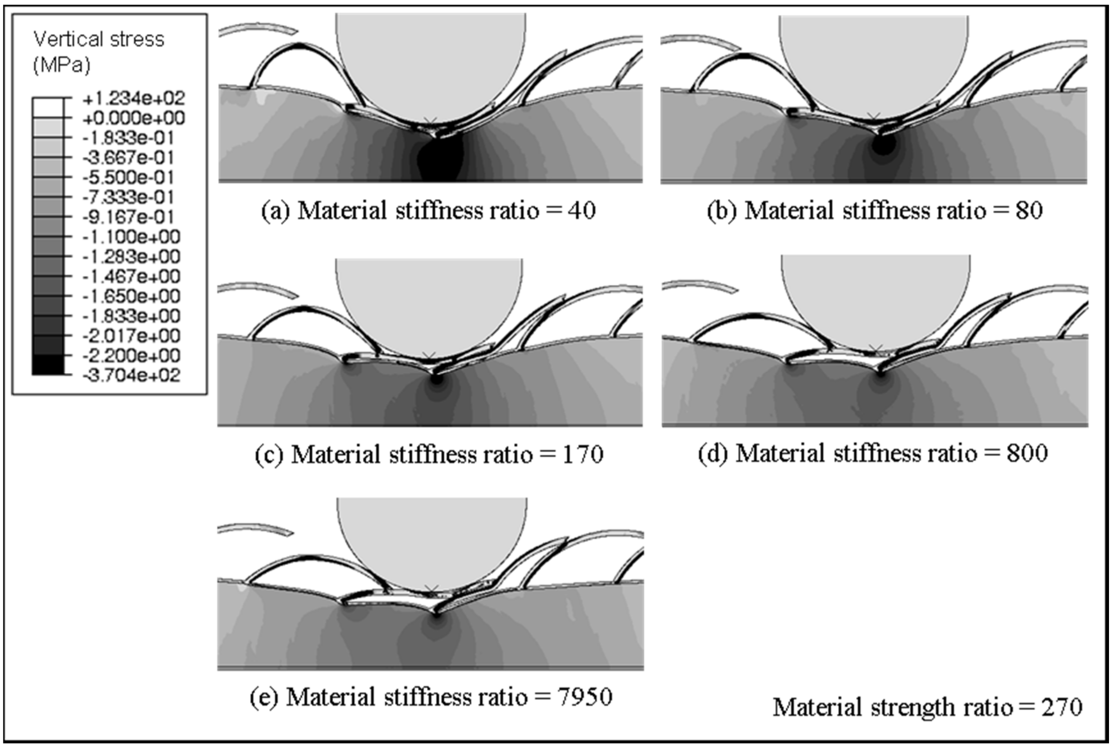

Figure 5.2: Deformation and vertical stress contour for composite specimens with various material stiffness ratios at maximum impactor penetration.

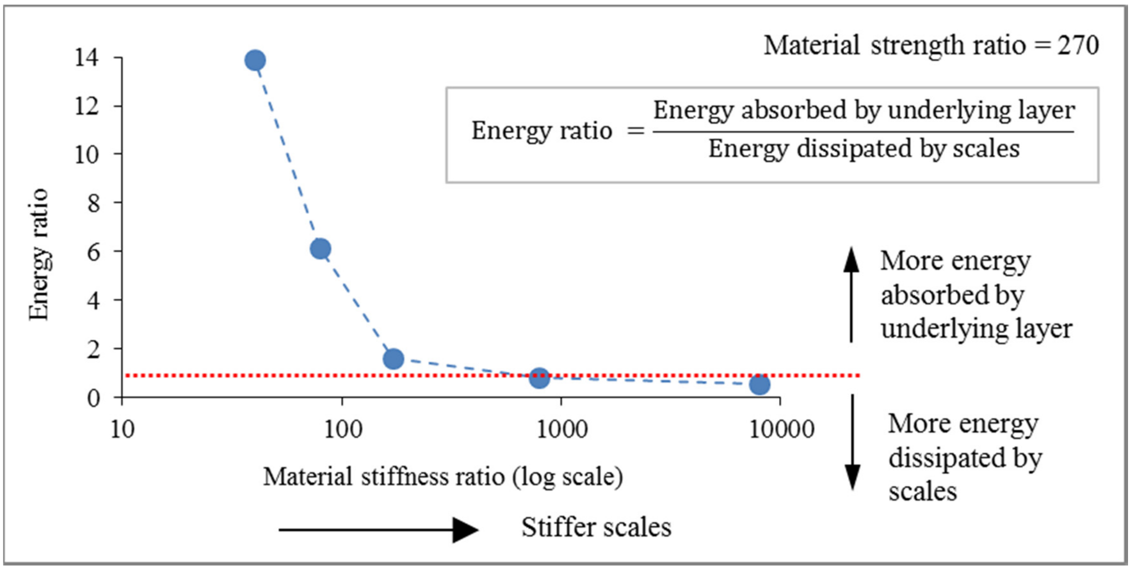

Figure 5.3: Ratio of energy absorbed by the underlying layer to energy dissipated by the scales for specimens with various material stiffness ratios.

to dissipate most of the impact energy and the amount of energy absorbed by the underlying layer reduces as shown in Figure 5.3. Consequently, densification does not occur in the underlying layer. For these cases, the stress induced within the underlying layer still falls within the plateau region of its compressive stress-strain response as illustrated earlier in Figure 2.4. Therefore, the peak stress transferred at this stage is approximately the same as the average plateau stress of the underlying cellular layer. As there is minimal change in stress within the plateau region, the peak stress transferred also does not change significantly for these cases.

Hence, these results show that the material stiffness ratio must be sufficiently high, i.e. the assembly of scales must be sufficiently stiff compared to the underlying cellular layer, for the composite system to be effective in minimizing the stress transferred to the protected surface. Figure 5.1 also shows that the impact performance of the specimen with curved scales becomes increasingly better than a sandwich specimen with the same volume of materials when the material stiffness ratio increases due to improvements in the bending resistance and energy dissipated by the scales.

5.2 Yield strength of scales

The effect of yield strength of the scales can be represented by the material strength ratio which is defined as the ratio of the yield strength of the scales to the strength of the underlying cellular layer. For a cellular material, this strength can be taken as the average plateau stress in its compressive stress-strain response. For the results presented in this section, the material strength ratio was varied by changing the yield strength of the scales while keeping the material properties of the underlying layer constant. For all cases the same assembly of scales was used: $L_s/t_s = 28.6$, $L_s/R = 1.5$, $L_h/D = 0.8$, and $L_h/S = 1.5$. Figure 5.4 shows the peak stress transferred by the specimens with different material strength ratios while the deformed shapes of these specimens are illustrated in Figure 5.5. Similar to the effect of material stiffness ratio, the peak stress transferred is high when the material strength ratio is very low (i.e. yield strength of the scales is relatively low compared to the average plateau stress of the underlying layer). Scales with low yield strength are too weak to resist the impact force, as shown in Figure 5.5(a), thus they are unable to dissipate much of the impact energy. Consequently, a high proportion of the impact energy is absorbed by the underlying cellular layer as shown in Figure 5.6. This causes densification of the underlying layer and results in significantly high stress on the underside of the composite system.

As the yield strength of the scales increases, the peak stress transferred reduces as shown in Figure 5.4. The scales are able to dissipate more impact energy (because plastic dissipation is proportional to yield strength), minimizing compression on the underlying cellular layer as shown in Figure 5.5(c). The impact energy taken by the underlying layer is correspondingly lower as shown in Figure 5.6. However, when the material strength increases beyond a certain value, the peak stress transferred increases again. This is because the scales become too strong such that they barely deform when subject

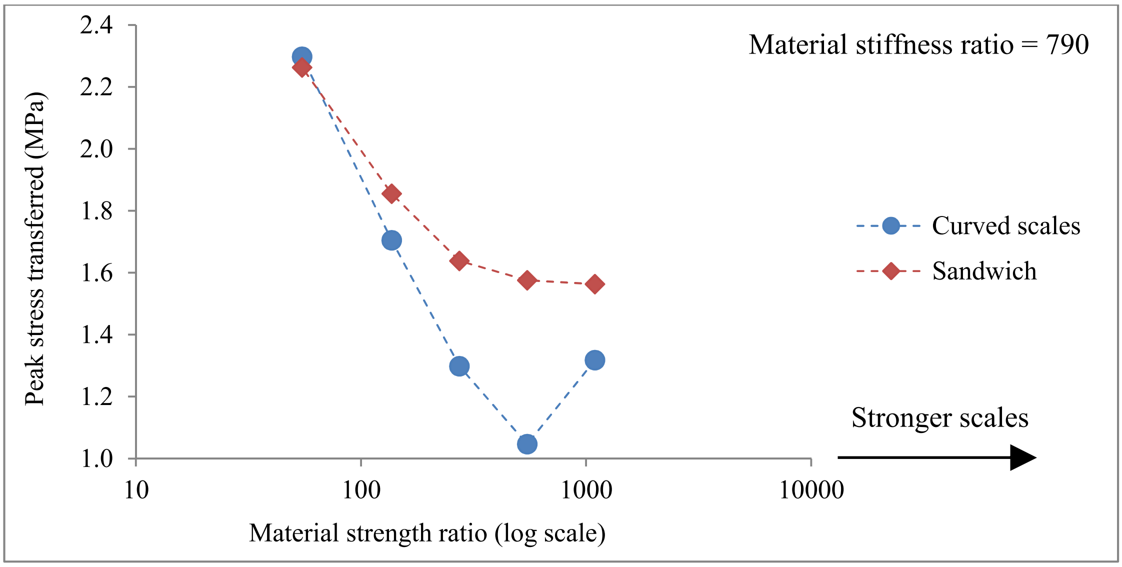

Figure 5.4: Peak stress transferred versus material strength ratio for curved scales and sandwich specimens.

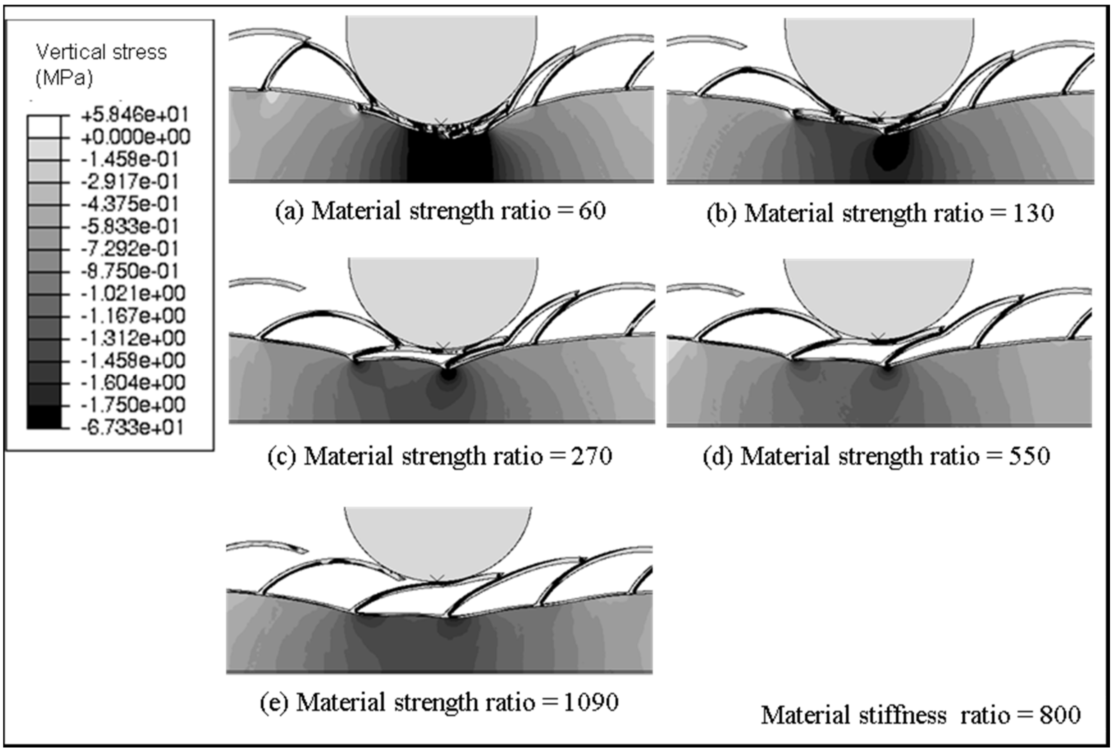

Figure 5.5: Deformation and vertical stress contour for composite specimens with various material strength ratios at maximum impactor penetration.

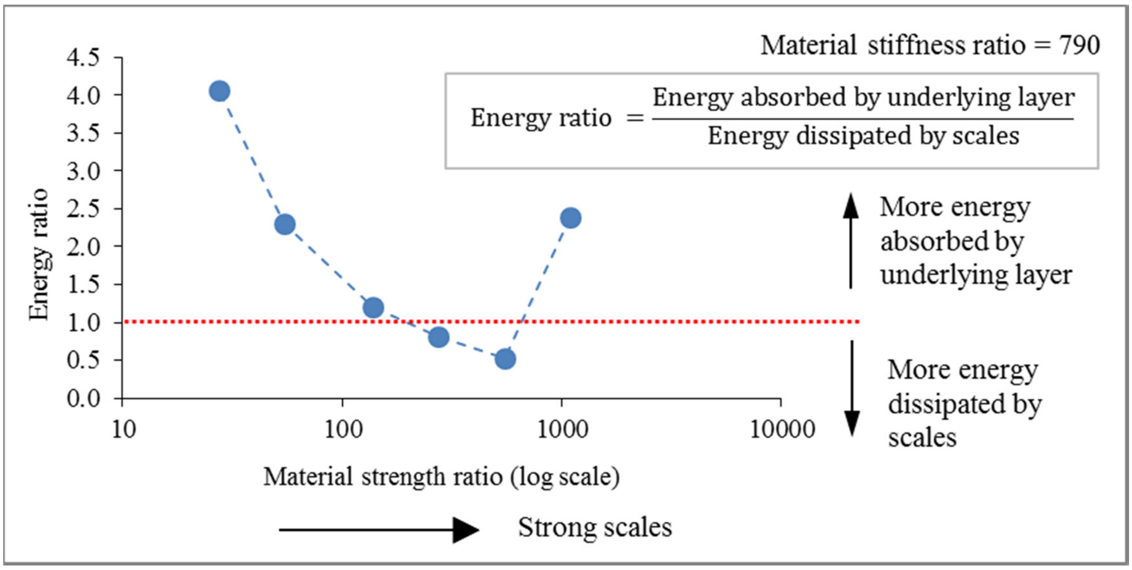

Figure 5.6: Ratio of energy absorbed by the underlying layer to energy dissipated by the scales for specimens with various material strength ratios.

to impact, causing stress concentration at their joints with the underlying layer as shown as Figure 5.5(e). Localized densification of the underlying layer occurs resulting in higher energy absorbed by the underlying layer as shown in Figure 5.6. Consequently, higher peak stress is transferred.

These results show that there is an optimum material strength ratio to effectively dissipate the impact energy and minimize compression on the underlying layer. Figure 5.4 also shows that the impact performance of the specimen with curved scales generally becomes increasingly better than a sandwich specimen with the same volume of materials when the material strength ratio increases because the scales are able to dissipate more impact energy, as long as they do not become too strong.

5.3 Combined effects of Young's modulus and yield strength of scales

The results shown in Sections 5.1 and 5.2 indicate that the Young's modulus and yield strength of the scales have a significant and similar influence on the deformation

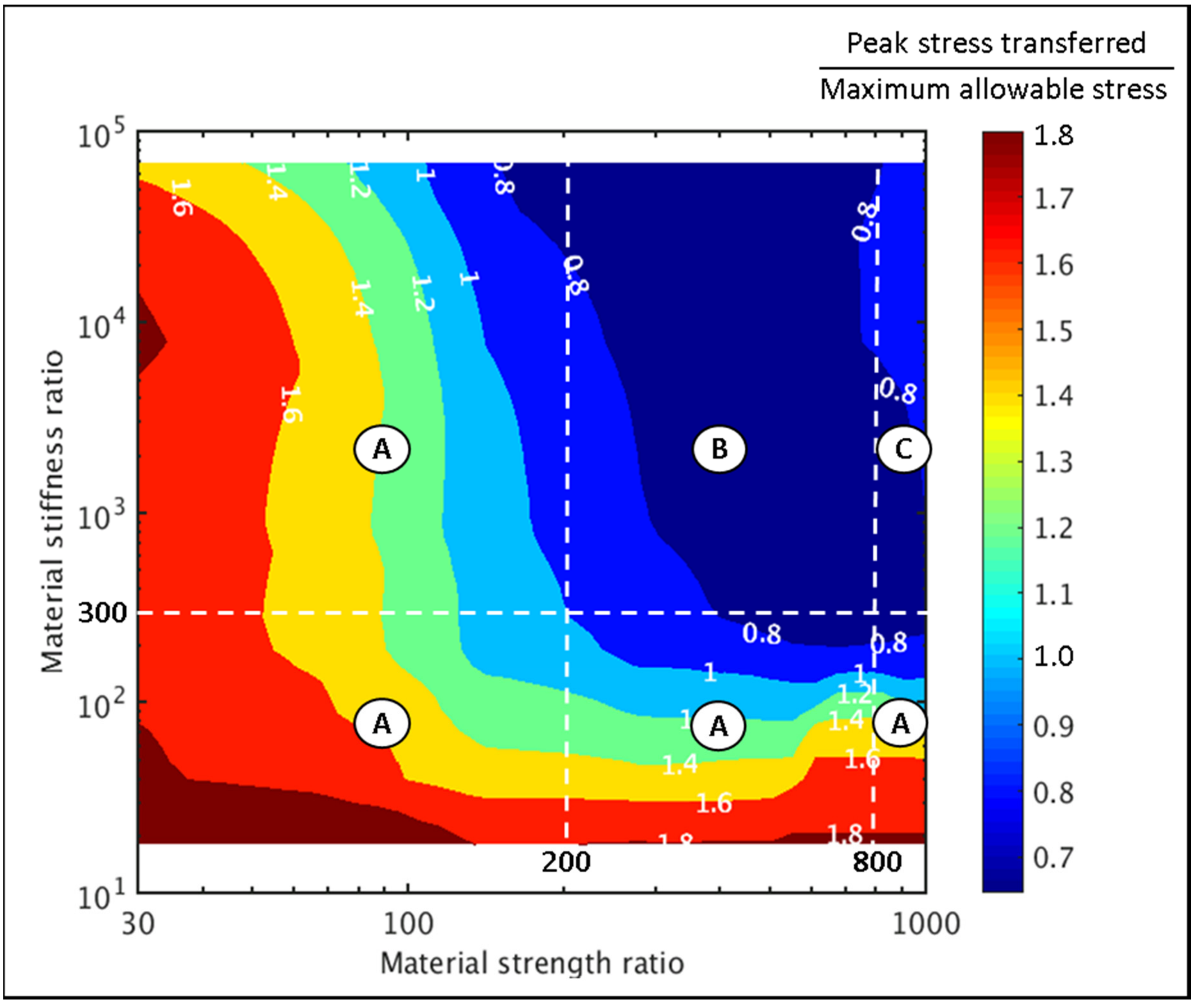

Figure 5.7: Peak stress transferred (normalized with maximum allowable stress of underlying layer) versus material stiffness and strength ratios for curved scales specimens.

behaviour and impact performance of the composite system. In this section, the combined effects of these parameters are examined.

Figure 5.7 shows the peak stress transferred (normalized with maximum allowable stress of underlying layer) for specimens with different combinations of material stiffness and strength ratios, while Figure 5.8 displays the ratio of impact energy absorbed by the underlying layer to that dissipated by the scales for these cases. It is apparent that there are a number of distinct outcomes based on the range of these ratios. Firstly, when the scales are too weak (i.e. low material strength), they collapse easily

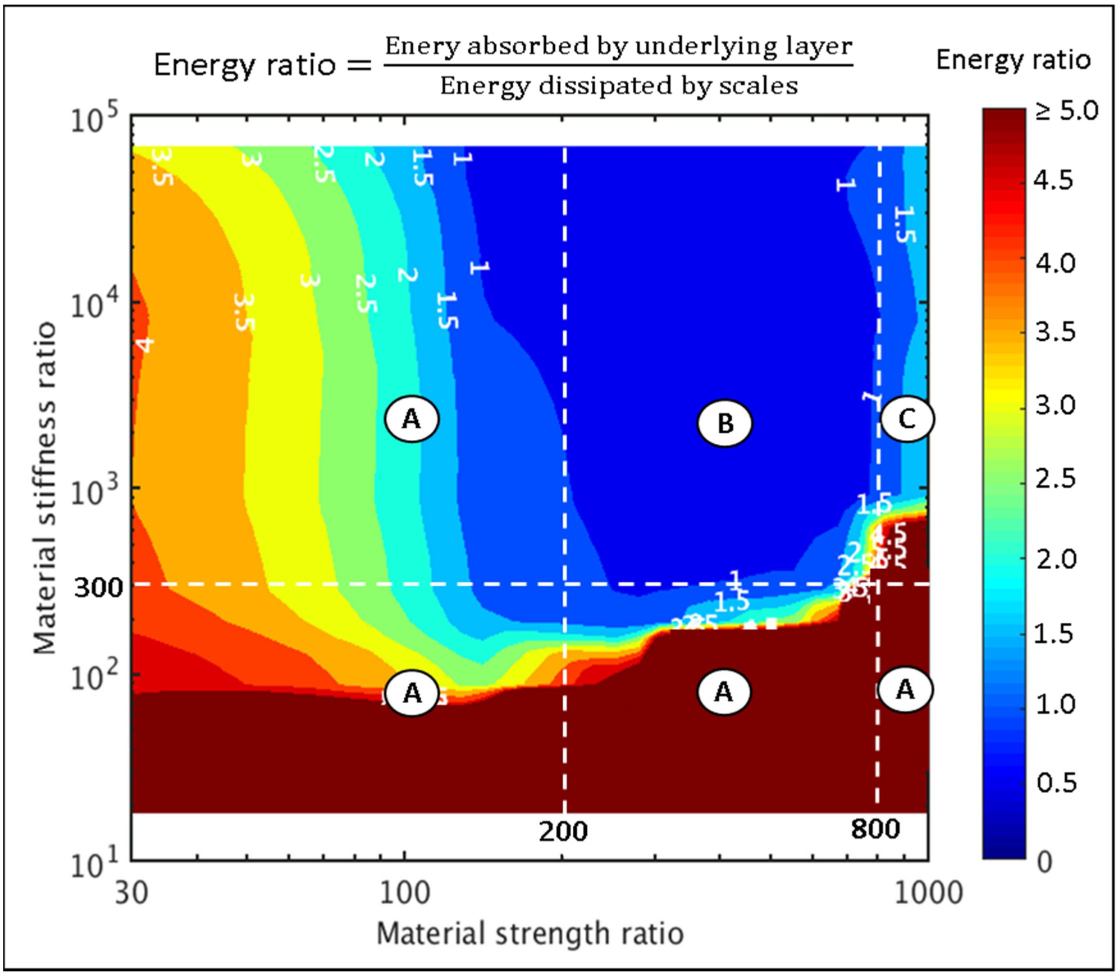

Figure 5.8: Ratio of energy absorbed by underlying layer to energy dissipated by scales versus material stiffness and strength ratios for curved scales specimens.

when subject to impact and are not able to dissipate much of the impact energy as shown in Figure 5.8. This causes most of the impact energy to be taken by the underlying layer which leads to high peak stress transferred. Such cases fall within the zones marked "*A*" in Figures 5.7 and 5.8. On the other hand, if the scales are too strong (i.e. high material strength ratio), they are not effective in dissipating the impact energy. This causes stress concentrations at the joints between the scales and the underlying layer, causing scales push into underlying layer as shown in Figure 5.9(d). Such cases belong to the zone marked "*C*" in Figures 5.7 and 5.8. Thirdly, at an intermediate strength ratio between the scales and the underlying layer, the peak stress transferred is low while the impact energy dissipated by the scales is high relative to that absorbed by the underlying layer.

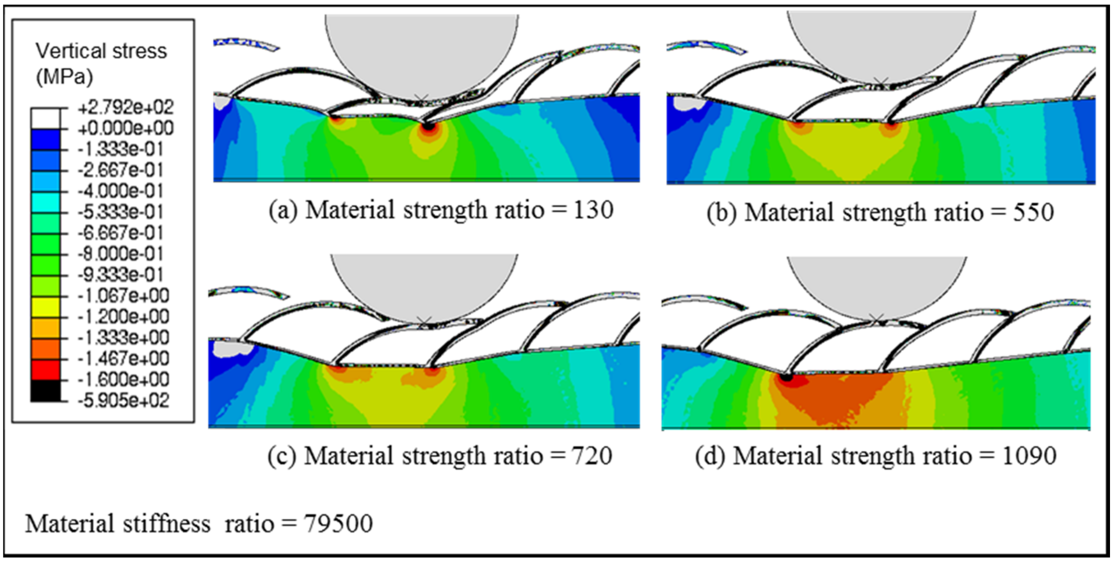

Figure 5.9: Deformation and vertical stress contour for composite specimens with various material strength ratios and material stiffness ratio of 79500 at maximum impactor penetration.

This desired impact performance occurs for cases in the zone marked "*B*" in Figures 5.7 and 5.8.

Figures 5.7 and 5.8 also show that there is a threshold value for the material stiffness ratio such that the peak stress transferred is minimized while the energy dissipated by the scales is maximized. Similar to the effect of yield strength, scales that have relatively low Young's modulus collapse easily when subject to impact and hence dissipates virtually no impact energy. These cases are in the zones marked "*A*" in Figures 5.7 and 5.8. It appears that the Young's modulus of scales needs to be large enough compared to that of the underlying cellular layer such that the scales can undergo significant plastic deformation and form plastic hinges as they deform. Such cases belong to the zone marked "*B*" in Figures 5.7 and 5.8.

Table 5.1 summarizes the effects of these material properties on the mechanical behaviour and impact performance of the fish scale-cellular composite system. From Figures 5.7 and 5.8, the material stiffness ratio should be more than 300 while the

Table 5.1: Summary of effects of material properties on mechanical behaviour and impact performance of fish scale-cellular composite system.

Material strength ratio Material stiffness ratio	< 200	200 to 800	> 800
< 300	☒ Scales collapse too easily. ☒ Low energy dissipated by scales. ☒ High stress transferred.	☒ Scales collapse too easily. ☒ Low energy dissipated by scales. ☒ High stress transferred.	☒ Scales collapse too easily. ☒ Low energy dissipated by scales. ☒ High stress transferred.
> 300	☒ Scales collapse too easily. ☒ Low energy dissipated by scales. ☒ High stress transferred.	☑ Scales are stiff yet deformable. ☑ High energy dissipated by scales. ☑ Low stress transferred.	☒ Scales are too strong and tend to puncture into underlying layer. ☒ Low energy dissipated by scales. ☒ High stress transferred.

optimum range for the material strength ratio falls between 200 and 800. Within these optimum bounds, the scales of the composite system are able deform yet dissipate a significant proportion of impact energy while minimizing compression on the underlying cellular layer. This would ensure that the peak stress transferred to the protected structure does not exceed the maximum allowable stress of the underlying cellular layer.

5.4 Combined effects of geometrical and material properties

As discussed in Section 4.5, the impact performance of the composite system is governed by the overall geometric stiffness factor $K_{geometry}$ which is a function of aspect ratio, curvature, degree of overlapping, and relative size of the scales. It was proposed in that section that there is an optimal range for $K_{geometry}$ such that the peak stress transferred and the amount of materials used are minimized. However, the optimal range for $K_{geometry}$ is also a function of the material properties of the scales and underlying cellular layer. Therefore, the combined effects of the geometrical and material properties of the scales and underlying layer shall be discussed in this section.

To examine the effect of material stiffness ratio on the optimum range for $K_{geometry}$, the Young's modulus of the scales was varied for cases with different $K_{geometry}$ values while keeping the material properties of underlying cellular layer fixed. Figure 5.10 displays the peak stress transferred (normalized with maximum allowable stress of underlying layer) as a function of $K_{geometry}$ with various material stiffness ratios. The optimum range of $K_{geometry}$ in each plot is shown by the shaded region between the two dashed lines (i.e. K_{max} and K_{min}) which mark the transition between Groups "*A*", "*B*", and "*C*" discussed earlier in Section 4.5. It seems that the optimum range for $K_{geometry}$ remains relatively constant as long as the material stiffness ratio exceeds the recommended threshold in Table 5.1. This is because the deformation mode and impact resistance of the composite system are governed by the yield strength rather than Young's modulus of the scales when the latter is high enough.

On the other hand, the optimum range for $K_{geometry}$ is a function of the material strength ratio as shown in Figure 5.11 which displays the peak stress transferred (normalized with maximum allowable stress of underlying layer) as a function of $K_{geometry}$ for cases

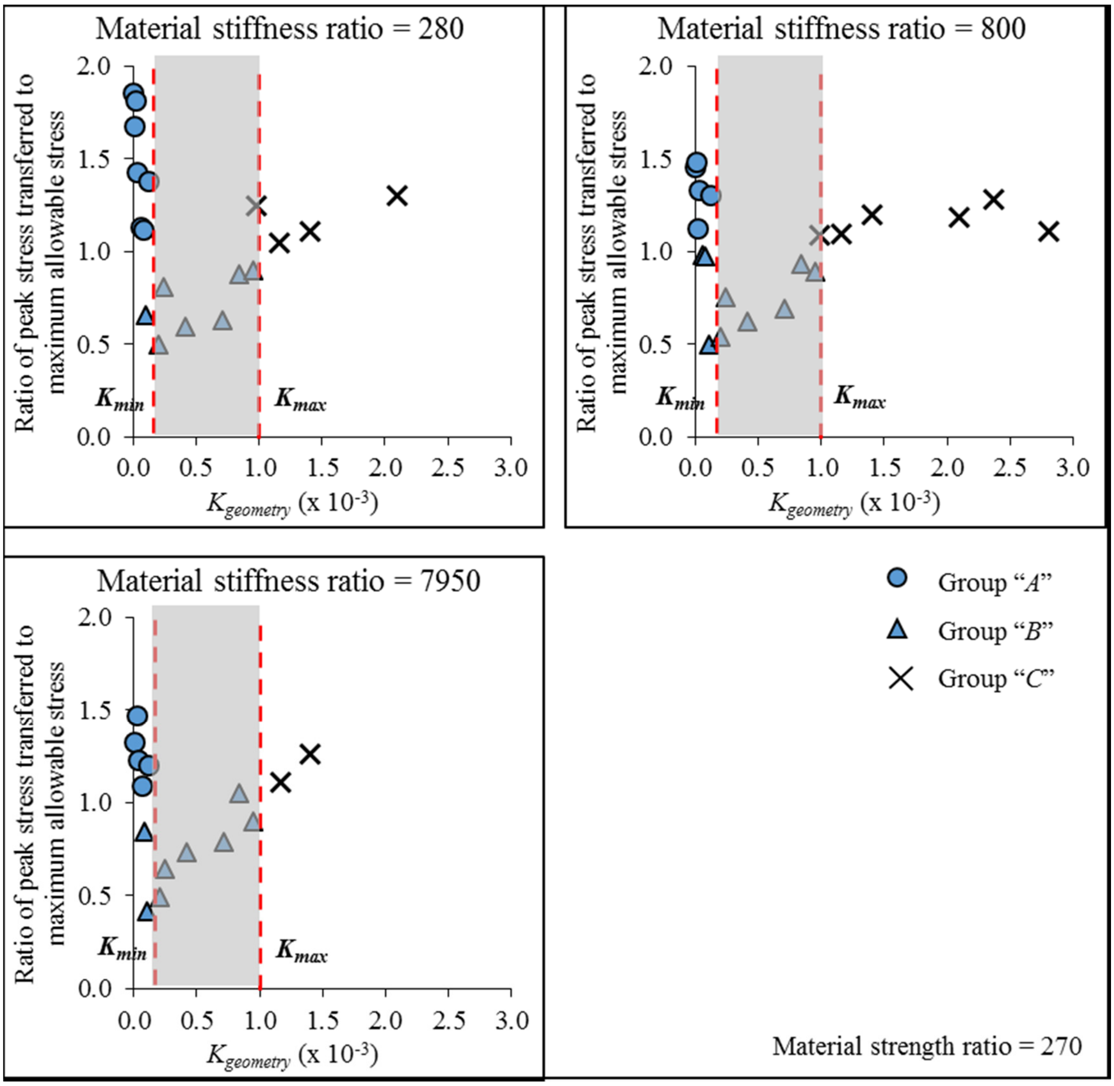

Figure 5.10: Peak stress transferred (normalized with maximum allowable stress of underlying layer) as a function of geometric stiffness factor $K_{geometry}$ of scales with various material stiffness ratios.

with different material strength ratios (where the yield strength of scales is varied). Figure 5.11 indicates that the optimum range for $K_{geometry}$ reduces with increasing material strength ratio. When the specimens have relatively low material strength ratio (i.e. yield strength of scales is relatively low compared to the strength of the underlying layer), the optimum range for $K_{geometry}$ is higher because the scales can yield more easily, hence they need to be geometrically stiffer in order to ensure that they do not collapse too quickly. On the other hand, when the material strength ratio is high (i.e. yield strength of the scales is relatively high compared to the strength of the underlying layer), the optimum range for $K_{geometry}$ is lower. This is because when a stronger material is used for the scales, the geometric stiffness of the scales must be reduced (e.g. the scales need to be more slender, less curved or spaced further apart) to prevent them from becoming over-stiff.

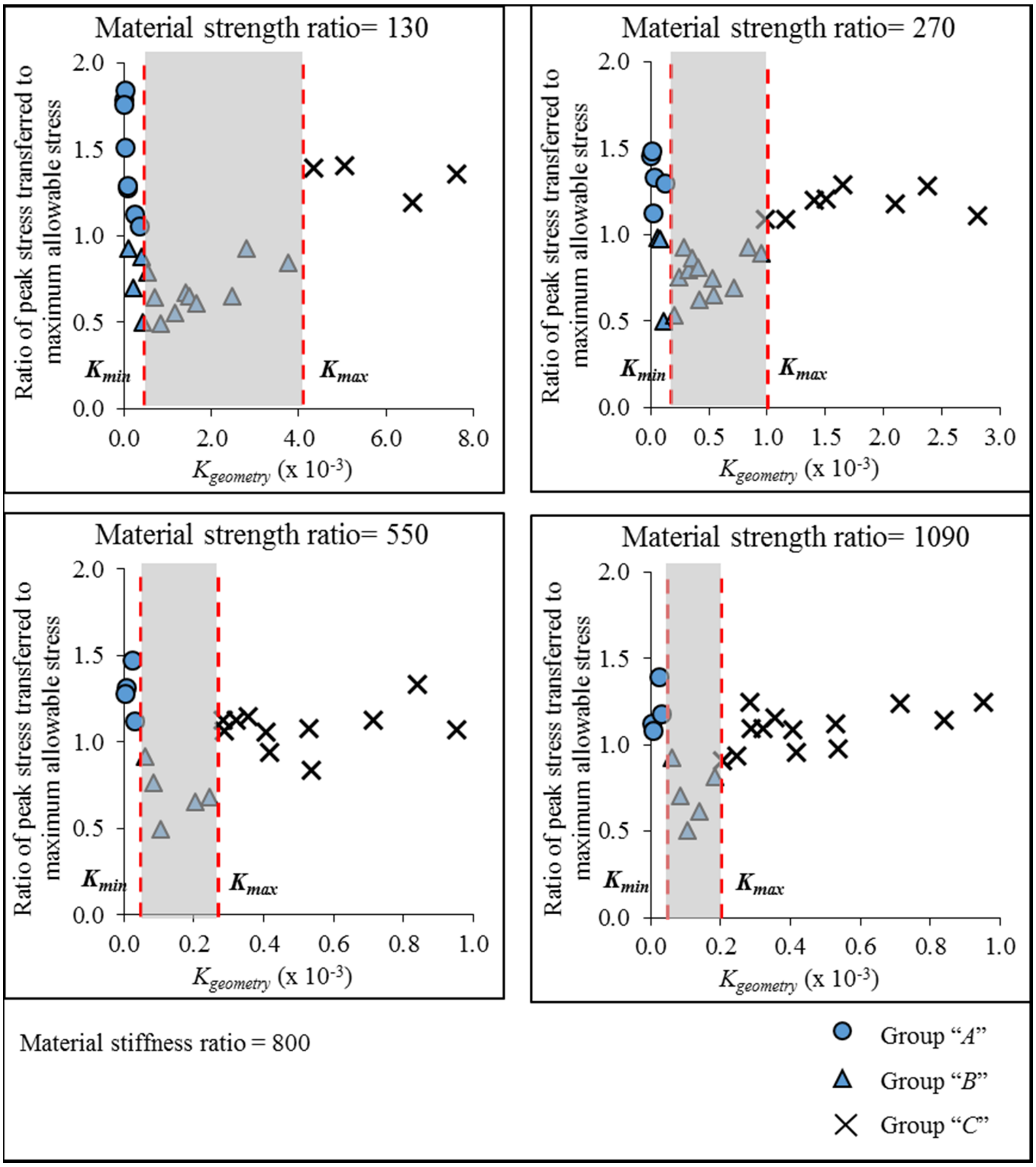

Figure 5.11: Peak stress transferred (normalized with maximum allowable stress of underlying layer) as a function of geometric stiffness factor $K_{geometry}$ of the scales with various material strength ratios.

Figure 5.12 summarizes the relationship between the optimum range for $K_{geometry}$ and material strength ratio. It is observed that the optimum range for $K_{geometry}$ also becomes narrower with the increasing material strength ratio. When the yield strength of the scales is relatively low compared to the strength of the underlying cellular layer, it is easier for the scales to deform rather than compressing on the underlying layer.

As a result, a wider variation of geometrical designs for the assembly of scales can be adopted while ensuring that it is able to dissipate a significant proportion of the impact energy as the scales deform. Conversely, when the yield strength of the scales is relatively high compared to the strength of the underlying cellular layer, it is harder to deform the scales. Thus regardless of the geometrical design of the assembly of scales, there is a significantly higher tendency for the scales to puncture into the underlying cellular layer.

Therefore, the results presented in Chapter 4 and in this section show that the combined effects of the geometrical and material properties of the scales and underlying layer on the deformation behaviour of the composite system can be captured by the composite

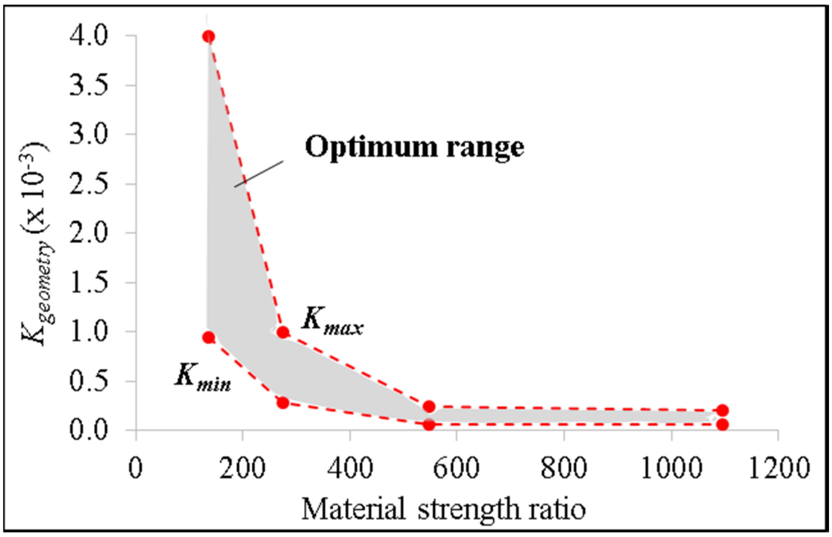

Figure 5.12: Optimum range for geometric stiffness factor $K_{geometry}$ as a function of material strength ratio.

parameter $K_{geometry}$ which describes the stiffness of scale assembly as a function of their geometrical properties, and the optimum range for $K_{geometry}$ which is a function of the yield strength of the scales and strength of the underlying cellular layer. This finding may be used to facilitate the development of a design approach to determine the optimum combinations for the geometrical and material properties of the scales to achieve a desired impact performance.

5.5 Compressive stress-strain behaviour of cellular layer

It is obvious that the material properties of the underlying cellular layer govern the mechanical behaviour and impact performance of the composite system. Firstly, as shown in the preceding sections, the underlying layer of the composite system controls the range of stress transferred during impact – the underlying layer acts as a cushion to absorb the impact energy because it can undergo large deformation while maintaining low stress value when it is within its plateau region as shown in Figure 2.4. As long as the underlying layer is not densified, the peak stress transferred would not exceed the stress at its densification limit which corresponds to the point when there is a sharp increase in stress (i.e. sudden increase in slope of the compressive stress-strain curve). As discussed in Section 3.2.2, this densification limit may occur at engineering strain of up to 50 percent (Pereira, 2007). The stress value at this limit is henceforth denoted as the maximum allowable stress of the underlying layer assuming that it is designed such that densification does not occur.

Secondly, based on the results presented in Sections 5.1 and 5.2, the material properties of the underlying cellular layer may affect the deformation mode of the composite system which is governed by the stiffness and strength of the assembly of scales relative to those of the underlying cellular layer. However, the effects of these stiffness and strength parameters were examined in Section 5.3 by varying the Young's modulus and yield strength of the scales while keeping the material properties of the underlying layer constant. Therefore, for the cases presented in this section, the effects of these parameters shall be investigated by varying the material properties of the cellular layer while keeping those of the scales constant. For this purpose, the properties of the cellular layer were adjusted by multiplying the stress values of its compressive stress-strain curve shown in Figure 2.4 with a factor Q while keeping the strain values fixed. Hence, as can be seen in Figure 5.13, $Q = 1.0$ is the original compressive stress-strain curve, while $Q = 2.0$, $Q = 0.50$ and $Q = 0.25$ are cases where the compressive resistance is higher and lower, respectively, than the original one.

As mentioned earlier the range of stress transferred is controlled by the compressive stress-strain behaviour of the underlying cellular layer. By varying the latter, the peak stress transferred for cases with different stress-strain curves of the underlying layer cannot be compared directly. Instead, the impact performance of each case is assessed by comparing the peak stress transferred with the maximum allowable stress (i.e. stress at densification limit) of its underlying layer.

Figures 5.14 and 5.15 show the ratio of peak stress transferred to the maximum allowable stress of the underlying cellular layer, as well as the impact energy absorbed by the scales and underlying layer for cases with relatively low $K_{geometry}$ of 0.205 x 10^{-3}. Here, the varying compressive stress-strain behaviour of the underlying layer is represented as a function of the material strength ratio (i.e. ratio of yield strength of the scales to average plateau stress of the underlying cellular layer), since the elastic region (which defined as engineering strain of between 5 percent and 7 percent) is negligible. The assembly of scales is expected to be able to deform and dissipate a significant amount of the impact energy, minimizing the compression on the underlying cellular layer if the material stiffness and strength ratios fall within the recommended ranges proposed in Section 5.3.

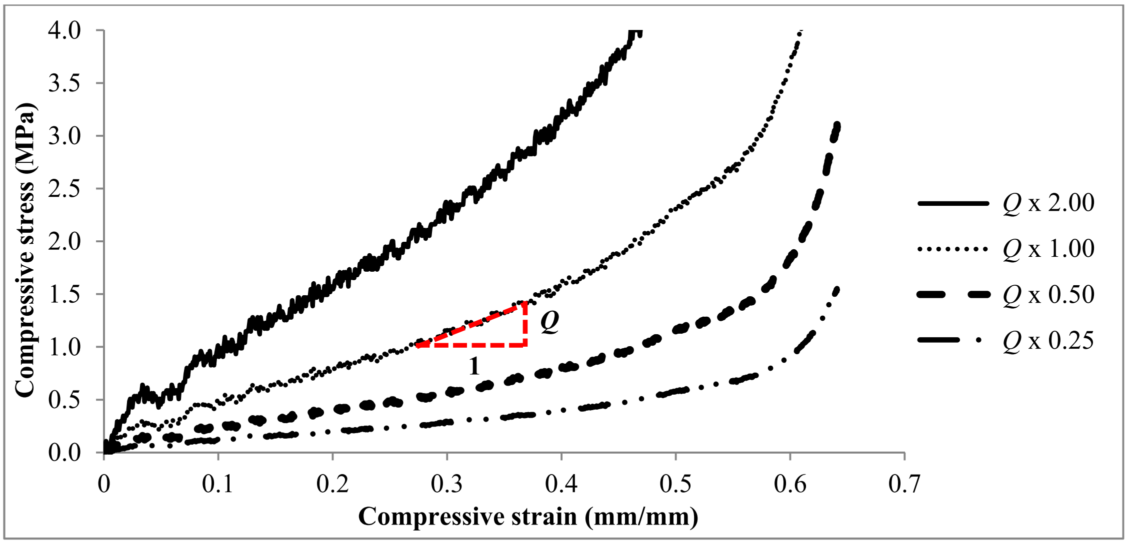

Figure 5.13: Uniaxial compressive stress-strain curves of underlying cellular layer with varying *Q* values.

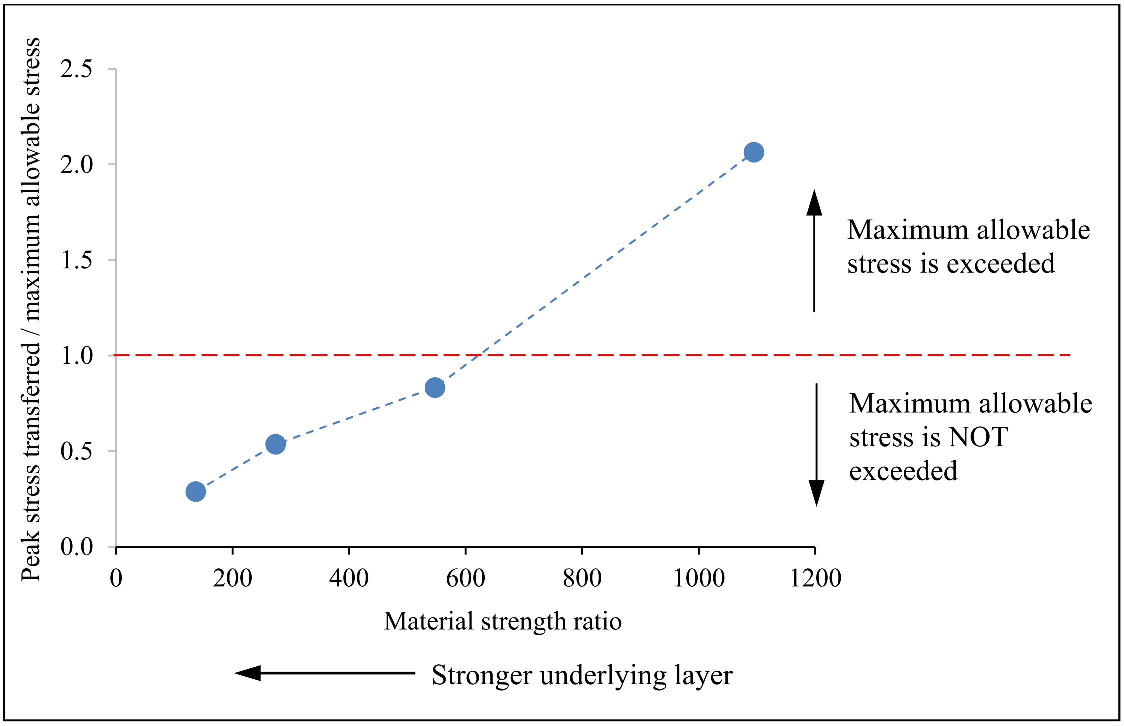

Figure 5.14: Peak stress transferred as function of material properties of underlying layer (represented by material strength ratio) for specimens with $K_{geometry}$ = 0.205 x 10^{-3}.

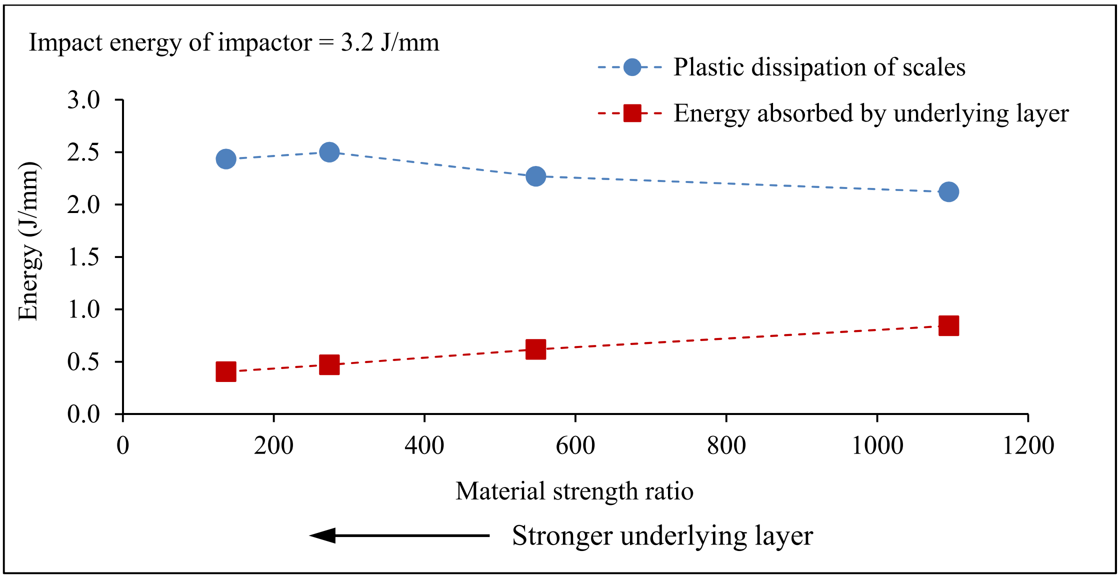

Figure 5.15: Impact energy dissipated by scales and absorbed by underlying layer as function of material properties of underlying layer (represented by material strength ratio) for specimens with $K_{geometry} = 0.205 \times 10^{-3}$.

It is apparent that the peak stress transferred (relative to the maximum allowable stress of the underlying layer) increases as the underlying layer becomes weaker relative to the scales (i.e. higher material strength ratio). When the underlying layer is stronger compared to the assembly of scales (i.e. material strength ratio is low), the peak stress transferred is low and less than the maximum allowable stress of the underlying layer because it is able to absorb more energy before it densifies. On the other hand, the peak stress transferred exceeds the maximum allowable stress of the underlying layer when it becomes weaker relative to the scales (i.e. material strength ratio is high). This is because less energy is required to cause densification of the underlying layer and the scales have a tendency to puncture into the underlying layer, leading to stress concentrations at the underlying layer underneath the point of impact as shown in Figure 5.16(d).

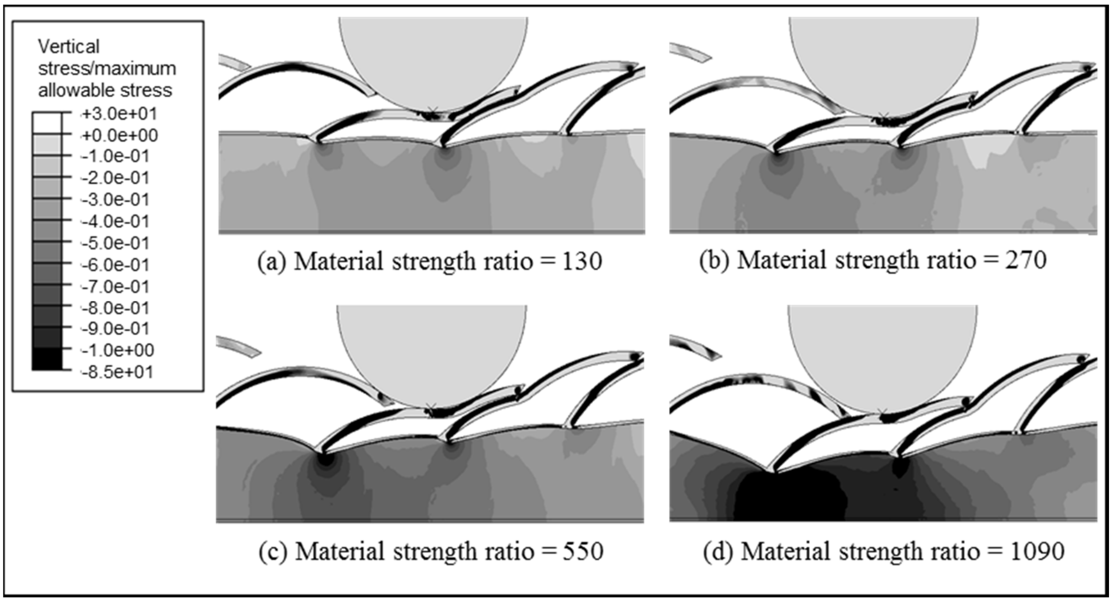

(a) Material strength ratio = 130 (b) Material strength ratio = 270

(c) Material strength ratio = 550 (d) Material strength ratio = 1090

Figure 5.16: Deformation and vertical stress contour for composite specimens with various material properties of underlying layer (represented by material strength ratio) and $K_{geometry}$ = 0.205 x 10^{-3} at maximum impactor penetration.

Nonetheless, since the scales are relatively deformable due to its low $K_{geometry}$, increasing the strength of the underlying cellular layer within the optimal range of the material strength ratio (200 to 800 as proposed in Section 5.3) does not negatively affect the deformation mode and impact performance of the composite system. This agrees well with the conclusion in Section 5.3 as well as the results from Figure 5.12 whereby $K_{geometry}$ = 0.205 x 10^{-3} falls within the optimum bounds for this range of material strength ratios. On the other hand, when the material strength ratio exceeds 600, this $K_{geometry}$ value exceeds the optimum bounds hence the scales become over-stiff and tend to puncture into the underlying layer.

The same trend of decreasing stress transferred with increased strength of the underlying layer (i.e. reduced material strength ratio) is also observed for specimens with stiffer assembly of scales. Figures 5.17 and 5.18 show the ratio of peak stress transferred to the maximum allowable stress of the underlying cellular layer, as well as the energy absorbed by the scales and underlying layer for cases with relatively high $K_{geometry}$ of

2.480 x 10^{-3}. It appears that only the scales in the specimen with low material strength ratio of 130 (i.e. as the underlying layer becomes stronger relative to the scales) has peak stress transferred that is lower than the maximum allowable stress of the underlying layer. For this case, the scales appear to be deformable as shown in Figure 5.19(a) and can dissipate a larger proportion of the impact energy than that absorbed by the underlying layer as shown in Figure 5.18. Conversely, the peak stress transferred is higher than the maximum allowable stress when the material strength ratio exceeds 270 (i.e. as the underlying layer becomes weaker relative to the scales). For these cases, the scales are relatively stiffer than the underlying layer. The impact energy that can be absorbed by the underlying layer before its densification is lower when its strength is reduced, hence it is compressed more significantly when subject to impact. This agrees well with the results from Figure 5.12 whereby $K_{geometry}$ of 2.480 x 10^{-3} exceeds the optimum bounds when the material strength ratio is above 200, hence the scales tend to puncture into the underlying layer as shown in Figures 5.19(b) to 5.19(d).

In conclusion, the material properties of underlying layer, specifically its compressive stress-strain behaviour, affect the deformation mode of the composite system and the magnitude of stress transferred during impact. The influence of the material properties of the underlying layer on the deformation mode can be captured by the material stiffness and strength ratios between the scales and underlying layer, and it agrees well with the observations in Section 5.3 and Figure 5.12. On the other hand, the range of stress transferred is controlled by the plateau region of the compressive stress-strain response. If the composite system performs optimally, i.e. the underlying layer is compressed minimally and does not densify, the stress transferred will not exceed the stress at the densification limit of the underlying layer.

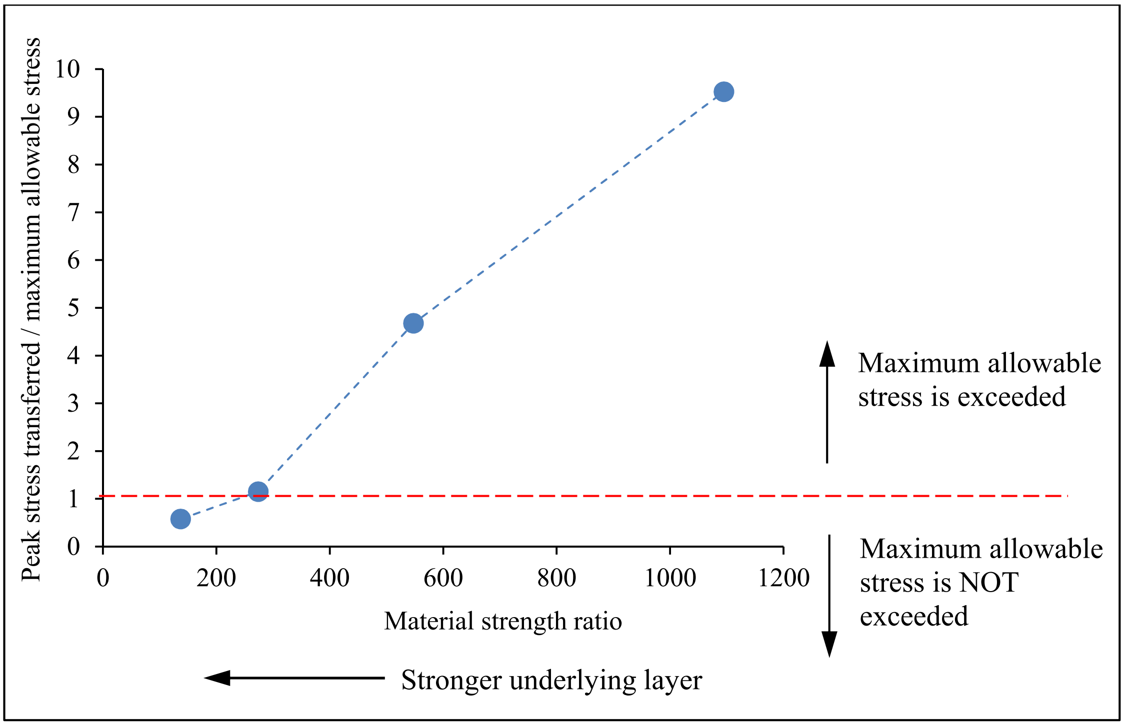

Figure 5.17: Peak stress transferred as function of material properties of underlying layer (represented by material strength ratio) for specimens with $K_{geometry} = 2.480 \times 10^{-3}$.

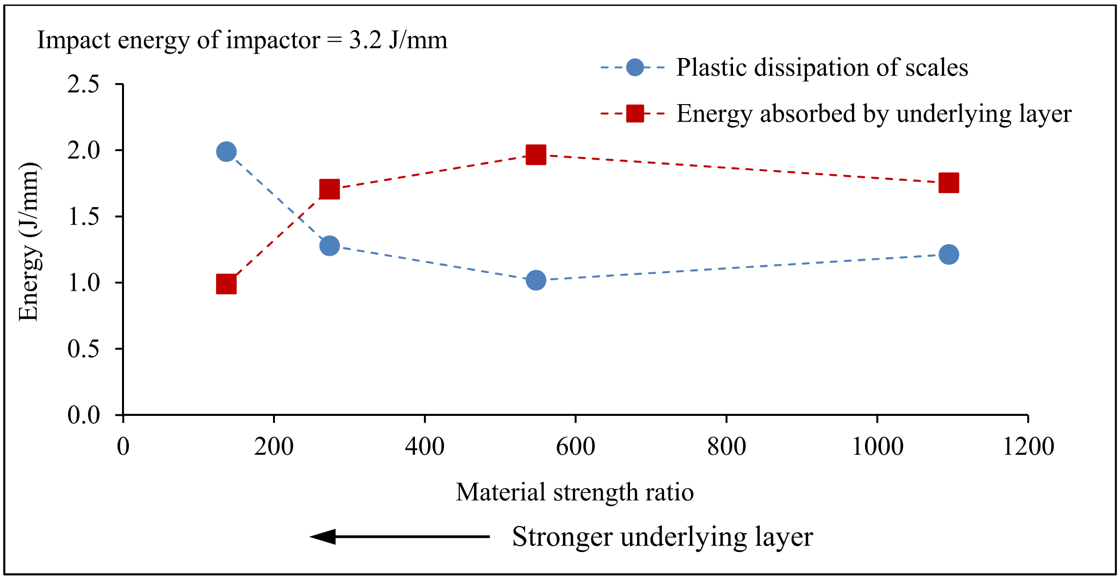

Figure 5.18: Impact energy dissipated by scales and absorbed by underlying layer as function of material properties of underlying layer (represented by material strength ratio) for specimens with $K_{geometry} = 2.480 \times 10^{-3}$.

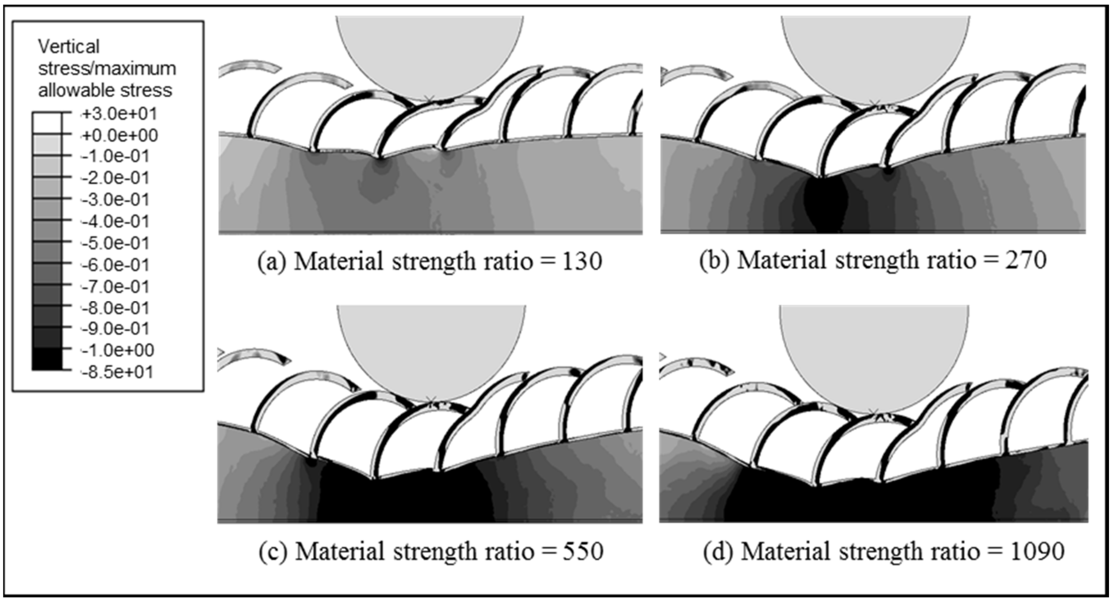

Figure 5.19: Deformation and vertical stress contour for composite specimens with various material properties of underlying layer (represented by material strength ratio) and $K_{geometry}$ = 2.480 x 10^{-3} at maximum impactor penetration.

5.6 Thickness of cellular layer

Besides material properties, the thickness of the underlying cellular layer also affects the impact performance of the composite system. Specifically, it is expected to influence the peak stress transferred as well as the amount of impact energy that can be absorbed before densification. For the cases presented in this section, the underlying cellular layer thickness T was varied (span L of the specimen and volume V_s of scales for all cases were kept constant) to examine its effect on the impact performance of the composite system. Unless otherwise stated, the material properties of the scales and underlying layer were unchanged; the material stiffness and strength ratios for all cases are 790 and 270 respectively.

Figure 5.20 shows the peak stress transferred while Figure 5.21 displays the deformation of specimens with varying thickness T of the underlying layer, with a scale assembly that has $K_{geometry}$ of 0.184 x 10^{-3}. Since this $K_{geometry}$ is within the optimum range for the material strength ratio used here, the scales can deform readily when subject to impact

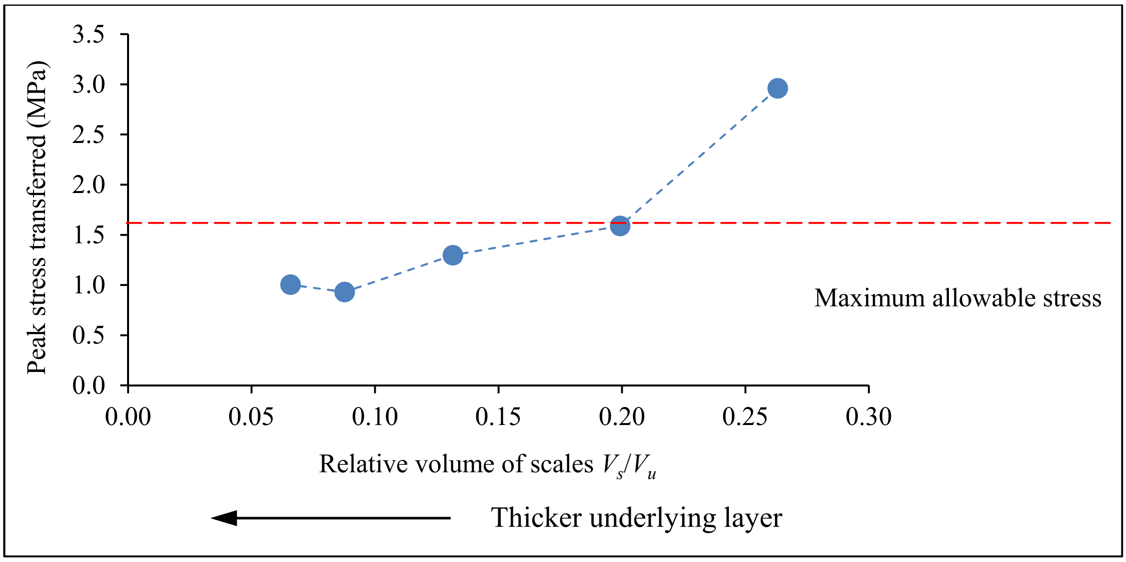

Figure 5.20: Peak stress transferred as function of thickness of underlying layer (represented by relative volume V_s/V_u of scales) for specimens with $K_{geometry} = 0.184 \times 10^{-3}$.

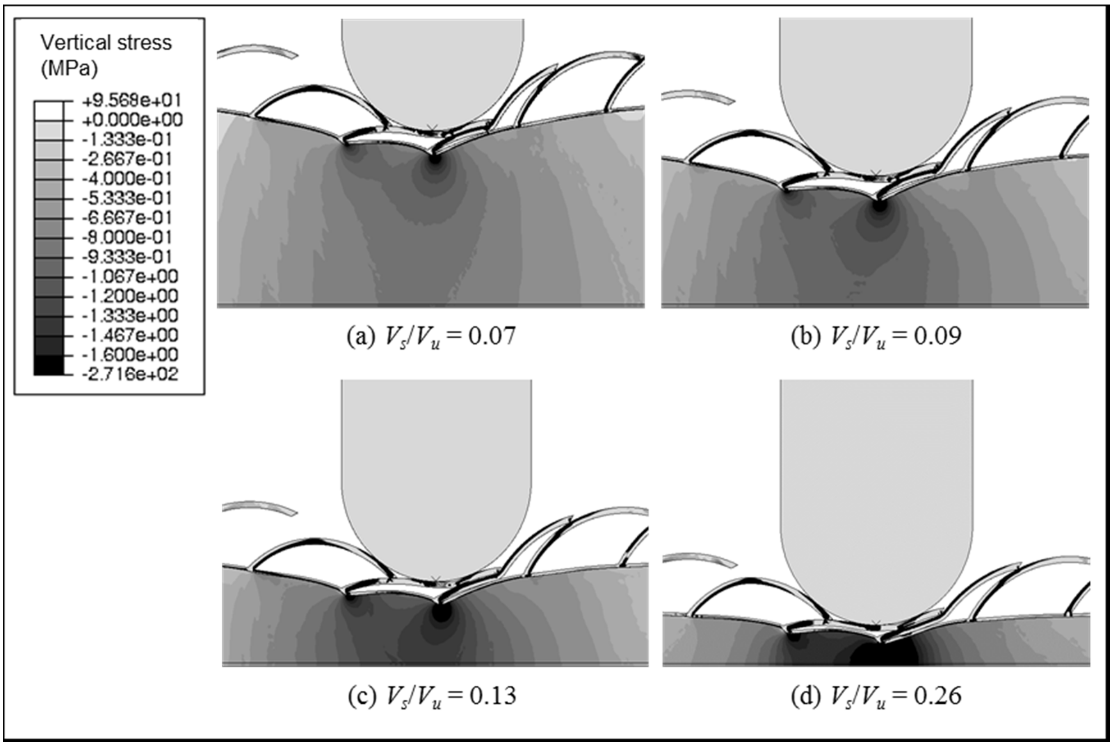

(a) $V_s/V_u = 0.07$

(b) $V_s/V_u = 0.09$

(c) $V_s/V_u = 0.13$

(d) $V_s/V_u = 0.26$

Figure 5.21: Deformation and vertical stress contour for composite specimens with various thicknesses of underlying layer (represented by relative volume V_s/V_u of scales) and $K_{geometry} = 0.184 \times 10^{-3}$ at maximum impactor penetration.

as shown in Figure 5.21. The thickness of underlying layer does not seem to affect the deformation of the scale assembly. However, it is apparent that the peak stress transferred reduces with increasing thickness of the underlying layer, which is represented in Figure 5.20 by the decreasing volume V_s of the scales relative to the volume V_u of the underlying layer. This is expected as a specimen with thicker underlying layer is able to absorb more impact energy before densification is reached and can spread the impact force over a wider region. On the other hand, specimens with thinner underlying layer (i.e. relatively high V_s/V_u) has lower energy absorption capacity (i.e. the maximum energy that can be absorbed before densification occurs) and less room for the impact force to spread out. Consequently, the underlying layer is more easily densified which results in higher peak stress transferred as shown in Figure 5.21(d). Therefore, it is apparent that the value of V_s/V_u should not exceed 0.2 for cases where the $K_{geometry}$ value of the scales falls within the optimal range. This agrees well with the recommended bounds for V_s/V_u presented earlier in Table 4.1.

The same trend of decreasing stress transferred with increasing thickness of underlying layer is also observed for specimens with a stiffer assembly of scales. Figure 5.22 shows the peak stress transferred while Figure 5.23 displays the deformation of specimens with varying thickness T of the underlying layer, with a scale assembly that has a relatively high $K_{geometry}$ of 1.403 x 10^{-3}. Since this $K_{geometry}$ is above the optimum range for the material strength ratio used here, the scales are over-stiff and tend to puncture into the underlying layer, causing stress concentrations at the joints. Hence, higher peak stress is transferred as shown in Figure 5.23. Changing the thickness of the underlying layer does not seem to change the deformation behaviour of the composite system. The improved impact performance with increasing thickness of the underlying layer may be attributed solely to the larger region over which the impact force can be distributed instead of the ability of the scales to dissipate the impact energy or spread the impact force.

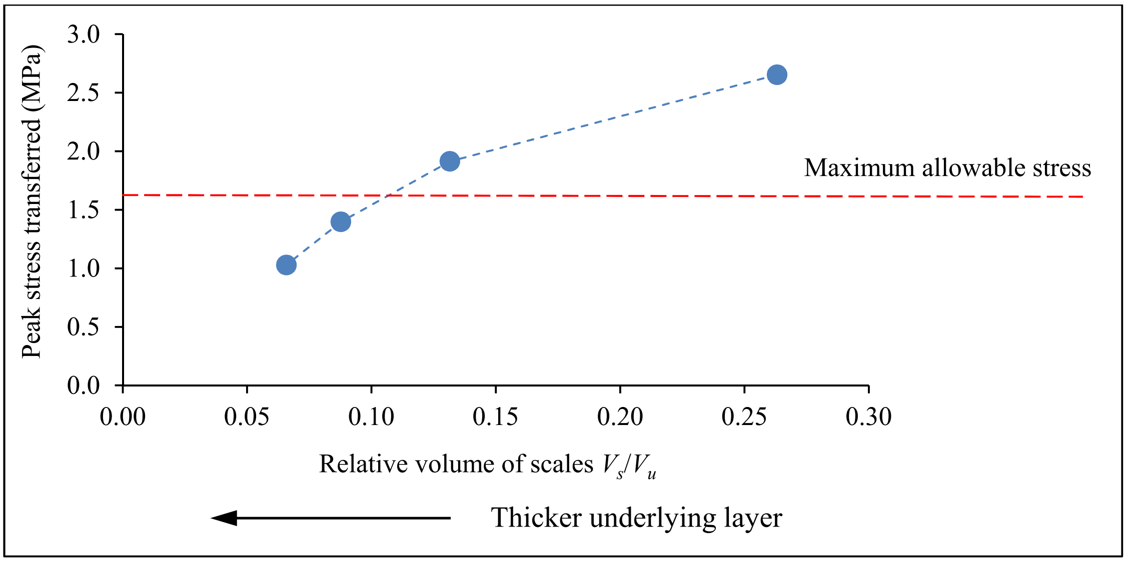

Figure 5.22: Peak stress transferred as function of thickness of underlying layer (represented by relative volume V_s/V_u of scales) for specimens with $K_{geometry} = 1.403 \times 10^{-3}$.

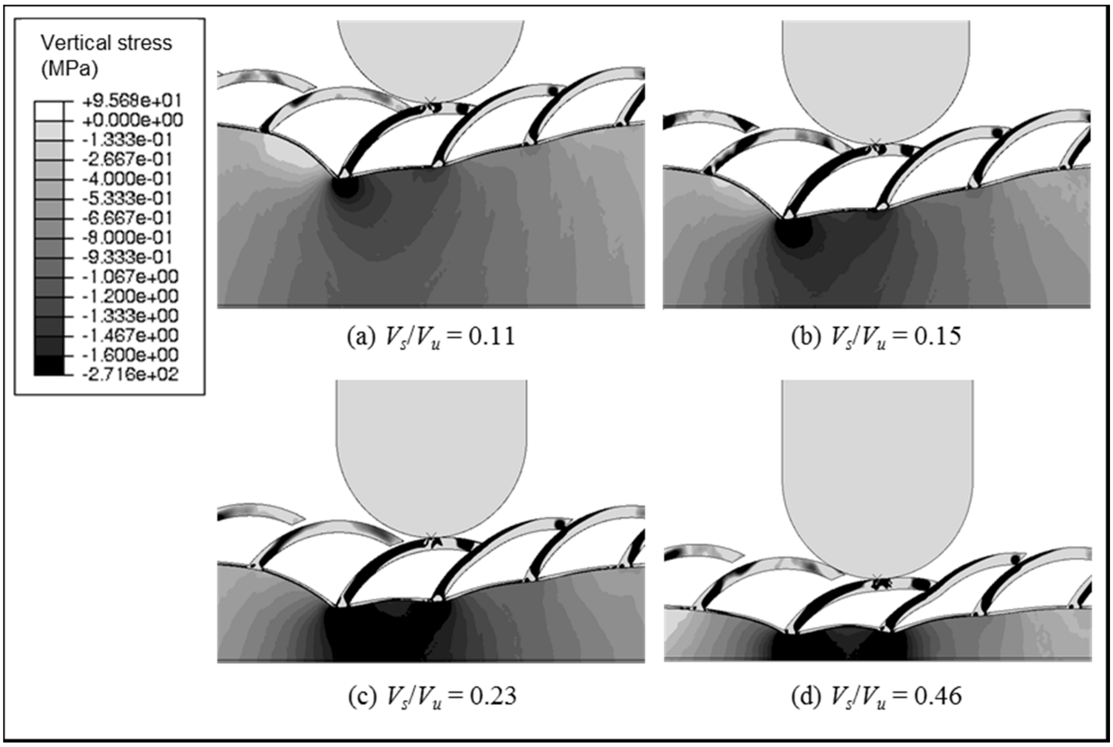

(a) $V_s/V_u = 0.11$ (b) $V_s/V_u = 0.15$

(c) $V_s/V_u = 0.23$ (d) $V_s/V_u = 0.46$

Figure 5.23: Deformation and vertical stress contour for composite specimens with various thicknesses of underlying layer (represented by relative volume V_s/V_u of scales) and $K_{geometry} = 1.403 \times 10^{-3}$ at maximum impactor penetration.

Therefore, the thickness of the underlying layer does not affect the deformation mode of the composite system. However, assuming the scales are designed such that they can deform readily and dissipate a significant proportion of the impact energy, there appears to be an optimum range for the thickness of underlying cellular layer. An underlying layer that is too thin may densify easily which causes high peak stress transferred, while one that is too thick is inefficient. This optimum range may be captured by the recommended bounds for the volume V_s of the scales relative to volume V_u of the underlying layer that have been given in Section 4.7.

5.7 Concluding remarks

The deformation behaviour and impact performance of the fish scale-cellular composite system are governed by the geometrical and material properties of the scales and underlying cellular layer. The results presented in this chapter showed that there are optimum ranges for stiffness and strength of the scales relative to those of the underlying layer so that the scales can deform readily yet dissipate a significant amount of impact energy while causing minimal compression on the underlying layer. It was proposed that the material stiffness ratio should be greater than 300 while the optimum range of the material strength ratio falls within 200 to 800.

Furthermore, the combined effects of the geometrical and material properties on the deformation behaviour of the composite system can be captured by the geometric stiffness factor $K_{geometry}$ that was introduced in Chapter 4 and its optimum range. It has been shown in the current chapter that the optimum range for $K_{geometry}$ reduces with increasing material strength ratio.

Lastly, the compressive stress-strain behaviour and thickness of the underlying layer control the range of stress transferred by the composite system, even though the thickness of the underlying layer does not affect the deformation mode. Their effects may be represented by the material stiffness and strength ratios as well as the volume of scales relative to that of the underlying layer. As long as the values for these parameters fall within their recommended bounds, the stress transferred would not exceed the stress at the densification limit of the underlying layer while minimizing the amount of materials used.

6.0 Design procedure for the fish scale-cellular composite system

As discussed in the preceding chapters, the assembly of scales should be able to deform and dissipate a significant amount of energy from the impactor such that the remaining energy absorbed by the underlying cellular layer is not excessive and does not cause it to densify. As shown in Figure 4.17, the amount of energy dissipated through plastic deformation of the scales should be more than the energy absorbed by the underlying layer if the composite system is to perform well under impact. When this occurs, compression of the underlying cellular layer is minimized and the stress transferred to the protected surface does not exceed the stress within the plateau region of the cellular material's compressive stress-strain response.

Therefore, besides determining the optimum geometrical configuration of the scales and combination of materials for the scales and underlying layer, which have been discussed in Chapters 4 and 5 respectively, methods to estimate the energy that can be dissipated by the scales and absorbed by the underlying cellular layer need to be established to facilitate the design of the composite system for any given application. Preferably, these methods should be reasonably simple yet accurate enough for the purpose of design. These methods are discussed in this chapter. Subsequently, a design procedure for the composite system is proposed and its numerical validation is presented.

6.1 Energy dissipated by scales

As mentioned in Section 4.5, the scales can deform plastically if the overall stiffness factor $K_{geometry}$ of the assembly of scales is within certain bounds that are governed by the material properties of the scales and underlying layer. Additionally, when $K_{geometry}$ is within the optimum bounds, most of the impact energy transferred to the scales is dissipated through plastic deformation while the strain energy in the scales is relatively negligible. Hence, plastic analysis can be adopted to estimate the amount of energy that can be dissipated by the assembly of scales. For this purpose, the following simplifying assumptions are made:

i. Energy is dissipated by the scales through rotation of plastic hinges.

ii. The underlying layer does not deform significantly until the scales immediately underneath the impactor are fully flattened, i.e. the base of the scales (the joints between the scales and the top plate) are fixed in position.

iii. Only the scale immediately underneath the impactor (labelled as “Scale 1” in Figure 6.1) and the one to its right (labelled as “Scale 2”) are accounted for; energy dissipated through deformation of other scales is assumed to be less significant.

iv. The scales are deformed and the resulting plastic hinges are formed in the manner displayed in Figures 6.2 and 6.3.

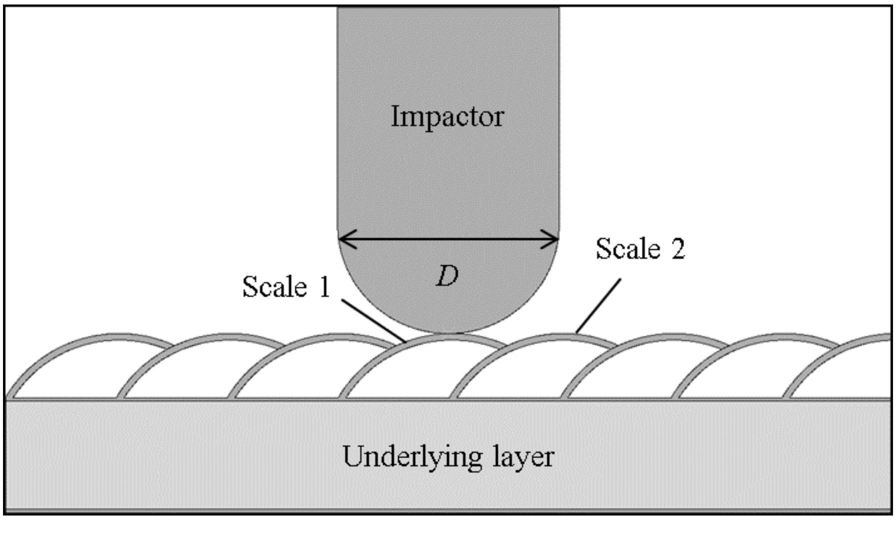

Figure 6.1: Activated scales underneath the impactor for estimation of plastic dissipation of the scale assembly.

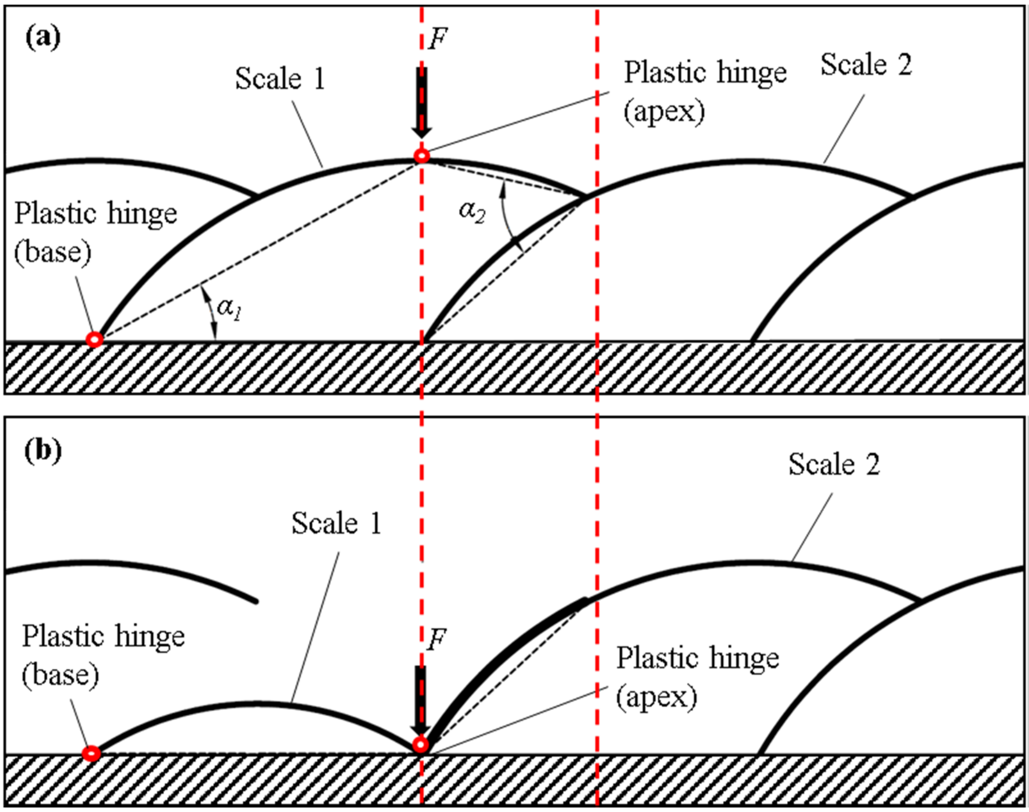

Figure 6.2: (a) Undeformed shape and (b) assumed deformed shape of Scale 1 when it is fully flattened.

Based on Figures 6.2 and 6.3, the rotations of plastic hinges in Scales 1 and 2 can be determined as shown below.

Rotation of plastic hinges in Scale 1 = $2\,\alpha_1 + \alpha_2$ (6.1)

Rotation of plastic hinges in Scale 2 = $2\,\beta_1 + \beta_2$ (6.2)

Hence, the total plastic dissipation W_s of the scales can be calculated as follows:

$$W_s = \frac{f_y t_s^{2}}{4} \times (2\,\alpha_1 + \alpha_2 + 2\,\beta_1 + \beta_2) \tag{6.3}$$

where f_y and t_s are the yield strength and thickness of the scales respectively.

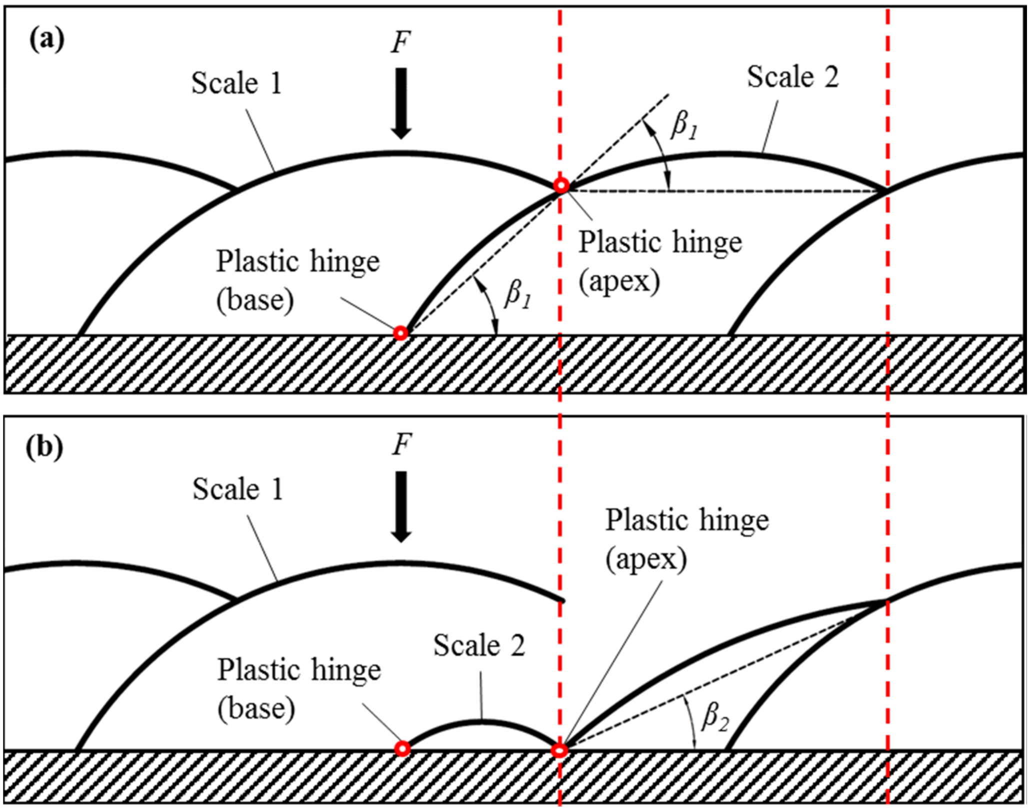

Figure 6.3: (a) Undeformed shape and (b) assumed deformed shape of Scale 2 when it is fully flattened.

To assess the accuracy of the above-mentioned method, several cases with different design configurations of the scales as shown in Figure 6.4 were simulated. The material properties of aluminium and cork as listed in Section 2.2 were used for the scales and underlying layer. The estimated plastic dissipation of the scales for each case is compared with the actual value obtained from Abaqus in Figure 6.5. These cases have $K_{geometry}$ values that fall within the optimum range (i.e. Group "*B*") defined in Section 4.5. In the simulations, the energy of the impactor for each case was equal to the sum of the estimated plastic dissipation W_s of the scales and the energy absorption capacity W_u of the underlying layer (as defined in Section 6.2).

Figure 6.5 presents the actual (obtained from Abaqus) versus estimated plastic dissipation of the scales for each case. The results can be grouped into three scenarios.

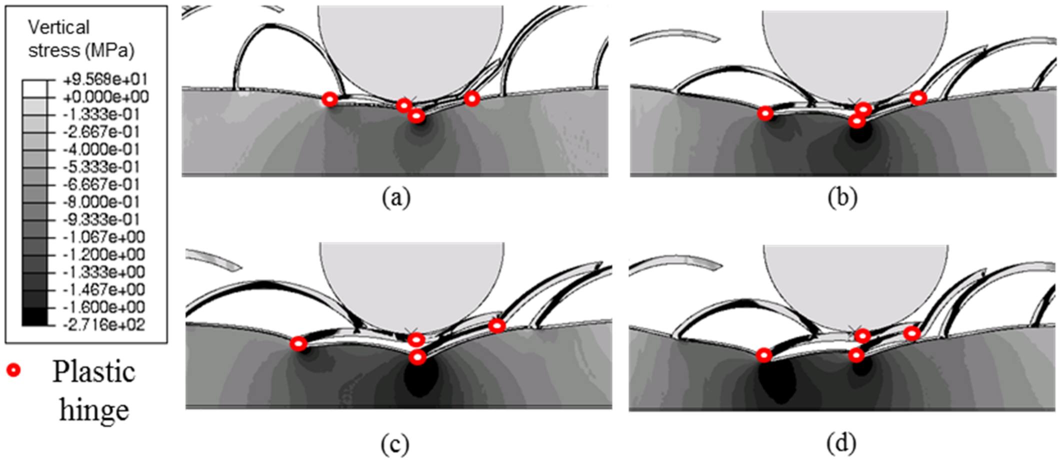

Specimen	L_s/t_s	L_s/R	L_h/S	L_h/D	V_s/V_u	$K_{geometry}$ (x 10^{-3})
(a)	44	2.1	1.5	0.8	0.13	0.106
(b)	29	1.5	1.5	0.8	0.13	0.184
(c)	26	1.5	1.5	1.0	0.19	0.205
(d)	20	1.7	1.5	0.8	0.19	0.708

Figure 6.4: Deformation and location of plastic hinges at maximum impactor penetration for various specimens.

Firstly, for case (a) which has higher curvature and thinner scales (i.e. higher aspect ratio L_s/t_s), the actual plastic dissipation is more than the estimated value. This may be due to the plastic deformation that occurs along the scales apart from the plastic hinges which has been excluded in the estimation. Also, the contribution from the scale to the left of Scale 1 (as shown in Figure 6.4(a)) has been conservatively omitted. Secondly, the actual plastic dissipation is lower than the estimated value when the assembly of scales become stiffer as a result of reduced aspect ratio L_s/t_s and/or increased relative volume V_s/V_u of the scales as shown by cases (c) and (d) in Figure 6.5. In contrast to the assumption made earlier, it is clear from Figures 6.4(c) and 6.4(d) that it is harder to completely flatten the scales for these cases and fully mobilize the plastic dissipation capacity of the scales before the underlying layer begins to deform. For thicker scales, larger stress is transferred to the joints between the scales and the underlying layer. This

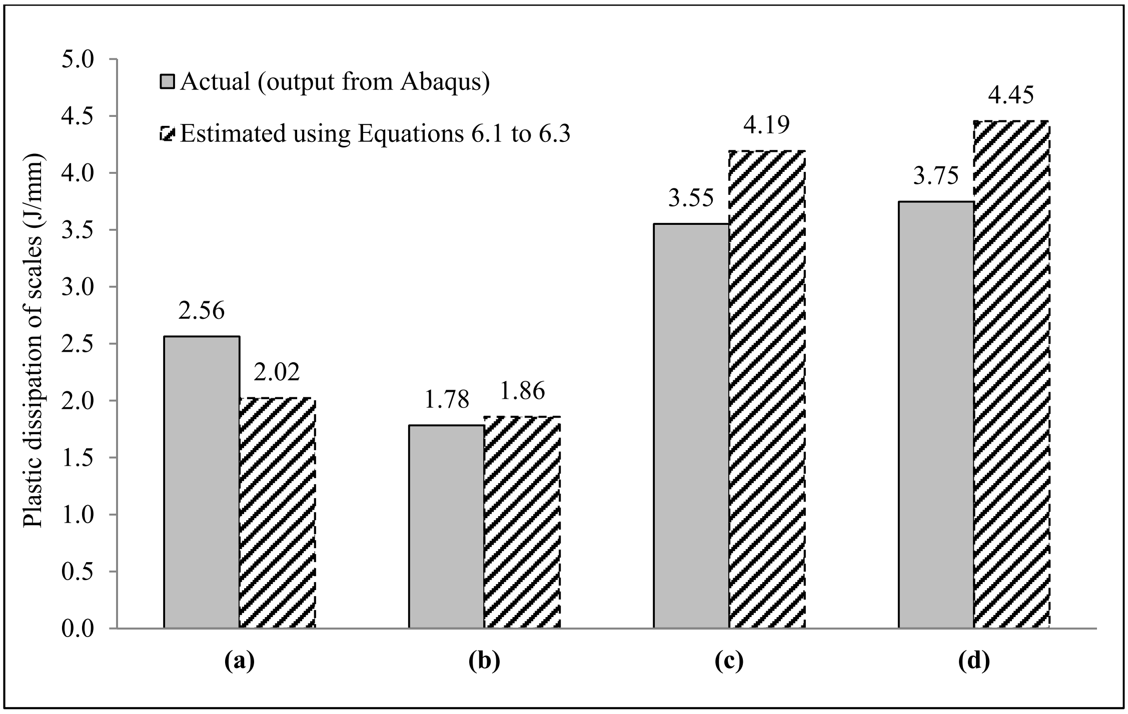

Figure 6.5: Plastic dissipation of scales for cases with different design configurations of scales.

reduces the effectiveness of the rotation of the plastic hinges at the joints in dissipating the impact energy. Moreover, while the scales in cases (c) and (d) are still deformable, their aspect ratio L_s/t_s and relative volume V_s/V_u are close to the lower and higher ends of their recommended bounds, respectively, as presented earlier in Table 4.1. Thus, these cases may not be the optimum among a host of other alternative designs. Thirdly, Figure 6.5 shows that the actual plastic dissipation of the scales in case (b) is approximately the same as its estimated capacity. The aspect ratio, curvature, and relative volume of the scales for this case are close to the midpoints of their proposed optimum ranges, and are between the values for case (a) and cases (c) and (d).

Nonetheless, despite the under and over-estimation of the plastic dissipation of the scales for the cases shown in Figure 6.4, the peak stresses transferred for all these cases do not exceed the maximum allowable stress (which is defined as the stress at the

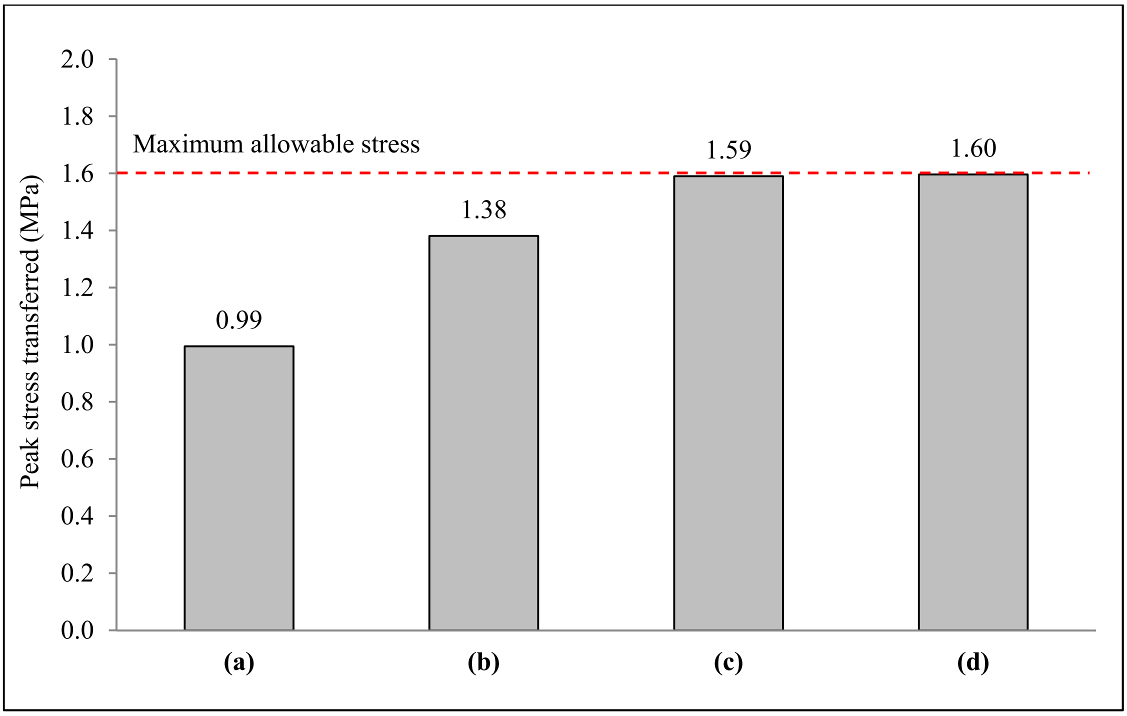

Figure 6.6: Peak stress transferred by cases with different design configurations of scales.

densification limit of the underlying layer, as mentioned in Section 3.2.2) as shown in Figure 6.6. Thus, it can be concluded that the simple method proposed here – which is based only on the initial geometry, yield strength, and thickness of the scales – provides a reasonably good approximation of the impact energy that can be dissipated through plastic deformation of the scales. The difference between the actual and estimated values is within 20 percent.

6.2 Energy absorption capacity of underlying layer

In order to minimize the stress transferred by the composite system, the energy absorbed by the underlying cellular layer should not cause it to densify. Therefore, the maximum energy which can be absorbed by the underlying cellular layer before its densification, henceforth termed as its energy absorption capacity, needs to be determined.

For this purpose, a simplifying assumption is made where the region of the underlying layer underneath the point of impact is assumed to be uniformly compressed while deformation of the adjacent regions is assumed to be negligible. This assumption is made because the deformation of the underlying layer tends to be localized immediately underneath the impactor as shown in Chapters 4 and 5. Based on the results in Section 4.4, the activated area is a function of span L_h of the scales and size D of the impactor. It is observed that when the size of the impactor is larger than the span of a scale (i.e. L_h/D smaller than 1.0), the region of the underlying layer activated to absorb the impact energy can be conservatively assumed as the area underneath the impactor as shown in Figure 6.7. Conversely, when the size of the impactor is smaller than the span of a scale (i.e. L_h/D larger than 1.0), the width of the activated region may be assumed to be equal to the span of the scales as depicted in Figure 6.8.

Moreover, it was observed in Section 5.6 that the entire thickness of the underlying layer underneath the impactor may not be uniformly compressed for cases with relatively thick underlying layer. Thus, it should not be assumed that the entire thickness of the underlying layer can be fully utilized to absorb the impact energy. Instead, for such cases compression of the underlying layer is concentrated in the region directly around the point of impact. Therefore, the ratio of the size D of the impactor to the thickness T of the underlying layer should be taken into account in estimating the amount of impact energy that can be safely absorbed by the underlying layer. For this purpose, a limiting D/T ratio may be introduced. This parameter is henceforth denoted as J. When D/T is greater than J, the entire thickness T of the underlying layer may be utilized as shown in Figure 6.7. On the other hand, when D/T is smaller than J, the effective thickness of the underlying layer is D/J as depicted in Figure 6.9.

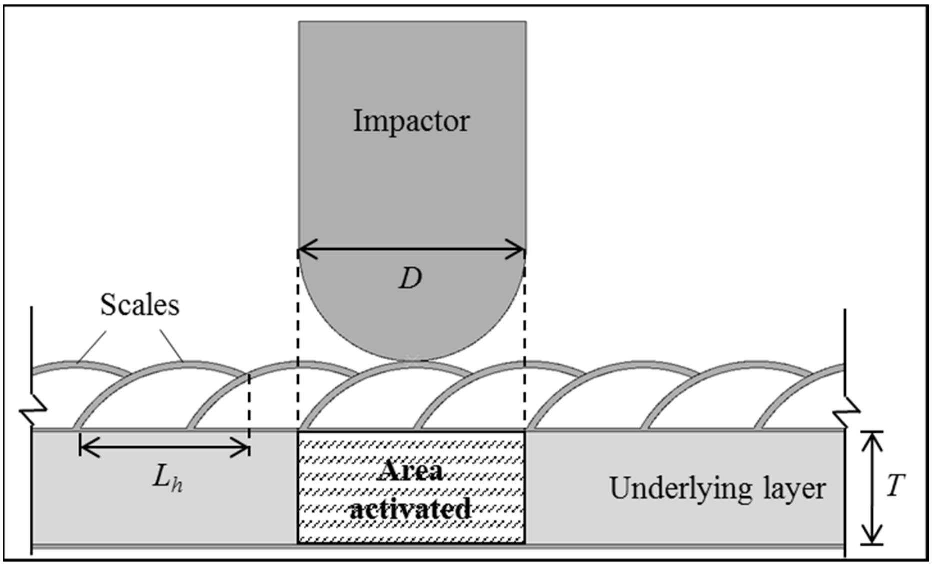

Figure 6.7: Estimation of area of underlying cellular layer activated to resist impactor when $D > L_h$.

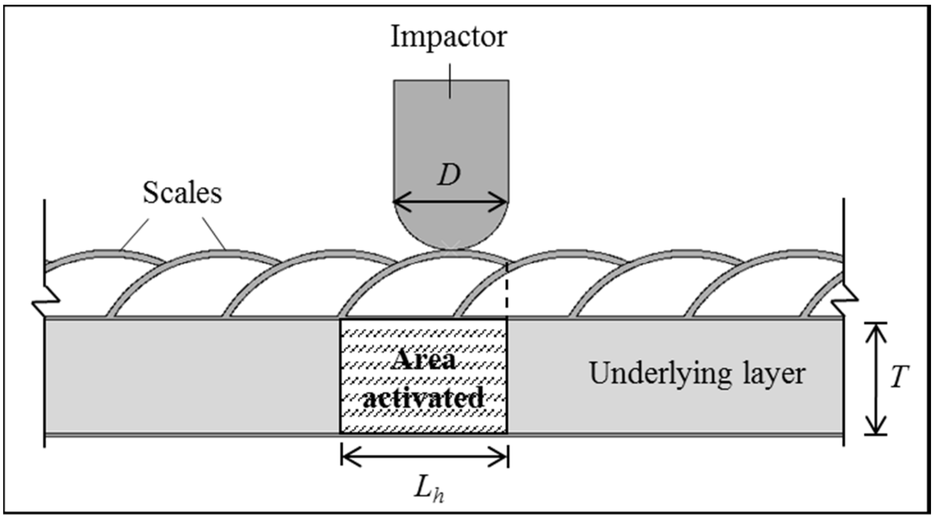

Figure 6.8: Estimation of area of underlying cellular layer activated to resist impactor when $D < L_h$.

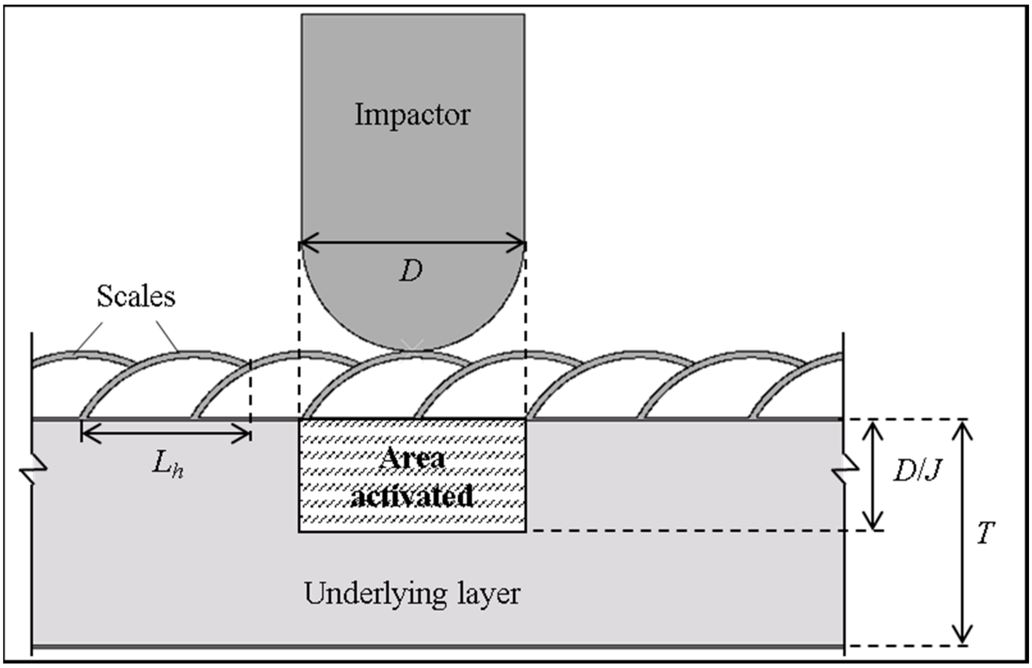

Figure 6.9: Estimation of area of underlying cellular layer activated to resist impactor when $D/T < J$.

Therefore, based on the preceding assumptions, the energy absorption capacity W_u of the underlying cellular layer may be defined by the following equations:

$$W_u = \text{Energy density} \times A \times B \tag{6.4}$$

where

$$A = \begin{cases} D & \text{if} \quad D > L_h \\ L_h & \text{if} \quad D < L_h \end{cases} \tag{6.5}$$

$$B = \begin{cases} T & \text{if} \quad D/T > J \\ D/J & \text{if} \quad D/T < J \end{cases} \tag{6.6}$$

In Equation 6.4, the energy density is defined as the area under the underlying cellular material's compressive stress-strain curve up to its densification limit as shown in Figure 6.10.

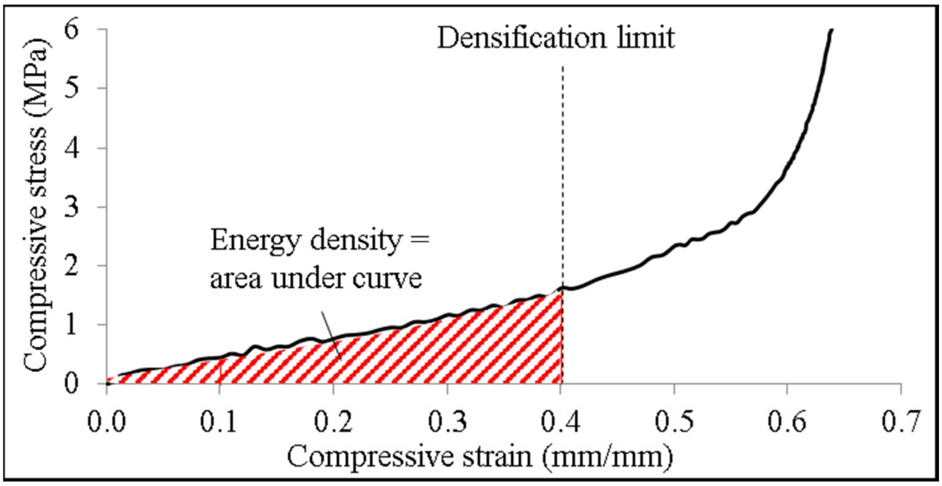

Figure 6.10: Definition of energy density of cellular material.

To test the accuracy of this estimation, cases with varying thickness and energy density of underlying layer, as well as the size of impactor, are presented in the following sections. The design configuration of the cases chosen for this purpose is shown in Figure 6.7 (and also in Figure 6.4(b)). The assembly of scales in this configuration has a $K_{geometry}$ value of 0.184 x 10^{-3}. The material properties of aluminium and cork as listed in Section 2.2 were used for the scales and underlying layer.

6.2.1 Effects of underlying layer thickness

Figures 6.11 and 6.12 show the energy absorbed by the underlying layer and the peak stress transferred for specimens with various thicknesses T of the underlying layer (represented by the ratio of volume V_s of the scales, which was kept constant in the simulations, to volume V_u of the underlying layer), while Figure 6.13 displays the deformed shape of the specimens. Unless otherwise stated, the relative size L_h/D of the scales for all cases is 0.8. For each specimen, the energy W_i exerted by the impactor is equal to the sum of the estimated plastic dissipation W_s of the scales (as defined in Section 6.1) and the energy absorption capacity W_u of the underlying layer (as defined by Equations 6.4 to 6.6). Since the limiting D/T ratio J is still an unknown, the entire

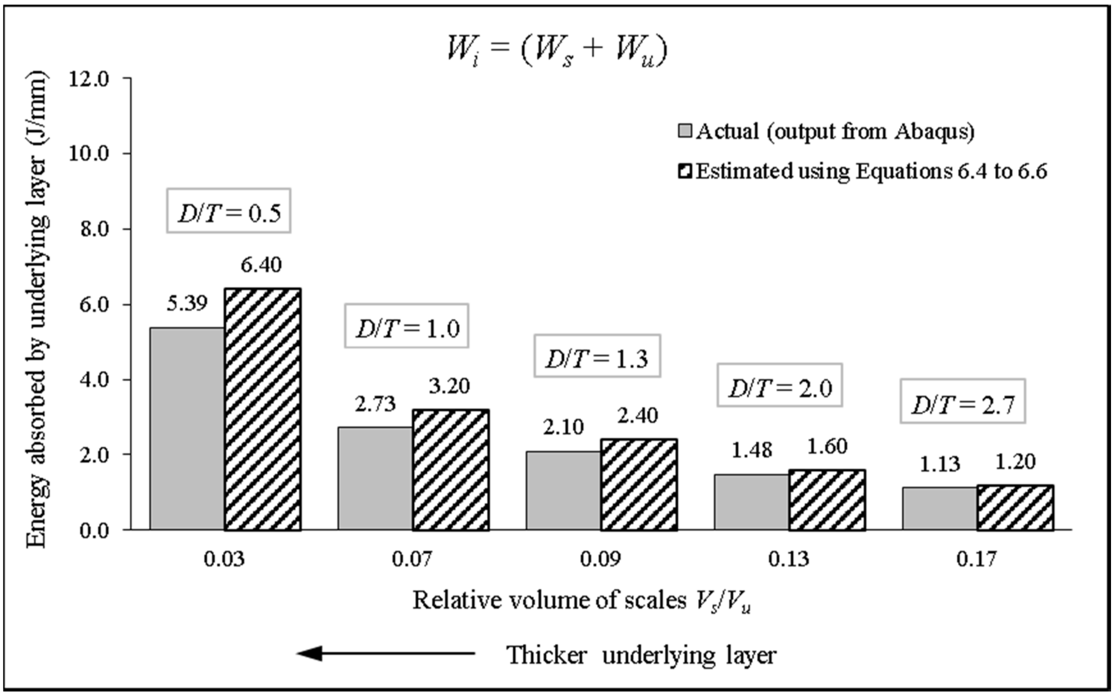

Figure 6.11: Energy absorbed by underlying layer against relative volume V_s/V_u of scales subject to impact energy $W_i = (W_s + W_u)$.

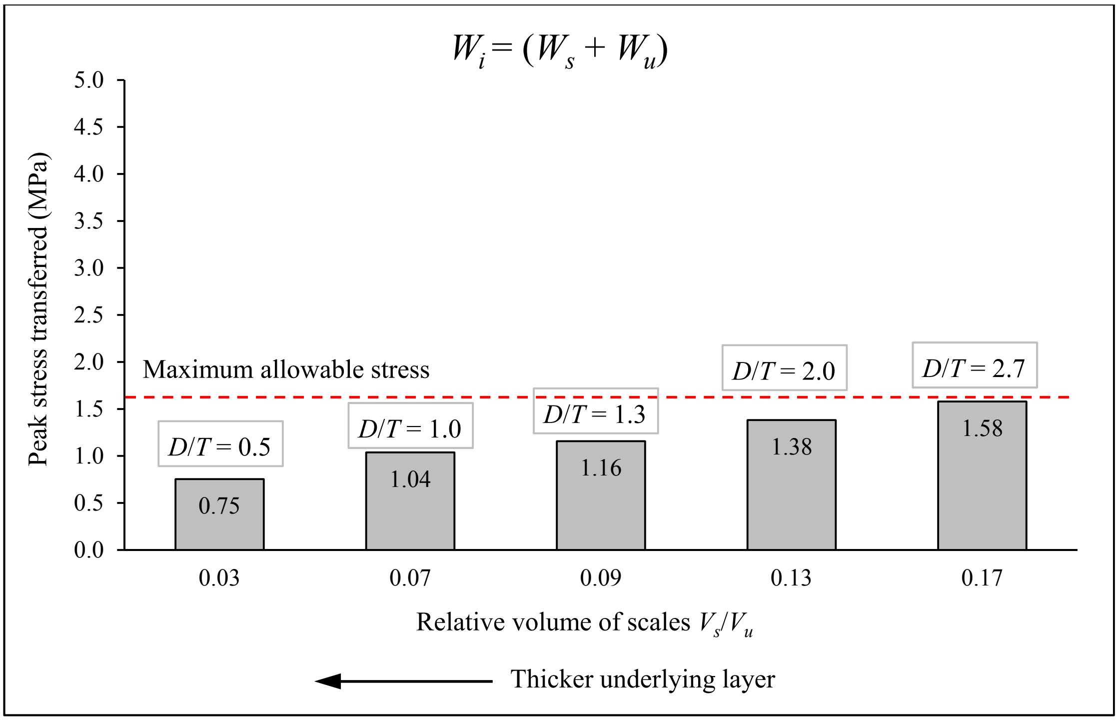

Figure 6.12: Peak stress transferred against relative volume V_s/V_u of scales subject to impact energy $W_i = (W_s + W_u)$.

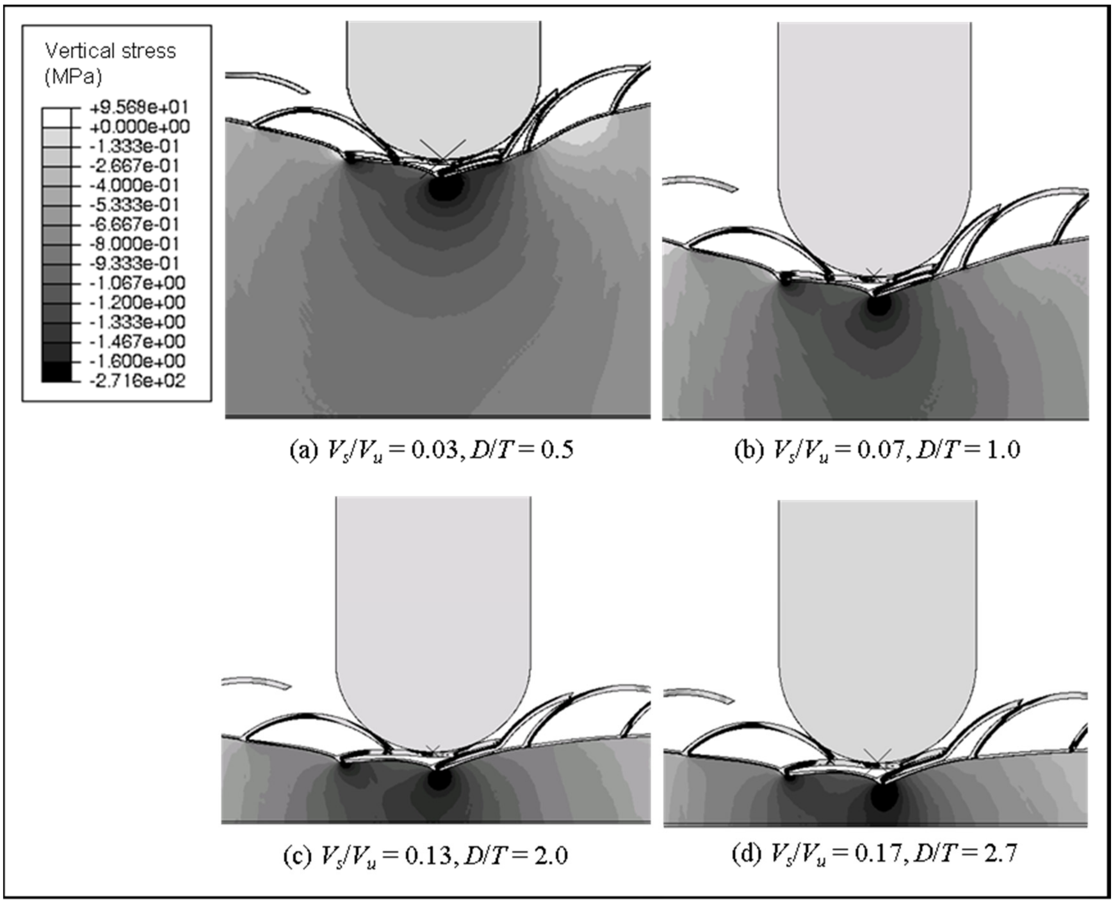

(a) $V_s/V_u = 0.03, D/T = 0.5$

(b) $V_s/V_u = 0.07, D/T = 1.0$

(c) $V_s/V_u = 0.13, D/T = 2.0$

(d) $V_s/V_u = 0.17, D/T = 2.7$

Figure 6.13: Deformation and vertical stress contour for composite specimens with various relative volumes V_s/V_u of scales at maximum impactor penetration subject to impact energy $W_i = (W_s + W_u)$.

thickness T of the underlying layer is first assumed to be fully effective in estimating W_u. The results show that the energy absorbed by the underlying layer, both estimated and actual (output from Abaqus), becomes higher with increasing underlying layer thickness (i.e. lower V_s/V_u), which is expected from Equation 6.4. More importantly, the actual energy absorbed by the underlying is close to but generally lower than the estimated capacity and this discrepancy increases with increasing thickness of the underlying layer. This may be a result of assuming that the entire thickness T of the cellular layer immediately underneath the impactor is compressed uniformly to absorb the impact energy.

As shown in Figures 6.13(a) and 6.13(b), for cases with relatively thick underlying cellular layer the compression of this layer is not uniform across its entire thickness T. Instead, it is localized at the part directly around the point of impact due to inertia effects. Moreover, with increasing thickness of the underlying layer, the stress is distributed over a wider region. As a result, the entire thickness T of the underlying layer underneath of the impactor is not fully utilized to absorb the impact energy, resulting in the discrepancy between the actual and estimated energy absorbed by the underlying layer. To address this discrepancy, the thickness of the underlying layer which may be assumed to contribute towards its energy absorption capacity should be a function of D/T as shown in Equation 6.6. When the underlying layer is considered thin relative to the size of the impactor, i.e. D/T is greater than a certain value J, the full thickness T of the underlying layer may be assumed to be effective. Conversely, when the underlying layer is considered thick relative to the size of the impactor, i.e. D/T is smaller than J, the effective thickness is less than T and may be taken as D/J. Based on Figure 6.11, the recommended value for J is 2.0. However, despite the increasing discrepancy between the actual and estimated energy absorbed by the underlying layer with increasing thickness of the underlying layer, the peak stress transferred by these specimens does not exceed the maximum allowable stress as shown in Figure 6.12.

For the cases presented in Figures 6.11 to 6.13, the accuracy of Equations 6.4 to 6.6 in estimating the energy W_u that can be absorbed safely by the underlying layer is assessed by subjecting various specimens to an impact energy of $W_i = (W_s + W_u)$. To further evaluate the validity of these equations, the specimens may be subject to higher and lower impact energies. Figures 6.14 and 6.15 depict the energy absorbed by the underlying layer and the peak stress transferred for the same set of specimens but with increased impact energy $W_i = (W_s + 2\ W_u)$. It is apparent that the actual energy absorbed by the underlying layer (output from Abaqus) exceeds the estimated capacity for all cases. Moreover, the peak stresses transferred generally exceed the maximum allowable stress of the underlying layer because the energy absorbed by the underlying layer is more than its capacity. Thus, it is observed that the underlying layer is compressed severely until it is densified, which leads to the high peak stress transferred. The only exception is the specimen with $V_s/V_u = 0.03$ which has the thickest underlying layer among the cases presented here. As shown in Figure 6.16(a), the thicker underlying layer allows the stress within to be distributed over a wider region before reaching the base of the specimen.

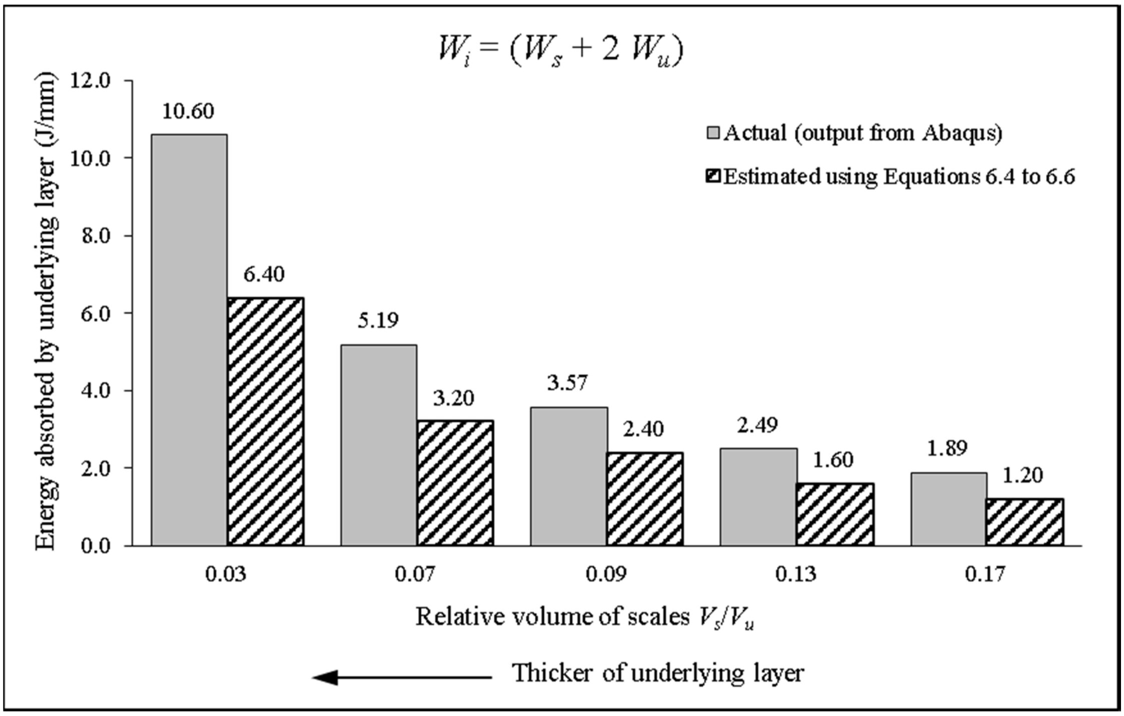

Figure 6.14: Energy absorbed by underlying layer as function of relative volume V_s/V_u of scales subject to impact energy $W_i = (W_s + 2\ W_u)$.

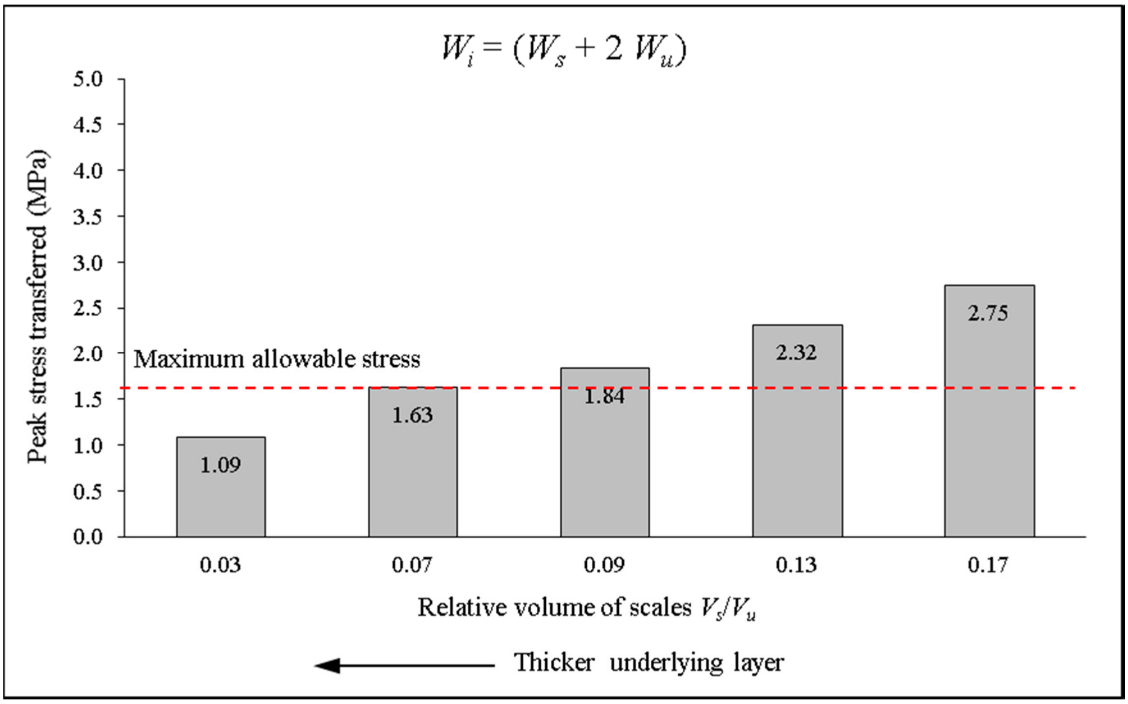

Figure 6.15: Peak stress transferred as function of relative volume V_s/V_u of scales subject to impact energy $W_i = (W_s + 2\ W_u)$.

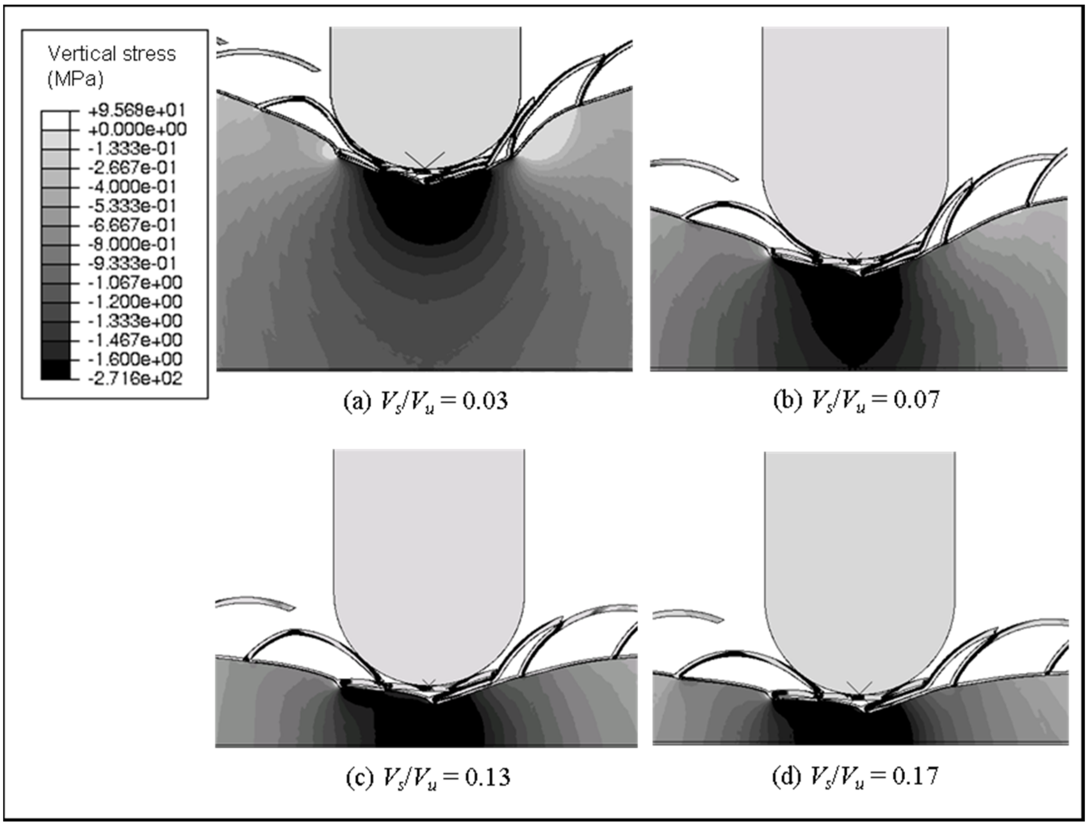

Figure 6.16: Deformation and vertical stress contour for composite specimens with various relative volumes V_s/V_u of scales at maximum impactor penetration subject to impact energy $W_i = (W_s + 2\ W_u)$.

Lastly, Figures 6.17 and 6.18 show the energy absorbed by the underlying layer and the peak stress transferred for the same set of specimens but with reduced impact energy of $W_i = (W_s + 0.5\ W_u)$. It is apparent that the actual energy absorbed by the underlying layer is lower than its estimated capacity by about 30 percent while the peak stress transferred is lower than the maximum allowable limit of the underlying layer by about 40 percent. As shown in Figure 6.19, there is minimal deformation of the underlying layer as well as the scales compared to the earlier cases shown in Figures 6.13 and 6.16. This suggests that the composite specimens are over-designed for this amount of energy exerted by the impactor. Thus, it appears that Equations 6.4 to 6.6 can provide a sufficiently good estimation of the maximum energy which can be absorbed safely by the underlying layer before its densification such that the peak stress transferred does not exceed its maximum allowable stress.

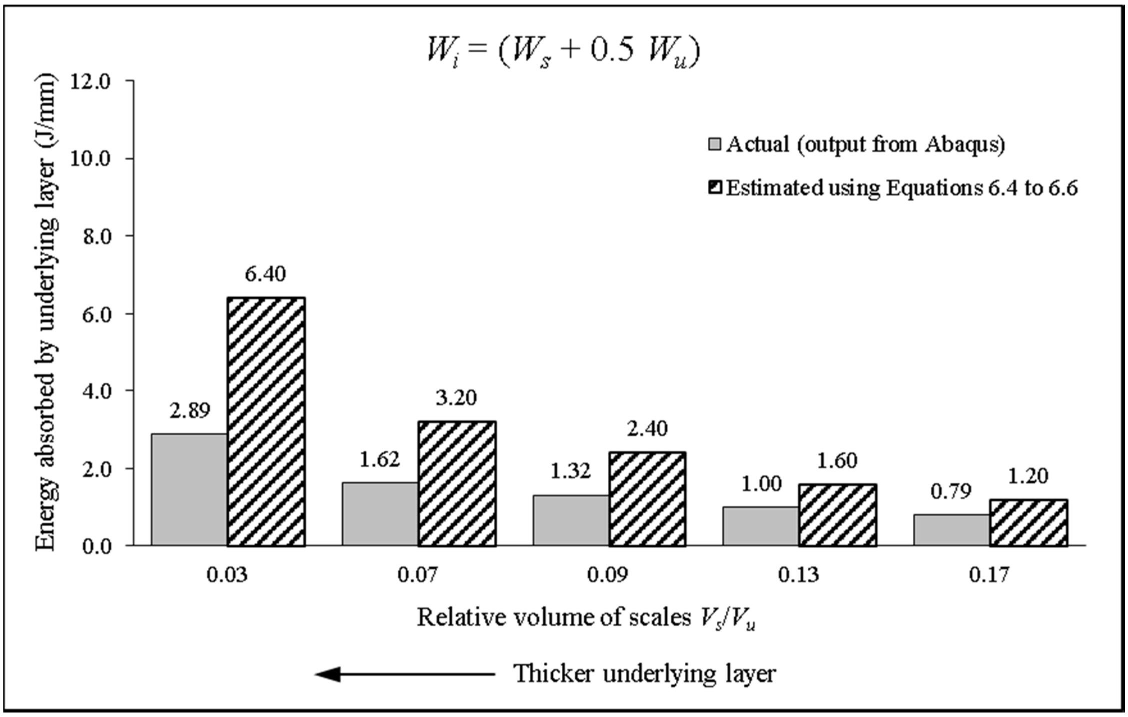

Figure 6.17: Energy absorbed by underlying layer against relative volume V_s/V_u of scales subject to impact energy $W_i = (W_s + 0.5\ W_u)$.

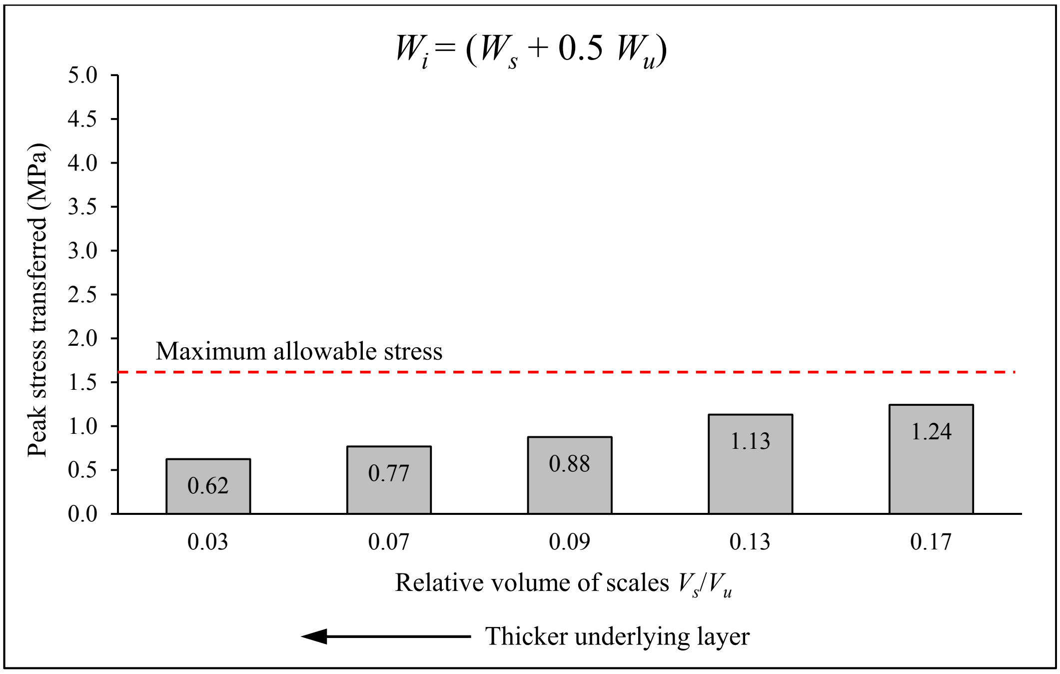

Figure 6.18: Peak stress transferred as function of relative volume V_s/V_u of scales subject to impact energy $W_i = (W_s + 0.5\ W_u)$.

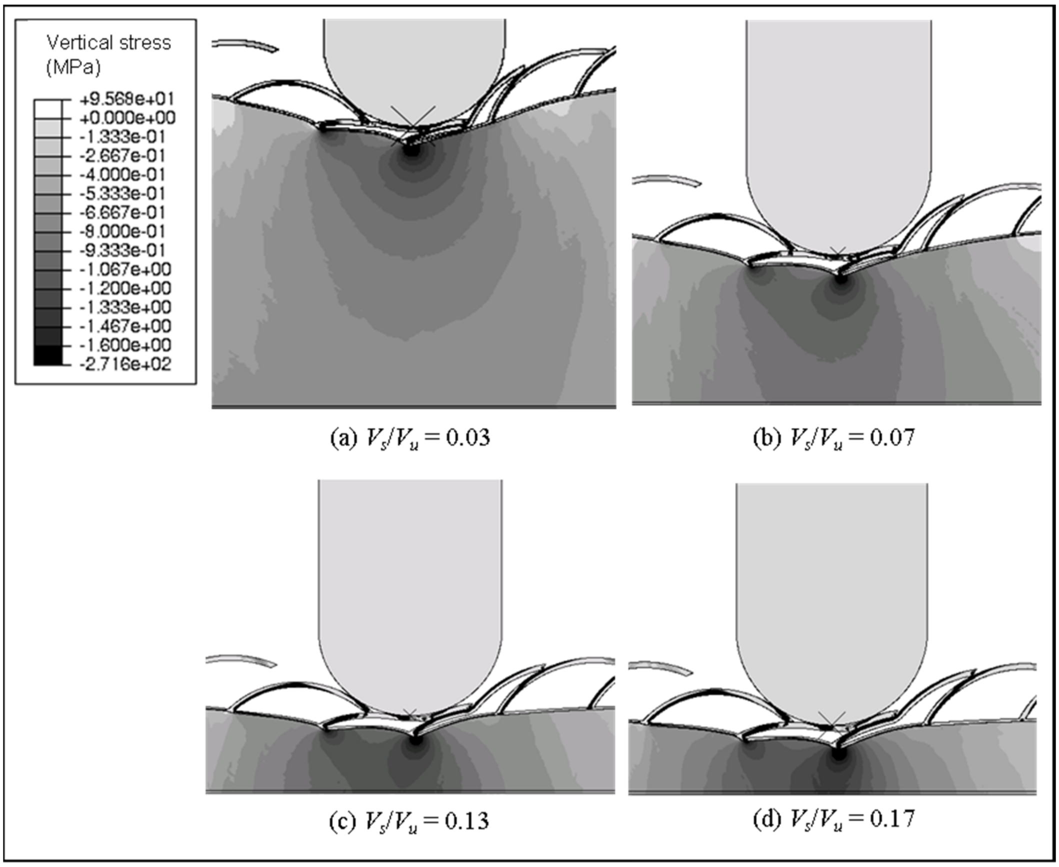

(a) $V_s/V_u = 0.03$
(b) $V_s/V_u = 0.07$
(c) $V_s/V_u = 0.13$
(d) $V_s/V_u = 0.17$

Figure 6.19: Deformation and vertical stress contour for composite specimens with various relative volumes V_s/V_u of scales at maximum impactor penetration subject to impact energy $W_i = (W_s + 0.5\ W_u)$.

6.2.2 Effects of material properties of underlying cellular layer

As shown earlier in Figure 6.10, the energy density of the underlying cellular layer is governed by its material properties specifically its compressive stress-strain curve. To examine this effect, the strength of the underlying layer (i.e. average plateau stress) was varied without changing the design configuration of the composite system and material properties of the scales, using the same approach presented earlier in Section 5.5. Figures 6.20 and 6.21 show the energy absorbed by the underlying layer and the peak stress transferred for specimens with varying strength (and hence, energy density) of the underlying layer, represented by the material strength ratio which is the ratio of yield strength of the scales to strength of the underlying layer. For each specimen, the energy W_i exerted by the impactor is equal to the sum of the estimated plastic dissipation W_s of the scales (as defined in Section 6.1) and the energy absorption capacity W_u of the underlying layer (as defined in Equations 6.4 to 6.6).

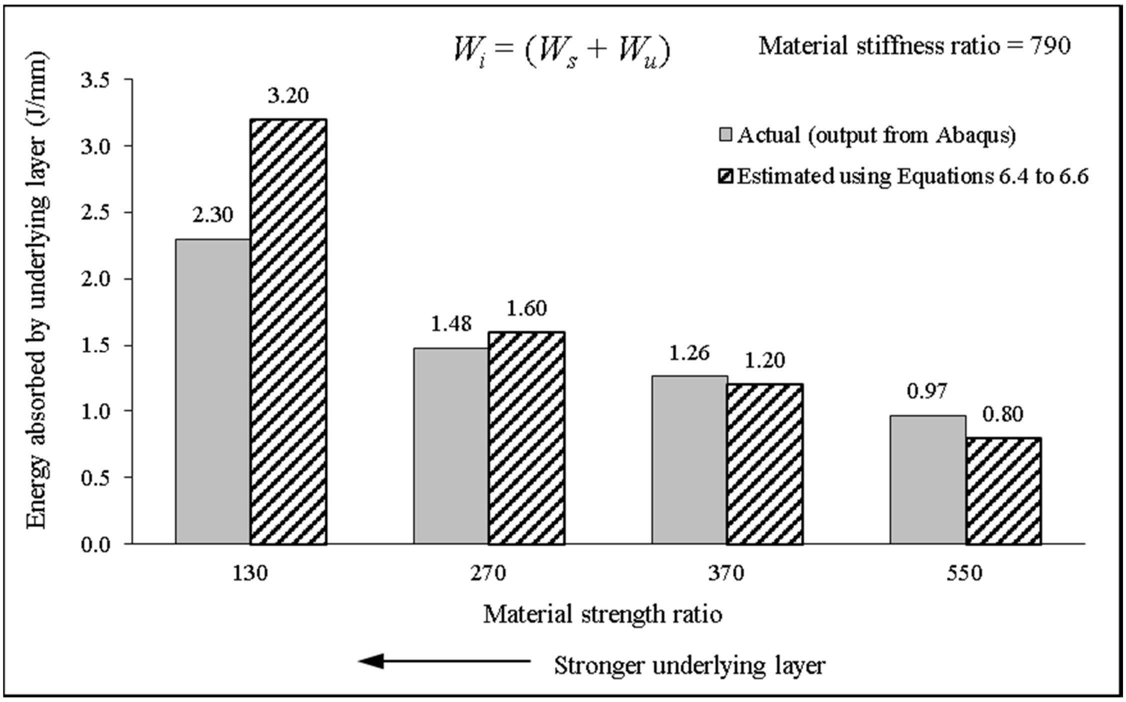

Figure 6.20: Energy absorbed by underlying layer against material strength ratio for cases with impact energy $W_i = (W_s + W_u)$.

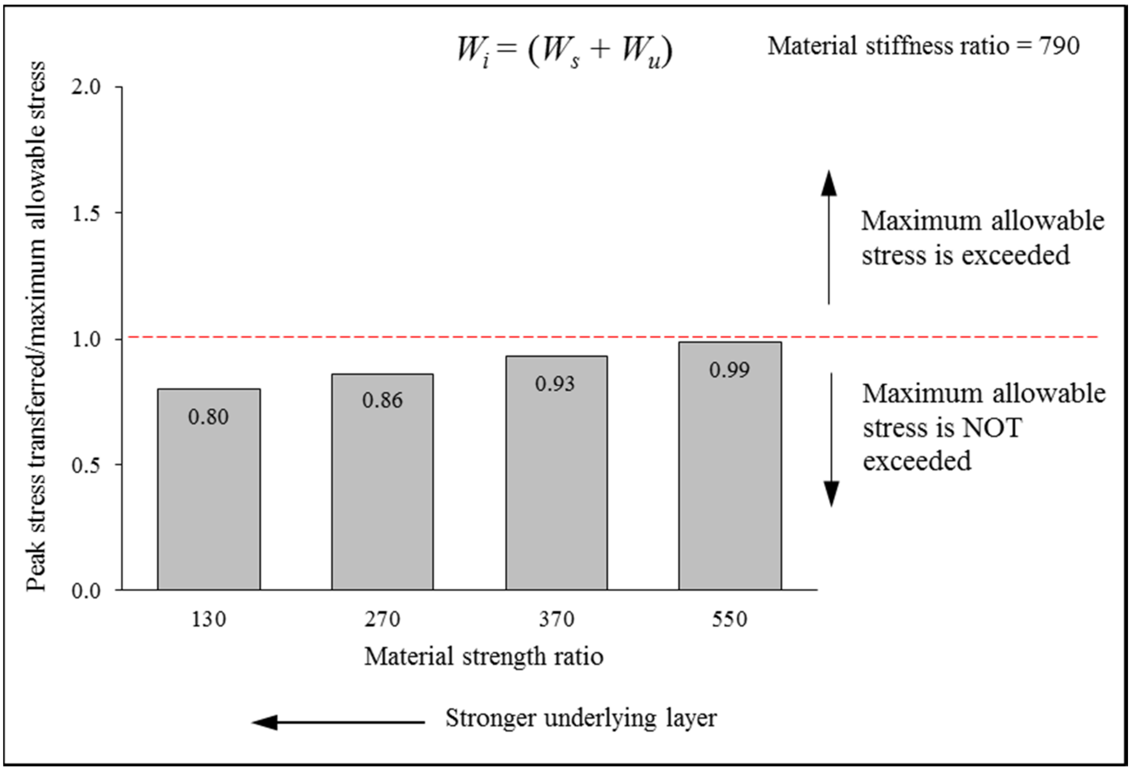

Figure 6.21: Peak stress transferred against material strength ratio for cases with impact energy $W_i = (W_s + W_u)$.

It is apparent that the energy absorbed by the underlying cellular layer, both estimated and actual (output from Abaqus), becomes higher with increasing strength and hence energy density of the underlying layer (i.e. lower material strength ratio), which is expected from Equation 6.4. Also, for most cases the actual energy absorbed by the underlying layer is generally close to the estimated capacity. On the other hand, the actual energy absorbed is markedly lower than the estimated capacity for the case with low material strength ratio of 130 which has a relatively strong underlying layer (i.e. high energy density). This is because the scales underneath the impactor are deformed more significantly as shown in Figure 6.22(a) due to the increased strength of the underlying layer which results in a higher proportion of impact energy dissipated by the scales instead of being absorbed by the underlying layer. However, Figure 6.21 shows that the peak stresses transferred by the specimens are lower than their respective allowable limits which are proportional to the strength of the underlying layer.

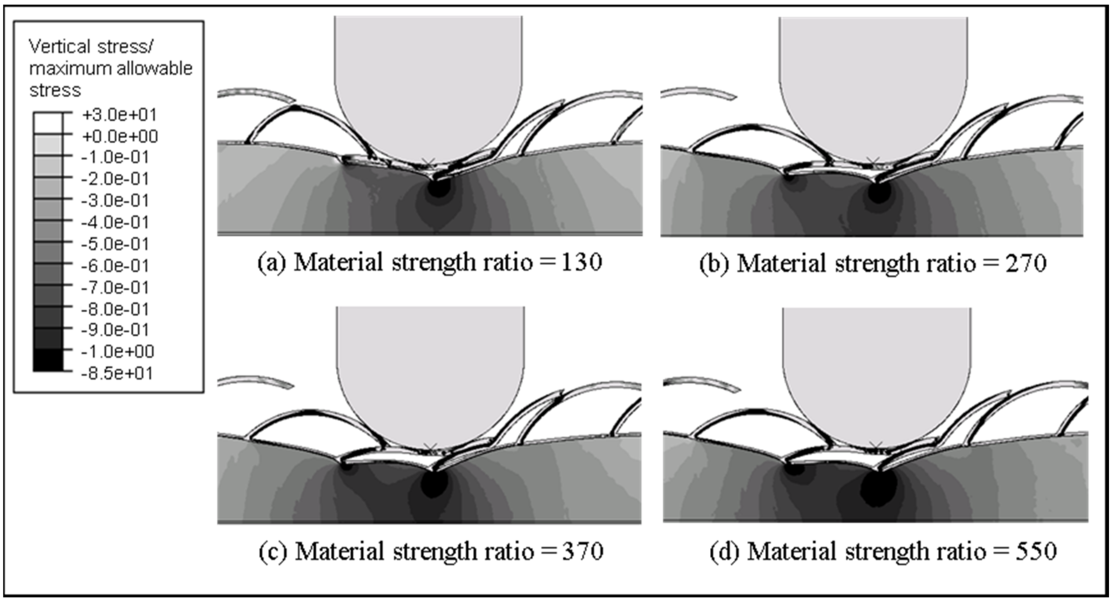

(a) Material strength ratio = 130

(b) Material strength ratio = 270

(c) Material strength ratio = 370

(d) Material strength ratio = 550

Figure 6.22: Deformation and vertical stress contour for composite specimens with various material strength ratios at maximum impactor penetration subject to impact energy $W_i = (W_s + W_u)$.

Figure 6.22 shows that the scales in these specimens performed in the intended manner: they are able to deform in order to dissipate the impact energy while causing minimal compression on the underlying layer.

To further evaluate the accuracy of Equations 6.4 to 6.6 in estimating the energy W_u that can be absorbed safely by the underlying layer, the same specimens are subject to a higher impact energy of $W_i = (W_s + 2\ W_u)$. Figures 6.23 and 6.24 show the energy absorbed by the underlying layer and the peak stress transferred for these cases. It is apparent that the actual energy absorbed by the underlying layer exceeds the estimated capacity for all cases. Moreover, the higher peak stresses transferred exceed the maximum allowable stress of the underlying layer. The underlying layer is compressed severely until it is densified as displayed in Figure 6.25. Therefore, it can be concluded that Equations 6.4 to 6.6 give a fairly good estimation of the impact energy that can be safely absorbed by the underlying layer.

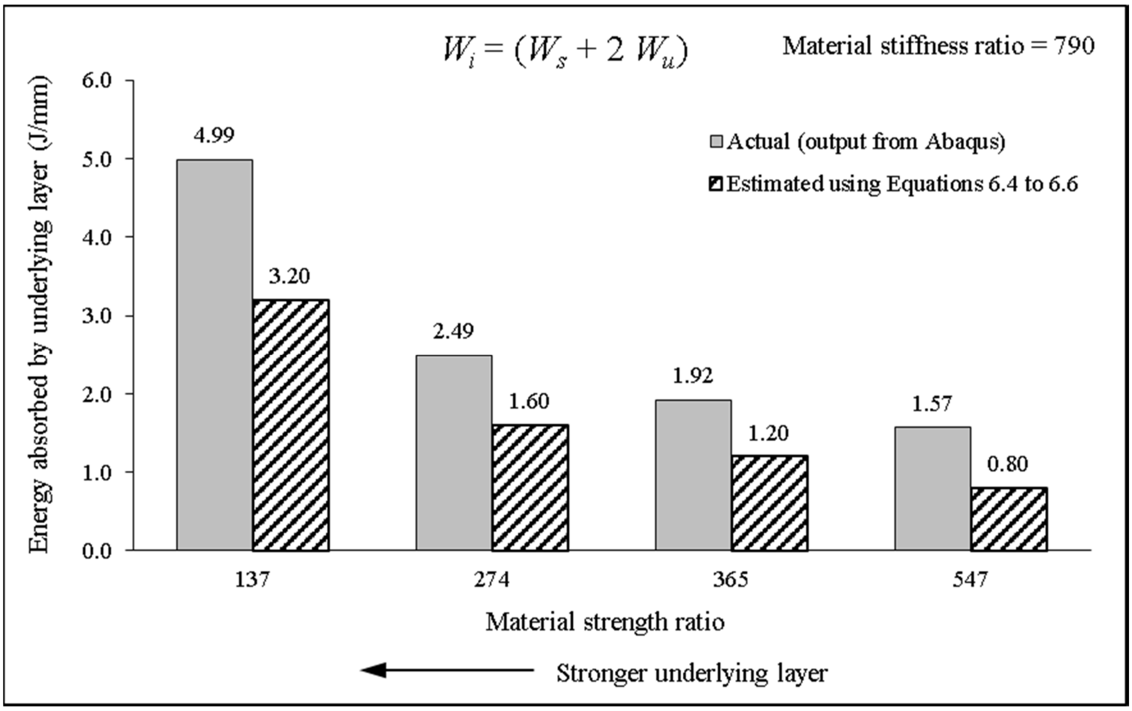

Figure 6.23: Energy absorbed by underlying layer against material strength ratio for cases with impact energy $W_i = (W_s + 2\ W_u)$.

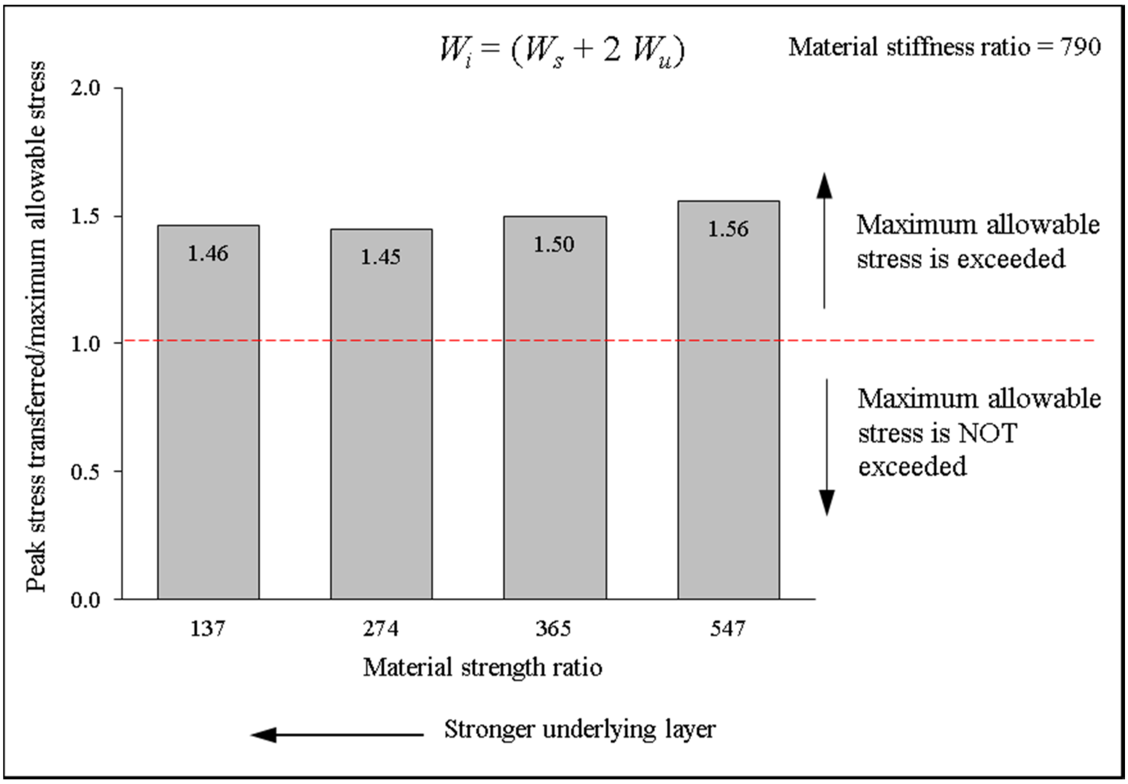

Figure 6.24: Peak stress transferred against material strength ratio for cases with impact energy $W_i = (W_s + 2\ W_u)$.

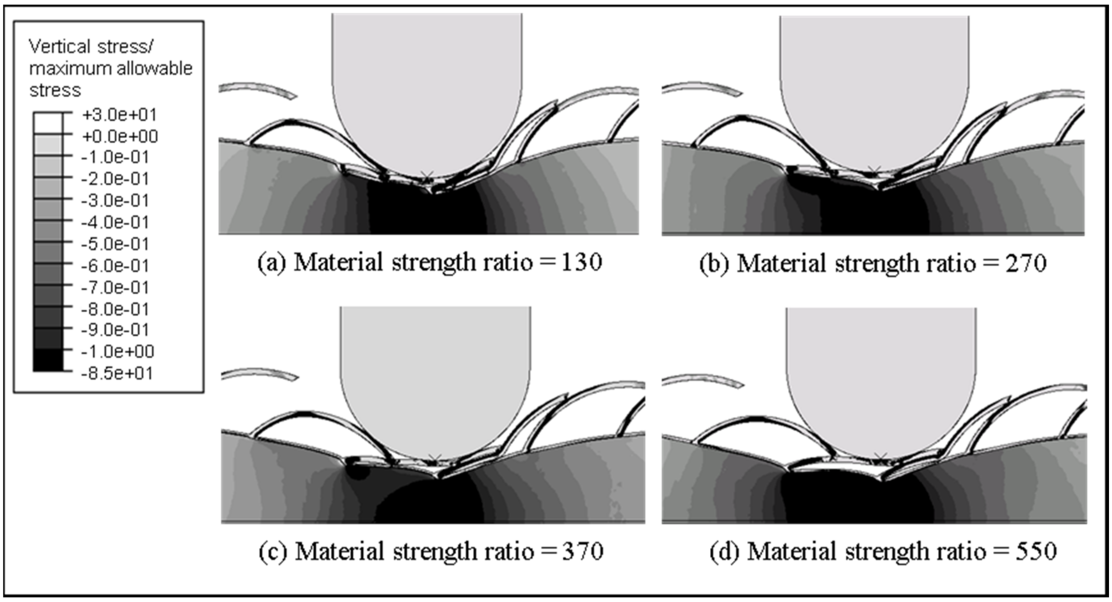

Figure 6.25: Deformation and vertical stress contour for composite specimens with various material strength ratios at maximum impactor penetration subject to impact energy $W_i = (W_s + 2\ W_u)$.

6.2.3 Effects of size of scales relative to size of impactor

Lastly, the relative size L_h/D of the scales influences the width of underlying cellular layer that is activated to absorb the impact energy. Figures 6.26 and 6.27 show the energy absorbed by the underlying layer and the peak stress transferred for specimens with various relative sizes L_h/D of the scales (in the simulations, D was varied while L_h was kept constant) while Figure 6.28 displays their deformed states. For each specimen, the energy W_i exerted by the impactor is equal to the sum of the estimated plastic dissipation W_s of the scales (as defined in Section 6.1) and the energy absorption capacity W_u of the underlying layer as defined by Equations 6.4 to 6.6. As shown in Figure 6.26, the actual energy absorbed by the underlying layer (output from Abaqus) is within 20 percent of the estimated value for each case, while the peak stresses transferred for all cases are within the allowable limit as shown in Figure 6.27. Moreover, it can be observed in Figures 6.28(b) and 6.28(c) that the width of the underlying layer as well as the number of scales activated to resist the impactor are roughly similar for specimens

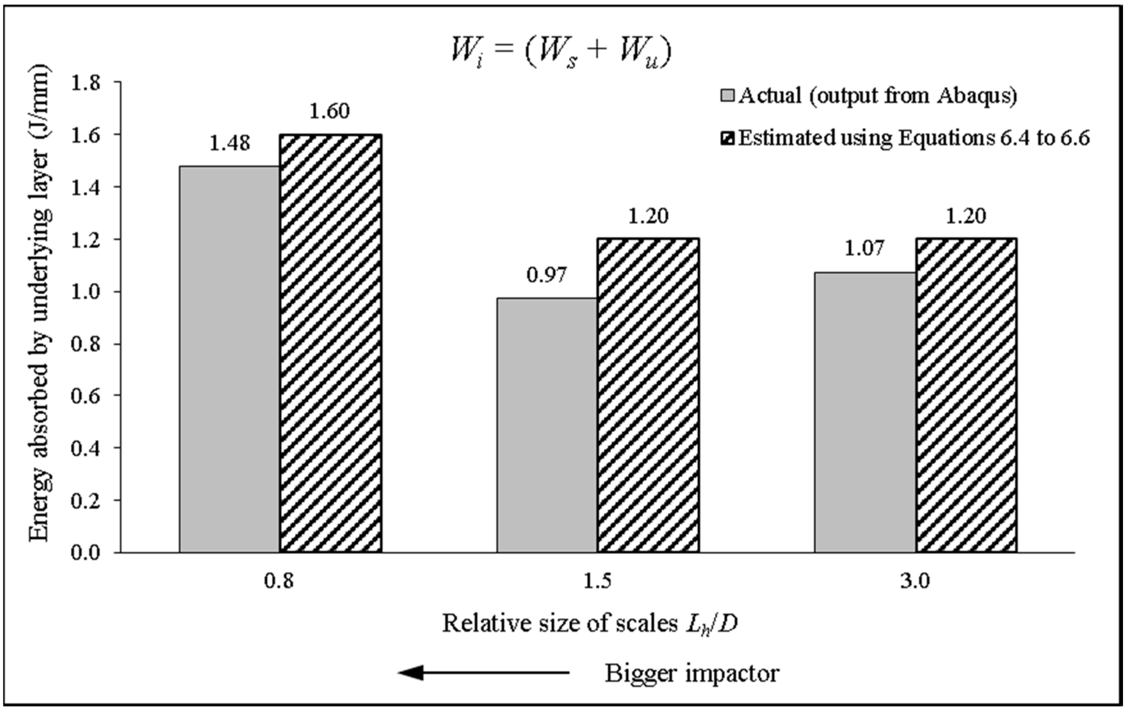

Figure 6.26: Energy absorbed by underlying layer against relative size L_h/D of scales subject to impact energy $W_i = (W_s + W_u)$.

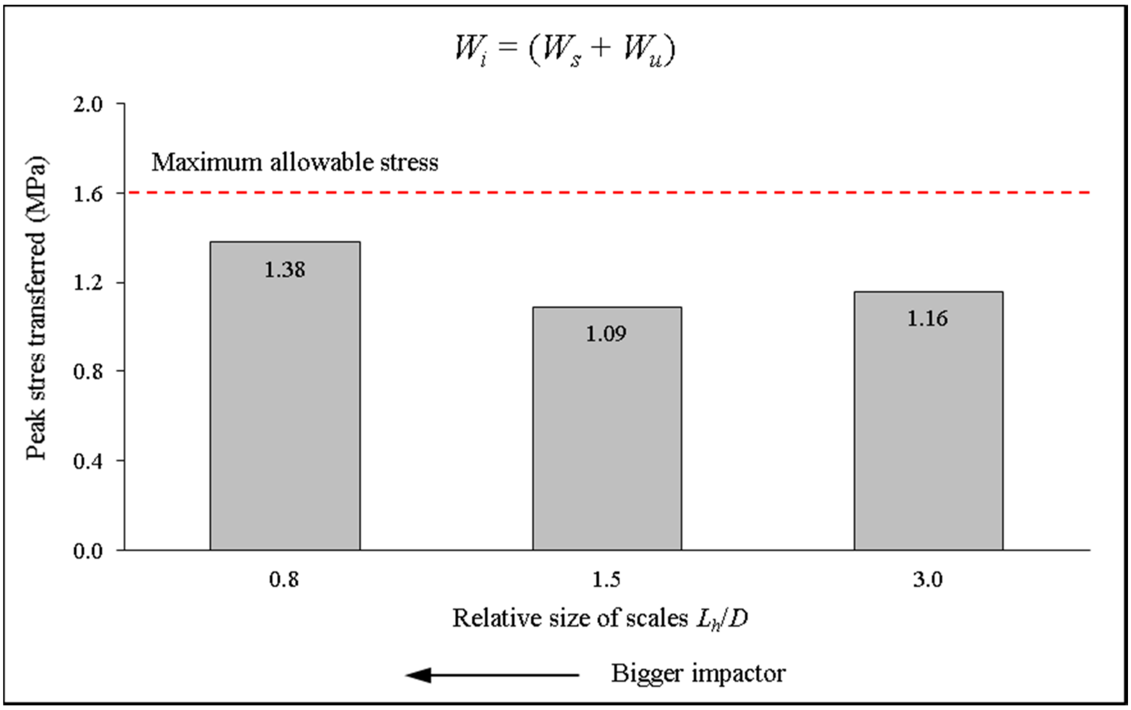

Figure 6.27: Peak stress transferred against relative size L_h/D of scales subject to impact energy $W_i = (W_s + W_u)$.

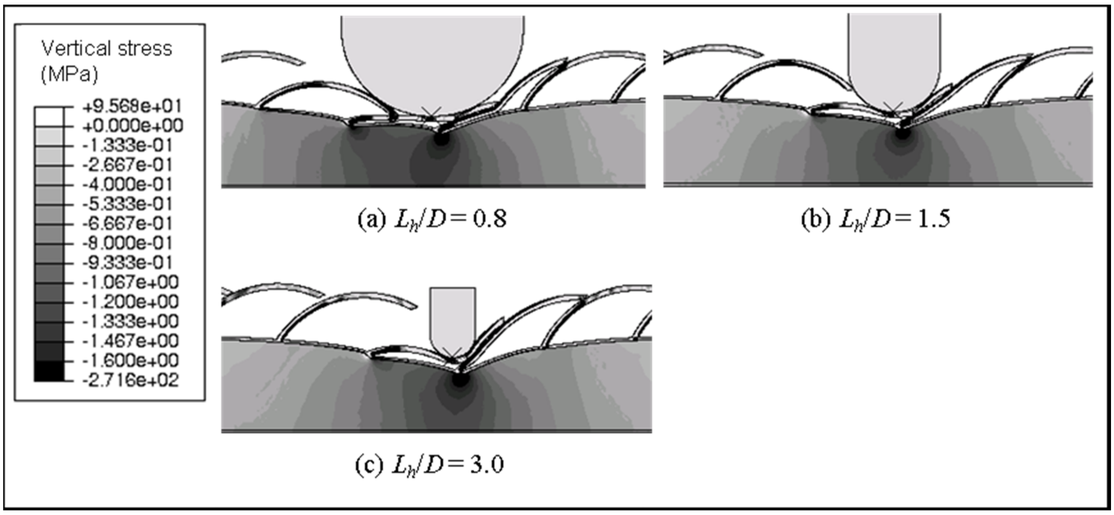

(a) $L_h/D = 0.8$ (b) $L_h/D = 1.5$ (c) $L_h/D = 3.0$

Figure 6.28: Deformation and vertical stress contour for composite specimens with various relative size L_h/D of scales at maximum impactor penetration subject to impact energy $W_i = (W_s + W_u)$.

with $L_h/D = 1.5$ and $L_h/D = 3.0$. For both cases, the span L_h of scales is larger than D but the width of the underlying layer that is activated to resist the impactor is approximately equal to L_h rather than D. On the other hand, the width of the underlying layer that is activated to resist the impactor is approximately equal to D rather than L_h for the specimen with L_h smaller than D as shown in Figure 6.28(a).

To test whether it would be simpler to assume that the width of the underlying layer which is activated to resist the impactor is always equal to D rather than being a function of L_h/D, the same set of cases were re-examined by imposing an impact energy of $W_i = (W_s + W_u)$ with W_u being directly proportional to D and without considering L_h. Figure 6.29 shows that the actual energy absorbed by the underlying layer of the specimen with $L_h/D = 3.0$ is significantly higher than its estimated capacity but the peak stress transferred is below than the maximum allowable value as shown in Figure 6.30, even though the deformation of the specimen is unchanged as shown in Figure 6.31(c). This finding suggests that the underlying layer is able to absorb more impact energy before it densifies, hence the energy absorption capacity of the underlying layer is under-

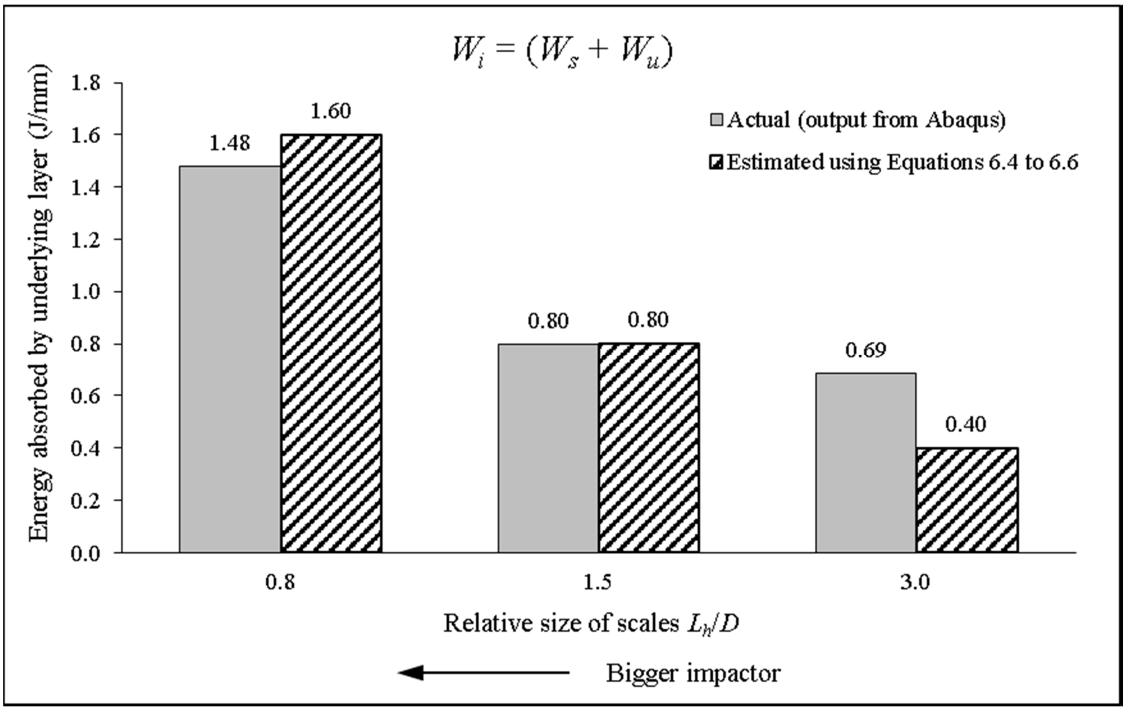

Figure 6.29: Energy absorbed by underlying layer against relative size L_h/D of scales for specimens subject to impact energy $W_i = (W_s + W_u)$ assuming W_u is proportional to D.

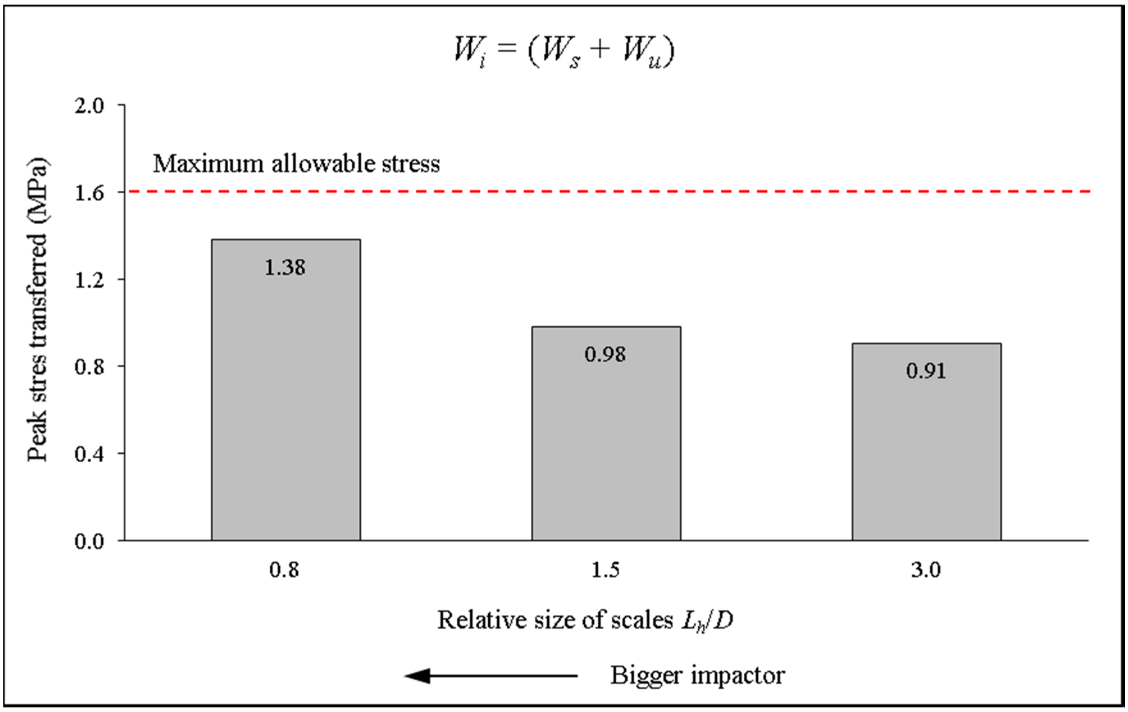

Figure 6.30: Peak stress transferred against relative size L_h/D of scales subject to impact energy $W_i = (W_s + W_u)$ assuming W_u is proportional to D.

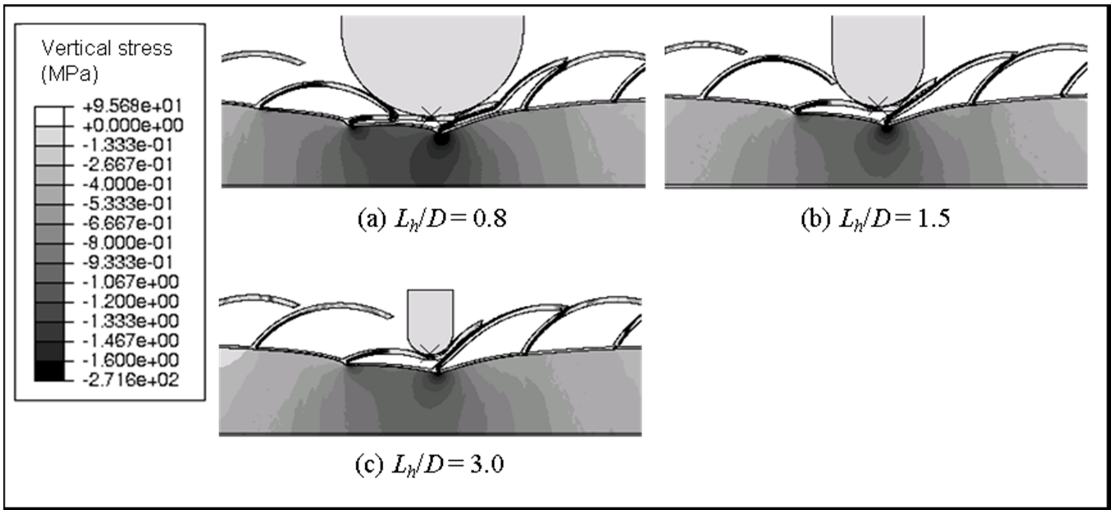

(a) $L_h/D = 0.8$ (b) $L_h/D = 1.5$ (c) $L_h/D = 3.0$

Figure 6.31: Deformation and vertical stress contour for composite specimens with various relative sizes L_h/D of scales at maximum impactor penetration subject to impact energy $W_i = (W_s + W_u)$ assuming W_u is proportional to D.

estimated if the effect of L_h is not taken into account. Therefore, the results prove that the effects of relative size of the scales should be considered in Equation 6.4 in order to provide a better approximation for the maximum amount of energy that can be absorbed by the underlying layer before densification.

The results shown in this section indicate that the maximum energy that can be safely absorbed by the underlying layer can be estimated rather simply and reasonably well using Equations 6.4 to 6.6 by assuming that it is proportional to the thickness and material properties of the underlying layer, as well as the size of the scales or the impactor whichever is bigger. Based on this means of estimating the energy that can be dissipated by the scales and absorbed by the underlying layer, a design procedure for the composite system is proposed in the next section.

6.3 Recommended design procedure

To design the composite system as a protective layer for a given application, the properties of the impactor (namely its impact velocity v, mass M, and size D) and the level of protection required (which can be represented by a limit on the peak stress transferred, above which failure of the protected object is expected to occur) must first to be known and specified for the particular application. Once these are obtained, the design of the fish scale-cellular composite system may be performed. It involves three steps. Firstly, appropriate materials for the scales and underlying cellular layer must be carefully selected to ensure the right combination is used to achieve the desired mechanical behaviour. Thereafter, the amount of materials for the scales and underlying cellular layer needs to be determined to provide sufficient energy absorption capacity. Lastly, the right design configuration of the scales (i.e. their geometrical properties) must be selected such that the scales can deform in the intended manner to perform its energy dissipation role.

6.3.1 Selection of materials for scales and underlying cellular layer

Selection of materials for the scales and underlying layer is governed by two factors. Firstly, since the underlying layer acts as a cushion to minimize the peak stress transferred, the right material must be selected for this underlying layer such that the range of stress transferred does not exceed the allowable limit of the protected surface or object. This can be achieved by choosing a cellular material whose stress value at the densification limit of its compressive stress-strain curve (as explained in Section 5.5) is sufficiently low compared to the allowable limit of the protected surface or object.

Secondly, the assembly of scales must have sufficient stiffness and strength relative to the underlying layer. After the material for the underlying layer is selected, the material used for the scale assembly can be determined based on the optimal ranges for material stiffness and strength ratios proposed in Section 5.3. In addition, the material selected for the scales should have sufficient ductility to deform plastically to absorb the impact energy without fracturing.

6.3.2 Amount of materials for scales and underlying cellular layer

The amount of materials for the scales and underlying cellular layer controls two aspects of the composite system: (a) deformation mode, and (b) amount of impact energy that can be safely absorbed. To achieve the optimal deformation mode, the ratio of the volume V_s of the scales to volume V_u of the underlying layer should fall within the recommended bounds proposed in Table 4.1. As for impact energy, the sum of energy W_s dissipated by the scales (as shown in Section 6.1) and energy absorption capacity W_u of the underlying layer (as defined in Section 6.2) should be greater than energy W_i exerted by the impactor, which is equal to its kinetic energy. Based on the results shown in Figure 4.17, it can be assumed that the ratio of energy absorbed by the underlying layer to that dissipated by the scales (as known as "energy ratio") should not exceed 1.0 such that there is minimal compression on the underlying layer and low peak stress is transferred to the protected surface. Assuming that the right configuration of scales is chosen (as explained in Section 4.5), this ratio can be conservatively assumed as 1.0 even though it is less than this value for many passable cases.

6.3.3 Design configuration of scales

As discussed in Chapter 4, the deformation mode of the fish scale-cellular composite system is governed by the stiffness of the scale assembly relative to the underlying layer. The parameter $K_{geometry}$ was introduced in Section 4.5 to capture this effect and shown to be a function of the geometrical properties of the scales, namely, aspect ratio L_s/t_s, curvature L_s/R, degree of overlapping L_h/S, and relative size L_h/D. The chosen design values for these four geometrical parameters, as well as relative volume V_s/V_u of the scales and $K_{geometry}$, should be within the optimum bounds recommended in Table 4.1 and Figure 5.12. The design configuration of the scales should adhere to these bounds so as to ensure that the scales are able to deform plastically and dissipate a significant proportion of the impact energy instead of collapsing too easily or becoming over-stiff and puncturing into the underlying layer.

6.3.4 Design flow chart

The recommended design procedure is iterative as shown by the flow chart in Figure 6.32. First, an underlying layer material whose compressive stress at its densification limit approximately matches the maximum allowable stress of the protected surface or object is chosen. Then, the material for the scales is selected such that the resulting material stiffness and strength ratios are within the optimal ranges proposed in Section 5.3.

Secondly, given the mass M and impact velocity v of the impactor, the energy W_i that is exerted by the impactor is taken as its kinetic energy given by $0.5Mv^2$. Assuming that this impact energy is to be distributed equally between the scales and underlying layer (i.e. energy ratio of 1.0), the thickness T of underlying layer can be determined using Equations 6.4 to 6.6 by first assuming that $D > L_h$.

Thirdly, the relative volume V_s/V_u, aspect ratio L_s/t_s, curvature L_s/R, and degree of overlapping L_h/S of the scales are chosen based on the optimal ranges proposed in Table 4.1. From the chosen value of V_s/V_u, the volume V_s of scales is determined from which the thickness t_s of the scales is calculated using Equation 6.7 (assuming L_s/S is approximately equal to L_h/S):

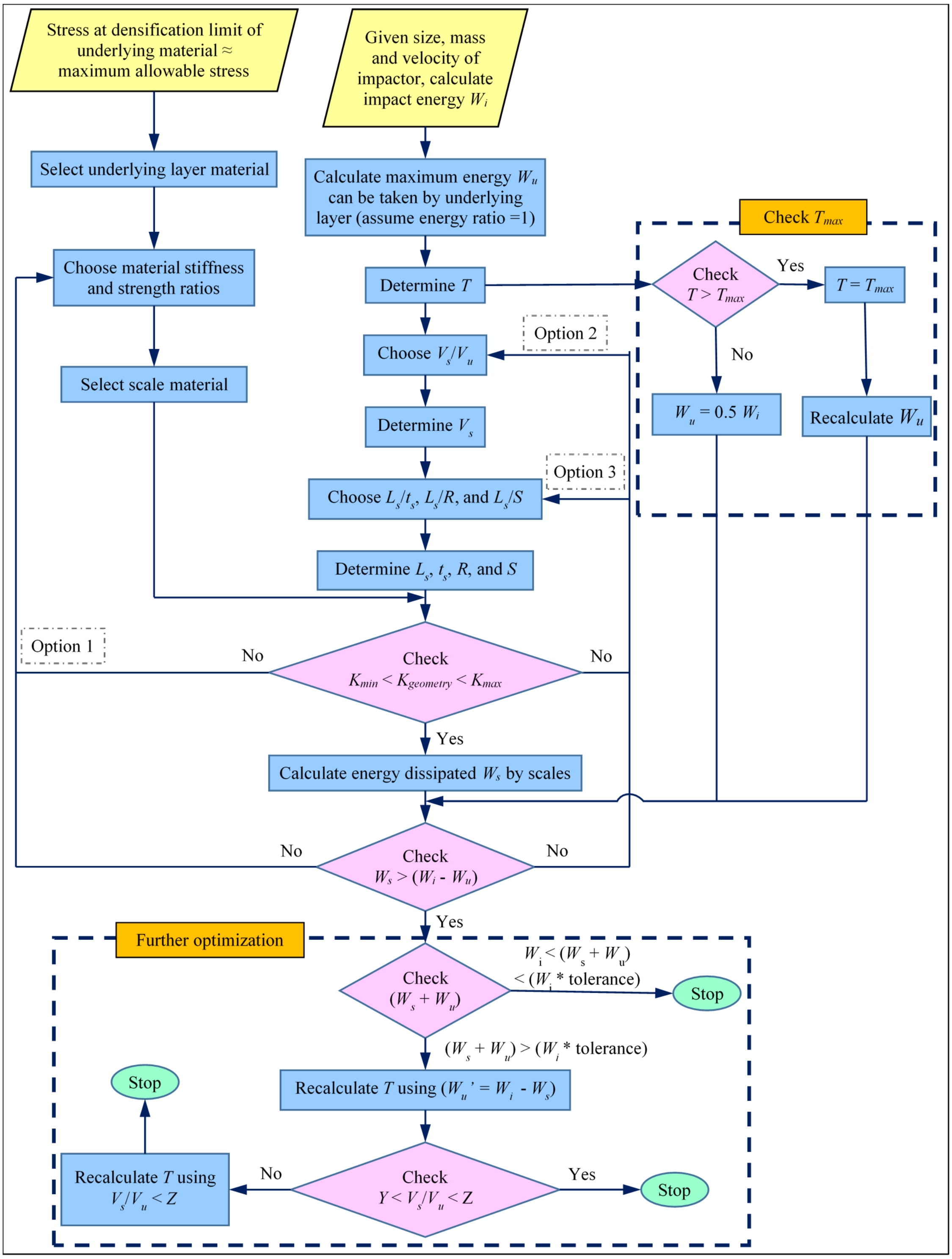

Figure 6.32: Recommended design procedure for fish scale-cellular composite system.

$$V_s = \left(\frac{L_h}{S}\right) \times t_s \tag{6.7}$$

Thereafter, the curved length L_s, radius R, and horizontal spacing S of the scales are calculated using L_s/t_s, L_s/R, and L_h/S that have been selected earlier. The resulting L_h/D ratio is also checked to ensure that it is within the recommended bounds proposed in Table 4.1. Once the geometry of the assembly of scales has been determined, its $K_{geometry}$ value is checked. If the $K_{geometry}$ value falls within the optimum bounds, the design may proceed to the next step. Otherwise, the assembly of scales needs to be redesigned by changing its material, relative volume V_s/V_u, or the geometrical properties mentioned above. These are shown as "Option 1", "Option 2", and "Option 3" in Figure 6.32.

Once the value of $K_{geometry}$ falls within the optimum range, the energy W_s dissipated through plastic deformation of the scales is calculated following the method shown in Section 6.1. If W_s is less than (W_i - W_u), the energy absorption capacity of the composite system is insufficient. Should this occur, there are three alternatives to increase the value of W_s which are shown as "Option 1", "Option 2", and "Option 3" in Figure 6.32. Firstly, the material for the scales can be re-selected such that the yield strength of the scales is increased while maintaining the material strength ratio within its optimal range. Secondly, volume V_s of the scales can be increased by increasing the thickness of the scales while keeping V_s/V_u within its optimal range to prevent the scales from becoming over-stiff. Thirdly, L_s/R and L_h/S can be increased while reducing L_s/t_s (V_s is kept constant) so as to increase the rotation of plastic hinges in the scales when they are deformed. This iterative process is to be continued until W_s exceeds (W_i - W_u). Once this is achieved, the design is complete.

If the total energy dissipated by the scales and absorbed by the underlying cellular layer far exceeds the input energy from the impactor, the composite system is over-designed and might not be cost effective. Further optimization of the design can be done by recalculating the thickness *T* of underlying layer based on the difference between the impact energy W_i and the energy W_s dissipated by the scales. As this new thickness *T* is lower than its original value, the resulting value of V_s/V_u should be checked to ensure it is within its optimal range (denoted by the minimum and maximum bounds *Y* and *Z* respectively in Figure 6.32). If it exceeds the optimal range, the thickness *T* is recalculated based on the value of *Z*, which is the maximum allowable value for V_s/V_u.

Finally, the design procedure depicted in Figure 6.32 also shows an alternative path for scenarios where a limiting value for *T* (denoted as T_{max}) may be imposed because of application-specific factors. If the value of *T* exceeds T_{max}, the latter should be used for the underlying cellular layer. The impact energy that is to be absorbed by the underlying layer would be determined based on T_{max}, while the assembly of scales should be designed to dissipate the remaining impact energy.

6.4 Numerical validation of design procedure

An example was chosen to validate the recommended design procedure numerically. The example may represent a range of scenarios such as barge collision on bridge structures spanning across navigable coastal or inland waterways, vehicle collision on highway structures, and other similar situations.

In the example, the following were assumed for the impactor and the protected object based on Jiang and Chorzepa (2014):

i. Mass *M* of impactor = 168 tons/m
ii. Size *D* of impactor = 2.74 m
iii. Velocity *v* of impactor = 3 m/s

iv. Maximum allowable stress of protected object = 0.5 MPa

Using the design procedure shown in Figure 6.32, the resulting values obtained are shown in Table 6.1. For this example, four iterations were required before the final design was obtained. Polyurethane (PU) foam with density of 48 g/cm^3 was selected as the underlying material in this example; the compressive stress-strain curves of this material is shown in Figure 6.33, and the energy density of this foam is 0.29 MJ/m^3. It was assumed in this example that there is no constraint on the maximum thickness of the underlying layer.

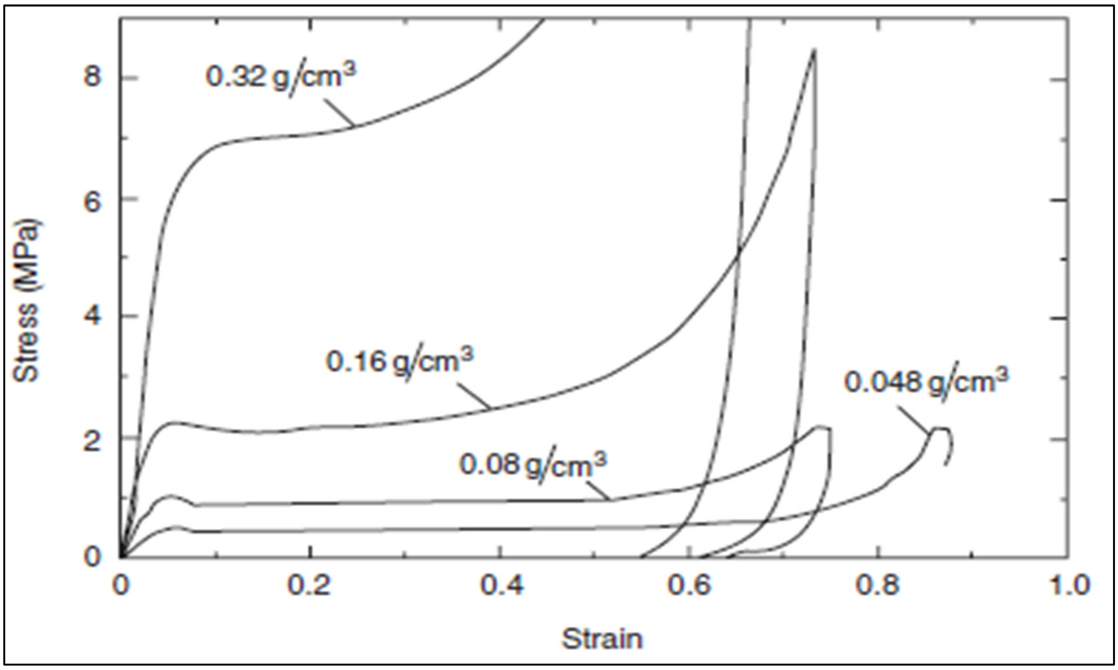

Figure 6.33: Compressive stress-strain curves of closed cell rigid polyurethane foam with different densities (Lu and Yu, 2003).

Table 6.1: Results from design for an example problem.

Design steps	Initial	1st iteration	2nd iteration	3rd iteration	4th iteration
		Reduce material strength ratio to increase K_{max}	Increase V_s/V_u to increase W_s	Change design configuration of scales to increase W_s	Increase V_s/V_u to increase W_s
Choose underlying material	PU foam	PU foam	PU foam	PU foam	PU foam
E_u (MPa)	30	30	30	30	30
σ_u (MPa)	0.5	0.5	0.5	0.5	0.5
Choose material stiffness ratio	5000	5000	5000	5000	5000
Choose material strength ratio	500	250	500	500	500
Choose scale material	Steel	Aluminium	Steel	Steel	Steel
E_s (MPa)	210000	70000	210000	210000	210000
σ_s (MPa)	275	150	275	275	275
K_{min} (x 10^{-3})	0.06	0.10	0.06	0.06	0.06
K_{max} (x 10^{-3})	0.25	0.90	0.25	0.25	0.25
T (m)	0.48	0.48	0.48	0.48	0.48
Choose V_s/V_u	0.13	0.13	0.15	0.13	0.19
V_s ($m^3/m/m$)	0.062	0.062	0.072	0.062	0.091
Choose L_s/t_s	38	38	38	40	38
Choose L_s/R	1.8	1.8	1.8	1.8	1.8
Choose L_h/S	1.85	1.85	1.85	1.85	1.85
L_s (m)	1.000	1.000	1.200	1.000	1.600
R (m)	0.548	0.548	0.657	0.577	0.876
t_s (m)	0.026	0.026	0.031	0.026	0.042
S (m)	0.533	0.533	0.640	0.561	0.853
$K_{geometry}$ (x 10^{-3})	$0.30 > K_{max}$ ☒	$K_{min} < 0.30 < K_{max}$ ☑	$K_{min} < 0.25 < K_{max}$ ☑	$K_{min} < 0.25 < K_{max}$ ☑	$K_{min} < 0.19 < K_{max}$ ☑
W_s (MJ/m)	-	$0.13 < (0.5\ W_i)$ ☒	$0.31 < (0.5\ W_i)$ ☒	$0.23 < (0.5\ W_i)$ ☒	$0.52 > (0.5\ W_i)$ ☑ **(Design 1)**

E_s : Young's modulus of scale material
σ_s : Yield strength of scale material
E_u : Young's modulus of underlying material
σ_u : Average plateau stress of underlying material

The design obtained at the end of the process in Table 6.1 was further optimized since the sum of W_s and W_u exceeded the impact energy W_i by a certain tolerance, which was taken as 20 percent in this example. For this purpose, the thickness T of underlying layer was reduced following the optional steps shown in Figure 6.32:

$W_u' = W_i - W_s = 0.76 - 0.52 = 0.24$ MJ/m

$T = \frac{W_u'}{\text{Energy density} \times D} = \frac{0.24}{0.29 \times 2.74} = 0.30$ m **(Design 2)**

$V_s/V_u = 0.091/0.30 = 0.30 > Z = 0.2$

Since V_s/V_u exceeded the optimal range, the thickness T of underlying layer was increased:

$T = V_s/Z = 0.091/0.2 = 0.46$ m **(Design 3)**

To validate the outcome of the design obtained in Table 6.1, numerical simulations were conducted for Designs 1 to 3 denoted in Table 6.1 and this page. Figure 6.34 shows the deformation of these designs at maximum impactor penetration, while Figures 6.35 to 6.37 present the peak stress transferred, energy dissipated by the scales, and energy absorbed by the underlying layer respectively. The results indicate that Design 1 is a safe design. The peak stress transferred and plastic dissipation of the scales match their expected values; the scales are able to deform and dissipate the impact energy, resulting in minimal compression of the underlying layer as shown in Figure 6.34(a). However, as shown in Figure 6.37, the energy absorbed by the underlying cellular layer is much lower than the estimated capacity confirming that the specimen is over-designed as mentioned earlier.

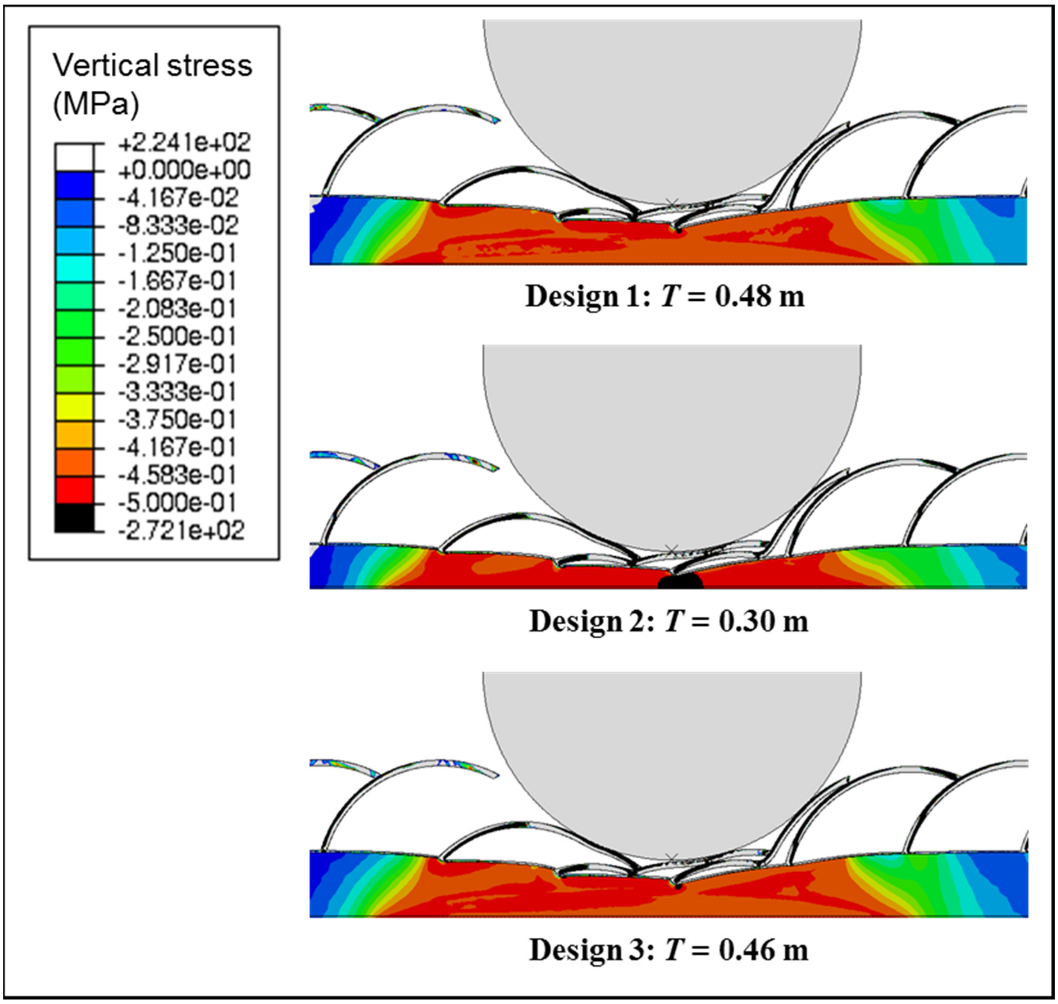

Figure 6.34: Deformation and vertical stress contour for Designs 1, 2, and 3 at maximum impactor penetration.

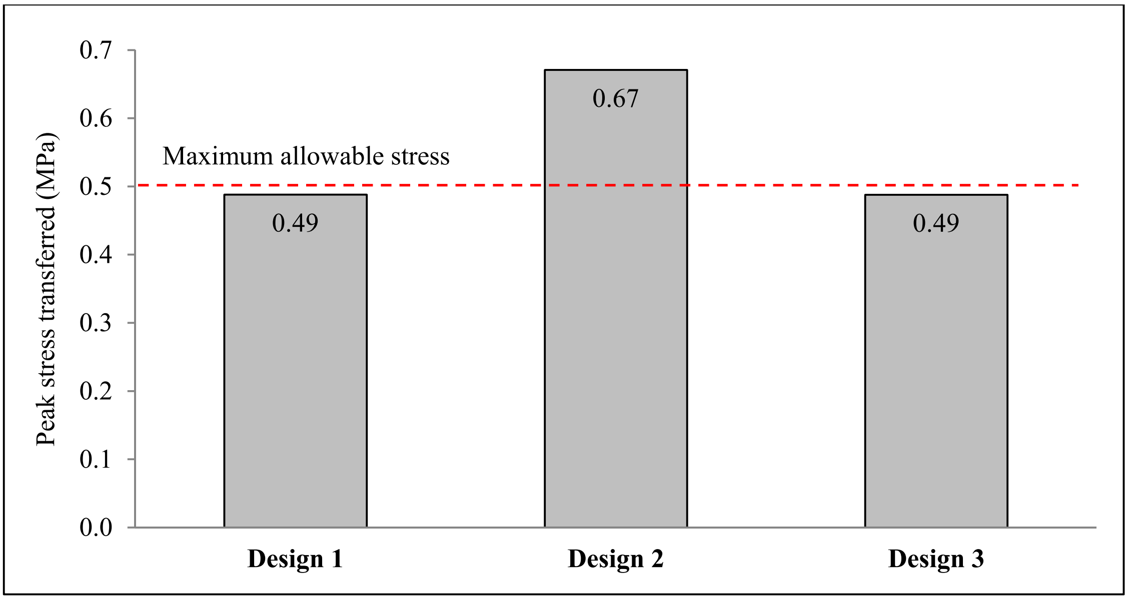

Figure 6.35: Peak stress transferred by Designs 1, 2, and 3.

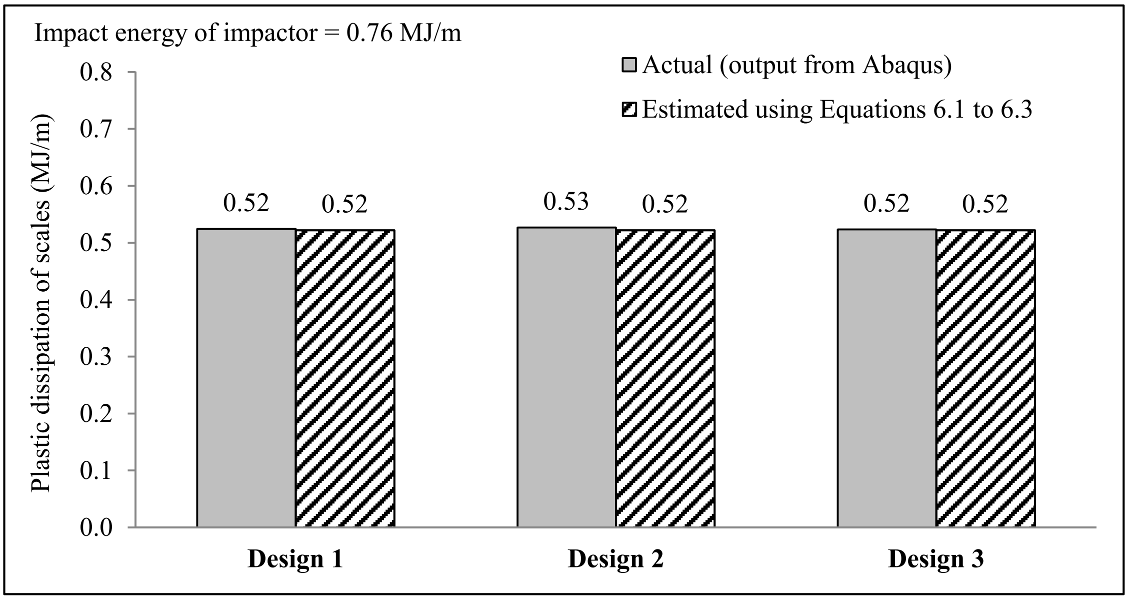

Figure 6.36: Plastic dissipation of scales for Designs 1, 2, and 3.

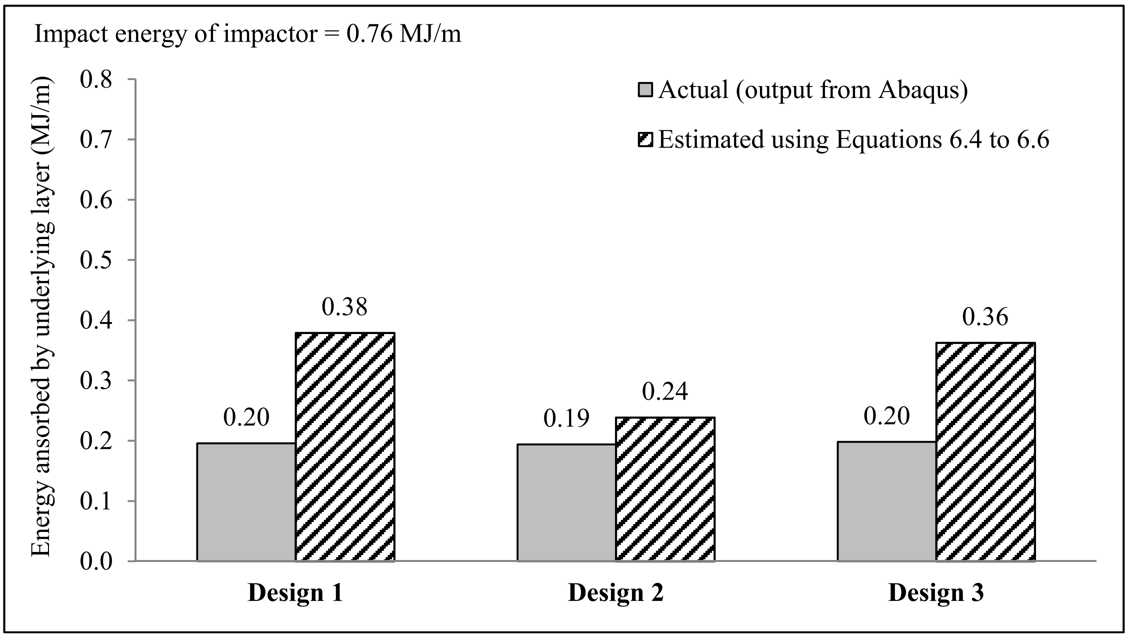

Figure 6.37: Energy absorbed by underlying layer for Designs 1, 2, and 3.

While Design 1 is over-designed, Design 2 has a thinner underlying layer. As shown in Figure 6.35, the peak stress transferred by this specimen is higher than the maximum allowable stress despite the energy absorbed by the underlying layer being lower than its estimated capacity as shown in Figure 6.37. This is because the underlying is too thin (i.e. relative volume V_s/V_u is too high), thus the stress transferred is highly localized around the point of impact instead of being distributed over a wider region of the underlying layer. As a result, densification of the underlying layer underneath the point of impact occurs as shown in Figure 6.34(b).

Lastly, the thickness of the underlying layer was increased such that the value of V_s/V_u falls within the recommended limit of 0.2 (as given in Table 4.1). This case corresponds to Design 3 shown in Figures 6.34 to 6.37. Its peak stress transferred is lower than the maximum allowable stress. Moreover, the impact energy dissipated by the scales is close to the estimated value. The energy absorbed by the underlying layer is lower than its estimated capacity, but the increased thickness of the underlying layer ensures that the peak stress transferred is low. Compared to Design 1, Design 3 which was obtained from the optional steps shown in Figure 6.32 is indeed more efficient as less material is used for the underlying layer. As shown in Figures 6.34(a) and 6.34(c), both Designs 1 and 3 deform in the same manner and the peak stress transferred is kept within the allowable limits even though the underlying layer for Design 3 is thinner.

As a final check, Design 3 is compared with a sandwich specimen (labelled as "Sandwich 1") with the same amount of materials as shown in Figure 6.38. Figure 6.39 shows that the peak stress transferred by Sandwich 1 is double of that of Design 3 and also exceeds the maximum allowable stress. The thick top plate is inefficient in dissipating the impact energy as shown in Figure 6.40, thus the underlying layer is compressed severely which causes it to densify and transfer high stress. In order to keep the stress transferred below the maximum allowable limit, the top plate or the underlying layer of the sandwich specimen needs to be increased as depicted by "Sandwich 2" and "Sandwich 3" respectively in Figure 6.38. The thicker top plate results in more uniform

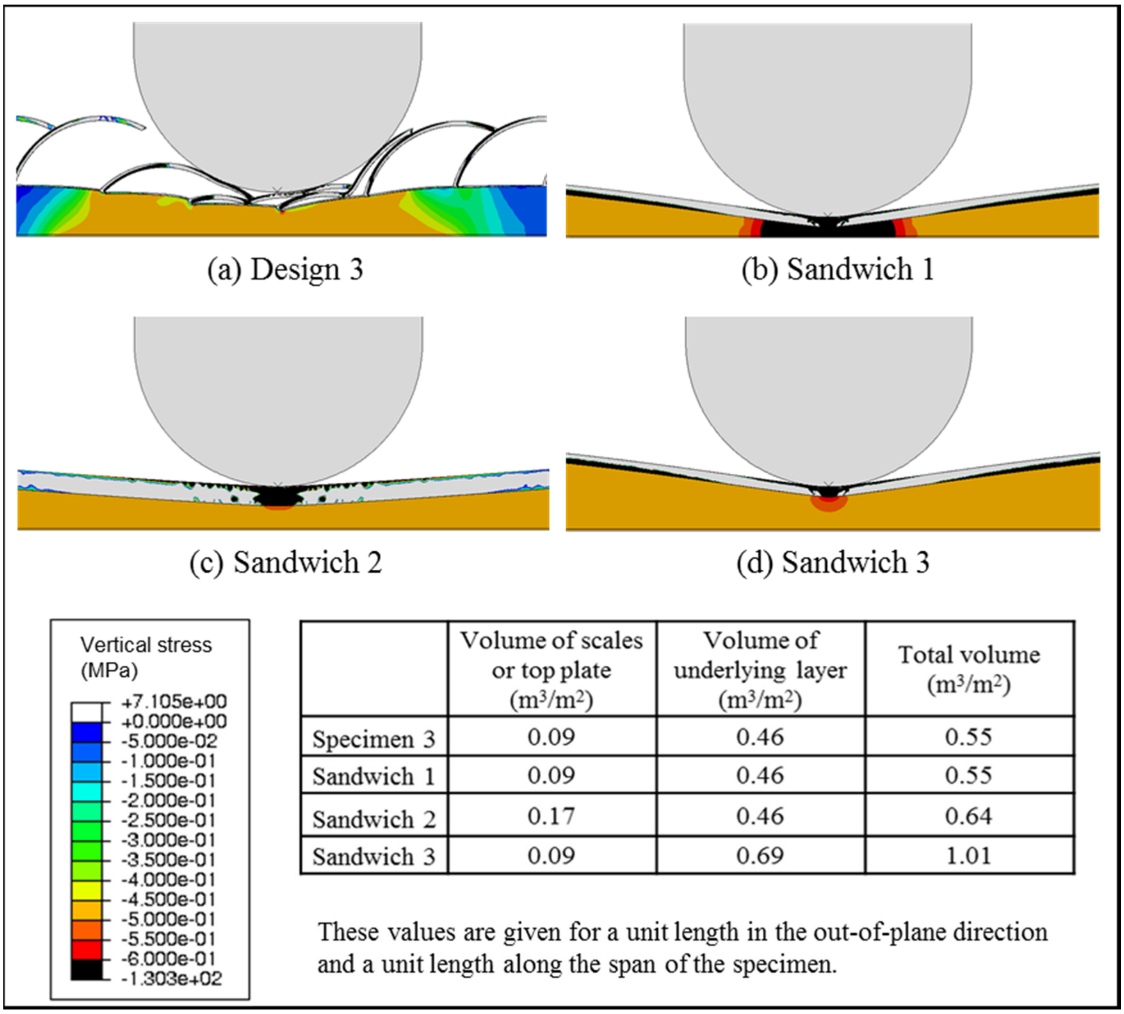
(a) Design 3

(b) Sandwich 1

(c) Sandwich 2

(d) Sandwich 3

	Volume of scales or top plate (m^3/m^2)	Volume of underlying layer (m^3/m^2)	Total volume (m^3/m^2)
Specimen 3	0.09	0.46	0.55
Sandwich 1	0.09	0.46	0.55
Sandwich 2	0.17	0.46	0.64
Sandwich 3	0.09	0.69	1.01

These values are given for a unit length in the out-of-plane direction and a unit length along the span of the specimen.

Figure 6.38: Deformation and vertical stress contour for Design 3 and Sandwich 1, 2, and 3 at maximum impactor penetration.

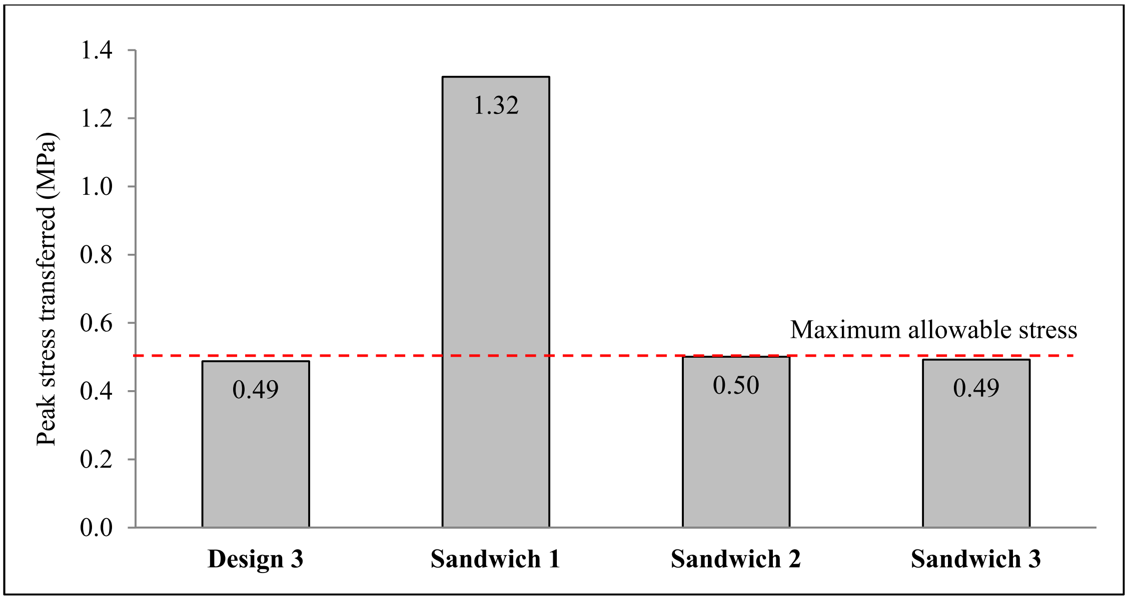

Figure 6.39: Peak stress transferred by Design 3 and Sandwich 1, 2, and 3.

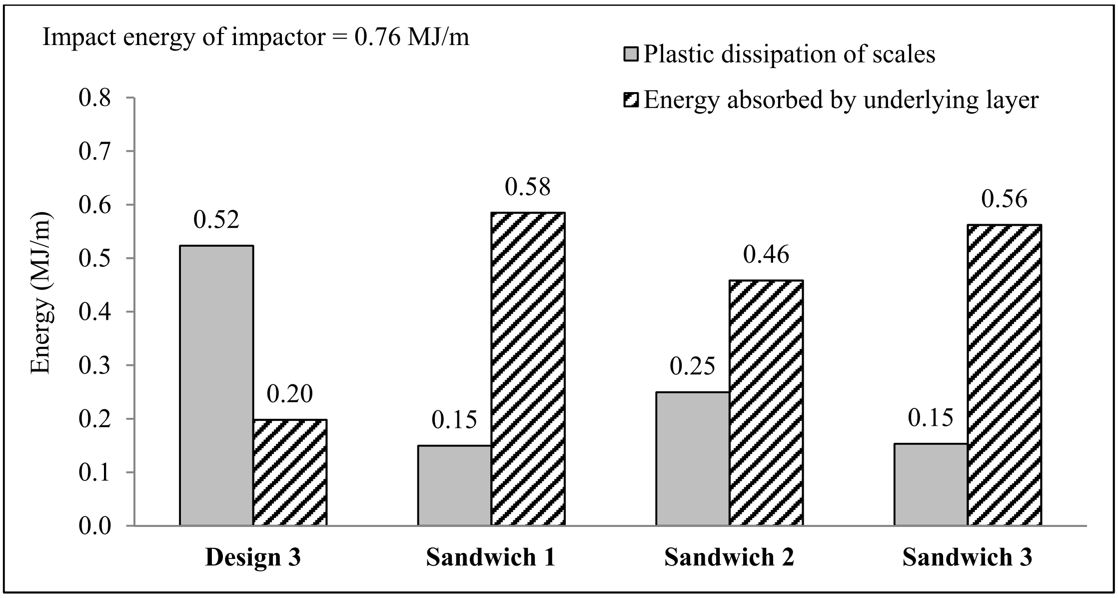

Figure 6.40: Impact energy dissipated by scales or top plate and absorbed by underlying layer for Design 3 and Sandwich 1, 2, and 3.

compression on the underlying layer, while the thicker underlying layer allows the impact force to be distributed over a wider region before it reaches the base of the specimen. Nonetheless, the results shown in Figure 6.40 indicate that most of the impact energy exerted on the sandwich specimens is absorbed by the underlying layer with minor contribution from the top plate, as compared to the scaled specimens where the scales dissipate a very significant proportion of the impact energy. More importantly, to achieve the same impact performance as the fish scale-cellular composite specimen, a higher amount of materials is required for the top plate and underlying cellular layer of a sandwich specimen. As shown in Figure 6.38, the amount of material used for the top plate in Sandwich 2 is approximately 100 percent more than that for the assembly of scales in Design 3, with the same thickness of the underlying layer. On the other hand, the amount of material for the underlying layer in Sandwich 3 is around 50 percent more than that in Design 3, when the same amount of material is used for the top layer of both specimens. These results show that the fish scale-cellular composite system can be more effective and efficient for protection against low-velocity impact compared to conventional sandwich designs.

Therefore, the results presented in this section show that the recommended design procedure is able to produce optimum designs of the fish scale-cellular composite system such that the peak stress transferred to the protected surface does not exceed the maximum allowable stress while minimizing the amount of materials used. The design procedure is the culmination of all the simulations and experiments that have been performed in this study to understand the mechanical behaviour and impact performance of the composite system.

7.0 Conclusions and future work

This chapter summarizes the work that has been completed in this study and lists several areas for future studies.

7.1 Conclusions

In this study, the mechanical behaviour and feasibility of a fish scale-cellular composite system for protection against low-velocity impact were investigated primarily using finite element simulations, supported by experimental work for a number of critical aspects. This composite system has an assembly of overlapping plates (which represent scales) that is underlain by a cellular material layer and used to protect a surface or object from impact. Optimization of this composite system was explored and a design procedure was proposed.

The simulations and experiments that have been performed in this study showed that the composite system resists impact via two primary deformation modes: (a) bending of scales, and (b) compression of underlying layer. The scales dissipate part of the impact energy as they deform, while the remaining energy is absorbed by the underlying cellular layer. The underlying layer should not densify in order to minimize the peak stress transferred to the underside of the composite system. It was shown that the composite system with suitable configuration of curved scales and combination of materials can perform better than a conventional sandwich design with the same amount of materials. This is due to the additional hoop resistance from the curved shape of the scales which allows them to dissipate more energy before they are flattened and the impactor starts compressing on the underlying layer. This minimizes the compression on the underlying layer and hence reduces the peak stress transferred.

The deformation behaviour and impact performance of the composite system are governed by the geometrical and material properties of the scales and underlying cellular layer. The impact performance of the composite system generally improves with decreasing aspect ratio, increasing curvature, increasing degree of overlapping, and decreasing size of the scales. A geometric stiffness factor $K_{geometry}$ which accounts for the combined effects of the four aforementioned parameters was defined. It was shown that there is a range for $K_{geometry}$ which can lead to optimum impact performance. Within this range, the scales are sufficiently stiff so that they do not deform too easily, and yet able to dissipate a significant amount of impact energy. Additionally, the energy dissipated by the scales is higher than that absorbed by the underlying cellular layer for cases within the optimum $K_{geometry}$ range, and the peak stress transferred by the composite system is lower than that of a sandwich design with the same volume of materials. The optimum range for $K_{geometry}$, as well as those for aspect ratio, curvature, degree of overlapping, size, and relative volume of the scales, were found in Chapter 4 and may be used as the basis of designing the assembly of scales of the composite system.

With regards to material properties of the scales and cellular underlying layer, it was found that there are optimum ranges for stiffness and strength of the scales relative to those of the underlying layer so that the scales can deform readily yet dissipate a significant amount of impact energy while inducing minimal compression on the underlying layer. The optimum values for these parameters were determined in Chapter 5. Furthermore, to account for the combined effects of the geometrical and material properties of the scales on the deformation behaviour of composite system, it was found that the optimum range for the geometric stiffness factor $K_{geometry}$ reduces as the yield strength of the scales increases relative to the average plateau stress of the underlying layer.

The compressive stress-strain behaviour and thickness of the underlying cellular layer also affect the range of stress transferred by the composite system, albeit the thickness of the underlying layer does not influence the deformation mode. It was shown that as long as the ratios of stiffness, strength, and volume of the scales to those of the underlying layer fall within their recommended bounds, the peak stress transferred would not exceed the stress at the densification limit of the underlying layer while minimizing the amount of materials for the composite system.

Finally, a design procedure for the composite system was proposed in this study. It involves three key steps, with the size and energy of an impactor and limiting stress of a protected object or surface as input parameters. Firstly, appropriate materials for the scales and underlying cellular layer must be carefully selected to ensure the right combination is used in order to achieve the desired deformation behaviour, as well as to limit the stress transferred within an allowable range. Secondly, the amount of materials for the scales and underlying cellular layer needs to be determined to ensure that the energy absorption capacity of the composite system exceeds the impact energy exerted by the impactor. For this purpose, simple methods to estimate the impact energy that can be safely dissipated by the scales and absorbed by the underlying layer have been proposed. The former can be estimated using plastic analysis based on the initial geometry, yield strength, and thickness of the scales. On the other hand, the latter can be estimated by assuming that the region of the underlying layer underneath the impactor is uniformly compressed while deformation of adjacent regions is negligible – this energy absorption capacity is proportional to the thickness and material properties of the underlying layer, as well as the size of the scales or the impactor whichever is bigger. Thirdly, the right design configuration of the scales (i.e. their geometrical properties) must be selected such that the scales can deform in the intended manner in order to dissipate a significant amount of impact energy.

The design procedure was validated numerically using an example and shown to be able to produce an optimum design of the fish scale-cellular composite system such that the peak stress transferred to the protected surface does not exceed the maximum allowable stress while minimizing the amount of materials used. The produced procedure is the culmination of all the simulations and experiments that have been performed in this study to gain insights into the mechanical behaviour and impact performance of the composite system.

7.2 Recommendations for future work

While this study suggests that the fish scale-cellular composite system has good potential for protection against impact loads, there are several key improvements that can be made in order to improve the accuracy of the numerical model. There are also other aspects of the composite system that may be further explored to optimize its performance.

7.2.1 Improvements to numerical model

In the simulation, the scales were assumed to be elastic-perfectly plastic, that is, there is no tensile rupture. However, depending on the ductility of the material used for the scales, cracks may be formed in the scale assembly when it is subject to impact. The impact performance of the composite system may be severely affected if this occurs as the amount of impact energy that can be dissipated by the scales would most probably be reduced. Therefore, a suitable method to model tensile cracking in the scales needs to be included in the numerical simulations for such cases so that the results are more realistic. This could possibly be achieved by specifying an appropriate tensile failure strain and eroding the damaged elements, or using cohesive elements at critical locations where fracture is expected to occur. Nevertheless, the work required to calibrate these additional properties is not trivial.

7.2.2 Experimental validation with alternative materials for scales and underlying layer

Specimens made with ABS scales and polyethylene foam for underlying layer were used in this study to experimentally validate the impact performance of the composite system as their strength and stiffness ratios fall within the optimum bounds proposed in Chapter 5. Future studies can widen the scope of this experimental validation by exploring other combinations of materials for the scales and underlying layer. Nevertheless, depending on the materials used, fabrication of the specimens may be rather challenging. Moreover, due to time and budgetary constraints, only one configuration with curved scales was tested in this study. However, to more comprehensively validate the impact performance of the composite system, more specimens with various configurations should be tested. This may provide further insight on the best configurations that can be used for real life applications.

7.2.3 Experimental validation of design procedure

In this study, the design procedure was validated using numerical simulations only. Experimental validation was not carried out due to time constraint, limited budget and availability of equipment in the laboratory, as well as limited choice of materials for the scales and underlying layer. Further validation of the design procedure would be ideal. However, the experimental setup and instrumentation must be chosen carefully so that the required range of impact energy and velocity can be achieved and the output parameters (e.g. stress transferred) can be measured reliably and accurately.

7.2.4 Application for specific problems

The purpose of this present study was to explore and understand the mechanical behaviour and feasibility of the fish scale-cellular composite system as a novel protective system against low-velocity impact. However, the conclusions obtained are general and have not been tailored for specific applications. To better evaluate the potential of this composite system, it should be tested for particular applications such as protection of coastal and marine structures against barge collisions, or protection of highway structures from vehicle collision. The different boundary conditions, type and magnitude of loading, and other application issues should be taken into account in the design of the composite structure.

References

3D Matter. (2015). What is The Influence of Infill %, Layer Height and Infill Pattern on My 3D Prints. Retrieved from http://my3dmatter.com.

ABAQUS. (2012). *User's Manual Version 6.12.* Dassault Systémes Simulia Corp., Providence, Rhode Island.

Abrate, S. (1991). Impact on Laminated Composite Materials. *Applied Mechanics Reviews* **44** (4): 155-190.

Abrate, S. (1998). *Impact on Composite Structures*. Cambridge University Press.

Afroughsabet, V. and Ozbakkaloglu, T. (2015). Mechanical and Durability Properties of High-Strength Concrete Containing Steel and Polypropylene Fibers. *Construction and Building Materials* **94**: 73-82.

Ajdari, A., Canavan, P., Nayeb-Hashemi, H. and Warner, G. (2009). Mechanical Properties of Functionally Graded 2D Cellular Structures: A Finite Element Simulation. *Material Science and Engineering* **499** (1-2): 434-439.

Anjos, O., Pereira, H. and Rosa, M. E. (2008). Effect of Quality, Porosity and Density on The Compression Properties of Cork. *Holz Roh- Werkst* **66** (4): 295–301.

Barthelat, F. (2007). Biomimetics for Next Generation Materials. *Philosophical Transactions of the Royal Society of London A: Mathematical, Physical and Engineering Sciences* **365** (1861): 2907-2919.

Browning, A. (2012). *Mechanics and Design of Flexible Composite Fish Armour* (Doctoral Thesis). Massachusetts Institute of Technology.

Cantwell, W. J. and Morton, J. (1991). The Impact Resistance of Composite Materials — a Review. *Composites* **22** (5): 347-362.

Castro, O., Silva, J. M., Devezas, T., Silva, A. and Gil, L. (2010). Cork Agglomerates as An Ideal Core Material in Lightweight Structures. *Material and Design* **31** (1): 425-432.

Chen, P.-Y., Schirer, J., Simpson, A., Nay, R., Lin, Y.-S., Yang, W., Lopez, M. I., Li, J., Olevsky, E. A. and Meyers, M. A. (2012). Predation versus Protection: Fish Teeth and Scales Evaluated by Nanoindentation. *Journal of Materials Research* **27** (1): 100-112.

Dancygier, A. N. and Yankelevsky, D. Z. (1996). High Strength Concrete Response to Hard Projectile Impact. *International Journal of Impact Engineering* **18** (6): 583-599.

Daniel, I. (2010). Impact Response and Damage Tolerance of Composite Sandwich Structures. *Dynamic Failure of Materials and Structures.* Springer US.

de Sousa, R. A., Gonçalves, D., Coelho, R. and Teixeira-Dias, F. (2012). Assessing The Effectiveness of A Natural Cellular Material used as Safety Padding Material in Motorcycle Helmets. *Simulation* **88** (5): 580-591.

Dvorak, G. J. and Suvorov, A. P. (2006). Protection of Sandwich Plates from Low-velocity Impact. *Journal of Composite Materials* **40** (15): 1317-1331.

Flores-Johnson, E. A. and Li, Q. M. (2010). Low Velocity Impact on Polymeric Foams. *Journal of Cellular Plastics* **47** (1): 45-63.

Fortes, M. A. and Rosa, M. E. (1992). Growth Stresses and Strains in Cork. *Wood Science and Technology* **26** (4): 241-258.

Fortes, M. A., Rosa, M. E. and Pereira, H. (2004). *Cork*. IST Press, Lisboa, Portugal.

Gameiro, C. P. and Cirne, J. (2007). Dynamic Axial Crushing of Short to Long Circular Aluminium Tubes with Agglomerate Cork Filler. *International Journal of Mechanical Sciences* **49** (9): 1029-1037.

Gameiro, C. P., Cirne, J. and Gary, G. (2007). Experimental Study of The Quasi-Static and Dynamic Behaviour of Cork under Compressive Loading. *Journal of Materials Science* **42** (12): 4316-4324.

Gibson, L. J. (1989). Modelling The Mechanical Behavior of Cellular Materials. *Materials Science and Engineering*: *A* **110**: 1-36.

Gibson, L. J. and Ashby, M. F. (1997). *Cellular Solids — Structure and Properties, 2nd Edition*. Cambridge University Press, Cambridge.

Gibson, L. J., Ashby, M. F. and Harley, B. A. (2010). *Cellular Materials in Nature and Medicine.* Cambridge University Press, Cambridge.

Green, S. J., Schierloh, F. L., Perkins, R. D. and Babcock, S. G. (1969). High-Velocity Deformation Properties of Polyurethane Foams. *Experimental Mechanics* **9** (3): 103-109.

Han, F., Zhu, Z., and Gao, J. (1998). Compressive Deformation and Energy Absorbing Characteristic of Foamed Aluminum. *Metallurgical and Materials Transactions A* **29** (10): 2497-2502.

Herrington, P. D. and Latorre, R. G. (1998). Development of An Aluminium Hull Panel for High-speed Craft. *Marine Structures* **11** (1–2): 47-71.

Jiang, H. and Chorzepa, M. G. (2014). Evaluation of A New FRP Fender System for Bridge Pier Protection against Vessel Collision. *Journal of Bridge Engineering* **20** (2): 05014010.

Jones, N., Birch, R. S. and Duan, R. (2008). Low-Velocity Perforation of Mild Steel Rectangular Plates with Projectiles Having Different Shaped Impact Faces. *Journal of Pressure Vessel Technology* **130** (3): 031206.

Jones, N. and Paik, J. K. (2012). Impact Perforation of Steel Plates. *Ships and Offshore Structures* **8** (5): 579-596.

Joshi, S. P. and Sun, C. T. (1987) Impact-Induced Fracture Initiation and Detailed Dynamic Stress Field in the Vicinity of the Impact (Retroactive Coverage). *American Society for Composites Second Technical Conference*: 177-185.

Kasten, M. (2010). Strength of Aluminum versus Strength of Steel. Retrieved from http://www.kastenmar ine.com/alumVSsteel.htm.

Kim, S. (2011). *A Study on Cork-based Plastic Composite Material* (Doctoral Thesis). Massachusetts Institute of Technology.

Lamb, T. and Beavers, N. (2010). The All Aluminum Naval Ship – The Way to Affordable Naval Ships. *10th International Naval Engineering Conference and Exhibition: HM Naval Base, Portsmouth, United Kingdom.*

Lepareux, M., Jamet, P. H., Matheron, P. H., Lieutenant, J. L., Couilleaux, J., Duboelle, D. and Aguilar, J. (1989). Experimental and Numerical Studies of Impacts on Stainless Steel Plates Subjected to Rigid Missiles at Low Velocity. *Nuclear Engineering and Design* **115** (1): 105-112.

Liew, J. Y. R., Sohel, K. M. A. and Koh, C. G. (2009). Impact Tests on Steel–Concrete–Steel Sandwich Beams with Lightweight Concrete Core. *Engineering Structures* **31** (9): 2045-2059.

Liu, D. and Malvern, L. E. (1987) Matrix Cracking in Impacted Glass/Epoxy Plates. *Journal of Composite Materials* **21** (7): 594-609.

Lu, G. and Yu, T. X. (2003). *Energy Absorption of Structures and Materials.* Woodhead Publishing, England.

Luo, X., Sun W. and Chan, S. Y. N. (2000). Characteristics of High-Performance Steel Fiber-Reinforced Concrete Subject to High Velocity Impact. *Cement and Concrete Research* **30** (6): 907-914.

Maji, A. K., Schreyer, H. L., Donald, S., Zuo, Q. and Satpathi, D. (1995). Mechanical Properties of Polyurethane-Foam Impact Limiters. *Journal of Engineering Mechanics* **121** (4): 528-540.

Marar, K., Eren, Ö. and Celik, T. (2001). Relationship between Impact Energy and Compression Toughness Energy of High-Strength Fiber-Reinforced Concrete. *Materials Letters* **47** (4–5): 297-304.

Masso-Moreu, Y. and Mills, N.J. (2004). Rapid Hydrostatic Testing of Rigid Polymer Foams. *Polymer Test* **23**: 313–322.

Meinecke, E. A. and Schwaber, D. M. (1971). Energy Absorption in Polymeric Foams: II--Prediction of Impact Behaviour from Instronc Data for Foam with Rate-Dependent Modulus. *Journal of Applied Polymer Science* **15**: 2381-2393.

Mohotti, D., Ali, M., Ngo, T., Lu, J., Mendis, P. and Ruan, D. (2013). Out-of-plane Impact Resistance of Aluminium Plates Subjected to Low Velocity Impacts. *Materials and Design* **50**: 413-426.

Moreira, R. A. S., de Melo, F. J. Q. and Rodrigues, J. F. D. (2010). Static and Dynamic Characterization of Composition Cork for Sandwich Beam Cores. *Journal of Materials Science* **45** (12): 3350-3366.

Miles, P. (2011, August). Inspired, Naturally. *Financial Times.* Retrieved from http://www.ft.com/cms/s/2/37bb18a2-bea7-11e0-ab21-00144feabdc0.html.

Naik, N. K. and Shrirao, P. (2004). Composite Structures under Ballistic Impact. *Composite Structures* **66** (1–4): 579-590.

O'Neil, E., Neeley, B. and Cargile, J. (1999). Tensile Properties of Very-High-Strength Concrete for Penetration-resistant Structures. *Shock and Vibration* **6** (5): 237-245.

Oh, W. T. (2013). *Fishscale Structure Inspired System for Protection against Projectile Impact* (Bachelor's Thesis). National University of Singapore.

Pereira, H. (2007). *Cork*. Elsevier Science B.V. Amsterdam.

Pereira, H., Rosa, M. E. and Fortes, M. A. (1987). The Cellular Structure of Cork from Quercus Suber L. *IAWA Journal* **8** (3): 213-218.

Pina, P. and Fortes, M. A. (1996). Characterization of Cells in Cork. *Journal of Physics D: Applied Physics* **29** (9): 2507.

Qian, C. X. and Stroeven, P. (2000). Development of Hybrid Polypropylene-Steel Fibre-Reinforced Concrete. *Cement and Concrete Research* **30** (1): 63-69.

Richard, P. and Cheyrezy, M. (1995). Composition of Reactive Powder Concretes. *Cement and Concrete Research* **25** (7): 1501-1511.

Riera, J. D. (1980). A Critical Reappraisal of Nuclear Power Plant Safety against Accidental Aircraft Impact. *Nuclear Engineering and Design* **57** (1): 193-206.

Rizov, V. I. (2007). Low Velocity Localized Impact Study of Cellular Foams. *Materials and Design* **28** (10): 2632-2640.

Rosa, M. E. and Fortes, M. A. (1991). Deformation and Fracture of Cork in Tension. *Journal of Materials Science* **26**(2): 341-348.

Rudykh, S., Ortiz, C., and Boyce, M. C. (2015). Flexibility and Protection by Design: Imbricated Hybrid Microstructures of Bio-Inspired Armor. *Soft Matter* **11** (13): 2547-2554.

Sanchez-Saez, S., Barbero, E. and Cirne, J. (2011). Experimental Study of Agglomerated-cork-cored Structures Subjected to Ballistic Impacts. *Materials Letters* **65** (14): 2152-2154.

Sharma, H., Hurlebaus, S. and Gardoni, P. (2012). Performance-Based Response Evaluation of Reinforced Concrete Columns Subject to Vehicle Impact. *International Journal of Impact Engineering* **43**: 52-62.

Shim, V. P. W. and K. Y. Yap. (1997). Modelling Impact Deformation of Foam-Plate Sandwich Systems. *International Journal of Impact Engineering* **19** (7): 615-636.

Shivakumar, K. N., Elber, W. and Illg, W. (1985). Prediction of Low-Velocity Impact Damage in Thin Circular Laminates. *AIAA Journal* **23** (3): 442-449.

Silva, S., Sabino, M., Fernandes, E., Correlo, V., Boesel, L. and Reis, R. (2005). Cork: Properties, Capabilities and Applications. *International Materials Reviews* **50** (6): 345-365.

Sjoblom, P. O., Hartness, H. J. and Cordell, T. M. (1988). On Low-Velocity Impact Testing of Composite Materials. *Journal of Composite Materials* **22** (1): 30-52.

Soares, B., Reis, L. and Sousa, L. (2011). Cork Composites and Their Role in Sustainable Development. *Procedia Engineering* **10**: 3214-3219.

Song, J., Ortiz, C. and Boyce, M. C. (2011). Threat-protection Mechanics of An Armoured Fish. *Journal of the Mechanical Behavior of Biomedical Materials* **4** (5): 699-712.

Song, P. S. and Hwang, S. (2004). Mechanical Properties of High-Strength Steel Fiber-Reinforced Concrete. *Construction and Building Materials* **18** (9): 669-673.

Sousa-Martins, J., Kakogiannis, D., Coghe, F., Reymen, B. and Teixeira-Dias, F. (2012). Behaviour of Sandwich Structures with Cork Compound Cores Subjected to Blast Waves. *Engineering Structures* **46**: 140-146.

Svensson, H. (2009). Protection of Bridge Piers against Ship Collision. *Steel Construction* **2** (1): 21-32.

Tsartsaris, N., Meo, M., Dolce, F., Polimeno, U., Guida, M. and Marulo, F. (2011). Low-Velocity Impact Behavior of Fiber Metal Laminates. *Journal of Composite Materials* **45** (7): 803-814.

Vernerey, F. J. and Barthelat, F. (2010). On The Mechanics of Fishscale Structures. *International Journal of Solids and Structures* **47** (17): 2268-2275.

Vinson, J. R. (1999). *The Behavior of Sandwich Structures of Isotropic and Composite Materials.* Technomic Publishing Company Inc., United States of America.

Wang, J., Waas, A. M. and Wang, H. (2013). Experimental and Numerical Study on The Low-Velocity Impact Behavior of Foam-Core Sandwich Panels. *Composite Structures* **96**: 298-311.

Yang, W., Chen, I. H., McKittrick, J. and Meyers, M. A. (2012). Flexible Dermal Armour in Nature. *Journal of Materials* **64** (4): 475-485,444-445.

Yang, W., Chen, I. H., Gludovatz, B., Zimmermann, E. A., Ritchie, R. O. and Meyers, M. A. (2013). Natural Flexible Dermal Armour. *Advanced Materials* **25** (1): 31-48.

Yang, W., Sherman, V. R., Gludovatz, B., Mackey, M., Zimmermann, E. A., Chang, E. H. and Meyers, M. A. (2014). Protective Role of Arapaima Gigas Fish Scales: Structure and Mechanical Behavior. *Acta Biomaterialia*, **10** (8): 3599-3614.

Zhu, S. (2012). *Composite Sandwich Panels Subjected to Impact of A Foreign Body* (Doctoral Thesis). Nanyang Technology University.

Appendix A: Selection of material model for underlying cellular layer

An appropriate material model must be chosen for the underlying cellular layer so that its mechanical response can be represented accurately in the finite element simulations. In this study, agglomerated cork was selected as the first candidate for the underlying cellular material due to its high compressibility and energy absorption capacity. However, there have been very few past studies which involved numerical simulations of cork. Hence, in order to determine the most appropriate material model for cork and also to calibrate this material model, experimental tests were carried out to determine the constitutive behaviour of the cork material used in this study and the results were compared with the numerical predictions.

A.1. Experimental stress-strain response

To determine the constitutive behaviour of the cork material that was used in this study, dynamic uniaxial compression tests were carried out on cork specimens measuring 50 mm x 50 mm x 50 mm. The mass density of these specimens was 180 kg/m^3 while the average cork granule size was 4 mm to 6 mm. The specimens were tested using a drop-weight impact machine as depicted in Figure A.1. They were subject to uniform compression from a steel compression platen dropped from a height of 156 cm. The compressive stress applied on the specimen was determined using the force exerted on the specimen (which is the product of acceleration measured using an accelerometer that was attached to the drop weight and mass of the drop weight) divided by its original cross-sectional area. On the other hand, the compressive strain of the specimen was estimated using the images taken by a high-speed camera, and is defined as its deformation divided by its original height or thickness.

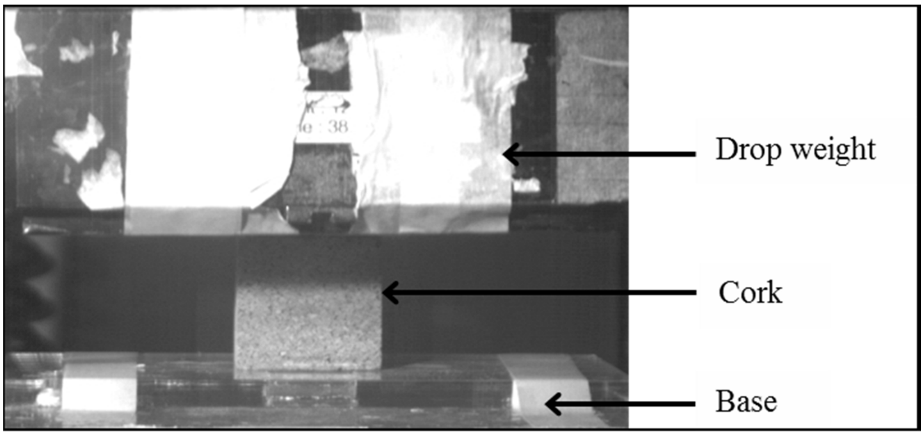

Figure A.1: Experimental setup for dynamic uniaxial compressive test of cork.

Besides dynamic uniaxial compression tests, quasi-static compression tests were also conducted on the same cork and PE foam specimens using an Instron 5969 universal testing machine. The compression force applied on the specimens as well as the deformation of the specimens were measured by the testing machine. They were then divided by the initial cross-sectional area and thickness of the specimens to obtain the compressive stress and strain values of the specimens.

The quasi-static and dynamic compressive stress-strain response of this cork material is shown in Figure A.2. It can be observed that the stress-strain response of the cork under both loading conditions shows the three distinct deformation stages typical of cellular materials: (a) linear elastic, (b) plateau, and (c) densification. The Young’s modulus of the cork is 88 MPa, but its linear elastic region is not distinct. Nevertheless, it is compressible and can undergo a large deformation of up to compressive strains of 60 percent and 70 percent under dynamic and quasit-static conditions, respectively, while showing gradual increase in stress. As a result, the cork material can absorb relatively high amount of energy while maintaining low stress. Beyond the aforementioned limits of compressive strain, the compressive stress increases dramatically as densification occurs. However, it is shown in Figure A.2 that the dynamic plateau stress of the cork material used in this study is significantly higher than the static one. This agrees with the results reported by Gameiro *et al*. (2007).

Furthermore, there was no observable lateral deformation of the cork specimens until they were almost fully densified. Consequently, the Poisson's ratio of the cork may be assumed to be zero.

On the other hand, since the uniaxial tensile stress-strain data of the cork used in this study was not available, the tensile behaviour of cork was assumed to follow that reported by Moreira *et al.* (2010) as shown in Figure 1.16 (repeated here in Figure A.3 for convenience). The tensile stiffness of cork is generally higher than its compressive stiffness, but it does not have a plateau region.

Thus, a material model for cork must be able to capture the large deformation behaviour under compression as well as densification that occurs at large compressive strains, while also accounting for the different properties under compressive and tensile stresses. In general, these requirements also apply to other cellular materials. Based on these requirements, there are three possible material models in Abaqus that could be used for cellular materials such as cork: (a) hyperfoam, (b) low-density foam, and (c) crushable foam. To determine the most appropriate material model for the cork material used in this study, the dynamic stress-strain data shown in Tables A.1 and A.2 were used as input and compared with the numerical predictions. Since the same impact velocity was used for all cases in the simulation, it was assumed that the stress-strain data of the cork material used in this study was rate-dependent despite the difference between its dynamic and quasi-static behaviours.

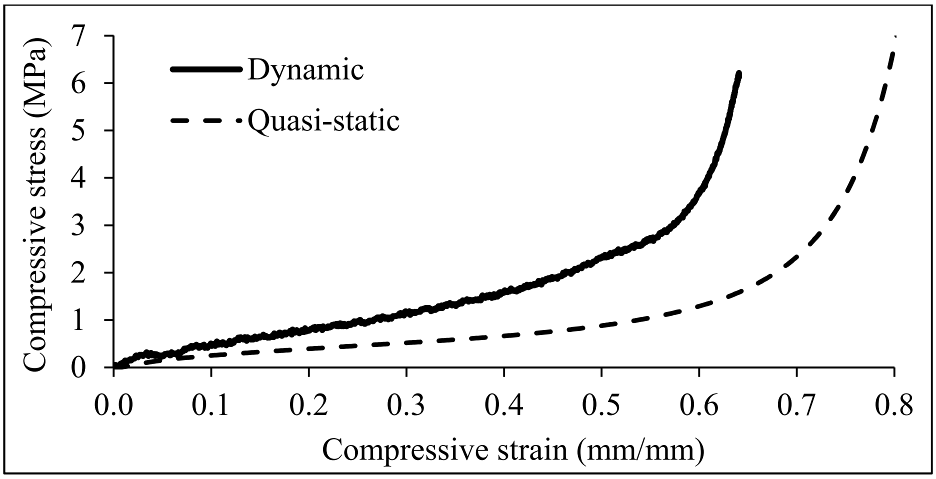

Figure A.2: Compressive stress-strain curve of cork from experiment.

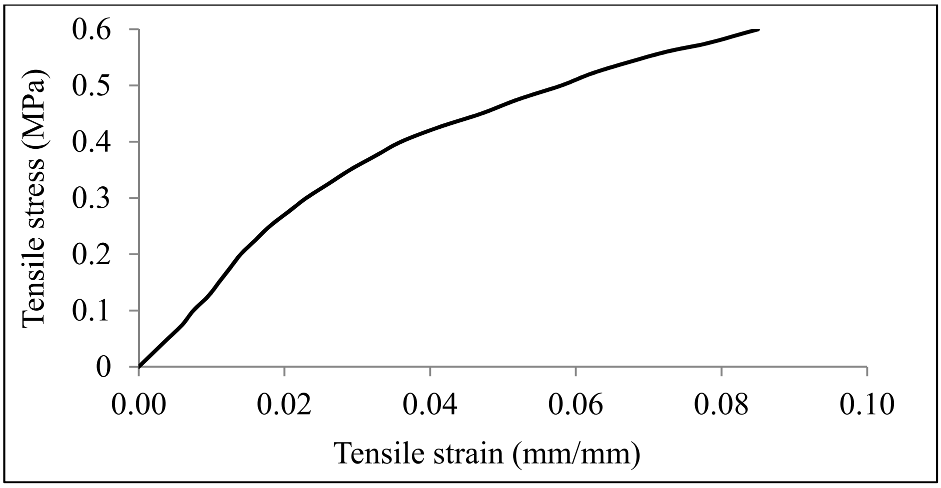

Figure A.3: Tensile stress-strain curve of cork (Moreira *et al.*, 2010).

Table A.1: Dynamic compressive stress-strain data of cork from experiment.

Stress (MPa)	Strain (mm/mm)
0.000	0.000
0.093	0.011
0.147	0.012
0.187	0.020
0.240	0.030
0.253	0.041
0.253	0.050
0.307	0.060
0.333	0.071
0.413	0.080
0.440	0.090
0.453	0.101
0.520	0.110
0.493	0.121
0.640	0.130
0.587	0.140
0.640	0.151
0.640	0.160
0.733	0.171
0.773	0.181
0.720	0.190
0.773	0.200
0.827	0.210
0.840	0.220
0.867	0.230
0.920	0.240
0.960	0.250
0.960	0.260
1.053	0.271
1.053	0.281
1.093	0.290
1.173	0.301
1.160	0.310
1.253	0.320
1.253	0.331
1.333	0.341
1.293	0.351
1.413	0.361
1.427	0.370
1.493	0.380
1.480	0.390
1.627	0.401
1.667	0.420
1.760	0.431
1.827	0.440
1.880	0.451
1.933	0.460
2.013	0.471
2.147	0.480
2.187	0.490
2.333	0.500
2.360	0.505
2.347	0.510
2.453	0.515
2.453	0.520
2.467	0.525
2.547	0.530
2.573	0.535
2.587	0.540
2.640	0.545
2.733	0.550
2.733	0.555
2.840	0.560
2.893	0.565
2.920	0.570
3.040	0.576
3.133	0.580
3.267	0.585
3.400	0.590
3.440	0.593
3.493	0.595
3.573	0.597
3.613	0.598
3.627	0.598
3.627	0.598
3.640	0.599
3.680	0.599
3.680	0.600
3.667	0.600
3.693	0.600
3.693	0.601
3.747	0.601

Stress (MPa)	Strain (mm/mm)
3.747	0.603
3.787	0.603
3.800	0.604
3.840	0.605
3.827	0.605
3.893	0.606
3.920	0.607
3.947	0.608
3.960	0.608
3.973	0.609
4.027	0.609
4.013	0.610
4.053	0.610
4.107	0.611
4.120	0.611
4.133	0.612
4.147	0.612
4.173	0.612
4.160	0.613
4.200	0.613
4.240	0.614
4.253	0.615
4.280	0.615
4.307	0.616
4.373	0.616
4.413	0.617
4.467	0.618
4.507	0.619
4.547	0.620
4.587	0.621
4.613	0.621
4.653	0.622
4.720	0.622
4.733	0.623
4.747	0.624
4.800	0.624
4.827	0.625
4.867	0.625

Stress (MPa)	Strain (mm/mm)
4.880	0.625
4.933	0.626
4.960	0.627
4.973	0.627
5.013	0.627
5.040	0.627
5.080	0.628
5.107	0.628
5.120	0.629
5.133	0.629
5.173	0.629
5.253	0.630
5.253	0.631
5.307	0.631
5.347	0.631
5.307	0.631
5.347	0.631
5.347	0.632
5.413	0.632
5.440	0.632
5.453	0.632
5.507	0.633
5.533	0.633
5.600	0.634
5.680	0.635
5.720	0.635
5.773	0.636
5.813	0.637
5.867	0.637
5.920	0.637
5.960	0.638
6.000	0.639
6.040	0.639
6.080	0.639
6.120	0.640
6.160	0.640
6.187	0.641
6.200	0.641

Table A.2: Tensile stress-strain data of cork (Moreira *et al*., 2010).

Stress (MPa)	Strain (mm/mm)
0.000	0.000
0.025	0.002
0.050	0.004
0.075	0.006
0.100	0.008
0.125	0.010
0.150	0.011
0.175	0.013
0.200	0.014
0.225	0.016
0.250	0.018
0.275	0.021
0.300	0.023
0.325	0.026
0.350	0.029
0.375	0.033
0.400	0.036
0.425	0.041
0.450	0.047
0.475	0.052
0.500	0.058
0.525	0.063
0.559	0.072
0.575	0.078
0.600	0.085

A.2. Hyperfoam

Hyperfoam is an isotropic, nonlinear hyperelastic material model that is normally used for cellular solids that have high porosities and can undergo very large volumetric changes. Hence, it is suitable for materials with high compressibility as it allows for large elastic strains of up to 90 percent under compression. Hyperfoam is commonly used to model cushions, padding, and packaging materials that have high energy absorption capacities. For instance, de Sousa *et al.* (2012) used hyperfoam to model cork as a safety padding material in motorcycle helmets.

In a hyperelastic model, the stresses are not calculated directly from strain values as is the case for small strain linear elastic materials. Instead, the stresses are derived from the principle of virtual work using the strain energy function U as (ABAQUS, 2012):

$$\boldsymbol{U} = \sum_{i=1}^{N} \frac{2\mu_i}{\alpha_i^2}\left[\hat{\boldsymbol{\lambda}}_1^{\alpha_i} + \hat{\boldsymbol{\lambda}}_2^{\alpha_i} + \hat{\boldsymbol{\lambda}}_3^{\alpha_i} - 3 + \frac{1}{\beta_i}\left(\left(J^{e\ell}\right)^{-\alpha_i\beta_i} - 1\right)\right] \tag{A.1}$$

where N is the strain energy potential order which is a material parameter; μ_i, α_i, and β_i are temperature-dependent material parameters; $\hat{\lambda}_i$ are the principal stretches; and $J^{e\ell} = \hat{\lambda}_1\hat{\lambda}_2\hat{\lambda}_3$ is the measure of the relative volume.

For each term in the energy function, the coefficients β_i determine the degree of compressibility. They are related to the Poisson's ratio, v_i, by the expressions

$$\boldsymbol{\beta_i} = \frac{v_i}{1-2v_i} \tag{A.2}$$

$$\boldsymbol{v_i} = \frac{\beta_i}{1+2\beta_i} \tag{A.3}$$

To calibrate this material model, the material parameters μ_i, α_i, and β_i in the strain energy function U can be defined directly or obtained experimentally. Where experimental data is available, these parameters can be determined using a least-squares-fit procedure in Abaqus. For the hyperfoam model, five types of experimental stress-strain data could be specified: uniaxial, biaxial, simple shear, planar, and volumetric tests. However, generally only experimental data for the dominant deformation modes are required, in particular those for uniaxial compression or tension and simple shear. This means that only either uniaxial compression data or uniaxial tension data, whichever dominates in the deformation, is used as input. In this study, only uniaxial compressive data was used since the cork was subject primarily to compression. The Poisson's ratio was assumed to be zero. Simple shear data was not provided since it was not available.

A.3. Low-density foam

The low-density foam material model is intended for low-density, highly compressible elastomeric foams with significant rate sensitive behaviour, such as those widely used in the automotive industry as energy absorbing materials. The model uses a pseudo visco-hyperelastic formulation whereby the strain energy potential is constructed numerically as a function of principal stretches and a set of internal variables associated with strain rate. The model is based on the assumption that the Poisson's ratio of the material is zero. With this assumption, the evaluation of the stress-strain response becomes uncoupled along the principal deformation directions. Additionally, this material model allows for the optional specification of unloading rate-dependent stress-strain curves in order to represent the hysteretic behaviour and energy absorption during cyclic loading.

In this material model, the stresses σ_{ij} are taken as the summation of two contributions:

$$\boldsymbol{\sigma_{ij} = \sigma^{f}_{ij} + \sigma^{r}_{ij}} \tag{A.4}$$

where σ^{f}_{ij} is the hyperelastic component while σ^{r}_{ij} is the rate-dependent (i.e. viscoelastic) component.

The hyperelastic component σ^{f}_{ij} is a function of the nominal stress τ_i:

$$\boldsymbol{\sigma_i = \frac{\tau_i}{\lambda_j \lambda_k}} \tag{A.5}$$

where τ_i are defined as a function of elongations ε_i which are defined in terms of principle stretches λ_i:

$$\boldsymbol{\varepsilon_i = \lambda_i - 1} \tag{A.6}$$

The rate-dependent component σ^{r}_{ij} is given by the following convolution integral:

$$\boldsymbol{\sigma^{r}_{ij} = \int_0^t g_{ijkl}(t - \tau) \frac{\partial \varepsilon_{kl}}{\partial \tau} d\tau} \tag{A.7}$$

where $g_{ijkl}(t - \tau)$ is the relaxation function.

To calibrate this material model, stress-strain response of the material under both tension and compression were required as input data. Stress-strain data for different strain rates could be specified. In this study, the compressive stress-strain data obtained here as shown in Figure A.2 was used. On the other hand, due to the absence of tensile test data for the cork material used in this study, the tensile behaviour reported by Moreira *et al.* (2010) as depicted in Figure A.3 was used as an approximation even though their cork material was not the same as the one used here.

A.4. Crushable foam

Crushable foam is a plasticity constitutive model that accounts for the difference between a foam's compressive strength which is due to cell wall buckling and its much smaller tensile strength that results from fracture of cell walls under tension. Unlike hyperfoam, which is a hyperelastic material model, deformation of the material in crushable foam is irreversible as it can undergo permanent (plastic) deformation. For example, Masso-Moreu and Mills (2004) used crushable foam to study the response and isotropy of extruded polystyrene, low density polyethylene (LDPE), and polypropylene bead foams.

Crushable foam model assumes that the material is linear elastic until the onset of plastic deformation. For the plastic behaviour of the material, the yield surface is a Mises circle in the deviatoric stress plane and an ellipse in the meridional (*p*-*q*) stress plane as depicted in Figure A.4. Two hardening models are available: (a) isotropic hardening, and (b) volumetric hardening. For isotropic hardening model the yield ellipse is centered at the origin of the *p*-*q* stress plane and evolves in a geometrically self-similar manner. It assumes that the material has similar behaviours in both hydrostatic tension and hydrostatic compression.

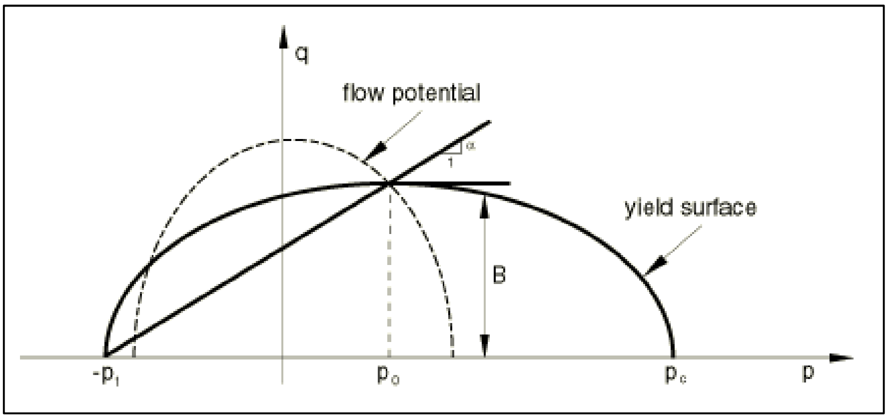

Figure A.4: Typical yield surface and flow potential for the crushable foam model (ABAQUS, 2012).

On the other hand, in the volumetric hardening model a point on the yield ellipse in the meridional plane represents fixed hydrostatic tension loading while the evolution of the yield surface is driven by the volumetric compacting plastic strain. In other words, when the volume of the foam reduces (i.e. the density of the foam increases), it hardens and the yield stress in hydrostatic compression p_c as shown in Figure A.4 moves to the right while the strength of the material in hydrostatic tension p_t remains constant. Also, since the plastic Poisson's ratio is assumed to be zero for crushable foam, the plastic volumetric strain is equal to the plastic axial strain.

In this study, volumetric hardening is more appropriate for cork since it shows significant differences in behaviour under compression and tension as mentioned in Section A.1. In order to calibrate crushable foam with volumetric hardening, the initial yield stress in uniaxial compression σ_c^0, initial yield stress in hydrostatic compression p_c^0, and the yield strength in hydrostatic tension p_t are required to obtain the strength ratios k and k_t as shown in Equations A.8 and A.9. These parameters are needed to define the shape of the yield surface.

$$k = \frac{\sigma_c^0}{p_c^0} \tag{A.8}$$

$$k_t = \frac{p_t}{p_c^0} \tag{A.9}$$

Generally, the choice of tensile strength should not have a strong effect on the numerical results unless the foam is stressed in hydrostatic tension. A common approximation is to set p_t equal to 5 percent to 10 percent of p_c^0 (ABAQUS, 2012).

Besides the parameters mentioned above, the Young's modulus and hardening stress-strain data under uniaxial compression are also required as input data. They must be given in the form of uniaxial compressive stress versus true plastic strain.

For the cork material used in this study, the strength ratio k was assumed to be 1.0 since the Poisson's ratio was taken as zero. Based on Figures A.2 and A.3, k_t was assumed as 1.33. The hardening data was extracted from the uniaxial compressive stress-strain response shown earlier in Figure A.2 while the Young's modulus of the cork used in this study is 88 MPa. Uniaxial tensile test data is not required in this material model as the tensile behaviour of the model is controlled by the k_t value.

A.5. Comparison of different material models

Figure A.5 displays the uniaxial compressive stress-strain curve of the cork predicted by the three material models as well as the one obtained experimentally in this study, while Table A.3 summarizes the input data used for the material models. It is apparent that the hyperfoam and low-density models show good agreement with the experimental results up to a compressive strain of 60 percent. The crushable foam model is able to reproduce the same general behaviour but over-predicts the compressive stress-strain response of the cork. This might be caused by the assumption that the Poisson's ratio of the cork is zero. For cellular materials such as cork, the Poisson's ratio is generally

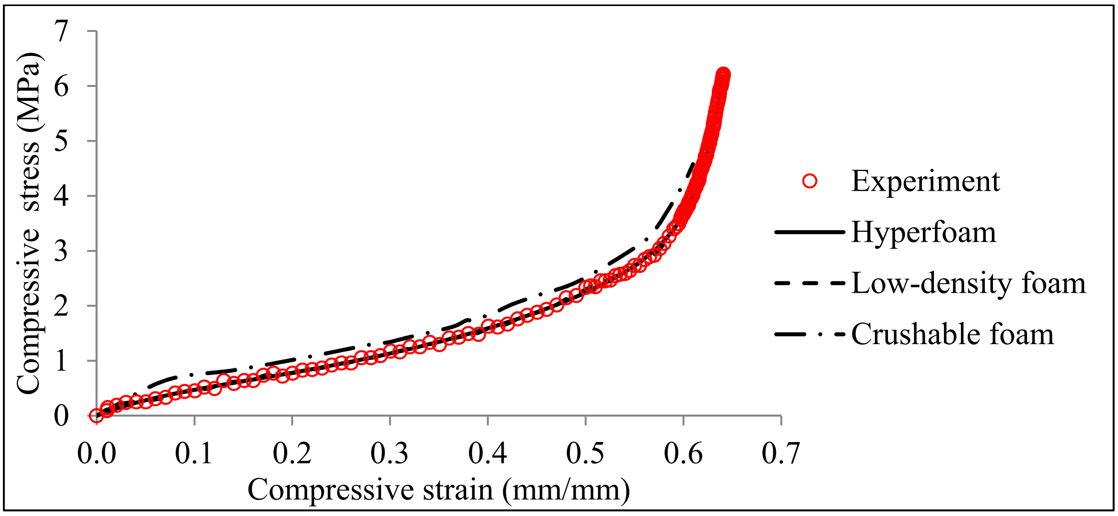

Figure A.5: Uniaxial compressive (engineering) stress-strain curves of cork obtained using different material models.

Table A.3: Summary of input data for material models for cork.

No.	Material Model	Input Data
1	Hyperfoam	• Uniaxial compressive test data • Poisson's ratio = 0
2	Low-density foam	• Uniaxial compressive test data • Uniaxial tensile test data
3	Crushable foam	• $k = 1.0$ • $k_t = 1.33$ • Foam hardening data • Young's Modulus = 88 MPa • Poisson's ratio = 0

close to zero throughout the plateau stage but it actually increases rapidly with strain during the densification stage.

Figure A.6 presents the uniaxial tensile stress-strain curve of the cork predicted by the three material models as well as the one obtained experimentally by Moreira *et al*. (2010). It is clear that the low-density foam model follows the trend of the tensile behaviour obtained from experiment well. On the other hand, the crushable foam model significantly under-predicts the tensile strength and stiffness of the cork. The volumetric hardening model in crushable foam assumes an elastic-perfectly plastic behaviour under hydrostatic tension. Lastly, the tensile behaviour predicted using the hyperfoam model has a completely different trend compared to the experimental results; the hyperfoam model over-estimates the tensile stiffness of the cork. This may be because only the uniaxial compressive test data was used here in calibrating this material model. Experimental simple shear response is also required as input in order to more accurately predict the tensile behaviour of the cork, but the simple shear stress-strain data for the cork used in this study was not available.

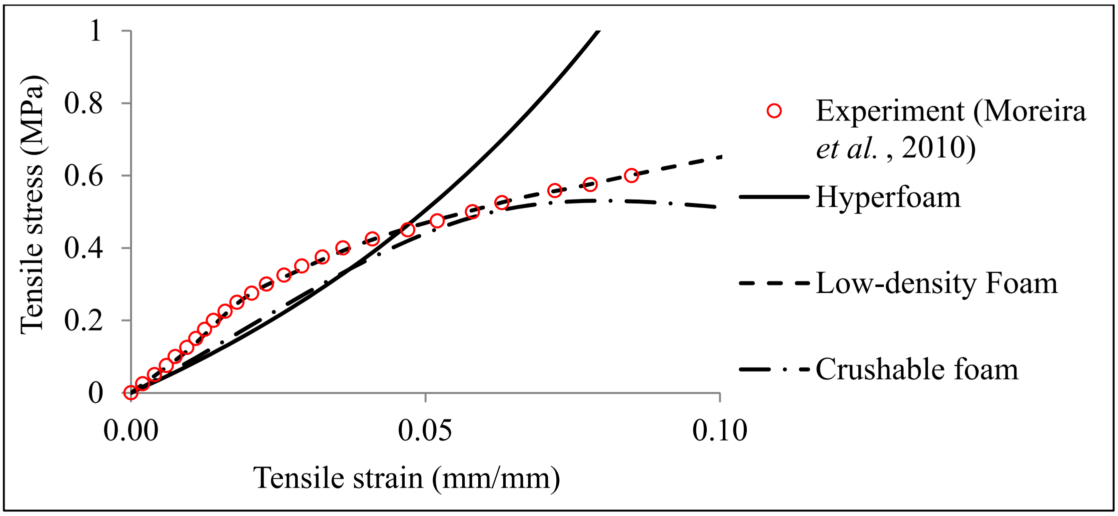

Figure A.6: Uniaxial tensile (engineering) stress-strain curves of cork obtained using different material models.

In conclusion, based on the limited experimental data in this study, the low-density foam model produces the best approximation for the constitutive behaviour of cork compared to hyperfoam and crushable foam. Hence, low-density foam was used to model cork throughout this work.

A.6. Effect of tensile stress-strain data of cellular layer on overall response of the composite system

As mentioned earlier in Section A.3, uniaxial compressive and tensile stress-strain data are required to calibrate the low-density foam material model for the underlying cellular layer which was first represented by cork. However, only the uniaxial compressive stress-strain data was available for the cork material used in this study, while the tensile data was obtained from Moreira *et al.* (2010) even though their cork material was different from the one used here. Hence, similar numerical simulations shown in Section 3.1 were conducted with different tensile stress-strain data of the cork layer to examine its influence on the numerical simulations. This was achieved by multiplying the stress values of the tensile stress-strain data in Moreira *et al*. (2010) with a constant factor *c* while keeping the strain values fixed as shown in Figure A.7. Thus, *c* = 1.0 is the original tensile stress-strain curve, while *c* = 10.0 and *c* = 0.1 are cases where the tensile resistance of the cork is higher and lower, respectively, than the original one.

Figure A.8 presents the overall impact force-time response for Specimen 1 (as shown earlier in Figure 3.1) with these different tensile stress-strain data. It is found that there is no observable difference between the results. This demonstrates that tensile behaviour of the underlying cork layer does not dominate the deformation of the fish scale-cellular composite system when it is subject to impact loading. Hence, using the uniaxial tensile stress-strain data from Moreira *et al.* (2010) to calibrate the low-density foam model adopted for the cork layer does not affect the accuracy of the numerical simulations. Thus, this tensile stress-strain data was adopted for the cork material used in this study.

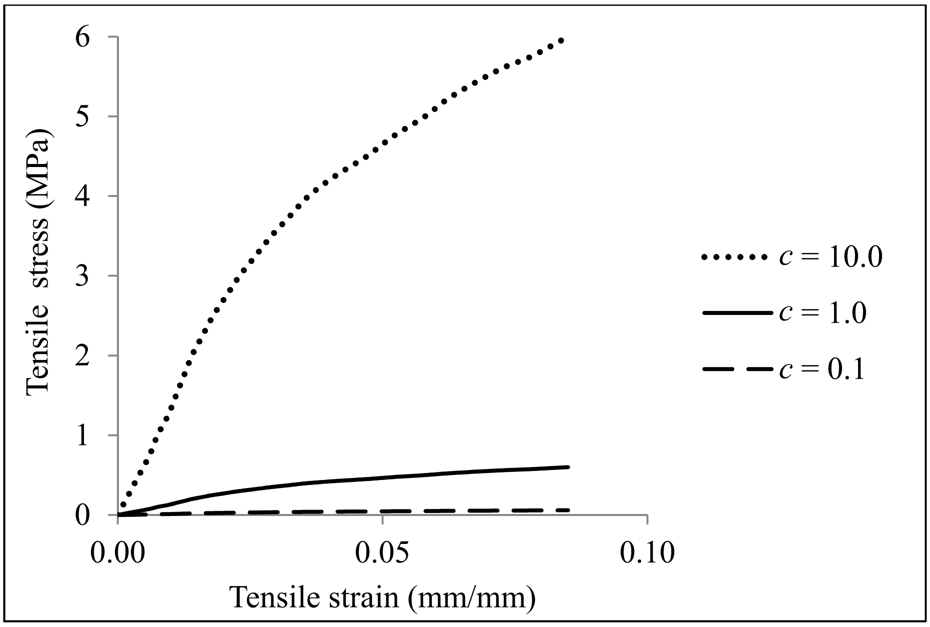

Figure A.7: Uniaxial tensile stress-strain curve with varying *c* values for cork.

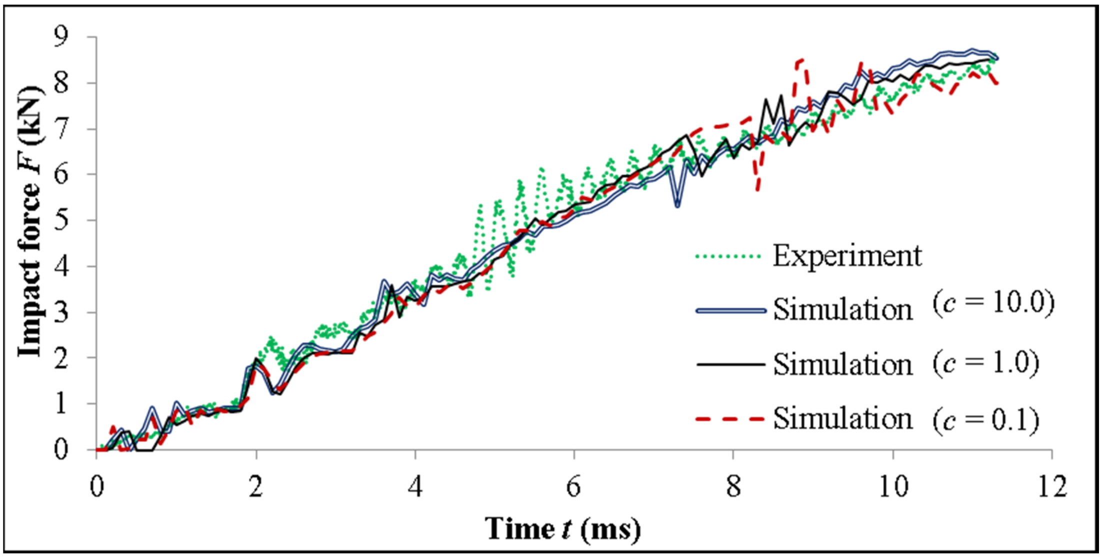

Figure A.8: Impact force-time response for Specimen 1 with various uniaxial tensile stress-strain data for the underlying cork layer.

Appendix B: Material characterization of 3D-printed acrylonitrile butadiene styrene and polyethylene foam

For the purpose of experimental validation in Section 3.3, 3D-printed acrylonitrile butadiene styrene (ABS) was chosen as the material for the scales and top plate. On the other hand, polyethylene (PE) foam was selected as the underlying cellular material in order to preserve the material stiffness and strength ratios between the scales and the underlying layer as those for aluminium and cork used in the simulations. Characterization tests were performed in order to determine the mechanical properties of these materials.

B.1 Acrylonitrile butadiene styrene

ABS was chosen as the material for the scales since it is known to be tough, is readily available, and can be formed into complex shapes using relatively low cost 3D printing. However, the material properties of 3D-printed ABS cannot be obtained from existing references such as ASTM D4673 because 3D-printed objects have different properties from those that are made through conventional means. Also, the material properties could also be affected by the specific type or model of the 3D printer used. Furthermore, infill density, layer height and infill pattern also affect the strength of 3D-printed material (3D Matters, 2015). Therefore, three-point bending tests were carried out in this study to determine the material properties of the 3D-printed ABS so as to assess whether it is suitable to be used as the material for the scales. The tests were performed following ASTM D790. Six 3D-printed ABS strips measuring 50 mm x 12.7 mm x 2 mm were produced using melted extrusion manufacturing and were tested using an Instron 5969 universal testing machine respectively for infill densities of 50 %., 75 %, 100 %. A typical force-displacement curve obtained from the tests is shown in Figure B.1.

The Young's modulus E of the 3D-printed ABS may be determined based on the slope m of the force-displacement curve during the elastic stage:

$$E = \frac{mL^3}{4bd^3} \tag{B.1}$$

where L, b and d are the span, width and thickness of the specimen respectively. On the other hand, the yield strength σ_y of the material may be determined based on the peak force P and assuming that the loaded section is fully plastic when the peak load is reached:

$$\sigma_y = \frac{PL}{bd^2} \tag{B.2}$$

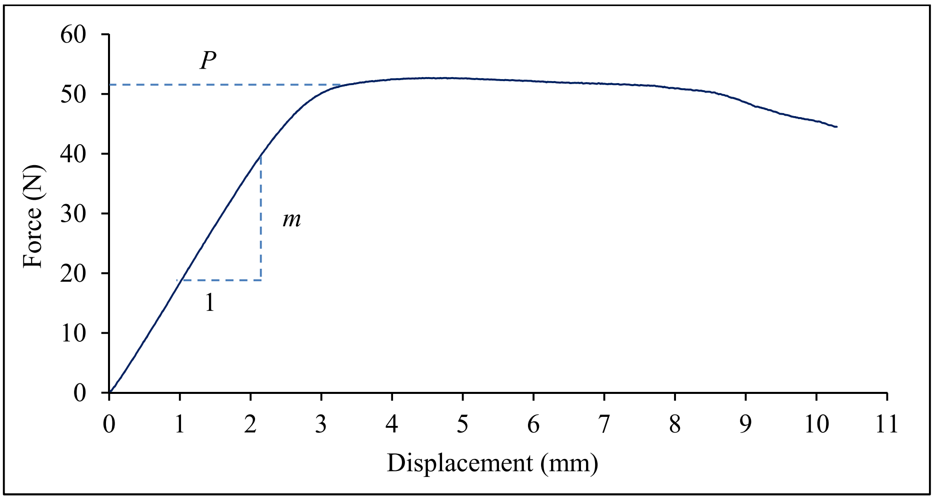

Figure B.1: Typical force-displacement curve obtained from the bending test of 3D-printed ABS specimens.

Table B.1: Young's modulus and yield strength of 3D-printed ABS specimens with different infill densities.

Infill density (%)	50	75	100
Young's modulus E (GPa)	1.8 ± 0.5	1.8 ± 0.2	1.8 ± 0.2
Yield strength σ_y (MPa)	36.1 ± 0.6	36.2 ± 0.6	36.2 ± 0.5
Density (kg/m^3)	1025 ± 5	1036 ± 6	1038 ± 2

Based on the average results shown in Table B.1, the Young's modulus and the yield strength of the 3D-printed ABS are 1.83 ± 0.03 GPa and 36.1 ± 0.6 MPa respectively. It was found that the infill density of 3D-printed ABS specimens does not influence its material properties significantly as shown in Table B.2. This may be due to the high area to volume ratio of the specimens. Despite of the difference in infill density, the surface finishing of the ABS specimens remained rather constant. This is reflected by the insignificant changes in the density of the ABS specimens with various infill densities.

B.2 Polyethylene foam

As mentioned in Section 3.3, the key principle in the selection of materials for the composite specimens in the experimental work is to preserve the material stiffness and strength ratios between the scales and the underlying layer as those used in the numerical simulations. Based on the material properties of aluminium and cork reported in Section 2.3, these stiffness and strength ratios are 790 and 270 respectively. Thus, if 3D-printed ABS is used as the material for the scales instead of aluminium, the underlying layer should have lower stiffness and strength compared to cork but with similar stiffness and strength ratios to ABS as those for aluminium and cork.

A number of candidate cellular materials which are readily available, mainly polymeric foams, were considered for the underlying layer in the experiments. Among these materials, polyethylene (PE) foam with density of 64 kg/m^3 seemed to be the best option. To test its suitability as the underlying cellular layer, uniaxial dynamic compression test on the foam was performed using a drop-weight impact machine as shown in Figure B.2 (the same setup as the one shown in Figure 2.8 was used, but without the wedge impactor). The dimensions of the foam specimens were 200 mm x 50 mm x 50 mm. Figure B.3 shows a typical compressive stress-strain curve of the polyethylene foam.

From Figure B.3, it can be noted that the PE foam shows the same type of compressive response as cork which was shown earlier in Figure 2.4. The foam undergoes elastic deformation up to a compressive strain of around 10 percent and then reaches a plateau stage between compressive strains of 10 percent and 50 percent, before finally undergoing densification after the compressive strain exceeds approximately 50 percent. Based on the stress-strain curve shown in Figure B.3, the Young's modulus of the PE foam is approximately 1 MPa. The strength of the foam, which for cellular materials may be taken as the average stress in the plateau region, is around 0.14 MPa. Lastly, since there was no observable lateral deformation during the compression test, the Poisson's ratio of the foam may be assumed to be zero.

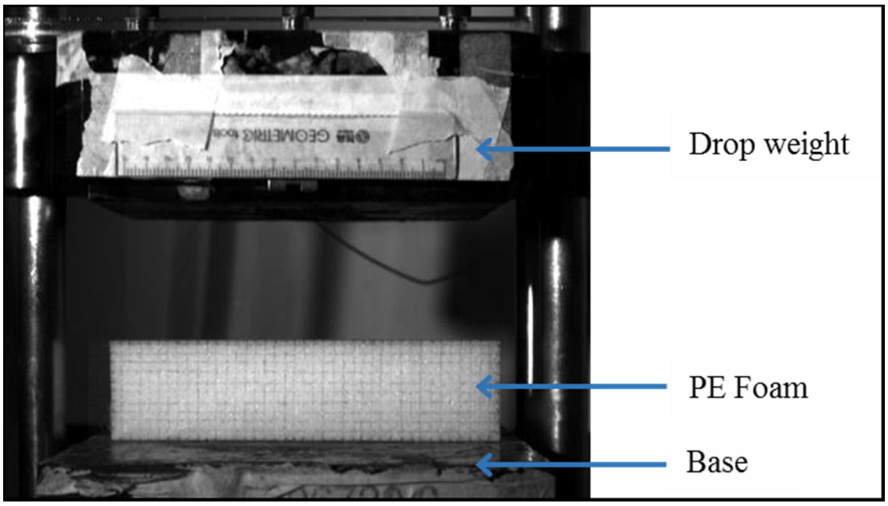

Figure B.2: Experimental setup for dynamic uniaxial compressive test of polyethylene foam.

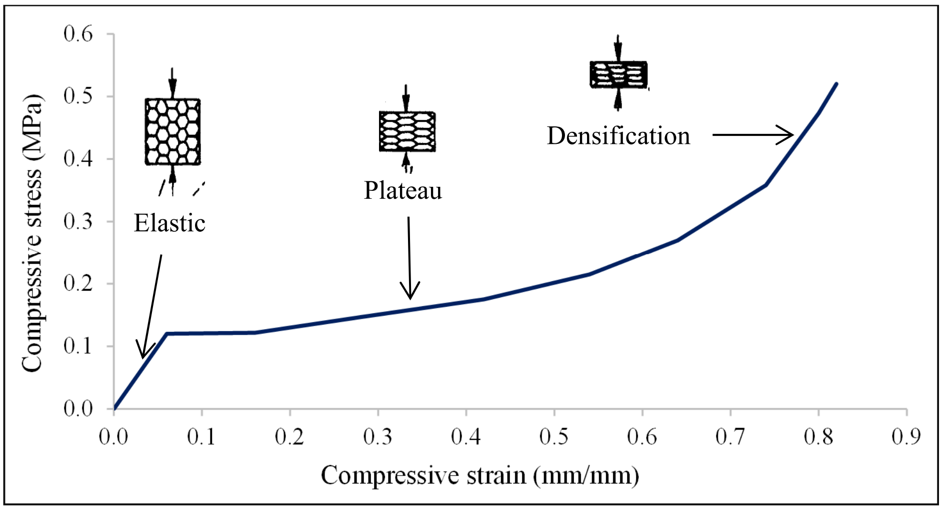

Figure B.3: Typical uniaxial compressive stress-strain curve of polyethylene foam.

Appendix C: List of publications

Chua, Y.S., Law, E., Pang, S.D and Quek, S.T. (2013). Fishscale Structure and Cork Composite System for Protection against Projectile Loading. *26th KKHTCNN Symposium on Civil Engineering, National University of Singapore, Singapore, November 18 – 20.*

Chua, Y.S., Law, E., Pang, S.D. and Quek, S.T. (2014). Bio-Inspired Fishscale-Cellular Composite System for Protection against Penetration Loads: A Proof of Concept Study. *ECCM16 - 16th European Conference on Composite Materials, Seville, Spain, June 22 – 26.*

Chua, Y.S., Law, E., Pang, S.D. and Quek, S.T. (2015). Finite Element Analysis of Fish Scale Structure-Cork Composite System under Low-Velocity Impact. *South East Asia SIMULIA Regional Users' Conference, Singapore, October 15 – 16.*

Chua, Y.S., Law, E., Pang, S.D. and Quek, S.T. (2015). Fish Scale-Cellular Composite Structure under Low-Velocity Impact. *28th KKHTCNN Symposium on Civil Engineering, Chulalongkorn University, Thailand, November 16 – 18.*

Chua, Y.S., Law, E., Pang, S.D. and Quek, S.T. (2016). Fish Scale-Cellular Composite System for Protection against Low-Velocity Impact. *Composite Structures* **145**: 217-225.

Chua, Y.S., Law, E., Pang, S.D. and Quek, S.T. (2016). Design Optimization of A Fish Scale-Cellular Composite System for Protection against Localized Impact. *International Journal of Solids and Structures* (under review).